A HYDRODYNAMIC CHARACTERIZATION OF SALTMARSH ECOSYSTEMS

A Thesis
Presented to
The Academic Faculty

by

David Louis Young

In Partial Fulfillment
of the Requirements for the Degree
Doctor of Philosophy in the
School of Civil and Environmental Engineering

Georgia Institute of Technology
August 2016

A HYDRODYNAMIC CHARACTERIZATION OF SALTMARSH ECOSYSTEMS

Approved by:

Dr. Donald R. Webster, Advisor
School of Civil and Environmental Engineering
Georgia Institute of Technology

Dr. Philip J. Roberts
School of Civil and Environmental Engineering
Georgia Institute of Technology

Dr. Kevin A. Haas
School of Civil and Environmental Engineering
Georgia Institute of Technology

Dr. Marc J. Weissburg
School of Biology
Georgia Institute of Technology

Dr. Hermann M. Fritz
School of Civil and Environmental Engineering
Georgia Institute of Technology

Date Approved: 04/22/2016

ACKNOWLEDGEMENTS

I am grateful to so many individuals who helped me along the path to submitting this thesis that I could write another thesis on all of your contributions. This section is in no way a complete list of all the assistance I have gotten to make it here. As hard the Masters thesis was on me, finishing this Ph.D. thesis has been comfortably worse. I've wanted to just walk away for a long time, and I want to thank everyone who encouraged me to keep my eyes on where I wanted to be ten years from now, rather than how miserable I was each day.

First and foremost I want to thank my Lord and Savior, Jesus Christ. Thank you for carrying me through this, because you know I did not have the strength for it. Thank you for all the blessings I have received, none of which I deserve. The greatest of these blessings is my beautiful, amazing, and brilliant fiance, Dr. Brittany Bruder. No matter how this turns out, all this time I have spent at Georgia Tech was more than worth it, so that I could get to know you. Thank you for believing in me and sticking with me through this! I cannot wait to start our life together. Next up, and unquestionably the blessings most responsible for me being here today, are my parents, Louis and Danita Young. I don't know what the future holds for me, but I do know that you two are to thank for everything I have and will accomplish. I especially want to thank the two of you for coming down to visit me in Savannah in the summer of 2016. When Brittany was in Delaware, the inflatable boat had holes all in it, the instruments were stolen, and it seemed like I would never be able to leave Savannah, let alone graduate, you were there for me. As with every difficult thing I have experienced in my life, there is no way I would have persevered without you.

I've heard that most important element required to successfully submit a Ph. D.

thesis is a good advisor. Fortunately, I have been blessed with the best advisor in Civil Engineering, possibly all of Georgia Tech, Dr. Don Webster. Thank you for this opportunity, and perhaps more importantly, thank you for your wisdom, patience, and your commitment to me. I know you have new responsibilities as associate dean, so I particularly want to thank you for keeping your door open to me, even when I am sure you might have preferred to close it for a moments peace. I'm also grateful to the rest of my committee, Dr. Kevin Haas, Dr. Philip Roberts, Dr. Hermann Fritz, and Dr. Marc Weissburg. Thank each of you for taking the time to review and help me improve my work. One committee member in particular went out of their way for this thesis. Dr. Haas was instrumental in formulating the idea and experimental design for the marsh vegetation chapter of this study. Additionally, when Brittany and I were out tromping through the mud in the marsh, Dr. Haas was right out there with us, and has the pictures to prove it. He also helped me work through several issues I has analyzing the data for that chapter, as well as the chapter on removing wave bias from ADV measurements. So thank you Dr. Haas.

Although we wound up having to scrap that whole section of the study, I want to thank Andy Udell and Blake Baklini for helping me build those ADV stands. The stands worked great, by the way. Andy really deserves an acknowledgment for my entire graduate career. Thank you Andy, for helping me with the hundred things that came up along the way.

Lastly, I want to thank my current and former lab-mates, in particular Dr. Aaron True, John Jung, Anna Skipper, and Dr. Deepak Adhikari. Aaron, I was so happy for you when you finished up, but Anna is not as good at pep-talks as you are. I have no idea how you managed to stay positive all the way to the end. That is a very impressive feat in my book. Thanks for getting me through my first two-and-a-half years in the lab. John graduated and moved on five months ago, so well done John! However, he was here for at least the first seven months of my worst year in

graduate school (and the year before that), and I'm sure that was plenty of time to hear me complain enough for the rest of his life. Thanks for going to lab lunch with me anyway, and managing not to punch me. Although she started at the same time as John, Anna is staying to pursue the Ph.D., so... good luck and have fun! She is much better at telling people to suck it up and quit whining then she is at pep-talks. Sometimes I needed someone to tell me that, even when I didn't like it. She is also the longest suffering of the Mason 2230 dwellers that were forced to deal with me towards the end. So thank you Anna for still going to lab lunch with me anyway! Also, thank you for your book suggestions and being an avid Game of Thrones fan. Finally, I am thankful to Deepak for a lot of things, including attending lab lunch with miserable me. What I perhaps enjoyed the most was the chance to talk to you about the differences between the United States and other places around the world. I've never been to another country, and I really enjoy talking to you to get a different perspective. We have talked about everything, from things as serious as the justice system in Singapore to things as benign as the pedal layout on a manual transmission car in the United Kingdom. I really appreciate how thoughtful you are, so that our discussions were always enjoyable and informative. The world would be much better off if more people were that way.

TABLE OF CONTENTS

LIST OF TABLES

LIST OF FIGURES

SUMMARY

In the studies presented in this thesis, we examine hydrodynamics of saltmarsh ecosystems at two spatial scales. The first is an assessment of tidally-driven surface flow through the saltmarsh. We find substantial water level differences between the estuary channel and the neighboring saltmarsh and correspondingly large pressure gradients, which strongly affect the flow in the marsh. At one marsh location, where the flow is unrestricted by bathymetry, the pressure gradient governs the flow through the marsh vegetation. At this location, the flow is effectively modeled as a balance between the pressure gradient force and the drag force due to marsh vegetation and bottom stress using the Darcy-Weisbach/Lindners equations developed for flow-through-vegetation analysis in open channel flow.

The second is an examination of the concentration field and turbulent mixing of meandering turbulent plumes, which are commonplace in both natural settings and in engineering applications. While much is known about the concentration field and turbulent mixing in straight plumes, comparatively little is understood regarding the dynamics of meandering plumes - partially due to the difficulty in separating the plume meander fluctuations from the turbulent fluctuations. To address this, we acquired simultaneous laser induced fluorescence (LIF) and particle image/tracking velocimetry (PIV/PTV) data of a phase-locked meandering plume as well as LIF for a straight plume for comparison. Analysis of the LIF data reveals that, compared to the straight plume, the centerline concentration of the meandering plume decreases more rapidly with distance downstream, and the plume width increases more rapidly with distance downstream, resulting in more rapid dilution of tracer concentration.

The PIV velocity analysis indicates the large-scale alternating vortices induced by the diverting plate are the dominant feature of the meandering plume, forcing the plume meander as well as governing the spatial variation of the mean concentration, Reynolds stress, turbulent kinetic energy (TKE), and turbulent flux. Finally, comparison of the turbulent flux measurements with the mean concentration field indicates that the eddy-diffusion hypothesis effectively models the turbulent flux in the plume. We found that when the plume width is less than the size of the large-scale alternating vortices, the eddy-diffusion coefficient scales with the plume width to the 3/4 power, and when it is greater than the size of the large-scale alternating vortices eddy-diffusion coefficient is constant ($K_{y_0} = 0.15Hu^*$), where H is water depth and u^* is the shear velocity.

As turbulence plays a key role in both flow through vegetation and the dynamics of turbulent plumes, the ability to describe and quantify turbulence is a key aspect of any hydrodynamic analysis in saltmarsh ecosystems. Unfortunately for field studies in estuarine and coastal settings, calculating turbulence characteristics, such as the Reynolds stress, TKE, and turbulence intensity, is complicated by the orbital velocity of surface waves remaining after subtraction of the mean velocity. In the final portion of this thesis, a new single-instrument method for removing wave bias from Reynolds stress estimates is proposed. This method is compared to two frequency-domain-based single-instrument techniques and a two-instrument method that uses a linear-filtration procedure of data collected from an adjacent instrument to remove the wave signal. The method proposed in this study offers superior performance over the other single-instrument techniques in shallow water, comparing favorably with the two-instrument method and thereby offering a more financially and logistically efficient means of removing wave bias.

CHAPTER I

INTRODUCTION

Saltmarshes in coastal estuaries are highly diverse, valuable, and productive ecosystems. The health of the estuarine and saltmarsh ecosystems and the benefits they provide are mediated, in large measure, by the hydrodynamics of the estuary, which are in turn influenced by the topographic and bathymetric features of the estuary. For example, the vegetation of estuarine saltmarshes can dampen wave and current energy from offshore storm systems (e.g., hurricanes), thereby acting as a buffer between these storms and the adjacent uplands [Allen, 2000, Gedan et al., 2011, Spalding et al., 2013]. Dampened estuarine currents allow the estuaries to serve as nursery habitats for numerous shellfish and fish species. Additionally, tidal hydrodynamics facilitate the transport of vital nutrients and tracers into and out of the estuary (during flood and ebb tides), affecting both inshore and offshore vegetation and animals [Alongi and Robertson, 1995, Mathieson et al., 2000, Mann and Lazier, 2006]. At smaller scales, turbulent flow downstream of biotic structures, such as oyster reefs, has been shown to affect foraging success of various predators [Ferner and Weissburg, 2005, Wilson and Weissburg, 2013] and the ability of the prey to detect predators [Smee and Weissburg, 2006].

1.1 Flow in the Vegetated Marsh

Significant effort has been devoted to understanding estuarine hydrodynamics at a variety of scales. At the scale of the full estuary, many studies attempt to model the tidally-driven flow of water into and out of the estuary. Perhaps the most critical role of these modeling studies is estimating the net flux of sediment or tracer quantities either through the estuary or between the estuary and the ocean. In

particular, the relative strength and duration of flood and ebb tide governs whether sediment, nutrients, and tracers move into or out of the estuary [Dronkers, 1986, Blanton et al., 2002]. Net flux of sediment out of the estuary (resulting from larger ebb tidal currents than flood tidal currents) has been linked to the presence of extensive vegetated saltmarshes adjacent to the estuary channels[Boone and Byrne, 1981, Speer and Aubrey, 1985, Dronkers, 1986, Friedrichs and Aubrey, 1988, Parker, 1991, Blanton et al., 2002, Zheng et al., 2003, Bruder et al., 2014]. However, despite its obvious importance to the estuary flow characteristics, the flows in the vegetated saltmarsh and between the saltmarsh and the neighboring estuarine channel are significantly less understood than the flows in the estuarine channels themselves, or in the network of tidal creeks that branch into the marsh [Allen, 2000, Mazda et al., 2007, Horstman et al., 2013].

The principle challenges to field studies investigating flow in the vegetated saltmarsh are the difficulty of (1) making flow measurements in the dense vegetation, and (2) acquiring sufficiently accurate water surface elevation measurements to quantify the forcing pressure gradient over comparatively small length scales [Horstman et al., 2013]. Consequently, although modeling results have shown that a channel-to-saltmarsh pressure gradient (i.e., differential water levels between the estuary main channel and the adjacent saltmarsh) was responsible for the surface transport of water between the saltmarsh and the neighboring channel at high spring tide [Bruder et al., 2014], we are aware of only a single published field study [Vandenbruwaene et al., 2015] that shows the presence of the differential water level. Further, the flow between the saltmarsh and the neighboring channel in Bruder et al. [2014] is very sensitive to the parameterization of the bottom stress in the marsh. However, these tidal modeling studies (e.g. Kjerfve et al. [1991], Huang et al. [2008], Bruder et al. [2014]) are unable to validate their parameterization of the vegetation-induced bottom stress in the marsh. This is due to the lack of direct flow measurements in the dense

vegetation coupled with the dearth of precise water surface elevation measurements in the marsh, which make it difficult to relate the flow through the saltmarsh vegetation to the quantitative relationships between the pressure-gradient and the velocity developed for pressure gradient-driven flow through vegetation in flumes. **In this study we will explore the relationship between the pressure gradient and the flow through the saltmarsh vegetation in the high marsh and apply a flume-developed flow-through-vegetation formulation to the problem.**

1.2 Scalar Plumes with Meander

At smaller scales, the movement of scaler quantities (such as chemical tracer) in a variety of flows, including estuarine flows, is an area of substantial interest. A release of a scalar quantity into a mean flow field of sufficiently high Reynolds number results in a turbulent plume, which is commonplace in both natural settings and in engineering applications [Crimaldi et al., 2002]. Odorant plumes from a food source tracked by crustaceans [Weissburg and Zimmer-Faust, 1993, 1994, Moore and Grills, 1999] and chemical releases from underwater munitions [Webster, 2007] are examples of turbulent plumes of scalar quantities that may be encountered in estuarine or coastal settings.

In many applications (such as the crustacean tracking example) the plume may be released near the bed, in which case the plume interacts with the bottom turbulent boundary layer. The dynamics of straight plumes (i.e., transport by a uni-directional mean flow) developing in a turbulent boundary layer have been extensively studied in laboratory settings [Fackrell and Robins, 1982, Bara et al., 1992, Yee et al., 1993, Crimaldi and Koseff, 2001, Crimaldi et al., 2002, Webster et al., 2003, Rahman and Webster, 2005, Crimaldi and Koseff, 2006] and their dynamics are comparatively well understood. The studies consider (among other things) the transverse and vertical profiles of the time-averaged concentration and concentration variance at positions

downstream of the plume source and whether these profiles are self-similar. Many studies also present PDF's of the concentration at various locations within the plume, which can be easily compared to field study results. In particular, these PDF's are commonly presented in field studies of scalar plumes released into the atmospheric boundary layer [Murlis and Jones, 1981, Jones, 1983, Murlis, 1986, Hanna and Insley, 1989, Mylne, 1992, 1993, Yee et al., 1994, 1995].

While much is known regarding the dynamics of straight plumes, many naturally occurring plumes meander, which is defined as large scale movement of the plume centerline. This phenomena is most commonly observed in atmospheric plumes [Thompson and Gower, 1977, Sykes, 1984, Wilson et al., 1985, Hanna, 1986, DeFelice et al., 2000], but also would be expected to occur in flows that naturally oscillate, such as the wake flow past a cylinder (the von Karmen vortex street) or other bluff body (e.g. islands in coastal seas or estuaries - Wolanski et al. [1984], Ingram and Chu [1987], Cramp et al. [1991], Fong and Stacey [2003]). Many of the studies that attempt to describe meandering atmospheric plumes struggle to separate fluctuations due to the movement of the plume centerline from the turbulent fluctuations [Yee et al., 1994, Luhar et al., 2000, Reynolds, 2000, Yee and Wilson, 2000, Franzese, 2003, Mortarini et al., 2009, Nironi et al., 2015, Marro et al., 2015, Mortarini et al., 2009]. In an attempt to model the plume, many of these studies resort to convolutions of a PDF of the location of the plume centerline (or the instantaneous location of the cloud centroid) with a PDF of the concentration in a frame of reference along the instantaneous centerline, under the assumption that the two are uncorrelated. **In this study, we will begin to fill in the knowledge gap regarding the structure and mixing of a meandering near-bed turbulent plume (released downstream of an oscillating bluff body). The fixed-frequency paddle motion allows the measurements to be phase-locked, which in turn allows us to separate the large scale plume meander from turbulent fluctuations. The mixing and**

mechanics will be compared to the results for a near-bed straight plume.

1.3 Removing Wave Bias from Reynolds Stress Estimates

The flow through vegetation and the mixing and mechanics of both straight and meandering plumes are critically affected by turbulence. In the case of flow through vegetation the turbulence in the wake of the plants mediates the drag experienced by the flow. Additionally, the tracer mixing in a turbulent plume is dominated by the turbulent flux of the scalar quantity as opposed to the molecular diffusion of the tracer. The rapid mixing of scalars is in fact a defining characteristic of turbulent flows [Tennekes and Lumley, 1972].

As a result, the ability to describe and quantify the turbulence is a key aspect of any hydrodynamic analysis, and estuarine and coastal hydrodynamics are no exception. Unfortunately for field studies in estuarine and coastal settings, calculating turbulence characteristics, such as the Reynolds stress, turbulent kinetic energy (TKE), and turbulence intensity, is complicated by the presence of surface waves. Wave velocity is orbital in nature, thus simple subtraction of the mean velocity defines a fluctuation that includes both a wave and a turbulence component [Dean and Dalrymple, 1991, Trowbridge, 1998]. The orbital wave motions do not directly contribute to the turbulent mixing of momentum or tracer. Therefore, they must be removed from the estimates of turbulent flow characteristics to properly describe the mechanics and mixing. Further exacerbating the issue, surface waves in coastal environments frequently contain several orders of magnitude more energy than the turbulent fluctuations [Grant et al., 1984, Grant and Madsen, 1986, Huntley and Hazen, 1988, Trowbridge, 1998]. Thus, additional data processing is required to separate the turbulence and wave components, else estimates of the Reynolds stresses and TKE will drastically overstate the true value as a result of the wave contamination.

Perhaps the most accepted data processing techniques are the family of two-instrument techniques following the velocity differencing methodology of Trowbridge [1998], e.g., Trowbridge [1998], Shaw and Trowbridge [2001], and Feddersen and Williams [2007], which have proven effective in the offshore [Shaw and Trowbridge, 2001] and nearshore [Feddersen and Williams, 2007] regions. However, as the name suggests, these techniques require two instruments placed nearby to simultaneously measure what is effectively the same signal. Obviously, it is desirable from both a financial and logistical standpoint to make use of a technique that requires a single instrument. Single-instrument techniques have been proposed that rely on frequency domain analysis to separate the wave signal from the turbulence signal [Bricker and Monismith, 2007, Wilson et al., 2013], but they suffer in effectiveness if the wave motions occupy the same frequency range as the turbulent fluctuations contributing to the Reynolds stress [Trowbridge, 1998]. Unfortunately, this is a common occurrence in many oceanic flow situations including coastal estuaries. **Consequently, we propose a new single-instrument method for removing wave bias from Reynolds stress estimates based upon the linear filtration scheme of Shaw and Trowbridge [2001] as opposed to a frequency-based decomposition. We will compare this new method to two published frequency-based single-instrument techniques [Bricker and Monismith, 2007, Wilson et al., 2013] and a published two-instrument technique [Feddersen and Williams, 2007].**

CHAPTER II

THE HYDRODYNAMICS OF SURFACE TIDAL FLOW EXCHANGE IN SALTMARSHES

2.1 Abstract

Modeling studies of estuary circulation show great sensitivity to the water exchange into and out of adjacent marshes, yet there is significant uncertainty in resolving the processes governing marsh surface flow. The objective of the study presented in this chapter is to measure the estuary channel-to-saltmarsh pressure gradient and to guide parameterization for how it affects the surface flow in the high marsh. Current meters and high-resolution pressure transducers were deployed along a transect perpendicular to the nearby Little Ogeechee River in a saltmarsh adjacent to Rose Dhu Island near Savannah, Georgia, USA. The vertical elevations of the transducers were surveyed with static GPS to yield high accuracy water surface elevation data. It is found that water level differences between the Little Ogeechee River and neighboring saltmarsh are up to 15 cm and pressure gradients are up to 0.0017 m of water surface elevation change per m of linear distance during rising and falling tides. The resulting Little-Ogeechee-River-to-saltmarsh pressure gradient substantially affects tidal velocities at all current meter locations. At the velocity measurement station located closest to the Little Ogeechee River bank, the tidal velocity is nearly perpendicular to the bank. At this location, surface flow is effectively modeled as a balance between the pressure gradient force and the drag force due to marsh vegetation and bottom stress using the Darcy-Weisbach/Lindners equations developed for flow-through-vegetation analysis in open channel flow. The study thus

provides a direct connection between the pressure gradient and surface flow velocity in the high marsh, thereby overcoming a long-standing barrier in directly relating flow-through-saltmarsh studies to flow-through-vegetation studies in the open channel flow literature.

2.2 Introduction

Saltmarshes are valuable and productive ecosystems that serve as storm buffers, fish nurseries, and nutrient sources, and they play a significant role in the dynamics of estuary circulation. The limited amount of precise field data on the spatial variation of water surface elevation in estuarine creeks, channels, and in particular high marshes, is a critical gap in the understanding of saltmarsh hydrodynamics. The lack of data negatively impacts our ability to assess the effect of vegetation on surface water flow and accurately estimate the bottom stress in these settings. For instance, modeling results show that a channel-to-saltmarsh pressure gradient (i.e., differential water levels between the estuary main channel and the adjacent saltmarsh) is responsible for surface transport of water between the saltmarsh and the channel at high spring tide [Bruder et al., 2014]. However, the modeling results are based on non-validated assumptions and the resulting pressure-gradient-driven surface flows show great sensitivity to the parameterization of the bottom stress, in agreement with earlier modeling results [Kjerfve et al., 1991]. Therefore, detailed measurements of the pressure gradient and corresponding surface flows, together with application of appropriate hydrodynamic models, are needed to improve our understanding of the flow into and out of the high marsh.

In an effort to determine the effect of vegetation on the transition from channelized flow to sheet flow on the marsh platform, Vandenbruwaene et al. [2015] directly measured the velocity of the surface flow and estimated the water surface elevation in a high marsh. Their study is the only published field measurements we are aware

of that show the presence of differential water levels between the high marsh and the adjacent main channel in a saltmarsh. No study to our knowledge has attempted to quantitatively relate the corresponding pressure gradient to the sheet flow through the high marsh vegetation.

Analyses of the effects of variable marsh friction (i.e., variable marsh vegetation) on the mean flow in tidal creeks and deeper estuary channels are predominantly restricted to modeling studies [Kjerfve et al., 1991, Rinaldo et al., 1999a,b, Bruder et al., 2014]. Attempts to quantify water surface elevations on high marsh platforms (and thus quantify the pressure gradient between the high marsh and the creeks and channels) are also chiefly limited to modeling studies [Kjerfve et al., 1991, Rinaldo et al., 1999a,b]. Unfortunately, due to the paucity of available field data, these models were unable to validate their results in the high marsh. The principal gaps in current knowledge are the lack of available water surface elevation measurements, the lack of directly observed flow patterns (although see Temmerman et al. [2012] and Vandenbruwaene et al. [2015]), and an inability to verify the models parameterization of the bed/vegetation friction (e.g., through Mannings n or drag-coefficient formulations; Kjerfve et al. [1991], Huang et al. [2008], Bruder et al. [2014]). We note that several recent studies have focused on the dissipation of wave energy by the marsh vegetation rather than addressing the relationship between the mean surface flow and bed/vegetation friction [Lowe et al., 2005, Augustin et al., 2009, Riffe et al., 2011, Wu, 2014]. Thus, the objective of this study is to determine the estuary channel-to-saltmarsh pressure gradient and to evaluate how it affects the surface flow in the high marsh.

2.2.1 Background

Studies on water movement in saltmarshes generally have focused on one of three areas: the surface flow in the network of branching tidal creeks (e.g., Bayliss-Smith

et al. [1979], French and Stoddart [1992], Allen [1994]), the surface flow high in the marsh platform [Eiser and Kjerfve, 1986, Leonard and Luther, 1995], and the groundwater flow [Howes and Goehringer, 1994, Gardner et al., 2002, Gardner, 2005, Wilson and Gardner, 2006]. The flow in tidal creeks depends on the water surface elevation relative to the marsh bathymetry. For low relative water surface elevation, the creeks remain below bankfull and the flow velocity is small, $\sim 0.1 - 0.2\ m/s$ [Bayliss-Smith et al., 1979, Pethick, 1980, Healey et al., 1981, Dankers et al., 1984, French and Stoddart, 1992, Leopold et al., 1993, Allen, 1994, Pringle, 1995]. The water surface elevation (i.e., pressure gradient) slopes into the tidal creek during flood and towards the ocean during ebb [Leopold et al., 1993]. For high relative water surface elevation, the flow velocity in the creeks remains small while the creek is below bankfull and peaks at much larger values ($\sim 1\ m/s$) once the marsh is flooded [Bayliss-Smith et al., 1979, Pethick, 1980, Healey et al., 1981, Dankers et al., 1984, French and Stoddart, 1992, Allen, 1994, Pringle, 1995, Rinaldo et al., 1999a,b]. Some studies observed pulses in the tidal creek velocity, which correspond to sudden changes in velocity as the marsh is flooded (e.g., Temmerman et al. [2005a], Torres and Styles [2007]). Similar pulses also have been observed as the creek itself initially flooded or became dry [Hazelden and Boorman, 1999]. Consistent with low relative water surface elevation conditions, the pressure gradient in high relative water surface elevation conditions slopes into the tidal creek during flood and towards the ocean during ebb [Healey et al., 1981, French and Stoddart, 1992].

Regarding the hydrodynamics on the high marsh platform, Allen [2000] writes, "the local hydraulics of channels has undoubtedly been over-emphasized at the expense of what are in effect tidal floodplains." Allen [2000] acknowledges that studies considering flow on the high marsh platform face formidable challenges due to the difficulty in accurately measuring small gradients in the water surface elevation [Horstman

et al., 2013] and the difficulty in making direct flow measurements in dense vegetation [Mazda et al., 2007]. Flow velocities across the high marsh surface are much smaller than in the creeks ($\sim 0.01 - 0.1\ m/s$) and decrease in proximity of bathymetric obstacles [Eiser and Kjerfve, 1986, Wang et al., 1993, Allen, 1994]. The flow is generally governed by the bathymetry of the high marsh [Eiser and Kjerfve, 1986, Davidson-Arnott et al., 2002, Temmerman et al., 2005b], the pressure gradient from the slope in the water surface elevation [Kjerfve et al., 1991, Bruder et al., 2014], and the vegetation characteristics [Leonard and Luther, 1995, Temmerman et al., 2012]. At low relative water surface elevation, the flow essentially follows the high marsh bathymetry [Eiser and Kjerfve, 1986, Davidson-Arnott et al., 2002]. As the relative water surface elevation becomes higher, currents in the high marsh begin to behave more analogously to sheet flow [Temmerman et al., 2005a, Vandenbruwaene et al., 2015] and are effectively forced by the water surface elevation slope between neighboring positions [Kjerfve et al., 1991, Bruder et al., 2014, Vandenbruwaene et al., 2015]. This interplay between bathymetry-driven flow and sheet flow is also observed in estuaries dominated by mangrove swamps (e.g., Aucan and Ridd [2000], Mazda et al. [2005], Horstman et al. [2013]). In all cases, the flow is mediated by the characteristics of the vegetation and the relative water surface elevation [Leonard and Luther, 1995, Temmerman et al., 2012, Vandenbruwaene et al., 2015]. When vegetation is partially submerged, the mean velocity depends on the plant morphology and density [Leonard and Luther, 1995]. For deeply submerged vegetation, the flow is characterized by a two-layer velocity profile [Leonard and Luther, 1995]. The bottom layer extends from the bed to the approximate height of the vegetation stems, and the flow characteristics are similar to the partially-submerged case. The upper layer is a logarithmic-law turbulent boundary layer that extends from essentially the top of the vegetation to the free surface Leonard and Luther [1995].

Groundwater flow rates in marshes are typically substantially smaller than flow

rates on the surface [Wolanski and Elliott, 2015]. However, the authors noted that groundwater flow is a critical area of study because it influences the soil properties and fluid salinity. Salinity is governed by a combination of marsh soil porosity, upland groundwater level, and tidal inundation [Wolanski and Elliott, 2015]. The water table and salinity respond rapidly to precipitation and tidal inundation, as groundwater moves rapidly through saltmarshes [Gardner et al., 2002, Gardner, 2005, Wolanski and Elliott, 2015]. It is important to note that rapid changes occur in response to the tide in areas that are not inundated due to tidal effects on subsurface pore pressure gradients [Gardner et al., 2002, Gardner, 2005, Wilson and Gardner, 2006]. Model results suggest that the majority of the direct groundwater interaction with seawater occurs during the recharge and drainage of groundwater along the banks of tidal creeks that branch into the marsh [Gardner, 2005, Wilson and Gardner, 2006].

2.3 Materials and Methods

A field experiment was conducted in the tidal marsh adjacent to Rose Dhu Island near Savannah, Georgia, USA (Figure 2.1) from 2 November 2014 to 6 November 2014, coinciding with the largest spring tide in November 2014. The project site was selected due to the availability of numerical model data of water levels [Bomminayuni et al., 2012, Bruder et al., 2014] and previously-collected bathymetric/topographic and vegetation data.

Three Onset HOBO pressure transducers (PTs), two Acoustic Doppler Velocimeters (ADVs, Nortek Vector Nortek AS, Rud, Norway) and a current profiler (Nortek Aquadopp HR-profiler) were deployed along a transect perpendicular to the Little Ogeechee River in the tidal marsh. The ADVs measure the fluid velocity at essentially a point in the flow, whereas the Aquadopp measures the flow velocity in a series of evenly-spaced vertical bins. Instrument locations are shown in Figure 2.1. The PTs were housed in custom-made PVC stands (Figure 2.2). The stands aluminum plate

prevented instrument settling during the deployment cycle and the bolt/dive-weight assembly fixed the vertical elevation of the PTs within the stand. The three PTs were surveyed daily with static GPS for at least two hours. Additionally, a GPS base station, located on the nearby fixed dock, was surveyed daily for at least eight hours to improve GPS vertical elevation accuracy during post-processing. The GPS antennae were Ashtech Duel Frequency Marine Antenna (Ashtech S.A.S., Carquefou, France) that were connected to either Ashtech ProFlex 500 GS or Z-Surveyor receivers and were programmed to record internally at 10 *sec* intervals. Further, the ADV and Aquadopp locations were surveyed daily using a total station. The water salinity was measured near the surface from the dock (Figure 2.1) at 4:15 PM on 3 November 2014 and 11:35 AM on 6 November 2014 and was 25.7 and 26.3, respectively.

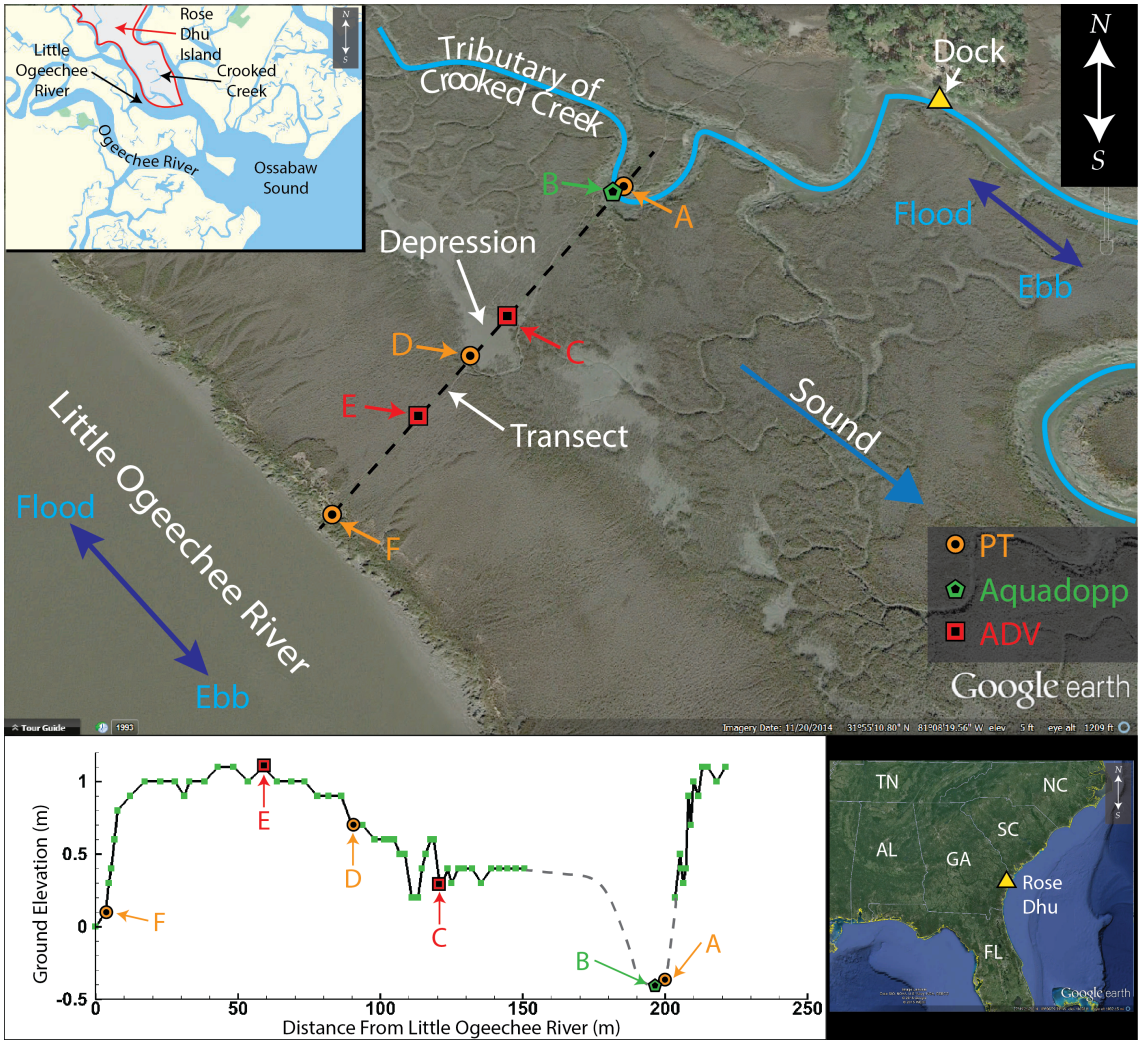

Figure 2.1: Map showing the locations of the six stations (courtesy of Google Earth). The instrument transect is shown as a dashed black line. Rose Dhu Island is outlined in red in the upper left image and shown as a yellow triangle on a map of the southeastern United States in the bottom right image. The lower left panel is the bathymetry (or topography, if exposed) along the transect in NAVD88. Green squares denote data points and the dashed gray line is the approximate bathymetry in the data gap. For reference, GPS coordinates for station D are Lat: 31° 55′ 11.62" N Long: 81° 8′ 20.99" W. Imagery data from 20 November 2014.

Field data collected at this site also included *Spartina alterniflora* vegetation surveys at 25 locations (1 m × 1 m quadrats) across the marsh (within 0.6 km of the

transect) conducted in December 2010. The data consisted of the number of stalks in each quadrat and the diameter of at least ten randomly-selected stalks. Visual comparison of the 2014 experiment and 2010 survey periods at ground level and via Google Earth images (20 November 2014 vs. 28 January 2011) indicate little change in the gross vegetation patterns.

2.3.1 Pressure to Water Surface Elevation

The PTs measured absolute pressure and temperature every 30 *sec*. To convert the absolute pressure to gauge pressure, atmospheric pressure readings from the nearby ($\sim$ 13 km away) weather station at Skidaway Institute of Oceanography were employed. Gauge pressure was converted to water depth above the PT by assuming the pressure variation in the vertical direction was solely due to hydrostatic effects. The water density was determined from the PT temperature measurement and the salinity measured at the dock, which was assumed to be equal to the salinity in the vicinity of the PTs. Temperature and salinity were assumed to be vertically homogeneous.

To improve the accuracy of the absolute pressure readings (and thus the estimated water surface elevation), the three PTs were calibrated in a 1 m deep tank at seven temperatures, ranging from 12 to 26 $^{\circ}C$. Linear calibration curves were developed to calculate the pressure difference between two of the PTs (stations A and D) and the third reference PT (station F) as a function of temperature. These curves were used during data processing to adjust the pressure data to a common reference pressure. The standard deviations of the mean pressure difference between the PTs at stations A and D and the reference PT at station F were calculated for each calibration temperature. The difference was found to be less than 10 Pa in all cases, which corresponded to less than 1 mm of water surface elevation difference. Note that the ADVs and the Aquadopp are equipped with built-in PTs. Unfortunately, the accuracy of the built-in PTs is one order-of-magnitude worse than the accuracy of

the Onset HOBO PTs and is not sufficient to resolve sub-*cm* water level differences.

The water surface elevation was calculated relative to the NAVD88 vertical datum by adding the water depth data to the PT elevation using the dimensions of the stand (shown in Figure 2.2) and the GPS measurement of the antenna position. To arrive at sufficiently accurate water surface elevation measurements, the GPS measurements were post-processed using GrafNet (NovAtel, Calgary, Alberta, Canada), treating the GPS system as a stationary closed loop network. The system included four GPS antenna/receivers (one at each PT and one on the dock) and several Continuously Operating Reference Stations (CORS) operated by the U.S. National Geodetic Survey (NGS). The estimated vertical accuracy from GrafNet was approximately 0.5 *cm* for all stations. This level of accuracy was obtained using simultaneous GPS measurements. The vertical positions of the PT stands did not vary during the experimental periods.

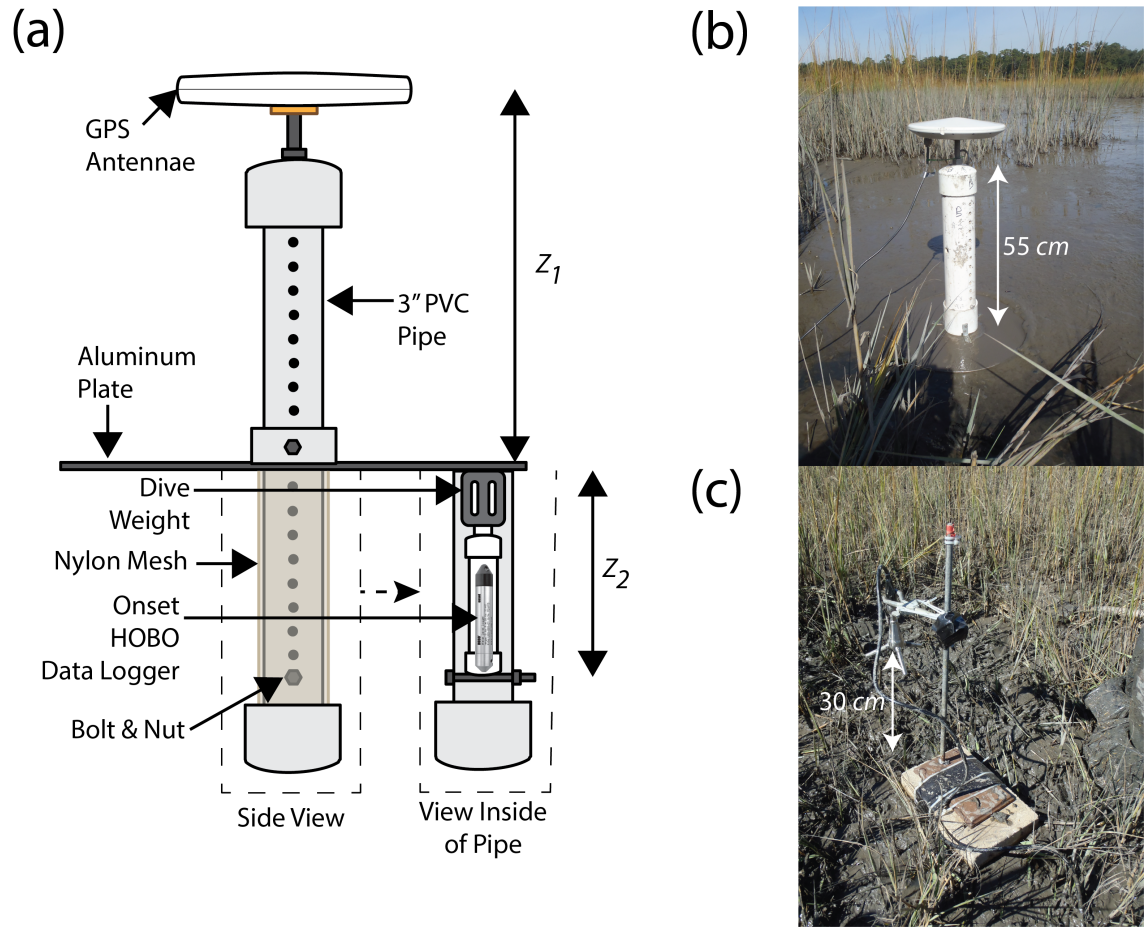

Figure 2.2: (a) Diagram of a pressure transducer stand, (b) in situ photograph of a pressure transducer stand during GPS survey, and (c) in situ photograph of an ADV during deployment.

2.3.2 ADV Data Processing

The ADV measurements have a resolution of 1 mm/s and were collected continuously at 1 Hz. Data collected during low tide (determined by instances of the PT at station D being dry) were discarded. Following the recommendations of Chanson et al. [2008] and Wilson et al. [2013], data for which the average correlation coefficient of the three beams was less than 70% for 45 consecutive samples, or for which the average over 300 samples of the mean correlation coefficient of the three beams

dropped below 70%, were discarded. This filtering predominately removed data collected while the instrument was not submerged, and less than 2% of the submerged instrument data were removed due to filtering. The dominant flow direction (if one was present) was determined for each ADV. An ellipse was fit to a scatter plot of the measured east and north velocity components for each ADV, and the major axis of the resulting ellipse is defined as the "along-stream" flow direction. Correspondingly, the minor axis is defined as the "cross-stream" direction. Figure 2.3 illustrates this process for the ADV at station E. Note that the length of the major and minor axis of this ellipse correspond to plue or minus one standard deviation of the velocity in the respective axis directions.

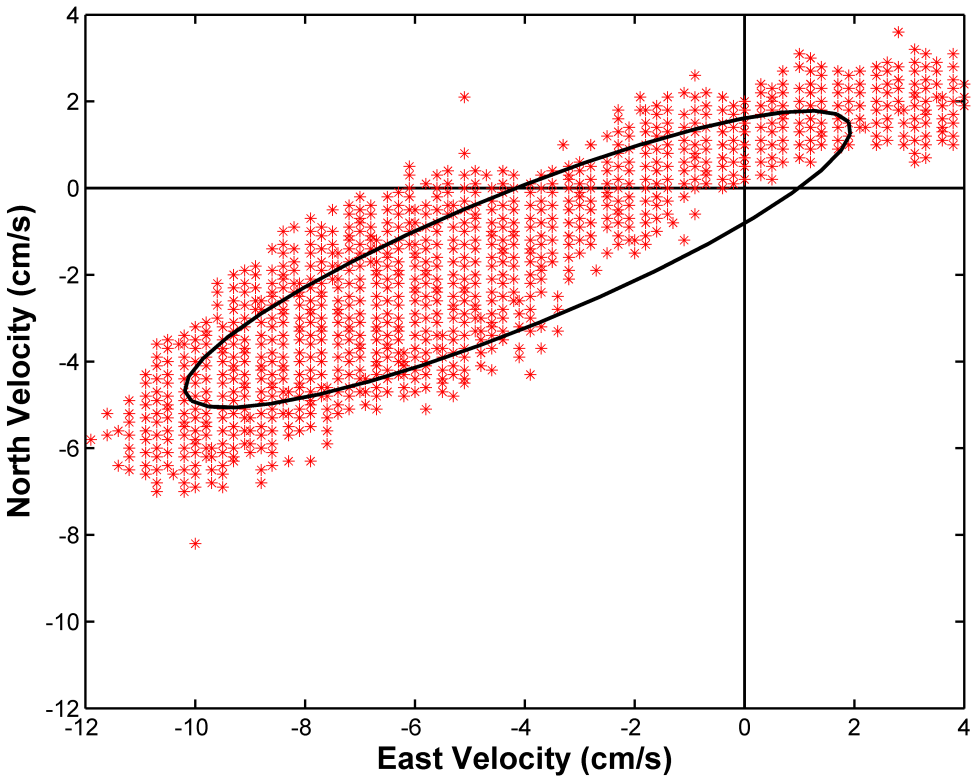

Figure 2.3: Scatter plot of the north and east velocity components at station E. Symbols indicate the measured data, and the ellipse is the best fit to the data. There are 24,100 velocity samples included in the plot.

2.3.3 Aquadopp Data Processing

Aquadopp measurements were collected at 1 Hz. The Aquadopp returned the velocity within 10 cm vertical bins, equally spaced from 0.3 to 2.2 m above the instrument. Dry bins were identified using the built-in PT and temperature gauges to estimate the water depth above the instrument. All bins in which the water depth had not reached at least the midpoint of the next highest bin were discarded. The velocity measurements in each bin were averaged over 30 sec intervals to smooth out turbulent velocity fluctuations. The flux-per-unit-width (q) was estimated by summing the velocity in each bin multiplied by the bin height. Flux-per-unit-width therefore corresponded to the fluid flow through a vertical line extending from the Aquadopp to the surface. The ellipse fitting technique (Section 2.3.2) combined with polar histograms of the flux vectors were used to determine the along-stream flow direction in the Crooked Creek tributary. The horizontal flux vector was rotated to correspond to the defined along-stream and cross-stream directions.

2.4 Results and Discussion

Tidal flow in and out of the saltmarsh is more complex than the typical behavior of estuarine channels due to the highly variable bathymetry and vegetation across the marsh. Further, the comparatively strong Little-Ogeechee-River-to-saltmarsh pressure gradient significantly affects the marsh flow characteristics, as presented below. A typical tidal cycle in this saltmarsh proceeds as follows (illustrated in Figure 2.4, which shows the relative water surface elevation at five instances in the tidal cycle):

1. Early Flood: Starting from low tide, the water begins to rise as the tide comes in. At the earliest stages of rising tide, the water in the Crooked Creek tributary and the nearby Little Ogeechee River rise at roughly the same rate. The water progresses into the marsh along the Crooked Creek tributary and the flux-per-unit-width (at station B see Figure 2.1) begins to increase towards a maximum

value as the water rises (see Figure 2.5). The ADV at station C becomes inundated after the Aquadopp (at station B) due to the stations higher elevation. Water at station C initially flows into the marsh towards the northwest along a small non-vegetated depression (see Figure 2.1).

2. Mid Flood: The water level begins to rise more rapidly in Little Ogeechee River than in the Crooked Creek tributary. As the water level in Little Ogeechee River rises above its banks, the high marsh floods from Little Ogeechee River towards the Crooked Creek tributary. The flow of water from Little Ogeechee River briefly (i.e., 20 to 30 minutes) forces the flow at station C out of alignment with the small northwesterly-oriented depression and shifts the flow direction towards the northeast along the instrument transect (i.e., towards the Crooked Creek tributary). Station E becomes inundated and the initial velocity at the instrument is similarly towards the northeast along the instrument transect. The flux-per-unit-width at station B, which has been increasing with the rising tide, begins to slow towards a local minimum value (Figure 2.5) as the water flooding into the marsh from Little Ogeechee River briefly restricts the water flooding along the Crooked Creek tributary.

3. Late Flood: Before high tide is reached, the water level in the Crooked Creek tributary (station A) catches up to and exceeds the water level in Little Ogeechee River (station F). Simultaneously, the flux-per-unit-width in the Crooked Creek tributary increases towards a local maximum value (smaller than the previous maximum described in 1. Early Flood, Figure 2.5), and the velocity at station E switches direction, flowing to the southwest (towards Little Ogeechee River) along the instrument transect. The velocity at station C returns to the direction aligned with the depression towards the northwest.

4. Early Ebb: The water level in Little Ogeechee River begins to drop slightly

before the water level in the Crooked Creek tributary. The water level in Little Ogeechee River drops substantially faster, such that the water level in the Crooked Creek tributary remains higher for the remainder of the tidal cycle. The water level in the marsh becomes sufficiently higher than that in Little Ogeechee River to once again temporarily force the flow at station C out of alignment with the small depression. The flow at station C shifts towards the southwest along the instrument transect (towards Little Ogeechee River). The flow at station E remains strongly southwestern towards Little Ogeechee River until the ADV becomes dry. Concurrently, the flow in the Crooked Creek tributary slows and switches to ebb upon which it follows a more standard tidal stage-flux pattern (Figure 2.5).

5. Mid-Late Ebb: As the water level in Little Ogeechee River drops below its banks, the flow at station C returns to alignment along the small depression, flowing towards the southeast.

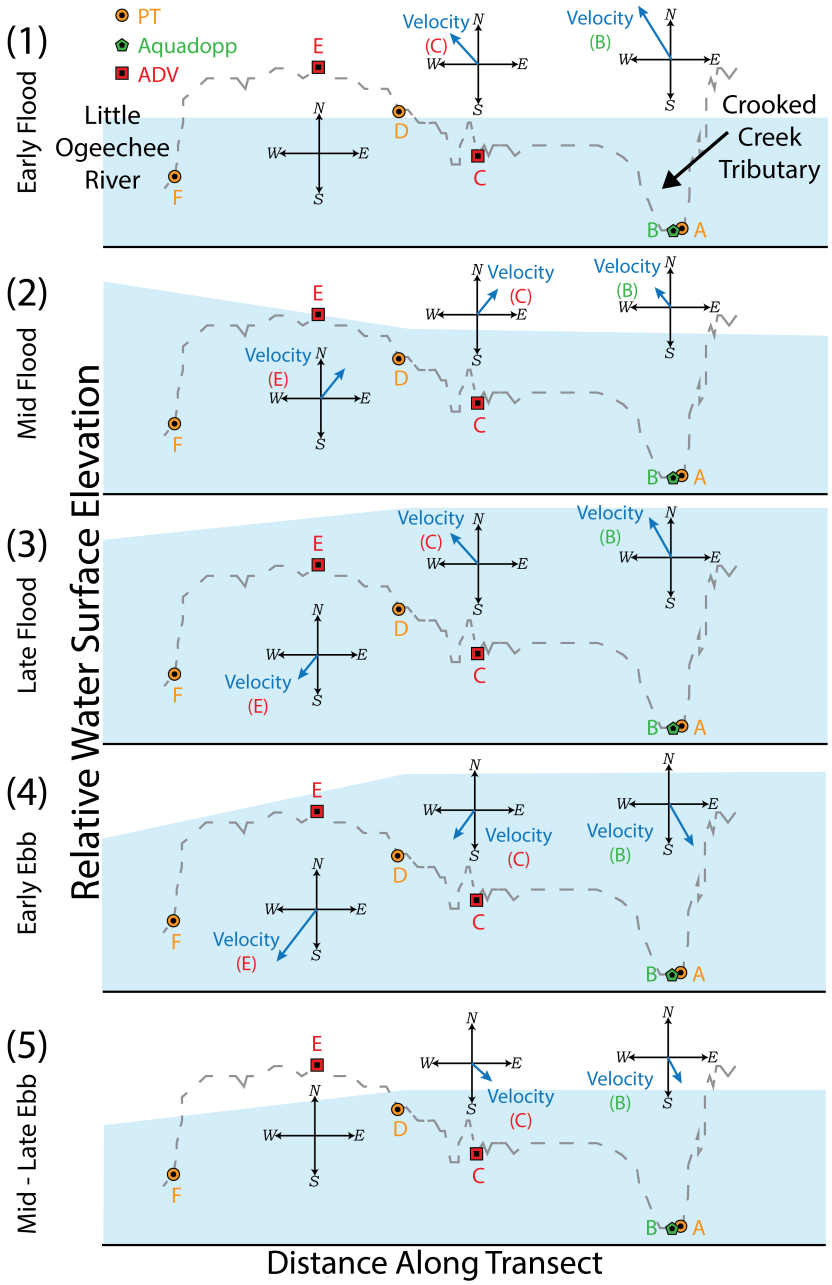

Figure 2.4: Illustration of the tidal flow sequence. The blue shade indicates the relative water surface elevation at the position along the transect for each stage. The bathymetry (or topography) along the transect is shown as a dashed grey line. The compass roses with velocity arrows indicate the velocity direction and magnitude at the respective instruments (lack of an arrow indicates the instrument was not submerged during that stage).

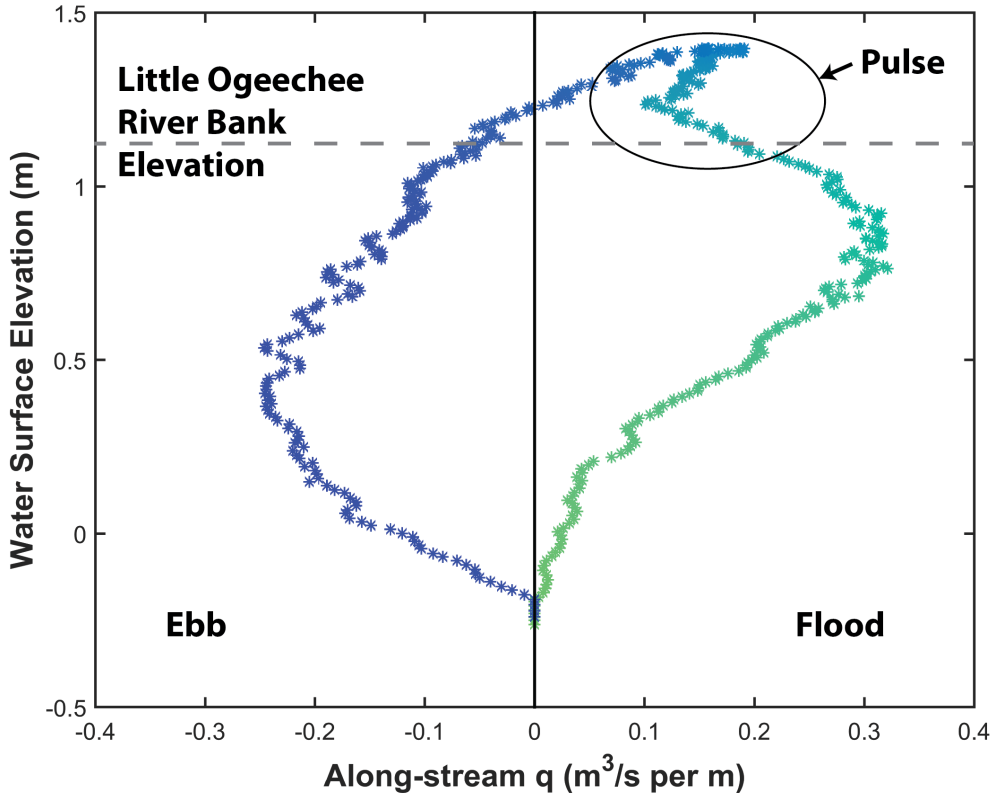

Figure 2.5: Tidal stage (NAVD88) along-stream-flux-per-unit-width (q) diagram at station B for a 5 November 2014 tidal cycle. Positive values of flux-per-unit-width denote flood (inundation) and negative values represent ebb (draining). The color transition indicates time progression from the beginning (green) to end (blue) of the tidal cycle. The dashed grey line marks the elevation of the bank of the Little Ogeechee River (1.1 m).

2.4.1 Water Levels and Pressure Gradients

As the narrative of the tidal cycle sequence made clear (illustrated in Figure 2.4), the differential water level between the high marsh and Little Ogeechee River strongly affects the flow characteristics at all instrument locations. To quantify the differential water levels (and corresponding pressure gradients), the water surface elevations at each PT are shown in Figure 2.6 for a representative tidal cycle.

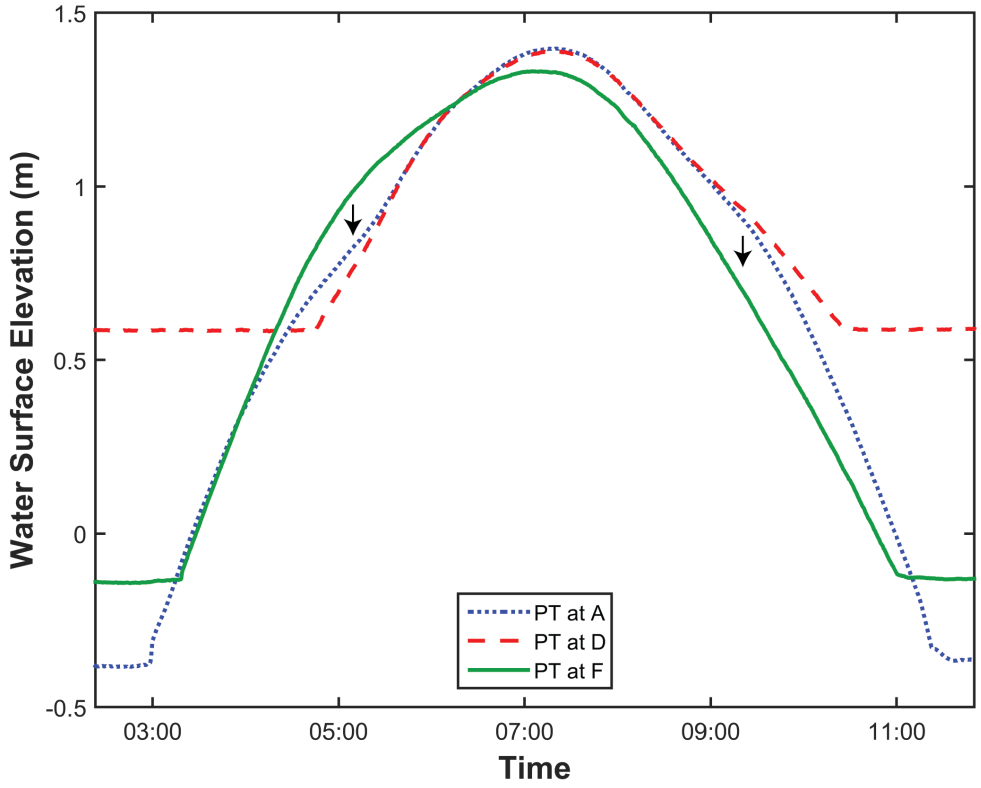

Figure 2.6: Water surface elevation (NAVD88) for the tidal cycle shown in Figure 2.5 for each pressure transducer (PT). Flat segments indicate dry periods for the instrument. If the pressure gradient is the dominant forcing term, then water flows from the location with higher water surface elevation to the location with lower water surface elevation, as indicated by the black arrows.

The water levels at the two PTs in the marsh (stations A and D) are nearly identical over much of the tidal cycle, but the data also reveal some differences. The water level in Crooked Creek tributary (station A) rises slightly faster and falls more quickly than the water level in the high marsh (station D), which is to be expected from the reduced tidal wave propagation speed in the high marsh [Parker, 1991].

In contrast, the water level in Little Ogeechee River (station F) is substantially different than the water level at either of the two marsh PT stations. The water level

difference between Little Ogeechee River and the marsh is approximately 7 - 8 cm at high tide and becomes as large as 15 cm during rising and falling tide. The water level difference is similar to that observed in Vandenbruwaene et al. [2015] during flood tide. Given that the distance between stations D and F is less than 90 m, the observed water surface elevations translate to a substantial Little-Ogeechee-River-to-saltmarsh pressure gradient.

Another interesting feature in Figure 2.6 is that the water level in the Crooked Creek tributary and Little Ogeechee River (stations A and F) are very similar at the beginning of flood tide prior to the inundation of the high marsh. Once the water level in the Crooked Creek tributary (station A) exceeds the level of the bank, approximately 0.4 m (Figure 2.1), its rate of rise decreases as the marsh is flooded until it matches the water level in the high marsh (station D). During ebb tide, the water surface elevation in the Crooked Creek tributary (Station A) and the high marsh (Station D) initially decrease at the same rate, then the water level in the Crooked Creek tributary (Station A) starts to decrease more rapidly. The water surface elevation in the Crooked Creek tributary (station A) is greater than that in the Little Ogeechee River (station F) throughout the ebb tide, which indicates the tributary drains at a slower rate.

2.4.2 Effects of Estuary Channel-to-Saltmarsh Pressure Gradient on Flow

The effect of the Little-Ogeechee-River-to-saltmarsh pressure gradient on the flow is more subtle at stations B and C than at station E (see Figure 2.1), largely due to the bathymetry. The effect of the Little-Ogeechee-River-to-saltmarsh pressure gradient at station B is apparent in the stage versus along-stream flux-per-unit-width (q) diagram shown in Figure 2.5. Typical estuary channel stage-flux (or velocity) diagrams appear as a tilted ellipse (with the angle depending on the standing versus progressive nature of the tidal wave). Therefore, a typical flow is characterized by a single maximum

value of flux during flood and a single maximum value of flux during ebb. Figure 2.5 shows an obvious "pulse" in the flood stage, where the flux-per-unit-width reaches a maximum value, then temporarily decreases and subsequently increases to a local maximum value before returning to a more standard diagram shape. As described in the tidal sequence, this brief slowing and local minimum value of flux-per-unit-width coincided with flow of water from Little Ogeechee River towards the Crooked Creek tributary due to the higher water level (in Little Ogeechee River) overtopping the Little Ogeechee River bank. This flow of water essentially retards the flux of water up the Crooked Creek tributary until the water level in the tributary rises above the water level in Little Ogeechee River and the tributary flux begins to increase again. Torres and Styles [2007] observed similar stage diagrams for a tidal creek near Winyah Bay (Georgetown, South Carolina, USA), in which marsh inundation was strong enough to temporarily reverse the tidal creek flow, thus producing a tidal stage diagram in the shape of a figure eight.

The flow at station C appears to be predominately confined to a natural mud-flat depression (see Figure 2.1) roughly parallel to Little Ogeechee River. However, during both rising and falling tide, the Little-Ogeechee-River-to-saltmarsh pressure gradient becomes sufficiently large to redirect the velocity at station C to be perpendicular to the alignment of the natural depression. The flow direction in these instances is aligned with the instrument transect towards either the Crooked Creek tributary (if the Little Ogeechee River water level is higher) or Little Ogeechee River (if the marsh water level is higher).

The flow at station E is obviously affected by the pressure gradient between stations D and F. The angle between the along-stream flow direction (i.e., major axis of the best fit ellipse in Figure 2.3) and the instrument transect is less than 9°, which indicates the adjacent PTs were well-placed to capture the pressure gradient driving the flow at this location. Figure 2.7 plots the along-stream velocity, averaged over 30

sec intervals, at station E against the corresponding pressure gradient (i.e., the water surface elevation differential between the PT at station D and the PT at station F divided by the distance between stations) for all measured tidal cycles. Along-stream velocity is defined as positive to the northwest, roughly along the PT transect, and positive pressure gradient is defined as higher water level in the high marsh (PT at station D) than in the Little Ogeechee River (PT at station F). Because of the direct correlation of the sign and magnitude of the surface flow and pressure gradient, Figure 2.7 strongly indicates the pressure gradient between stations D and F governs the flow characteristics at this location, regardless of tidal cycle or water level.

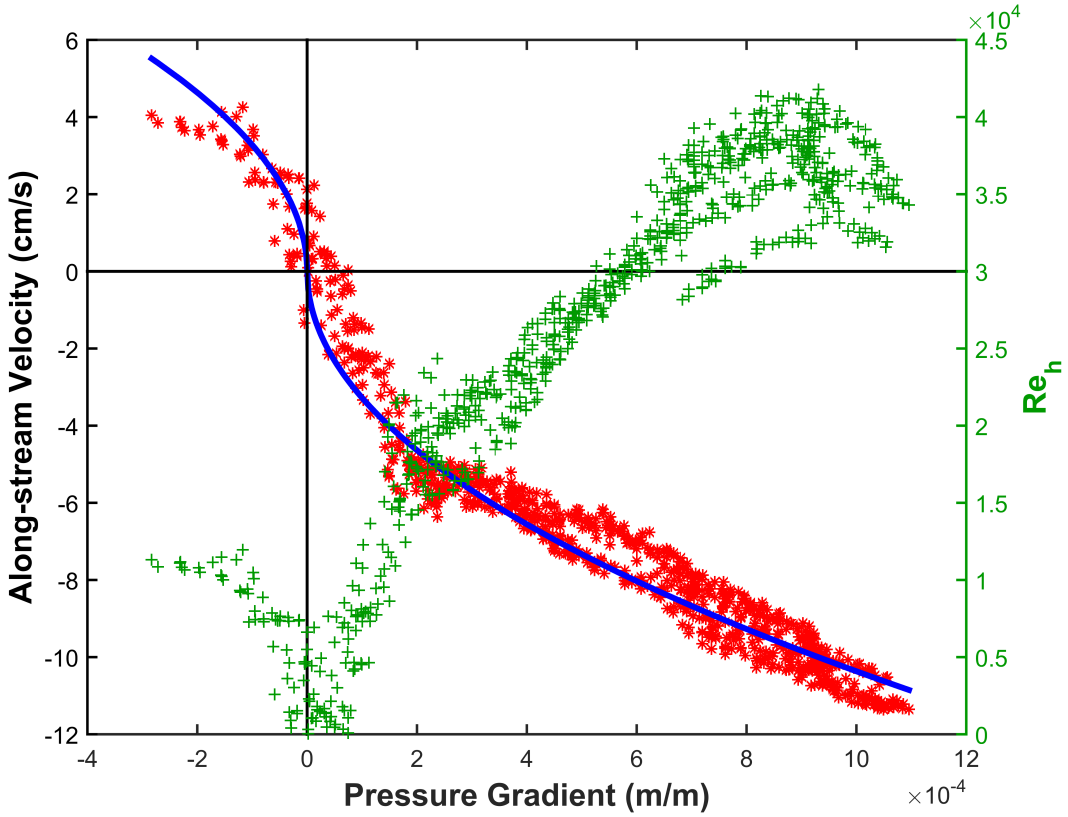

Figure 2.7: Along-stream velocity at station E (red stars) and depth-based Reynolds number (Re_h - green pluses) plotted as a function of the corresponding pressure gradient (m of water surface elevation drop per m of linear distance). The blue line represents the model for $d_{stalk} = 1\ cm$ and $N_{stalk} = 93$. 96% of the variance in the velocity parameter is explained by the model.

2.4.3 Predicting Velocity Given the Pressure Gradient

It is desirable to accurately predict the surface flow velocity given the slope of the water surface elevation by defining an equation (or set of equations) that relate these quantities. The data shown in Figure 2.7 afford an excellent opportunity to explore this relationship since the flow at station E appears unconfined by bathymetry and thus is driven by the pressure gradient between stations D and F. A simple control volume analysis yields the following force balance [Järvelä, 2004]:

$$\rho g A_b h \frac{\partial \zeta}{\partial x} = \frac{1}{2} \rho C_d A_p V^2 \tag{2.1}$$

The primary forcing is due to the pressure gradient (from the slope in the water surface elevation, $\frac{\partial \zeta}{\partial x}$, which accounts for the component of the fluid weight in the flow direction due to the bed slope and the net force on the control volume due to the variable water depth, i.e., the unequal hydrostatic pressure distributions). In the formulation on the left-hand-side of Eqn. 2.1, x is the coordinate direction along the instrument transect, ζ is the water surface elevation, h is the total water depth (i.e., $h = h_0 + \zeta$), h_0 is the still water depth, A_b is the bed area, and g is the acceleration due to gravity. The primary retarding force is the drag force due to the bed and vegetation (i.e., the right hand side of Eqn. 2.1). The drag force is modeled with a drag coefficient, C_d, formulation where ρ is the fluid density, V is the fluid velocity, and A_p is the projected area of the vegetation. The assumptions leading to the force balance in Eqn. 2.1 include neglecting the local (temporal) acceleration (the tidal variation occurred over comparatively large time scales, e.g., hours), neglecting the convective acceleration (because the velocity magnitude in Figure 2.7 is small in comparison to the marsh spatial scales, i.e., $V \sim 10 \, \frac{cm}{s}$ versus spatial scales of $\sim 100 \, m$), and neglecting the cross-stream flow (because the flow at station E is nearly aligned with the transect).

Much discussion in the flow through vegetation literature is devoted to the optimum parameterization of the drag coefficient and effective areas (A_b and A_p in Eqn. 2.1) under a variety of circumstances (e.g. Lindner [1992], Koch and Ladd [1997], Wu et al. [1999], Nepf [1999], Tsihrintzis [2001], Järvelä [2002], Stone and Shen [2002], Lee et al. [2004], Tanino and Nepf [2008], Cheng and Nguyen [2011]). The literature is generally in agreement that the effective areas must depend on marsh plant morphology and density (e.g., the stalk diameter and the spacing between the stalks), but the authors have not come to a consensus on the form of the dependence. Additionally,

the drag coefficient's dependence on the Reynolds number is unresolved. Some studies exclude the Reynolds number dependence entirely (e.g. Lindner [1992], Järvelä [2002]), others include the drag coefficient as a function of the depth-based Reynolds number ($Re_h = \frac{Vh}{\nu}$, e.g. Wu et al. [1999], Tsihrintzis [2001], Stone and Shen [2002], Lee et al. [2004]) or the stalk-diameter-based Reynolds number ($Re_d = \frac{Vd_{stalk}}{\nu}$, e.g. Koch and Ladd [1997], Nepf [1999]). The most recent studies incorporate the pore velocity between the cylinders/stalks as the relevant velocity scale [Tanino and Nepf, 2008] or the pore velocity as the velocity scale and the vegetation-related-hydraulic radius ($r_v = \frac{\pi}{4}\frac{1-\lambda}{\lambda}d_{stalk}$, where λ is the stem density) as the relevant length scale (e.g. Cheng and Nguyen [2011]) in the formulation of the Reynolds number. It is also important to note that the two-layer velocity profile described for deeply submerged saltmarsh vegetation in Leonard and Luther [1995] has previously been shown to exist in atmospheric turbulent boundary layers above crops or forests [Raupach et al., 1991, Kaimal and Finnigan, 1994], in flume studies of flow through submerged plants (e.g., Murota et al. [1984], Gambi et al. [1992]), and in flume studies of flow through roughened cylinders [Stone and Shen, 2002]. The vegetation in our study remained emergent in the vicinity of the ADV stations during spring tide, therefore we restrict our discussion to the partially submerged case.

The data in this study are best modeled by a Darcy-Weisbach friction factor (f) approach, making use of Lindner's equation [Lindner, 1992] to estimate f based on local vegetation related parameters. This modeling approach has been successfully applied in numerical studies of river floodplains [Stoesser et al., 2003], as well as flume studies with natural vegetation [Järvelä, 2002]. Originally intended for pipe flow, the Darcy-Weisbach equation (Eqn. 2.2) adopts a shear velocity, $u^* = \sqrt{\left(gh\frac{\partial\zeta}{\partial x}\right)}$, to account for the pressure gradient and parameterizes the velocity as follows:

$$\frac{V}{u^*} = \sqrt{\frac{8}{f}} \tag{2.2}$$

By comparing Eqns. 2.1 and 2.2, f can be written in terms of C_d as $f = 4C_d\frac{A_p}{A_b}$ [Lindner, 1992]. Lindner [1992] employs the plant stalk diameter (d_{stalk}) multiplied by the water depth (h) as a surrogate for projected vegetal area (A_p) and the longitudinal and lateral plant spacing (a_x and a_y, respectively) as a surrogate for bottom area (A_b):

$$f = 4C_d\frac{d_{stalk}h}{a_x a_y} \tag{2.3}$$

Flume experiments by Järvelä [2002] indicate the drag coefficient falls in the range $1.43 \leq C_d \leq 1.55$ for Lindners Equation (Eqn. 2.3).

To apply the model, the pressure gradient in Eqns. 2.1 and 2.2 $\left(\frac{\partial\zeta}{\partial x}\right)$ is taken as the absolute value of the measured quantity and the direction of the velocity is assumed to be opposite the sign of the measured pressure gradient. The water depth (h) is assumed to be equivalent to that at the nearby station D. The vegetation parameters (d_{stalk}, a_x, a_y) are determined from the vegetation survey of the grass within the quadrat located closest to station E (see Figure 2.1): the average stalk diameter is $d_{stalk} = 1.0 \pm 0.07\ cm$ [mean $\pm$ standard error of the mean] and the number of stalks in the quadrat is $N_{stalk} = 93$. The parameters a_x and a_y are both assumed to be equal to the mean spacing (s) between individual stalks given by $s = \frac{\sqrt{A_s}-\sqrt{N_{stalk}}d_{stalk}}{\sqrt{N_{stalk}}-1}$ for a square vegetation survey area (A_s). The value of C_d that results in the best fit is 2.0, which is slightly larger than the value range reported by Järvelä [2002]. This discrepancy is discussed in greater detail below.

2.4.4 Discussion of the Darcy-Weisbach/Lindner Equation Fit

The model results, employing Eqns. 2.2 and 2.3, are shown in Figure 2.7. The model effectively predicts the along-stream velocity at station E for the majority of the dataset. The model performs particularly well near the change in flow direction (i.e., velocity = 0) as well as in the range of large negative velocity values (which forms the majority of the data). The model does not predict as well the apparent

transition in slope at velocity values around $-6\ cm/s$ (and pressure gradients near $2 \times 10^{-4}\ m$ of water surface elevation drop per m of linear distance).

When applying the Darcy-Weisbach equation to pipe flow as originally intended, the dependence of C_d (or more properly, f) on Reynolds number is given by the Moody diagram [Moody, 1944]. Lindner's formulation effectively assumes f is independent of depth-based Reynolds number, analogous to the "fully rough" regime in pipe flow or the flow at stalk-based Reynolds numbers greater than 200 described in Nepf [1999], and thus may be entirely determined from vegetative properties. In contrast, some studies in the flow-through-vegetation literature (e.g., Wu et al. [1999], Tsihrintzis [2001], Lee et al. [2004]) parameterize C_d as a function of the depth-based Reynolds number $\left(Re_h = \frac{\rho V h}{\mu}\right)$. Tsihrintzis [2001] in particular raises the possibility that the dependence on Re_h may change with Re_h regime, analogous to the regime dependence of the drag coefficient for flow past cylinders.

The apparent transition in slope at pressure gradients near $2 \times 10^{-4}\ m$ of water surface elevation drop per m of linear distance in Figure 2.7 raises the possibility of a Reynolds number transition. Thus, the corresponding depth-based Reynolds number is also plotted in Figure 2.7, revealing a transition in the slope of the Re_h curve near pressure gradient values of $2 \times 10^{-4}\ m$ of water surface elevation drop per m of linear distance (a similar transition is observed for the stalk-diameter-based Reynolds number, although not shown in Figure 2.7). The transition occurs at a much higher Reynolds number than that observed for the transition to unsteady flow described in Koch and Ladd [1997] or Nepf [1999] and could be associated with the velocity becoming sufficiently large such that the stem flexibility is no longer negligible (note that dissipation of wave energy by saltmarsh vegetation is affected by stem flexibility, Riffe et al. [2011]). As a result, a two-equation approach was considered to model these data using the Tsihrintzis [2001] formulation for C_d ($C_d = \gamma Re_h^{-k}$, where γ and k are parameters determined via the procedures in Lee et al. [2004]) for the low Re_h regime

and the Darcy-Weisbach/Lindner approach for the high Re_h regime. This approach was ultimately discarded in favor of applying the Darcy-Weisbach/Lindner formulation to all data because γ and k must be determined from a multi-variable least-squares fit to an existing dataset and the resulting model performed only marginally better in the low Re_h regime than the Darcy-Weisbach/Lindner model. Formulations incorporating the stalk-diameter-based Reynolds number [Tanino and Nepf, 2008] or the hydraulic radius-based Reynolds number [Cheng and Nguyen, 2011] were similarly discarded.

2.4.5 Parameter Sensitivity and Uncertainty

It is beneficial to evaluate the sensitivity of the Darcy-Weisbach/Lindner formulation to the various input parameters (i.e., N_{stalk}, d_{stalk}, h, and the pressure gradient). The effect of the expected level of variability or uncertainty in each of the four input variables on the Darcy-Weisbach/Lindner model is shown in Figure 2.8. The variability observed in N_{stalk} and d_{stalk} among the 25 locations of the vegetation survey quadrats provides insight to the expected range of values of these parameters. Among the data from these quadrats, $N_{stalk} = 80.4 \pm 18.1$ and $d_{stalk} = 0.77 \pm 0.13\ cm$ [mean $\pm$ standard deviation], hence one standard deviation corresponds to approximately 20% for each parameter. Therefore, the potential variability in N_{stalk} and d_{stalk} is taken to be up to 20% higher or lower than the representative values used in the original formulation (which are specific for the quadrat location nearest to station E). The potential uncertainty in the water depth and pressure gradient estimates is based on the constraints of the measurements. The uncertainty in the water depth is assumed to be $\pm 0.54\ cm$ by combining the uncertainty in the PT water level measurements and the accuracy of the GPS survey elevation estimates. Similarly, combining the resolution of the physical measurements yields an uncertainty in the pressure gradient values of $\pm 8.9 \times 10^{-5}\ m$ water surface elevation difference per m of linear distance.

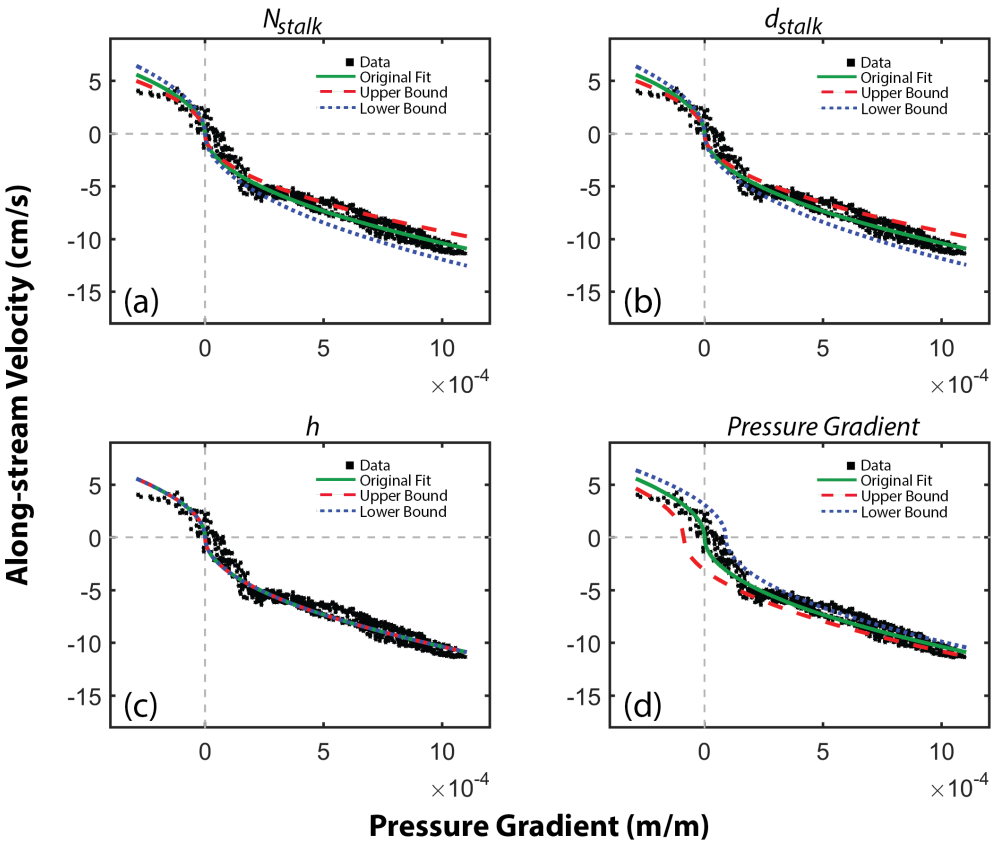

Figure 2.8: Sensitivity of Darcy-Weisbach/Lindner model to variation in (a) N_{stalk}, (b) d_{stalk}, (c) h, and (d) pressure gradient. The upper and lower bounds for each parameter are 20% higher/lower for N_{stalk} and d_{stalk}, $\pm 0.54\ cm$ for h, and $\pm 8.9 \times 10^{-5}$ m water surface elevation difference per m of linear distance for pressure gradient. Note that the curves are obscured by near perfect overlap in (c).

Figure 2.8 (a) and (b) indicate that variability in N_{stalk} and d_{stalk} influences the estimated velocity magnitude for a given pressure gradient, which highlights the need to accurately estimate these parameters via vegetation surveys or other means. Figure 2.8 (c) reveals that the net effect of water depth variation is negligible, as expected based on Eqns. 2.2 and 2.3. Lastly, despite the comparatively small expected uncertainty in the pressure gradient (relative to the vegetation-related quantities), the effect on the estimated velocity magnitude can be quite significant, particularly near

the predicted change in flow direction. At large values of the pressure gradient (regardless of sign), the impact on the predicted velocity magnitude is smaller because the velocity is proportional to the square root of the water surface elevation slope $\left(\sqrt{\frac{\partial \zeta}{\partial x}}\right)$.

The results shown in Figure 2.8 help explain the need to increase the value of C_d relative to the range recommended by Järvelä [2002] when modeling the flow velocity at station E. In addition to the uncertainties in the vegetation parameters already discussed, one must consider that the vegetation varies substantially along the transect between stations D and F (i.e., the PTs that bracket station E - see Figure 2.1). It is possible that the use of representative value of N_{stalk} and d_{stalk} near the site of the flow measurements is insufficient to adequately capture the effects of the variation in N_{stalk} and d_{stalk} along the transect. Similarly, the reported values of the pressure gradient at station E are the best estimate of the slope of the water surface elevation based on the information available (i.e., the slope of the line connecting two neighboring water surface elevation locations at stations D and F). As shown in Figure 2.8, even small errors in the pressure gradient estimates can have strong effects on the estimated velocity magnitude. Great care was taken in the current measurements to minimize the uncertainty in pressure gradient, and the results show that the change in sign of the calculated pressure gradient coincides very well with the change in velocity direction (see Figure 2.7). However, it is possible that the water level measurements at stations D and F are capturing the macro-scale pressure gradient switch properly, but overestimating the magnitude at station E due to localized variation in water level between the two PTs from effects induced by the variable bathymetry (Figure 2.1). Additionally, although the saltmarsh groundwater flow rate is typically much smaller than the surface flow rate [Wolanski and Elliott, 2015], this could be another contributing factor in the increase in the drag coefficient, e.g., if the pressure gradient

is driving groundwater flow unaccounted for in our force balance. Further, groundwater intrusion can affect the surface water salinity and temperature [Wolanski and Elliott, 2015], introducing an error in our calculated water density and thus the water surface elevation measurements. As a result, one can reasonably suggest that the need to increase C_d is an artifact of the uncertainty in quantifying the vegetation and/or pressure gradient parameters or potentially due to unaccounted groundwater flow.

2.5 Conclusions

The results of this study offer strong support for the existence of a Little-Ogeechee-River-to-saltmarsh pressure gradient, corroborating similar observations in the numerical study of Bruder et al. [2014] and field study ofVandenbruwaene et al. [2015]. Figure 2.6 clearly shows the existence of large differential water levels between Little Ogeechee River and the adjacent tidal marsh for the majority of the tidal cycle. Further, data from the current meters indicate that the resulting Little-Ogeechee-River-to-saltmarsh pressure gradient has a significant effect on the flow throughout the marsh.

At station E (on the high marsh near the bank of Little Ogeechee River) the flow characteristics are governed by the pressure gradient between the neighboring stations (Figure 2.7). At this site, the flow velocity is quantitatively related to the pressure gradient between stations D and F via modeling techniques adapted from the open-channel-flow-through-vegetation literature. The model is based on a balance between the force of the pressure gradient and the drag force due to the vegetation and bottom stress. Specifically, the Darcy-Weisbach/Lindner equations effectively model the velocity based on specific vegetation-related parameters and the pressure gradient between stations D and F.

This study demonstrates the ability to quantify the water surface elevation measurements to sufficient accuracy to directly relate the resulting pressure gradient to the flow velocity in the high marsh. The study, therefore, overcomes a long-standing barrier in directly relating flow-through-saltmarsh studies to quantitative relationships developed in flumes for flow through vegetation. Many of these formulations, such as the Darcy-Weisbach/Lindner model, may prove superior for estimating the drag coefficient in the high marsh (i.e., re-arranging Eqn. 2.3) than the current Finite Volume Coastal Ocean Model (FVCOM) technique of taking the greater of a user-entered drag coefficient or a logarithmic-boundary-layer-fit-estimated drag coefficient [Bruder et al., 2014]. The Darcy-Weisbach/Lindner model may likewise prove superior to single-coefficient equations that assume a logarithmic-law velocity profile, such as Manning's equation (e.g., Wolanski and Elliott [2015]), which is known to be ineffective in modeling flow through emergent vegetation [Kadlec, 1990, Jadhav and Buchberger, 1995, Nepf, 1999]. Estimating the drag coefficient via Eqn. 2.3 with spatial variability in the vegetation characteristics (and thus the drag coefficient) across the high marsh based on vegetation surveys and/or satellite image estimates of grass distributions will significantly enhance models of surface flows in the marsh.

CHAPTER III

THE HYDRODYNAMICS OF A PHASE-LOCKED MEANDERING PLUME

3.1 Abstract

While much is known about the concentration field and turbulent mixing in straight plumes of chemical tracer, comparatively little is understood regarding the dynamics of meandering plumes - partially due to the difficulty in separating the plume meander fluctuations from the turbulent fluctuations. Therefore, in the study presented in this Chapter we shall examine the mixing of tracer in a meandering plume by phase-locking the plume with the motion of a diverting plate (that forces the plume meander) to separate the periodic and turbulent fluctuations. Simultaneous laser induced fluorescence (LIF) and particle image/tracking velocimetry (PIV/PTV) data were collected at four phases for a meandering plume, along with LIF data of a straight plume for comparison. Analysis of the LIF data reveals that, compared to the straight plume, the centerline concentration of the meandering plume decreases more quickly with distance downstream, and the plume width increases more rapidly with distance downstream, resulting in more rapid dilution of tracer concentration. Analysis of the velocity data indicates the large-scale alternating vortices induced by the diverting plate are the dominant feature of the meandering plume, forcing the plume meander as well as governing the spatial variation of the mean concentration, Reynolds stress, turbulent kinetic energy (TKE), and turbulent flux. Comparison of the turbulent flux measurements with the mean concentration field indicates that the eddy-diffusion hypothesis effectively models the turbulent flux in the plume. It

is found that when the plume width is less than the size of the large-scale alternating vortices, the eddy-diffusion coefficient scales with the plume width to the 3/4 power, and when it is greater than the size of the large-scale alternating vortices eddy-diffusion coefficient is constant ($K_{y0} = 0.15Hu^*$), where H is water depth and u^* is the shear velocity. Thus, this study presents a detailed description of the concentration field and turbulence characteristics of a meandering plume, and allows the efficacy of the eddy-diffusivity hypothesis for the meandering plume to be directly assessed.

3.2 Introduction

While much is known regarding the dynamics of straight plumes, many naturally occurring plumes meander, which is defined as large scale movement of the plume centerline. This phenomena is most commonly observed in atmospheric plumes [Thompson and Gower, 1977, Sykes, 1984, Wilson et al., 1985, Hanna, 1986, DeFelice et al., 2000], but also would be expected to occur in flows that naturally oscillate, such as the wake flow past a cylinder (the von Karmen vortex street) or other bluff body (e.g. islands in coastal seas or estuaries - Wolanski et al. [1984], Ingram and Chu [1987], Cramp et al. [1991], Fong and Stacey [2003]). Many of the studies that attempt to describe meandering plumes struggle to separate fluctuations due to the movement of the plume centerline from the turbulent fluctuations [Yee et al., 1994, Luhar et al., 2000, Reynolds, 2000, Yee and Wilson, 2000, Franzese, 2003, Mortarini et al., 2009, Nironi et al., 2015, Marro et al., 2015, Mortarini et al., 2009]. Many of these studies resort to convolutions of a PDF of the location of the plume centerline (or the instantaneous location of the cloud centroid) with a PDF of the concentration in a frame of reference along the instantaneous centerline (under the assumption that the two are uncorrelated) in an attempt to model the plume behavior.

Consequently, in the study presented in this Chapter we shall examine the mixing

of tracer in a meandering plume by phase-locking the plume to separate the fluctuations due to the plume meander from the turbulent velocity and concentration fluctuations. Simultaneous laser induced fluorescence (LIF) and particle image/tracking velocimetry (PIV/PTV) data of the phase-locked meandering plume structure will allow us to: (1) directly compare the structure of the phase-locked concentration field for the meandering plume to prior straight plume studies [Crimaldi et al., 2002, Crimaldi and Koseff, 2006, Rahman and Webster, 2005] and (2) relate the turbulent flux of tracer for the meandering plume to more general turbulent mixing studies concerning the theory of the eddy-diffusivity hypothesis [Richardson, 1926, Batchelor, 1952, Okubo, 1968] and practice [Fischer et al., 1979, Okubo, 1971, Stacey et al., 2000, Fong and Stacey, 2003].

3.3 Literature Review

3.3.1 Turbulent Mixing

Mixing of scalar quantities such as mass and heat occur rapidly in a turbulent flow field [Roberts and Webster, 2002]. This is because the turbulent diffusion process is substantially more efficient at rapidly mixing tracers than molecular diffusion. As the overwhelming majority of all flows encountered in engineering and nature are turbulent, understanding the mixing of contaminants that occurs in a turbulent flow field is a critical area of study for a wide range of applications. To arrive at a reasonable understanding of the current research on turbulent diffusion, one must first be familiar with certain properties of turbulent flow fields. Turbulence can be thought of as consisting of a host of semi-coherent structures, called "eddies," that are constantly moving, reorienting, and evolving [Kundu and Cohen, 2004]. The motions of these eddies occur over a wide range of length and time scales. Most of the energy in turbulent flows is contained in the largest eddies. This energy is transferred to slightly smaller eddies, then to smaller eddies still, until it at last reaches the smallest

structures [Kundu and Cohen, 2004]. This process is referred to as the energy cascade, and was first identified by Lewis Richardson in 1922 [Kundu and Cohen, 2004]. Once the energy reaches the smallest eddies, it is dissipated as heat due to the effects of viscosity.

Thus, the scale of the largest and smallest motions in a turbulent flow are of particular interest. The largest motions are on the order of the "container" i.e., the water depth in a channel or the diameter of a pipe. The size of this large-scale motion is referred to as the integral length scale, l. The dissipation rate of energy in a turbulent flow is proportional to the kinetic energy of the flow multiplied by the rotational frequency [Tennekes and Lumley, 1972]. Thus, the dissipation rate, ϵ, is proportional to $\frac{\tilde{u}^3}{l}$, where the kinetic energy is proportional to the standard deviation of the velocity ($\tilde{u}$) squared and the rotational frequency is proportional to the standard deviation of the velocity divided by the integral length scale (l). The smallest motions in a turbulent flow field are those at which the dissipation actually occurs, the Kolmogorov microscale (η). The energy in a turbulent flow field is dissipated by the viscosity (ν) at this small scale, thus the Kolmogorov microscale must depend on the viscosity and the dissipation rate. From dimensional analysis, η is proportional to $\left(\frac{\nu^3}{\epsilon}\right)^{1/4}$ [Tennekes and Lumley, 1972].

If a tracer or scalar quantity is being mixed in the turbulent flow field, a further length scale can be specified, the Batchelor length scale, L_B, which refers to the scale at which molecular diffusion acts on the scalar quantity [Roberts and Webster, 2002]. L_B is proportional to $\left(\frac{\nu D^2}{\epsilon}\right)^{1/4}$, where D is the molecular diffusivity. The Schmidt number is defined as the kinematic viscosity divided by the molecular diffusivity $Sc = \frac{\nu}{D}$, in other words the ratio of the diffusion of momentum to the diffusion of the tracer. The ratio of the Kolmogorov microscale to the Batchelor length scale squared forms the Schmidt number, i.e., $Sc = \left(\frac{\eta}{L_B}\right)^2$. In aqueous flows, the molecular diffusivity of tracers is frequently several orders of magnitude smaller than the kinematic viscosity

of water, thus the concentration field in a turbulent water has much finer structure than the velocity field [Roberts and Webster, 2002].

Different eddy sizes play a role in making turbulent mixing efficient. For a patch of tracer of a given size, the turbulent eddies *smaller* than the patch continuously stretch and distort it [Roberts and Webster, 2002]. As a result, extremely large concentration gradients occur, which are quickly smoothed out by molecular diffusion (note that flux due to molecular diffusion is proportional to the concentration gradient). And thus the patch increases in size and the tracer is diluted. In contrast, eddies *larger* than the patch merely advect the patch and do not contribute to mixing.

The evolution equation for the time-averaged scalar concentration field in a turbulent flow is:

$$\frac{\partial \bar{c}}{\partial t} + \bar{u}_j \frac{\partial \bar{c}}{\partial x_j} = D \frac{\partial^2 \bar{c}}{\partial x_j^2} - \frac{\partial}{\partial x_j} \overline{u_j' c'} \tag{3.1}$$

where a Reynolds decomposition of both the concentration and the velocity is employed (i.e., $c = \bar{c} + c'$ and $u = \bar{u} + u'$) to separate the mean (denoted with an overbar) and fluctuating (denoted with a prime) components. The two terms on the right hand side of Eqn. 3.1 represent molecular diffusion $\left(D \frac{\partial^2 \bar{c}}{\partial x_j^2}\right)$ and the transport of the scalar due to the turbulent velocity fluctuations $\left(\frac{\partial}{\partial x_j} \overline{u_j' c'}\right)$, respectively. The molecular diffusivity (D) is frequently very small, thus $\frac{\partial}{\partial x_j} \overline{u_j' c'} \gg D \frac{\partial^2 \bar{c}}{\partial x_j^2}$. As a result, the presence of the $\overline{u_j' c'}$ term is what makes turbulent flows so much more effective at mixing scalars than laminar flows, which rely purely on molecular diffusion to mix the tracer. The molecular diffusivity is so much smaller relative to the turbulent flux of the *mean* scalar quantity that it is typically neglected [Roberts and Webster, 2002] and the turbulent advection-diffusion equation is approximated as (note that the overbar denoting mean value is typically dropped at this stage, and it is understood that $c = \overline{c}$, $u = \overline{u}$, etc.):

$$\frac{\partial c}{\partial t} + u\frac{\partial c}{\partial x} + v\frac{\partial c}{\partial y} + w\frac{\partial c}{\partial z} = -\frac{\partial}{\partial x}\overline{u'c'} - \frac{\partial}{\partial y}\overline{v'c'} - \frac{\partial}{\partial z}\overline{w'c'} \tag{3.2}$$

Unfortunately $\overline{u_j'c'}$ are unknown *a priori*, thus Eqn. 3.2 cannot be solved because it is not a closed mathematical model. To mathematically close Eqn. 3.2, the covariance of the velocity and concentration fluctuation terms are frequently modeled as a Fickian diffusion process (i.e., "the mass transport is proportional to the mean concentration gradient," [Roberts and Webster, 2002]), only with a much greater diffusion coefficient, called the eddy diffusivity or the turbulent diffusion coefficient (K_i):

$$\overline{u'c'} = -K_x\frac{\partial c}{\partial x} \tag{3.3}$$

$$\overline{v'c'} = -K_y\frac{\partial c}{\partial y} \tag{3.4}$$

$$\overline{w'c'} = -K_z\frac{\partial c}{\partial z} \tag{3.5}$$

The eddy diffusivity (K_i) varies based upon the flow type and the position within the flow. As it cannot be determined *a priori*; K_i is typically specified using experimental data [Roberts and Webster, 2002]. A natural next question is to wonder how one might be able to estimate the eddy diffusivity using easily measured properties of the flow?

Taylor [1921] and Richardson [1926], along with Batchelor [1952], are the pioneering studies on estimating the eddy diffusion coefficients from turbulent flow properties. In particular, their work concerns relating the motion of particles in turbulent flow to the eddy diffusion coefficient. The location ($\vec{X}$) of a particle after travel time T is [Roberts and Webster, 2002]:

$$\vec{X} = \int_0^T \vec{u} dt \tag{3.6}$$

where $\vec{u}$ is the Lagrangian velocity of the particle. If one were to release this particle many times from the same position in an isotropic turbulent flow field, then average the final position over the multitude of releases, the mean position of the particle would be zero [Roberts and Webster, 2002]. However, the variance of the particle position ($\overline{X^2}$) would be non-zero, and can be expressed by the following [Taylor, 1921, Kundu and Cohen, 2004]:

$$\overline{X^2(t)} = 2\overline{u'^2(t)}\, t \int_0^t \left(1 - \frac{\tau}{t}\right) R_L(\tau) d\tau \tag{3.7}$$

where $\overline{u'^2}$ is the variance of the turbulent velocity fluctuations and $R_L(\tau)$ is the autocorrelation of the Lagrangian velocity $\left(R_L(\tau) = \frac{\overline{u(t)u(t+\tau)}}{\overline{u'^2}}\right)$. The autocorrelation function approaches unity for very short time τ, and approaches zero for long times, as the particle "forgets" its original velocity [Roberts and Webster, 2002]. It is possible to define a time scale (the Lagrangian time scale, T_L) for which the velocity is strongly correlated with its original velocity:

$$T_L = \int_0^\infty R_L d\tau \tag{3.8}$$

For times less than T_L the velocity is assumed to be well correlated with the original velocity. Correspondingly, one may define a length scale associated with the Lagrangian time scale, the Lagrangian length scale (L_L):

$$L_L = \sqrt{\overline{u'^2}} T_L \tag{3.9}$$

Similar to the Lagrangian time scale correlation assumption, the particle motion is assumed to be well correlated in space for distances less than the Lagrangian length scale, L_L. Unsurprisingly, L_L is similar to the integral length scale, l, as the size of

the largest eddies dictate the length over which the flow is well correlated [Roberts and Webster, 2002].

The turbulent diffusion coefficient, K, is assumed to be proportional to one-half of the time derivative of the variance of the particle position:

$$K \sim \frac{1}{2}\frac{d\overline{X^2(t)}}{dt} \tag{3.10}$$

This assumption is made by analogy with the solution for the laminar advection-diffusion equation for a plume, in which the concentration distribution is a Gaussian function proportional to $exp\left(\frac{-r^2}{4Dt}\right)$, where r is the distance from the centerline and D is the diffusion coefficient. The standard deviation of the concentration distribution is $\sigma = \sqrt{2Dt}$ and it follows that the diffusion coefficient for a laminar plume is therefore equal to [Roberts and Webster, 2002]:

$$D = \frac{1}{2}\frac{d\sigma^2}{dt} \tag{3.11}$$

with obvious parallels to the formulation of the turbulent diffusion coefficient in Eqn. 3.10.

Numerous studies attempt to describe the standard deviation of the plume width as a means of estimating the turbulent diffusion coefficient, for example either for meandering atmospheric [Gifford, 1959, Barry, 1977, Gifford, 1982, Lee and Stone, 1983, Hanna, 1984a,b] or near-bed coastal [Fong and Stacey, 2003] plumes. Others attempt to define the autocorrelation function, R_L, as a means of estimating the the turbulent diffusion coefficient [Frenkiel, 1953, Murgatroyd, 1969, Anfossi et al., 2005, Oettl et al., 2005]. In the simplest formulations of the problem, an assumption is made that the turbulent diffusion coefficient is estimated at either times much shorter than T_L or times much longer than T_L.

If $\tau \ll T_L$ then $R_L \simeq 1$ and $\overline{X^2(t)} = \overline{u'^2(t)}t^2$. It follows that [Kundu and Cohen, 2004]:

$$K \sim \frac{1}{2}\frac{d\overline{X^2(t)}}{dt} = \overline{u'^2(t)}\, t \tag{3.12}$$

This reveals that the turbulent diffusion coefficient increases linearly with time for small times. This is a direct consequence of the assertion that only the eddies with scales less than or equal to the patch size contribute to the mixing. At very small time scales the patch continuously grows larger, increasing the range of turbulent eddies contributing to patch mixing and therefore increasing the diffusion coefficient. For $\tau \gg T_L$, the $\frac{\tau}{t}$ term inside the integral becomes negligibly small and $\overline{X^2(t)} = 2\overline{u'^2(t)}T_L t$ [Kundu and Cohen, 2004]. The turbulent diffusion coefficient is then proportional to:

$$K \sim \overline{u'^2(t)}T_L \tag{3.13}$$

or, substituting in the definition of the Lagrangian length scale (L_L), $K \sim \sqrt{\overline{u'^2}}L_L$. This formulation implies that the turbulent diffusion coefficient is constant for long times. This likewise follows from the assertion that eddies with scales less than or equal to the patch size contribute to the mixing. Once the patch has become very large (approaching the size of the integral length scale, l) there are few larger eddies left to increase the mixing and the turbulent diffusion coefficient becomes constant.

Richardson [1926] and Batchelor [1952] proposed relationships for the turbulent diffusion coefficient for patches of size less than L_L, under the assumption of high Reynolds number isotropic turbulence. Both studies make the assumption that the characteristic patch size, L, is located within the inertial subrange, i.e., that $\eta \ll L \ll l$ [Liao and Cowen, 2010]. Note that the existence of the inertial subrange is justified by the assumption of high enough Reynolds number such that the separation between the Kolmogorov microscale (η) and the integral length scale (l) is sufficiently large. Based on empirical analysis of atmospheric diffusion data, Richardson [1926] hypothesized that the turbulent diffusion coefficient was proportional to:

$$K \sim L^{\frac{4}{3}} \tag{3.14}$$

whereas Batchelor [1952], using a more rigorous consideration of the joint PDF of two fluid particles and Kolmogorov's similarity hypothesis [Kolmogorov, 1941], concluded that:

$$K \sim \left(\sqrt{\overline{L^2}}\right)^{\frac{4}{3}} \tag{3.15}$$

The similarities between the two formulations are obvious, and indeed the latter [Batchelor, 1952] is often offered as a proof of the former [Richardson, 1926] (e.g., in Fischer et al. [1979] and Roberts and Webster [2002]). However, while both formulations result in the same growth rate in time of the variance of the separation distance between two particles ($\overline{X^2(t)}$), they result in different shapes of the distance-neighbor function (the function that describes the probability that a pair of particles have a separation distance L among all particle pairs in the patch at a given time). A recent study by Liao and Cowen [2010] indicates that the Richardson [1926] scaling better predicts the distance-neighbor function for a plume in a turbulent boundary layer. It is worth mentioning that Fong and Stacey [2003] observed a turbulent diffusion coefficient growth rate proportional to L^2 for a near bed coastal plume, though the flow in their study fell in the "2-D turbulence" regime described in Batchelor [1969] (i.e., the horizontal extents of the flow were much larger than the vertical extent).

3.3.2 Straight Plumes Released Into a Turbulent Boundary Layer

Plumes of scalar quantities (such as mass or heat) released into a turbulent boundary layer are commonplace in both natural settings and in engineering applications [Crimaldi et al., 2002]. Crustaceans tracking odor plumes from a food source [Weissburg and Zimmer-Faust, 1994, Moore and Grills, 1999], a chemical release from underwater munitions [Webster, 2007], and a release of smoke or pollutant from a

smokestack into the atmosphere [Hanna, 1984a] are just a few of the many examples. As a consequence the concentration distribution of a straight plume released into a turbulent boundary layer has been studied extensively.

It is worthwhile to review the analytical solution for an idealized scalar plume released into a steady uniform flow, for comparison with the results of the presented studies. The governing equation for a scalar released into a turbulent flow with mean velocity equal to $(u, 0, 0)$ is (note that as in Eqn. 3.2, it is understood that $u = \overline{u}$ and $c = \overline{c}$):

$$u\frac{\partial c}{\partial x} = \frac{\partial}{\partial y}\left(K_y\frac{\partial c}{\partial y}\right) + \frac{\partial}{\partial z}\left(K_z\frac{\partial c}{\partial z}\right) \tag{3.16}$$

where longitudinal turbulent diffusion has been neglected, and Eqns. 3.4 and 3.5 have been subbed in to model the turbulent transport of the scalar in the lateral and vertical directions. If neither the mean velocity nor the turbulent diffusion coefficients vary spatially, this equation can be solved analytically [Crimaldi and Koseff, 2006] regardless of the release height of the plume above the bed. In all cases the solution for the mean concentration will be of the form [Crimaldi and Koseff, 2006]:

$$c\left(x, y, z\right) \propto \frac{\dot{m}}{4\pi x\sqrt{K_y K_z}} exp\left(-\frac{y^2}{2\sigma_y^2} - \frac{z^2}{2\sigma_z^2}\right) \tag{3.17}$$

where $\dot{m}$ is the continuous mass release rate at the source $(0, 0, 0)$, and σ_y and σ_z are the standard deviations of the Gaussian lateral and vertical concentration profiles. $\sigma_y = \sqrt{\frac{2D_y x}{u}}$ and $\sigma_z = \sqrt{\frac{2D_z x}{u}}$. The standard deviation of the lateral concentration profile is often used as an estimate of the plume width, e.g., when the "edge" of the plume is defined as the location where the mean concentration is two standard deviations away from the centerline mean concentration. For the Gaussian plume solution in Eqn. 3.17, the plume width grows as $x^{\frac{1}{2}}$ and the mean concentration values on the plume centerline decay as x^{-1}. The growth and decay rate in experiments of turbulent plumes are frequently compared to these values [Rahman and Webster,

2005, Crimaldi and Koseff, 2006].

In an effort to determine self-similarity, the lateral (at various y and fixed z positions) and vertical (at various z and fixed y positions) profiles are frequently seen in the form [Rahman and Webster, 2005]:

$$\frac{c\,(y)}{c_{y=0}} = exp\left(\frac{-y^2}{2\sigma_y^2}\right) \tag{3.18}$$

$$\frac{c\,(z)}{c_{z=z_0}} = exp\left(\frac{-z^2}{2\sigma_z^2}\right) \tag{3.19}$$

where the plume centerline is located at $y = 0$ and a height of $z = z_0$ above the bed. Note that the formulations in Eqns. 3.18 and 3.19 assume a Gaussian form, but experimental evidence suggests that, in particular, the vertical concentration profiles for a straight plume in a turbulent boundary layer may be of a different form [Rahman and Webster, 2005]. Nor are the vertical profiles necessarily self-similar for straight plumes released in a turbulent boundary layer [Rahman and Webster, 2005, Crimaldi and Koseff, 2006]. Similar normalized lateral and vertical profiles can be determined for the variance of the concentration.

Fackrell and Robins [1982] presented concentration distributions of a neutrally buoyant iso-kinetic (released with same velocity as ambient flow) plume in a wind tunnel with a rough bed released at two elevations, ground level and at $\sim 20\%$ of the boundary layer thickness above the bed. Bara et al. [1992] acquired concentration measurements of a neutrally buoyant iso-kinetic tracer released at the bed into a water channel with a rough bed. Yee et al. [1993] performed a similar study releasing the tracer at $\sim 35\%$ of the boundary layer thickness above the bed. Crimaldi and Koseff [2001], Crimaldi et al. [2002], and Crimaldi and Koseff [2006] captured the finescale structure of a vertical release of tracer at the bed. The tracer is released with extremely low momentum to mimic the release of a diffusive odorant. Webster et al. [2003] quantified the concentration field of a tracer released at 12.5% of the water

depth above the bed in a fully developed open channel flow. Similar experiments were performed in Rahman and Webster [2005] to access the effect of variable bed roughness of the plume characteristics. Several additional studies present field measurements of plumes released into the atmospheric boundary layer [Murlis and Jones, 1981, Jones, 1983, Murlis, 1986, Hanna and Insley, 1989, Mylne, 1992, 1993, Yee et al., 1994, 1995].

The profiles of the time averaged concentration along transverse sections were Gaussian and self-similar for all laboratory studies. When the tracer is released at a rough bed, the vertical profiles of the time averaged concentration are Gaussian and self-similar [Bara et al., 1992]. For the tracer released at a smooth bed case [Crimaldi and Koseff, 2006], the vertical profiles of the time averaged concentration are Gaussian and self-similar far from the source, but near the source the presence of the viscous sub-layer "traps" the dye, causing the concentration to be substantially higher near the bed than predicted by a Gaussian distribution. The authors [Crimaldi and Koseff, 2006] note that the observed effects of the viscous sub-layer "trapping" on the vertical profiles will likely not be observed in studies with larger Reynolds numbers or significant roughness. The vertical profiles of the time averaged concentration for a tracer released above the bed were not self-similar, due to the addition of the height above the bed as a relevant length scale [Fackrell and Robins, 1982, Yee et al., 1995, Webster et al., 2003]. Fackrell and Robins [1982] did fit reflected Gaussian profiles to the vertical concentration distribution with some success. Further, the maximum time averaged concentration was observed above the bed, rather than at the bed as with the bed release studies [Rahman and Webster, 2005].

There is less consensus on the profiles of the variance of the concentration fluctuations. Crimaldi et al. [2002] found that the transverse variance profiles were Gaussian and self-similar. This seems to contradict the findings of Fackrell and Robins [1982], who found the variance was maximized off the centerline. The difference in release geometries has been proposed as a possible cause of this discrepancy [Crimaldi et al.,

2002]. Rahman and Webster [2005] reported Gaussian and self-similar transverse variance profiles for smooth and low roughness beds. For the higher roughness cases, the transverse variance profiles were Gaussian near the source, but transitioned to bi-modal further downstream. The authors [Rahman and Webster, 2005] argue this is a result of the production term associated with the transverse mean concentration gradient becoming important in the scalar variance evolution equation. The transition from Gaussian to bi-modal of transverse concentration variance profiles is also reported in Crimaldi and Koseff [2006]. Similar disagreement in the literature is observed for the vertical profiles of the concentration variance. Fackrell and Robins [1982] reported self-similar profiles for a bed-level release, yet Bara et al. [1992] and Crimaldi and Koseff [2006] observed the profile shape evolving with distance downstream. Fackrell and Robins [1982] and Webster et al. [2003] observed a variable variance profile shape with distance downstream and a variance maxima located above the bed for the elevated release cases.

Many studies, particularly in the atmospheric boundary layer literature, quantify the probability density functions (PDFs) of the concentration fluctuations at specific positions within the plume. Fackrell and Robins [1982] and Yee et al. [1994] observed exponential PDFs with elongated tails near the source for the elevated release case. Fackrell and Robins [1982] observed Gaussian PDFs near the bed and exponential distributions above the bed at further downstream stations. In contrast Yee et al. [1994] observed concentration PDFs that transition to bi-modal further downstream of the source, finally transitioning back to exponential PDFs very far downstream of the source. For increased bed roughness, Rahman and Webster [2005] similarly observed highly skewed PDFs of concentration fluctuations near the source, which appeared to approach Gaussian PDFs farther downstream. Yee et al. [1993] observed highly asymmetric PDFs with elongated tails of concentration fluctuations at various locations within the plume. Elevation within the plume had a strong effect on the

shape of the PDFs, but the transverse position did not. The conjugate-beta distribution best modeled the concentration fluctuation distribution over the large majority of the positions observed in Yee et al. [1993]; several more common distributions were unable to satisfactorily model the concentration fluctuations. The conjugate-beta model parameters were determined from the skewness and fluctuation intensity.

3.3.3 Meandering Plumes In Turbulent Boundary Layer

The theory and the studies presented in Section 3.3.2 concerned straight plumes released into a turbulent boundary layer. That is to say that, although the instantaneous plume may appear sinuous, the time averaged centerline remained aligned with a straight path. In many circumstances, however, the plume centerline does not remain along a straight path, the plume centerline moves over large time scales, and the plume is said to "meander." In these meandering plumes the fluctuations in concentration are not only caused by the turbulence but also the large scale motion of the plume centerline [Sykes, 1984, Wilson et al., 1985, Hanna, 1986].

Plumes released in an atmospheric boundary layer are perhaps the most studied case of meandering plumes. Atmospheric plume meandering is very commonly observed in low-wind speed conditions, where large scale horizontal oscillations in the wind velocity become dominant in governing the plume motion [Etling, 1990, Anfossi et al., 2005, Oettl et al., 2005]. One of the earliest analytical models of meandering plumes is that of Gifford [1959], and the assumptions made in developing it are a natural starting point for many later studies (e.g. Hanna [1984a,b, 1986], Ride [1988], Bara et al. [1992], Nironi et al. [2015], Marro et al. [2015]).

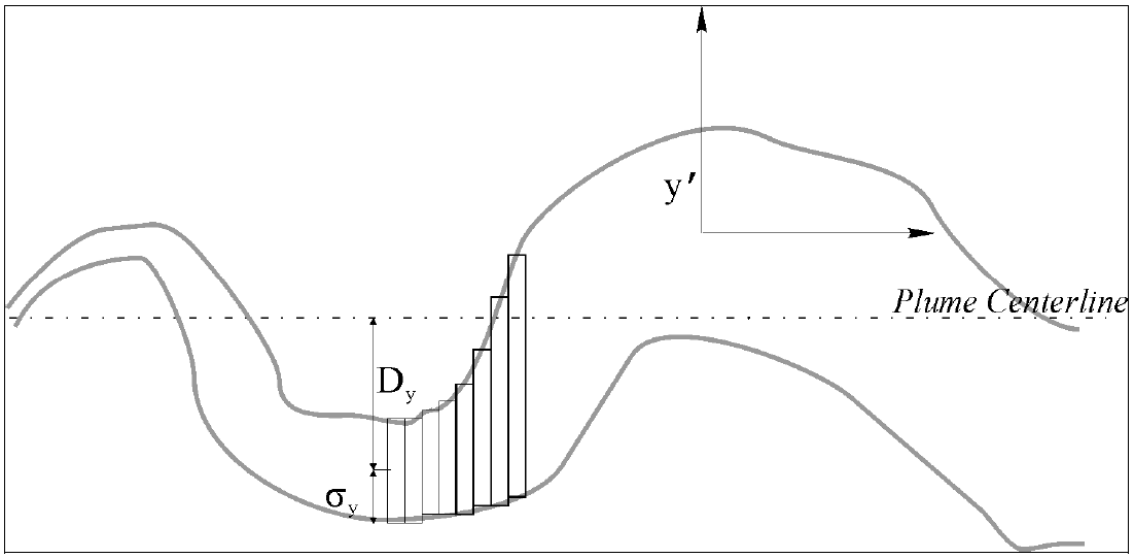

Figure 3.1: Sketch of the Gifford [1959] plume model, reproduced from Dickman [2008]. D_y is the location of the instantaneous plume centerline relative to the time-averaged plume centerline. y' denotes the modified coordinate system with the origin at the instantaneous plume centerline location, D_y.

A basic sketch of the Gifford [1959] plume model is shown in Figure 3.1. In the Gifford [1959] model, the plume disperses about an instantaneous centerline located at D_y from the time-averaged plume centerline. The transverse dispersion is entirely controlled by the plume width as measured by the standard deviation of the lateral concentration profile σ_y, and is unaffected by the plume meander. The key conceptual assumption in the Gifford [1959] plume model is that the meander of the plume is due to large scale eddies (eddies larger than the plume width), which move the plume centerline but do not contribute to the mixing. Thus, the plume meandering and the relative dispersion of the plume about the instantaneous centroid are considered independent processes. This is similar to the theory on turbulent mixing discussed Section 3.3.1, in which eddies larger than the tracer "patch" merely advect the patch and only eddies of the same size or smaller than the patch contribute to mixing. The Gifford [1959] model also entirely neglects longitudinal dispersion, and assumes that

the plume width falls within the inertial subrange (see Section 3.3.1).

Under these restrictions, Gifford [1959] proposes a model that is the solution to the turbulent advection-diffusion equation for a straight plume, with the caveat that plume centerline is located at some unknown position away from the time-averaged centerline. Thus, making no assumptions about the instantaneous centerline position (either in the lateral, D_y, or vertical, D_z, directions) the Gifford [1959] plume model predicts a mean concentration (c) given by:

$$\frac{c}{\dot{m}} = \frac{1}{2\pi \left(\sigma_y^2 \sigma_z^2\right)^{\frac{1}{2}} u} exp\left[-\frac{(y-D_y)^{\frac{1}{2}}}{2\sigma_y^2} - \frac{(z-D_z)^{\frac{1}{2}}}{2\sigma_z^2}\right] \tag{3.20}$$

for non-isotropic dispersion (where the lateral and vertical eddy diffusivities are different) and:

$$\frac{c}{\dot{m}} = \frac{1}{2\pi\sigma_y^2 u} exp\left[\frac{-(y-D_y)^{\frac{1}{2}} - (z-D_z)^{\frac{1}{2}}}{2\sigma_y^2}\right] \tag{3.21}$$

for isotropic dispersion. In Eqns. 3.20 and 3.21, $\dot{m}$ is the continuous tracer release rate at the source, u is the mean velocity, and σ_z is the standard deviation of the vertical concentration profile. It is important to keep in mind that σ_y and σ_z are expected to be functions of position along the time-averaged centerline (x). As shown in Eqns. 3.20 and 3.21, the Gifford [1959] model predicts a plume with a Gaussian mean concentration distribution about the instantaneous centerline.

The precise location of the instantaneous centerline (e.g., some description of D_y, D_z) presents significant challenges for modeling atmospheric plumes. Some of the more recent studies [Nironi et al., 2015, Marro et al., 2015] propose PDFs of the concentration at a given location downwind by taking the convolution of the PDF of the location of the plume centerline (or, in the case of a single release of tracer, the instantaneous location of the tracer cloud centroid) with the PDF of the concentration in a frame of reference along the instantaneous plume centerline/cloud centroid [Marro et al., 2015]. In the most recent literature on meandering atmospheric plumes,

the PDF of the concentration in a frame of reference along the instantaneous plume centerline/cloud centroid is typically assumed to have the form of a Gamma distribution [Yee et al., 1994, Yee and Wilson, 2000, Nironi et al., 2015, Marro et al., 2015], parameterized by the mean concentration at the instantaneous plume centerline/cloud centroid and the intensity of the relative concentration fluctuations (the standard deviation of the concentration at the instantaneous plume centerline/cloud centroid divided by the mean concentration). These parameters must be measured or modeled [Gailis et al., 2007, Ferrero et al., 2013]. The PDF of the location of the plume centerline/cloud centroid is generally assumed to be the product of the vertical (z) and transverse (x) PDFs of the plume centerline/cloud centroid, which is an assumption of convenience rather than theoretical rigor [Marro et al., 2015]. The transverse PDF of the plume centerline/cloud centroid is generally assumed to have a Gaussian form [Nironi et al., 2015, Marro et al., 2015]. Various forms of the vertical PDF of the plume centerline/ cloud centroid have been proposed, including a reflected Gaussian distribution [Arya, 1999, Nironi et al., 2015, Marro et al., 2015] or PDFs generated from stochastic Lagrangian "puff" tracking models [Reynolds, 2000, Luhar et al., 2000, Franzese, 2003, Mortarini et al., 2009]. It is important to note that for the PDF convolution approach to be applicable, it must be assumed that the location of the plume centerline/cloud centroid and the concentration within the frame of reference along the plume centerline/cloud centroid are independent random variables. That is to say that the assumptions of the Gifford [1959] approach, regarding the independence of the plume/cloud meander and the relative dispersion about the instantaneous centerline/centroid, must be valid.

Another key consideration is parameterizing the growth of the plume width (measured by the standard deviation of the concentration profiles σ_y and σ_z). As described in Section 3.3.1, an assumption is made that the standard deviation of the concentration profile is proportional to the variance of particle position, i.e., $\sigma \propto \overline{X^2(t)}$.

For very short times and very long times, estimating $\overline{X^2(t)}$ is fairly straightforward using the theory of Taylor [1921]. Very short times are assumed to be much shorter than the Lagrangian timescale (T_L, see Eqn. 3.8) and thus the plume width is given by $\overline{X^2(t)} = \overline{u'^2(t)}t^2$, as in the derivation of Eqn. 3.12, where $\overline{u'^2(t)}$ is the variance of the turbulent velocity fluctuations. Similarly, very long times are assumed to be much longer than T_L and thus the plume width is given by $\overline{X^2(t)} = 2\overline{u'^2(t)}T_L t$ (see derivation of Eqn. 3.13). The simplified long time case still requires an estimate of the Lagrangian timescale. In the meandering plume literature, the Lagrangian timescale is customarily given by $T_L = \frac{2\overline{u'^2(t)}}{C_0\epsilon}$ [Tennekes, 1982], where C_0 is the Kolmogorov constant (assumed equal to 4.5 in Nironi et al. [2015], Marro et al. [2015]) and ϵ is the dissipation rate of turbulent kinetic energy described in Sec 3.3.1. T_L can also be specified from a calculated or estimated Lagrangian autocorrelation function (R_L) from Eqn. 3.8.

The question of how to parameterize the growth of the meandering plume width for intermediate times still remains. One approach is to propose a function defining the growth rate of the plume in time to match empirical data [Nironi et al., 2015, Marro et al., 2015]. This function must necessarily satisfy the asymptotic conditions for very short times and very long times described above [Franzese, 2003, Franzese and Cassiani, 2007]. Another approach is to propose an Eulerian or Lagrangian autocorrelation function governing the variance of particle position based on a review of experimental data [Hanna, 1983, Degrazia et al., 1991, Maryon, 1998, Oettl et al., 2001, Anfossi et al., 2005, Oettl et al., 2005]. Note that the Eulerian autocorrelation function is not equivalent to the Lagrangian autocorrelation function described in Eqns. 3.7 and 3.8, but the two are related by a transformation in time [Anfossi et al., 2005].

3.3.4 Wake Downstream of Bluff Bodies

Although plumes released into the atmosphere are perhaps the most-studied instance of plume meandering, that is not the sole situation in which the flow (and thus the plume) is observed to meander. Consider for example the flow past a circular cylinder at Reynolds number ($Re = \frac{U_\infty d}{\nu}$, where U_∞ is the free-stream velocity, d is the cylinder diameter, and ν is the kinematic viscosity) greater than 40. Images (see Figure 3.2) show that the wake oscillates, and the velocity is periodic in time and with distance downstream [Kundu and Cohen, 2004].

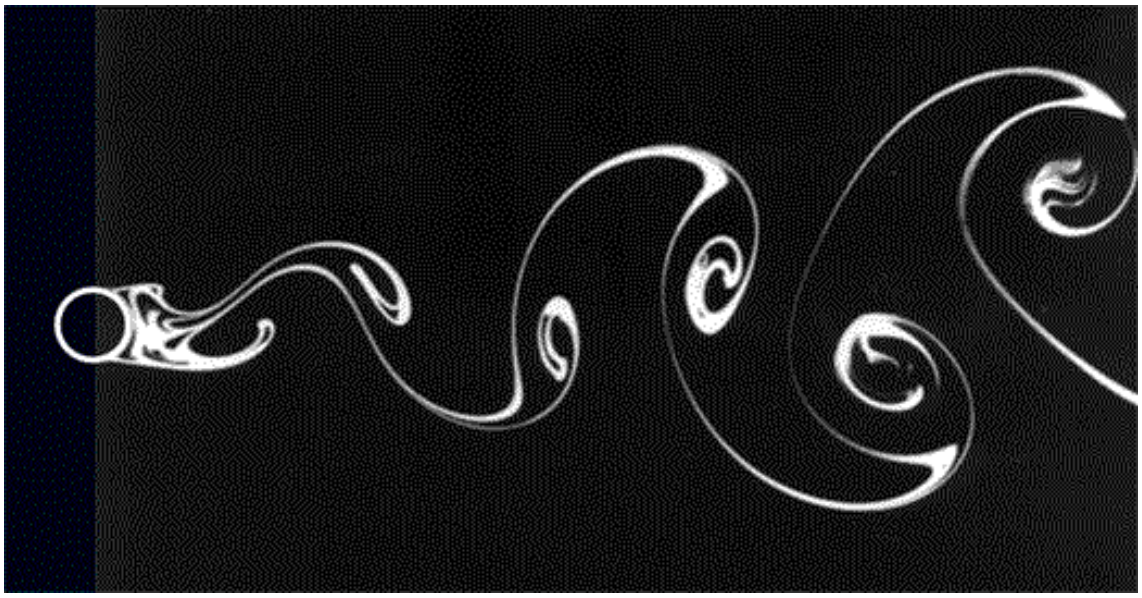

Figure 3.2: The wake structure downstream of a circular cylinder. Image reprinted from Van Dyke [2002].

As observed in Figure 3.2, the amplitude of the oscillation grows with distance downstream. The wake structure "rolls up" into rows of staggered vortices with alternating senses of rotation due to the shear generated between the comparatively high velocity fluid to either side of the circular cylinder and the low velocity fluid immediately behind it [Kundu and Cohen, 2004]. The staggered row of vortices in the flow downstream of a bluff body is referred to as a *von Karman vortex street*, after

the first individual to describe the phenomenon, von Karman [1921]. The vortices in the von Karman vortex street propagate downstream slower than the free-stream velocity (U_∞). The dominant frequency of the oscillations is characterized by the non-dimensional Strouhal number (St), which is defined as [Kundu and Cohen, 2004]:

$$St = \frac{nd}{U_\infty} \tag{3.22}$$

where n is the frequency of the oscillation. For flows past a circular cylinder, the Strouhal number is near 0.21 for a wide range of Reynolds numbers [Kundu and Cohen, 2004]. Below $Re = 200$, the flow immediately downstream of the cylinder is laminar, and the vortices continue to be laminar as they propagate far downstream. Above $Re = 200$, the vortices become unstable, and the flow within the vortices becomes very chaotic [Kundu and Cohen, 2004]. However, the wake still exhibits very strong periodicity corresponding to $St = 0.21$. At very high Reynolds number (e.g., $Re > 5000$), the wake becomes completely turbulent with no discernible periodicity.

von Karman vortex streets or similar structures can be observed in the environment when the wake structure is largely two-dimensional. Predominantly two-dimensional wake structure can be the result of density stratification in the ambient fluid inhibiting vertical mixing [Thompson and Gower, 1977], or can be observed in very shallow flows with large horizontal extent [v. Carmer and Jirka, 2001]. Quasi-periodic vortex shedding has been observed in a variety of flows, including: shallow 2-D wake flows past islands in coastal seas and estuaries [Wolanski et al., 1984, Ingram and Chu, 1987, Cramp et al., 1991], shallow 2-D wake flows past anthropogenic obstacles [Van Dyke, 1982], as well as in the wake structure behind mountain peaks under very strong density stratification [Thompson and Gower, 1977, DeFelice et al., 2000].

For three-dimensional flows with weak or no density stratification, orderly, fully-developed von Karman vortex streets are unable to form, as vortex stretching and

tilting, as well as mixing uninhibited by density stratification, break down the staggered rows of vortices. Nonetheless, large-scale oscillations perpendicular to the major axis have been observed in 3-D wake flows past bluff bodies. The 3-D wake structure downstream of both a square cylinder [Luo et al., 2007] and a circular cylinder [Fu and Rockwell, 2005a,b, Sahin et al., 2007, Ozturk et al., 2009, Sahin and Ozturk, 2009] attached to a base plate both exhibit large scale periodic motion perpendicular to the cylinder axis. Similar large-scale oscillations have been observed to either side of the wing in the wake of wing-body junctions [Rood, 1984a,b, Rood and Keller, 1984, Fleming et al., 1991, 1993].

Given the large-scale oscillations of the wake structure behind bluff bodies for a wide range of Reynolds numbers, it is reasonable to expect the plume of a tracer released in the wake to meander. Indeed, studies of concentration fields in the wake of flows past bluff bodies have observed large scale periodic plume meandering [Bo et al., 2003, von Carmer et al., 2009]. That the wake structure of flows past bluff bodies frequently exhibit a dominant periodicity (corresponding to a Strouhal number near $St = 0.21$) offers some hope that the plume centerline may be defined by a simple oscillatory function. This would make the problem of plume meandering more tractable than the complex PDF convolution described in Section 3.3.3 for atmospheric plumes, in which the plume centerline was undefined. For example, it is possible to extend the Gifford [1959] meandering plume model if the location of instantaneous centerline (D_y) has a periodic component, using the extended Reynolds decomposition of Reynolds and Hussain [1972]. Reynolds and Hussain [1972] included a phase-averaged velocity to the Reynolds decomposition described in Section 3.3.1. Note that phase-averaged component of the velocity is to some extent a mathematical artifact of the phase-averaging, and therefore does not correspond to a "real-world" component of the velocity directly experienced by the flow.

In the Reynolds and Hussain [1972] decomposition the instantaneous velocity (u)

is broken down into three components, the mean velocity ($\overline{u}$), the fluctuating velocity (u'), and the phase-averaged velocity ($\hat{u}$):

$$u = \overline{u} + u' + \hat{u} \tag{3.23}$$

Concentration, pressure, etc. can be decomposed in a similar fashion [Dickman, 2008]. The phase-averaged velocity ($\hat{u}(\tau_m)$) is defined by averaging the instantaneous velocity (u) at a specific period (τ_m):

$$\hat{u}(\tau_m) = \frac{1}{N}\sum_{j=1}^{N}\left[u(j\tau_m) - \overline{u}\right] \tag{3.24}$$

where N is an integer large enough that the phase-average of the turbulent velocity fluctuations (u') converges to zero. By definition, the time-average of the phase-averaged velocity is zero. Similarly, phase-averaged and turbulent quantities are uncorrelated, e.g. $\overline{u'\hat{u}} = 0$. The velocity and concentration decompositions described in Eqn. 3.23 can be substituted into the advection-diffusion equation, and if the resulting formulation is time-averaged, one obtains [Dickman, 2008]:

$$\frac{Dc}{Dt} = \frac{\partial}{\partial x_j}\left(D_j\frac{\partial c}{\partial x_j} - \overline{u_j'c'} - \overline{\hat{u}_j\hat{c}}\right) \tag{3.25}$$

Note that as in Eqn. 3.2 and Eqn. 3.16, in Eqn. 3.25 it is understood that $u = \overline{u}$ and $c = \overline{c}$. As in our discussion of Eqn. 3.1 in Section 3.3.1, the molecular diffusion term can be neglected, and the turbulent scalar transport modeled with an eddy-diffusion coefficient (i.e., $\overline{u_j'c'} = -K_j\frac{\partial c}{\partial x_j}$), simplifying the formulation somewhat:

$$\frac{Dc}{Dt} = \frac{\partial}{\partial x_j}\left(K_j\frac{\partial c}{\partial x_j} - \overline{\hat{u}_j\hat{c}}\right) \tag{3.26}$$

However, the $\overline{\hat{u}_j\hat{c}}$ term remains, and closure models of the term are generally application-specific [Dickman, 2008]. If $\overline{\hat{u}_j\hat{c}}$ is neglected, the Gifford [1959] plume solution may be adapted to the problem, given the appropriate coordinate transformation to account

for the now partially-periodic plume meander. As a simple example, for a partially-periodic meander in the y-direction only, the modified transverse coordinate moving with the plume centerline, y' (see Figure 3.1), is defined as [Dickman, 2008]:

$$y' = y - D_y\left(x, \tau_m\right) sin\left(\frac{2\pi\tau_m}{T_m}\right) \tag{3.27}$$

where τ_m is the specific period introduced in Eqn. 3.24 and T_m is the dominant plume meander period. Note that this definition (Eqn. 3.27) still allows for non-periodic meander as a function of distance downstream (x) and Reynolds decomposition phase-averaging period (τ_m). Under the assumptions in Gifford [1959] (i.e., negligible longitudinal dispersion and transverse dispersion independent of plume meander), the phase-averaged concentration along the plume centerline is [Dickman, 2008]:

$$\frac{c\left(x, y, z_0, \tau_m\right)}{c_0} = \frac{1}{\sqrt{\pi}} exp\left[\frac{-\left(y'\right)^2}{2\left(\sigma_y(x)\right)^2}\right] \tag{3.28}$$

where c_0 is the centerline concentration.

3.3.5 The Horseshoe Vortex and 3-D Structure of the Wake Downstream of a Junction

The discussion in Section 3.3.4 is principally concerned with describing the bluff body wake structure in a 2-D plane perpendicular to the major axis of the bluff body. The periodic or quasi-periodic shedding of vortices with vorticity aligned with the major axis from either side of a long cylinder or similar feature is conceptually easy to grasp. However, a recent study on the wake structure of a junction of a plate and circular cylinder [Ozturk et al., 2009] has observed wake motion aligned with the major axis of the bluff body, in addition to the large-scale periodicity described in Section 3.3.4. To understand the wake motion aligned with the major axis of the bluff body, it is necessary to expand the scope of our discussion from solely the wake structure downstream, and briefly consider the characteristics of the flow upstream and around a bluff body.

In the case of a very long circular cylinder, the flow field upstream and in the wake is relatively unaffected by the end boundary conditions (e.g., the mounting plate), thus the variability in the flow field is principally in the 2-D plane perpendicular to the major axis of the cylinder. In very shallow flows around bluff bodies, the end boundary conditions are quite relevant to the physics of the problem. The shearing of the flow parallel to the boundary over such a limited spatial extent (e.g. the flow depth) results in rapid mixing of tracer perpendicular to the boundary. However, from an analysis perspective, the mixing is so rapid that it is possible and substantially more convenient to consider the flow field as two-dimensional. In intermediate depth cases, one must consider the effects of the boundary layer that develops on the substrate upstream of the bluff body. As the boundary layer approaches the bluff body, the streamwise adverse pressure gradient induced by the bluff body causes the approach boundary layer to separate from the substrate [Simpson, 2001]. This causes the flow to "roll up" into a vortex immediately upstream of the bluff body (see Figure 3.3). Spanwise (across the face of the bluff body) pressure gradients force the fluid to either side of the bluff body [Simpson, 2001]. The flow around the bluff body forces the aforementioned vortex to wrap around the bluff body to form a horseshoe shape (see Figure 3.4). Thus, this vortex is described as a "horseshoe vortex" [Simpson, 2001, Sahin et al., 2007]. As discussed in Simpson [2001], the primary horseshoe vortex has the same sense of rotation as the approach boundary layer. Smaller secondary vortices with an opposite sense of rotation may be generated immediately upstream of the primary horseshoe vortex (see Figure 3.3) to preserve the shape of the streamlines [Simpson, 2001].

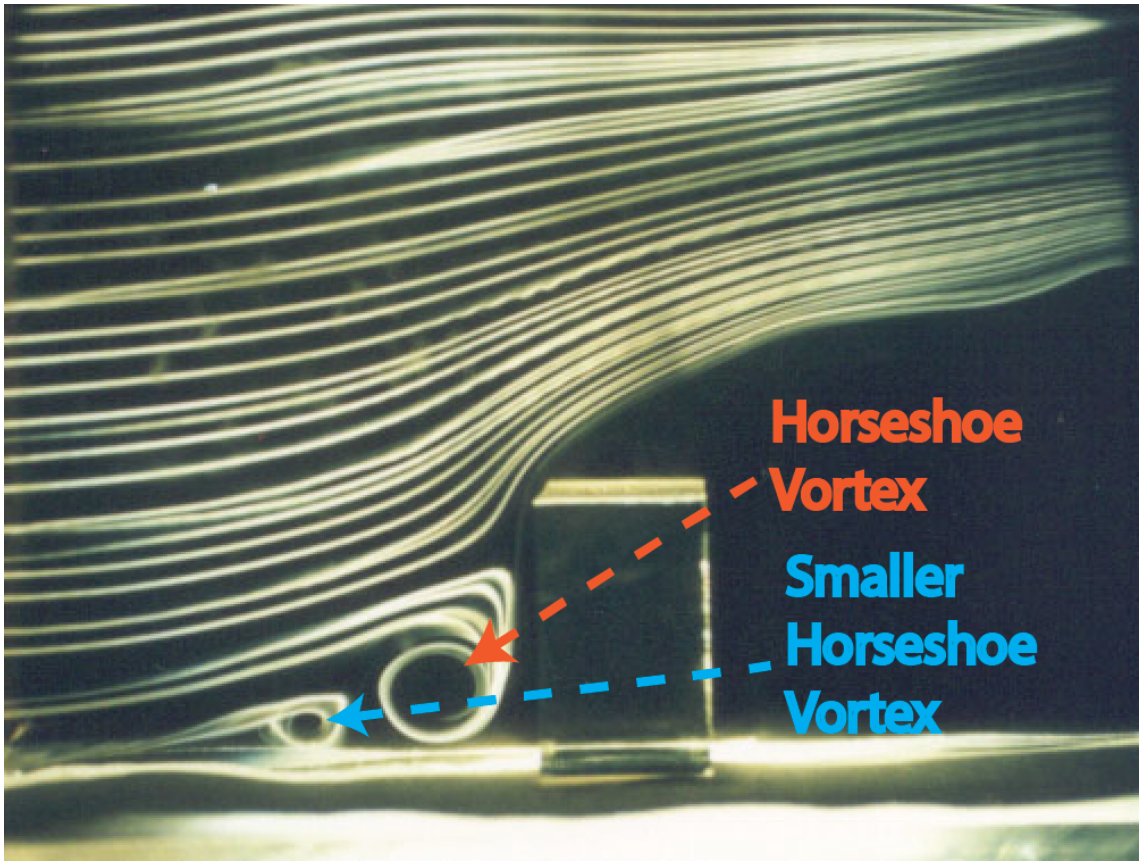

Figure 3.3: Smoke-wire image of a horseshoe vortex around rectangular block (side view). Image adapted from Fluid Dynamics and Flow Control Research Laboratory - Chulalongkorn University.

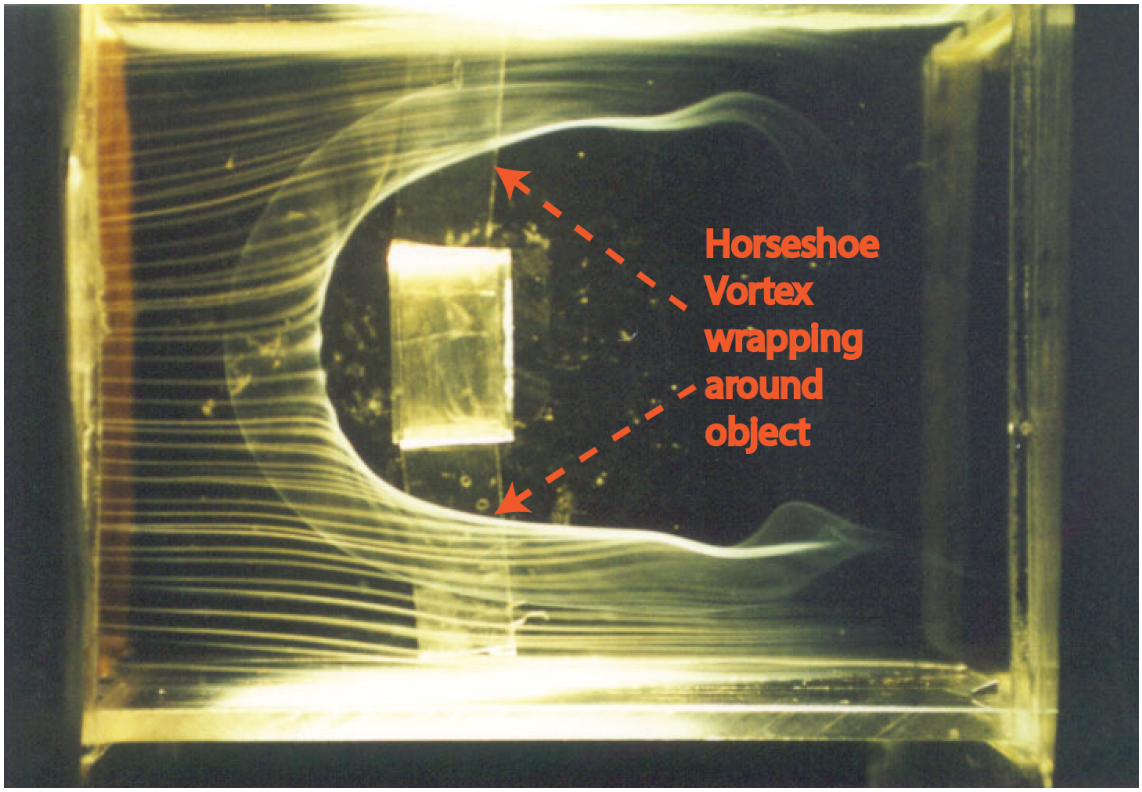

Figure 3.4: Smoke-wire image of a horseshoe vortex around rectangular block (top-down view). Image adapted from Fluid Dynamics and Flow Control Research Laboratory - Chulalongkorn University.

Many studies are devoted to examining the horseshoe vortex system in the immediate vicinity of the bluff body due to the ramifications for aviation and industrial applications. The primary horseshoe vortex entrains high speed fluid from the free-stream, forcing it near bluff body, which increases drag on the body and heat transfer in the region [Simpson, 2001]. The unsteady nature of the horseshoe vortex system similarly increases heat transfer and can induce vibration of the bluff body. The horseshoe vortex system in the immediate vicinity of a bluff body has also been extensively studied in the context of sediment scour around bridge piers. The horseshoe vortex that develops around bridge piers scours the river bed at the base of the piers, weakening the bridge foundation and potentially leading to failure [Dargahi, 1990,

Kim et al., 1991, Melville, 1997, Simpson, 2001].

For laminar boundary layers approaching a circular cylinder, a lone steady horseshoe vortex is observed at very low Reynolds numbers [Baker, 1979, 1985, Kaul et al., 1985, Thomas, 1987, Baker, 1991, Visbal, 1991, Ballio et al., 1998, Simpson, 2001]. As the Reynolds number increases, the number of horseshoe vortices increases up to three. The vortices remain steady up to a threshold Reynolds number, at which point they oscillate periodically in time (for laminar approach boundary layers). As discussed in Simpson [2001], the periodicity is due to instability of the horseshoe vortex and is not related to the von Karman vortex shedding in the wake of the cylinder. The Reynolds number at which transition to multiple vortices and the transition to oscillating vortices occur is variable among studies [Simpson, 2001]. Similar experiments have been performed on a Rood wing [Khan et al., 1995] and a rectangular bluff body [Seal et al., 1995]. For fully turbulent approach boundary layers, the horseshoe vortices upstream of the junction are not steady, nor constant in position, size, or strength [Hunt et al., 1978, Baker, 1980, Dargahi, 1989, Pierce and Shin, 1992, Simpson, 2001].

Although less extensively studied, it is unsurprising that the horseshoe vortices can affect the flow downstream of the junction. A recent study by Ozturk et al. [2009] observed a horseshoe vortex whose trailing edges (which wrap around the cylinder shape) extended downstream past the downstream face of the cylinder (see Figure 3.5). The horseshoe vortices are unsteadily shed from the bluff body and propagate downstream in the wake [Sahin et al., 2007]. It is possible for the shed horseshoe vortices to "leapfrog" past one another in the wake, but they may also merge together to form a larger vortex [Simpson, 2001]. The shed horseshoe vortices also interact with the large vortices which force the meandering of the flow described in Section 3.3.4. This interaction increases the mixing of the wake fluid with the free-stream flow, which in turn increases the strength of the velocity fluctuations in

the wake [Sahin et al., 2007, Ozturk et al., 2009, Kirkil and Constantinescu, 2012, El Hassan et al., 2015]. It seems likely that this increased mixing of fluid would lead to a corresponding increase in mixing and dilution of any scalar quantity released in the wake.

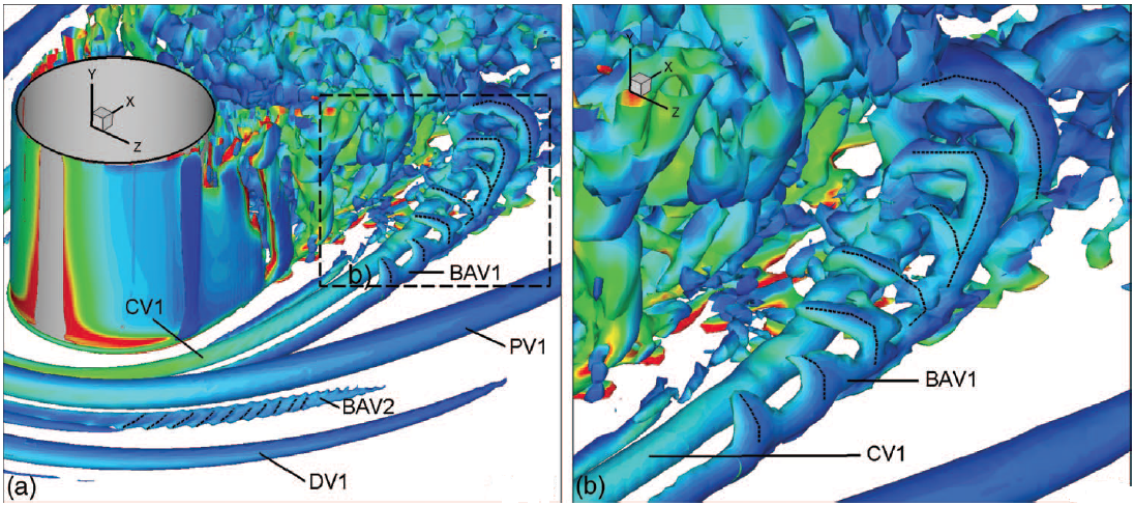

Figure 3.5: The vortical structure of flow around a cylinder from the LES of Kirkil and Constantinescu [2012]. The vortices are identified with Q isosurfaces. CV1 is the horsehsoe vortex that forms closest to the front face of the cylinder, BAV1 is a secondary vortex with an opposite sense of rotation as CV1, PV1 is a second horsehsoe vortex that forms upstream of CV1, BAV2 is an additional secondary vortex, and DV1 is the third and final horseshoe vortex that forms upstream of PV1. Image adapted from Kirkil and Constantinescu [2012].

3.4 Materials and Methods

An experiment was performed to study the turbulent flux of a passive scalar in a meandering turbulent plume. Measurements consisted of simultaneous particle-image-velocimetry (PIV) and laser-inducer-fluorescence (LIF) measurements to quantify the instantaneous velocity and concentration field. Data were also collected (LIF only) for the turbulent flux in a straight plume in the same flume, for comparison

with the meandering plume results. Note that Dr. Ann Larsson conducted the experiments in $2012-2013$. Dr. Larsson also performed the preliminary image processing. The author of this thesis performed all of the analysis and interpretations presented herein.

3.4.1 Experimental Design

All experiments were performed in a 1.07 m wide by 24.4 m long rectangular cross section tilting flume. The flume head box was filled with water at $22°C$ from an underground sump by a submerged pump. The water was dechlorinated prior to the experiments. A stilling device in the flume head box minimized the turbulence intensity of the flow entering the flume. Uniform depth ($H = 200 \pm 0.1mm$) flow was created for at least 12 m upstream of the test section by adjusting the tailgate position and bed slope. Tracy and Lester [1961] and Rahman and Webster [2005] confirmed that a fully-developed turbulent boundary layer is generated in the test section under these conditions. The sidewall of the flume in the vicinity of the text section is glass.

A PVC plastic diverting plate (25.3 cm tall, 10.1 cm long, and 2.54 cm thick) suspended in the flume induced the plume meandering. The base of the plate was positioned less than 1 mm above the flume bed and the top of the plate extended above the free surface. A vertical rod through the upstream edge of the plate fixed the pivot location. A DC motor attached to to the diverting plate via a disk and linkage mechanism forced the motion of the downstream edge of the plate. An image of the diverting plate setup being tested prior to installation in the flume is shown in Figure 3.6.

Figure 3.6: Image of the diverting plate apparatus being tested prior to installation in the flume. The streamlined PVC diverting plate is at the bottom of the image near the floor. It is mounted to the support structure via a pivot rod and the driving rod from the DC motor. The DC motor is in black to the upper left of the image.

The period of the plate oscillation was 9.5 s, and the amplitude of the transverse displacement of the downstream edge of the plate was 5.08 cm. The diverting plate was designed such that the flow characteristics in the wake were analogous to the wake downstream of a 10.1 cm circular cylinder for the same water depth and free-stream velocity ($H = 200 \pm 0.1$ mm and $U = 50$ mm/s, respectively). The resulting Strouhal number is $St = 0.21$. The advantage of a meandering plume generated by a periodically-oscillating plate was that it allowed the extraction of a trigger signal (via a mechanical trigger attached to the diverting plate apparatus) to collect data at specific phases in the plate motion.

The passive scalar (florescent dye) was released 400 mm downstream of the center of the diverting plate and 46 mm upstream of the test section. The dye was released iso-kinetically through a 4.2 mm diameter nozzle, located 20 mm above the flume bed. The nozzle fairing was streamlined to minimize the flow disturbance.

3.4.2 Optics

Illumination for the LIF measurements was provided by a 3.6 W Argon-ion laser (Coherent Innova 100-10, Coherent Inc., Santa Clara, CA) with a wavelength of 514 nm. The laser was run in open aperture mode and passed through two 4 m focal lenses, resulting in a beam diameter of 1 mm in the center of the plume.

The illumination for the PIV measurements was provided by a $5.2 - 5.4$ W Krypton-ion laser (Coherent Innova Sabre, Coherent Inc., Santa Clara, CA) with a wavelength of 647.1 nm. The aperture on the laser was set to 18 and did not pass through any focal lenses, resulting in a beam diameter in the center of the plume of $1.5 - 2$ mm.

The laser beams were swept in the streamwise direction via scanning mirrors controlled with a National Instruments multi-purpose I/O module programmed in LabView (National Instruments Corporation, Austin, TX). The resulting horizontal

light sheets were formed 20 mm above the flume bed (the same height as the florescent dye release). The LIF and PIV images were captured with two side-by-side digital cameras (sCMOS pco.edge, PCO AG, Kelheim, Germany) run in global shutter mode and mounted 1.5 m above the flume bed at the test section. Each camera was equipped with a 24 mm Nikon lens (Nikon, Tokyo, Japan) at an f-stop of f/2.0. The LIF camera was further equipped with a bandpass filter (Omega Optical Inc., Brattleboro, Vermont) passed light with a wavelength of 555 ± 15 nm (i.e., in the band of the wavelength emitted by the fluorescent dye). The cameras provide 16-bit 2560×2160 pixel images that span 1000 mm of the flume in the streamwise direction and 840 mm in the transverse direction. A 19 mm thick acrylic sheet was suspended just above the water surface (wetting the bottom surface of the sheet only) during the experiment to prevent optical distortion from the free surface.

3.4.3 Timing System and Laser Scanning

The PIV and LIF images were acquired simultaneously for four phases ($\phi = 0°$, $\phi = 90°$, $\phi = 150°$, and $\phi = 240°$) in the diverting plate motion. $\phi = 0°$ is defined as the maximum transverse displacement of the diverting plate position. For the LIF dataset, 6706 images were acquired for each phase, with a 9.5 s delay between successive images. Similarly, for the PIV/PTV dataset, 6706 image pairs were acquired for each phase. Thus, the total experiment time is approximately 17.5 hr.

To synchronize the image acquisition to the diverting plate motion, a mechanical push switch was installed on the diverting plate to trigger the image acquisition sequence. The sequence of collecting the four images (at 0°, 90°, 150°, and 240°) proceeded as follows: (1) The push switch was mechanically triggered by the motion of the diverting plate, sending a 5 V pulse to the external trigger input of a pulse

generator (Model 500D, Berkeley Nucleonics Corporation, San Rafael, CA). The allowable length of the triggering pulse was set to 0.7 s, to remove secondary spikes in the pulse signal. (2) the pulse generator adjusted the output voltage to $> 12\ V$ and sent four output signal pulses to a second pulse generator (Model 500D, Berkeley Nucleonics Corporation, San Rafael, CA) set to trigger on the rising edge. The pulses were delayed 0, 2.375, 3.958, and 6.330 s relative to the triggering pulse (phases of 0°, 90°, 150°, and 240°, given the 9.5 s period of the diverting plate motion). (3) The second pulse generator adjusted the output voltage to 5 V. The four output channels of the second pulse generator were connected to the I/O module and the cameras. Upon receiving a trigger signal from the first pulse generator, the first output channel of the second pulse generator triggered the I/O module with no delay, the second output channel triggered the LIF camera with a 16 ms delay, the third output channel triggered the first image of the PIV image pair with no delay, and the fourth output channel triggered the second image of the PIV image pair with a delay of 55 ms.

Upon receiving the triggering signal, the I/O module began a set of laser sweeps as governed by the LabView code. First the PIV laser was swept to acquire the first image of the PIV image pair, second the LIF laser was swept to acquire the LIF image, and finally the PIV laser was swept to acquire the second image of the PIV image pair. The LabView software programmed the laser sweeps based on the user-entered exposure times of the PIV (15 ms) and LIF (38 ms) images as well as the PIV frame rate. The timing of the LIF laser sweep was halfway between the two PIV laser sweeps. The PIV laser sweep rates were uniform, and the LIF laser sweep rates were non-uniform, such that the light intensity increased with distance away from the source. The non-uniform LIF laser sweep was governed by the power law control voltage signal described in Webster et al. [2003], $E = E_0 + (E_1 - E_0)\left(\frac{t}{T}\right)^{\frac{1}{n+1}}$. E_0 and E_1 are the start and end voltages, respectively, and T is the period of the sweep. The value of $n = 1$ produced the most uniform raw LIF images for both the meandering

plume and straight plume cases, thereby taking advantage of the camera's dynamic range over the entire pixel array.

3.4.4 Particle Tracking Velocimetry and Particle Image Velocimetry

Both Particle Tracking Velocimetry (PTV) and Particle Image Velocimetry (PIV) techniques are used to process the images from the PIV camera. The two techniques yield instantaneous velocity measurements in the fluid, albeit through different processes. Both techniques require successive images of the moving fluid seeded with particles. As the name suggests, PTV techniques attempt to match individual particles in successive frames [Maas et al., 1993, Malik et al., 1993]. The velocity is then simply the displacement of the particle divided by the time between the two frames. This results in high spatial resolution but unevenly-located velocity vector fields, as the velocity is only calculated where particle matches are found rather than on a uniform grid. In contrast, PIV splits the image into a series of interrogation windows (e.g. 16×16 pixels) and determines the displacement of particles in each interrogation window using cross-correlation techniques with the next image [Raffel et al., 2007]. This technique is substantially more robust than PTV, as it essentially averages the displacement of all the particles in the interrogation window, rather than attempting to identify individual particle matches (as in PTV). However, PIV is less spatially resolved than PTV, as the velocity is calculated at each interrogation window, rather than at the location of an individual particle.

To acquire the PIV (and PTV) images, the water was seeded with a solution (0.9 g/L) of 20 μm diameter polyamide particles (Orgasol 2002 D NAT 1, Arkema Inc., King of Prussia, PA) mixed with methanol and sump water. The seeding solution was pumped through a copper diffuser with eight 1.6 mm diameter holes spanning the width of the flume at 38 L/hr. The diffuser was located 30 mm above the flume bed, 9 m upstream of the test section. This resulted in a well-mixed particle distribution

with an average particle concentration in the flume of 0.9 mg/L.

Images from the PIV camera were captured using Camware (CamWare International Sdn Bhd, Selangor, Malaysia) on the fast image sensor readout speed (286 MHz) to avoid frame dropping, resulting in 12-bit images rather than the full camera resolution (16-bit). The images were imported into DaVis (LaVision GmbH, Göttingen, Germany) to acquire the velocity vectors using both the 2D-PIV and 2D-PTV algorithm packages.

3.4.5 Laser Induced Fluorescence

Laser Induced Fluorescence (LIF) was used to acquire the instantaneous concentration field in the plume. To perform LIF, fluorescent dye is released into the flow (through the 4.2 mm diameter nozzle described in Section 3.4.1 in our case). A light sheet from a laser passes through the flow and causes the dye in the flow to fluoresce [Seitzman and Hanson, 1993]. The amount of light released by the fluorescent dye is proportional to the concentration. Images of the flow and fluorescing dye are captured by a digital camera, and the amount of light at each pixel is converted to concentration by an LIF calibration function. As the concentration is measured at each pixel, the LIF concentration fields are highly spatially resolved (0.4 mm per pixel in these experiments).

The fluorescent dye used in our experiments was Rhodamine 6G, which has peak light absorption at 530 nm (near the wavelength of the Argon-ion laser) and peak emission near 560 nm [Arcoumanis et al., 1990]. First Rhodamine 6G was mixed with deionized water to yield high concentration stock solution of dye (200 mg/L). This stock solution was used for LIF calibration and to mix the dye solution that was released into the flume. The plume source was chosen to be 1 mg/L (0.5 mg/L for the straight plume) to make use of the full dynamic range of the LIF camera.

The images from the LIF camera were captured using Camware at a slower image

sensor readout speed (95 MHz) resulting in 16-bit images. The images were imported into DaVis to calculate the concentration fields using the LIF analysis package. The fluorescent light intensity was corrected to account for the non-uniform sweep rate of the LIF laser using the DaVis laser sheet correction function.

3.4.5.1 Laser Induced Fluorescence Calibration

The calibration required for accurate concentration estimates via LIF merits additional scrutiny. As discussed in Section 3.4.2, the LIF laser sweep was non-uniform. The geometry of the sweep additionally induces inhomogeneities in the laser intensity distribution. The DaVis laser sheet correction function was used to account for this, but it requires images of the laser sheet passing through a uniform low concentration of dye. To achieve this the test section was isolated from the rest of the flume by dams located upstream and downstream of the test section. The test section was filled to a depth of 200 mm with a known volume of sump water, and Rhodamine 6G fluorescent dye was added to reach a uniform concentration of 5 $\mu g/L$ in the test section. 200 images of this configuration using the non-uniformly swept LIF laser were used to generate the DaVis laser sheet correction function.

Further, the relationship between the dye concentration and the emitted light intensity is necessary to calibrate LIF technique and ensure accurate concentration results. Therefore, a polyacrylic tank ($1200 \times 500 \times 250$ mm) was centrally placed in the test section, and filled with sump water to a depth of 200 mm. To perform the calibration, Rhodamine 6G was added to the tank to a concentration of 1.7 $\mu g/L$. 100 images of this configuration using a uniform sweep of the LIF laser were acquired. These steps were repeated eleven additional times to yield calibration images for uniform Rhodamine 6G concentrations between 1.7 $\mu g/L$ - 157 $\mu g/L$. The relationship between the dye concentration and the emitted light intensity was non-linear (particularly at low dye concentrations), thus a 2^{nd} order polynomial calibration

function was used ($R^2 = 0.999$).

3.4.6 Camera Calibration

The PIV, PTV, and LIF image processing software packages all require camera calibration to convert pixel location to physical position. To calibrate the cameras, images of a 2-D calibration panel (a grid of 20 mm dots spaced 80 mm apart) placed in the flume bed were taken by each camera. The flume was filled with water and the acrylic sheet described in Section 3.4.1 was in place on the free surface during camera calibration. The calibration images are processed in DaVis to yield a 3^{rd} order polynomial calibration function.

3.4.7 Calculation of the Turbulent Flux Terms

The velocity vector estimates from the PTV analysis were used to determine the turbulent flux terms (due to their higher spatial resolution over PIV velocity measurements - see Section 3.4.4). The PTV processing algorithm in DaVis yielded approximately $12,000$ velocity vectors in each of 6706 frames. Prior to calculation of the turbulent flux terms, the velocity vectors were filtered using an adaptive filtering algorithm to remove spurious vectors. To perform the adaptive filtering, the camera viewing window was partitioned into bins, then the mean and standard deviation of the x and y components of velocity were calculated for each bin. Spurious vectors were identified as those in which either component of the velocity lay outside the range of the mean velocity plus or minus a coefficient multiplied by the standard deviation of the velocity for the bin. These vectors were identified and removed, then the procedure was repeated until no vectors are identified for removal. For the first pass of the adaptive filtering algorithm the standard deviation coefficient is 2 and for every subsequent pass it is 3. Approximately 2.5% of the PTV velocity vectors were removed via the adaptive filtering.

The turbulent flux terms ($\overline{u'c'}$ and $\overline{v'c'}$ in Equation 3.1) were calculated by combining the LIF estimates of concentration with the PTV estimates of velocity. The value of the instantaneous concentration with the phase-averaged concentration subtracted off was computed at the position of each PTV velocity vector to estimate c'. The phase-averaged velocity was estimated at the position of each PTV velocity vector by interpolating the phase-averaged velocity from PIV, then that value was subtracted from the instantaneous PTV velocity vector to estimate u' and v'. The camera viewing window was partitioned into bins, then $\overline{u'c'}$ and $\overline{v'c'}$ were calculated at the centroid of each bin as the average of $u'c'$ and $v'c'$ for every PTV vector located in each bin in time. Note that the phase-averaged velocity was also acquired from the PTV velocity fields using the same partitioning method, but the resulting estimates of $\overline{u'c'}$ and $\overline{v'c'}$ using the phase-averaged velocity from PTV were indistinguishable from those using the PIV phase-averaged velocity field.

3.5 Results and Discussion

3.5.1 Straight Plume Structure

Let us briefly discuss the structure of our straight plume to contrast with our subsequent discussion of the meandering plume.

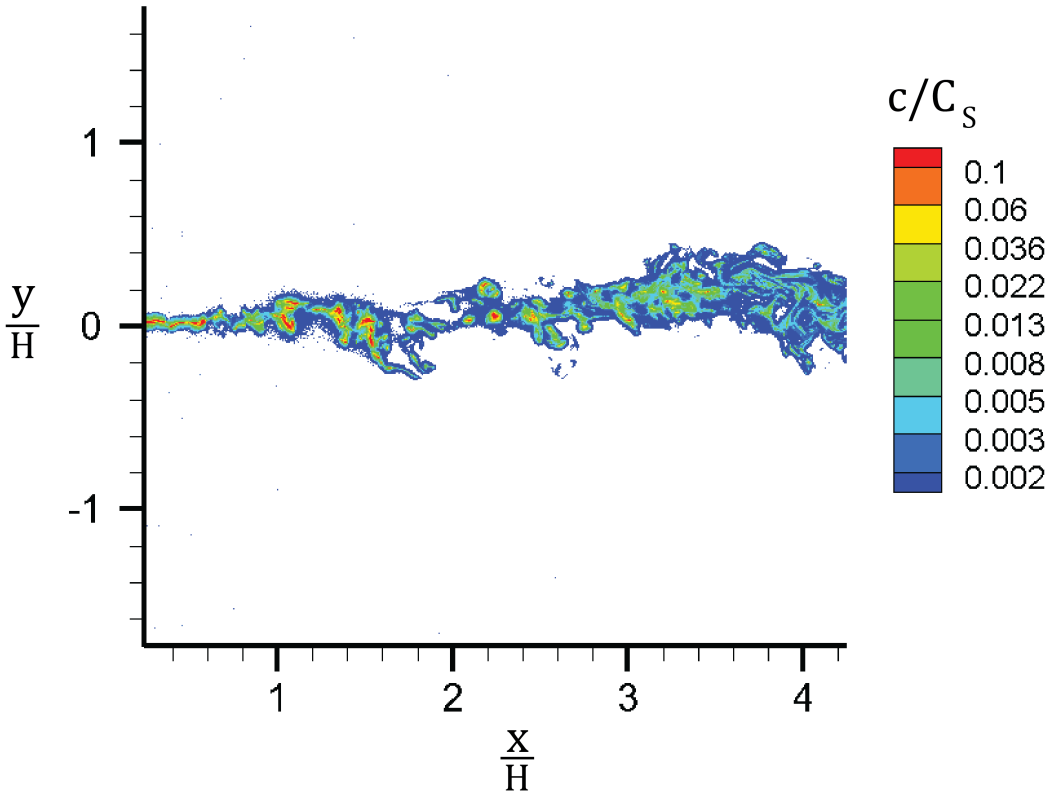

Figure 3.7: An example instantaneous concentration field of the straight plume. Note the contours are logarithmically spaced.

Figure 3.7 shows an example instantaneous concentration field for the straight plume. Note that the dye filaments appear to advect downstream while spreading transversely and they have a seemingly random instantaneous distribution. Also note that despite the randomness of the concentration field, the concentration generally declines with distance downstream.

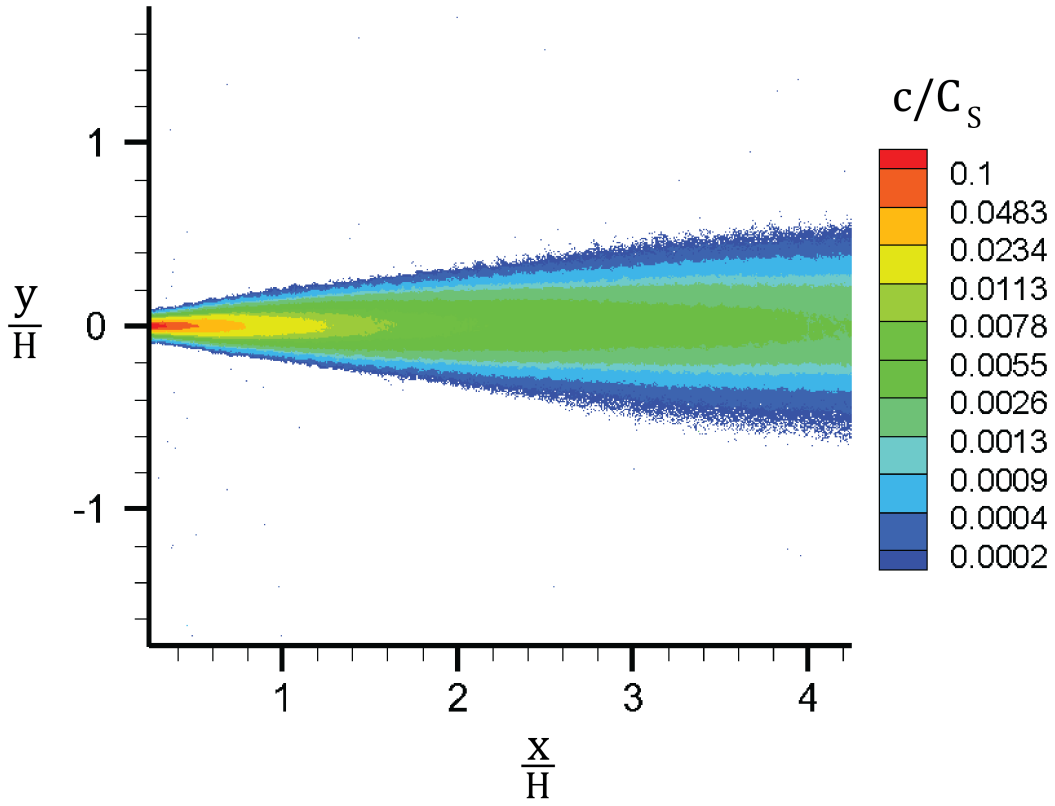

Figure 3.8: Time-averaged concentration field for the straight plume. Note that the contours are logarithmically spaced.

Figure 3.8 shows the time-averaged concentration field for the straight plume. The time-averaged concentration field visually appears symmetric about the plume centerline (this is confirmed in the profiles of time-averaged concentration for the straight plume in Figure 3.10) and the time-averaged concentration declines with distance downstream as expected.

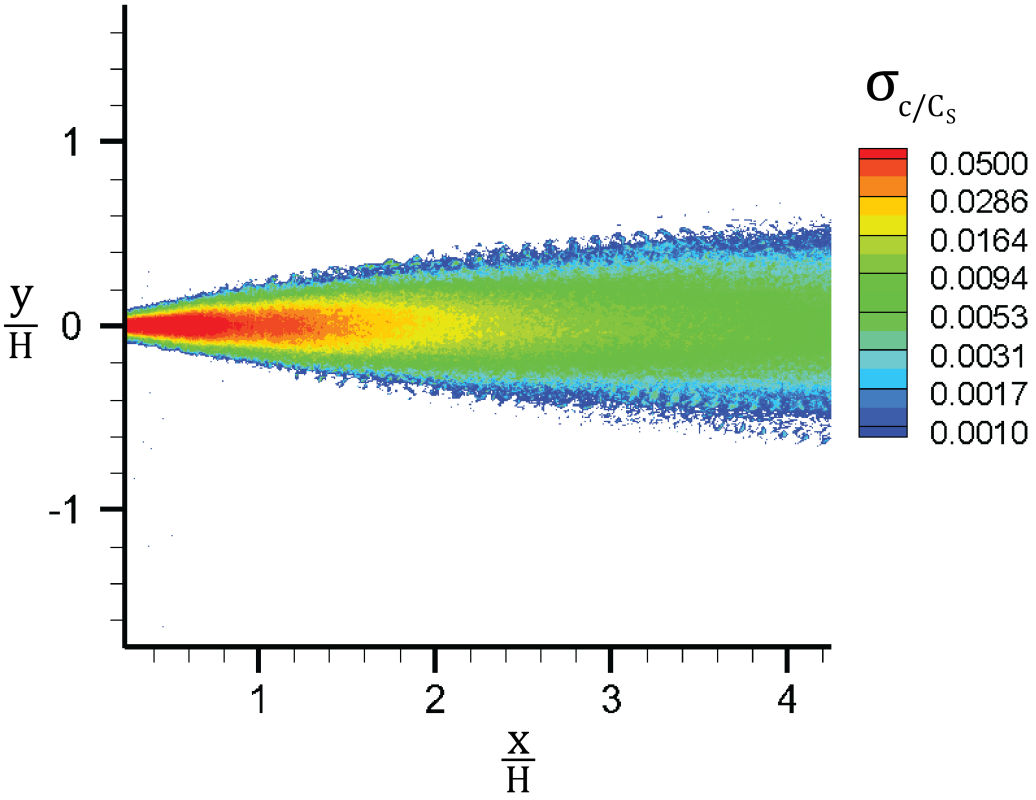

Figure 3.9: Standard deviation of the concentration fluctuations (σ_{c/C_s}) for the straight plume. Note that the contours are logarithmically spaced.

Figure 3.9 shows the standard deviation of the concentration field for the straight plume. The standard deviation of the concentration likewise appears symmetric about the plume centerline and the strength of the concentration fluctuations declines with distance downstream. Note that the standard deviation of the concentration field is noticeably more noisy than the time-averaged concentration field (see Figure 3.8) .

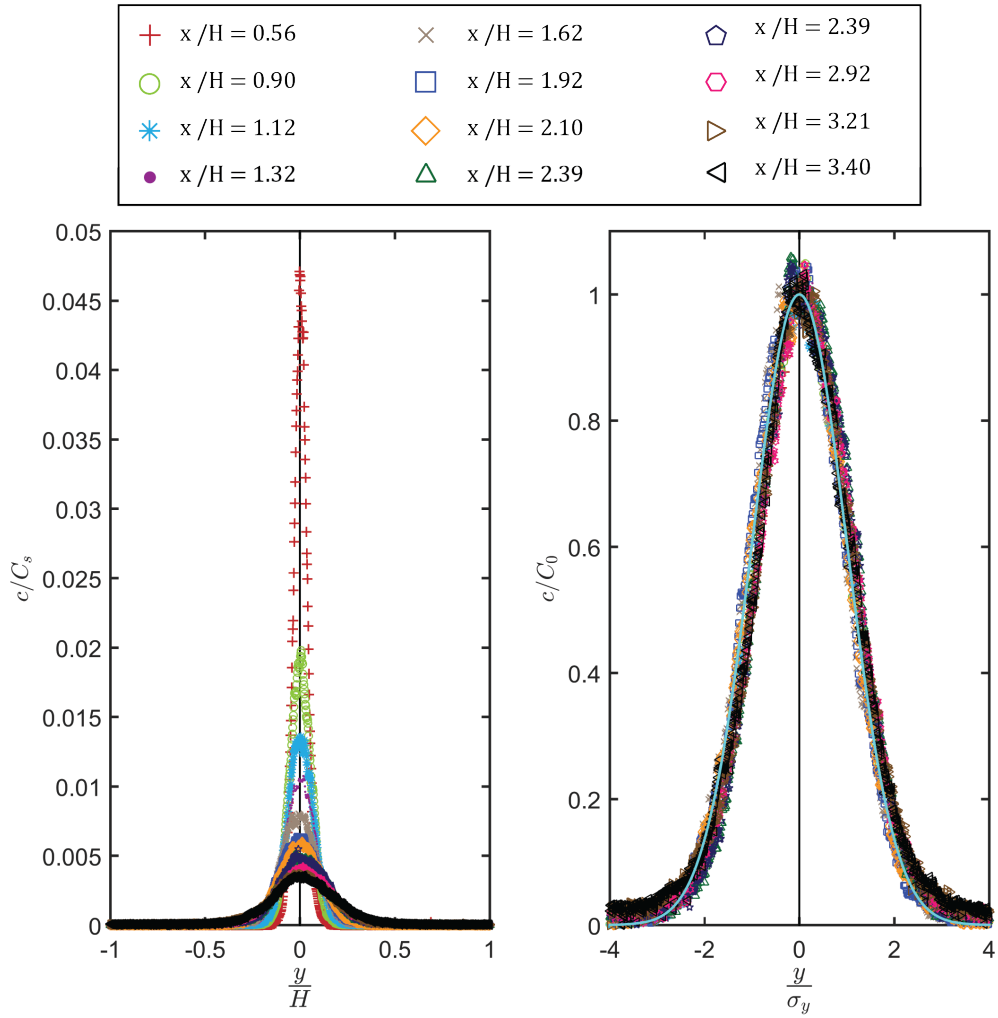

Figure 3.10: Transverse profiles of time-averaged concentration for the straight plume. The left panel shows the time-averaged concentration profiles normalized by the source concentration (c/C_s). The right panel shows the time averaged concentration profiles normalized by the centerline concentration (c/C_0) versus the transverse coordinate normalized the plume width (σ_y). The cyan line shows a standard Gaussian profile shape.

Figure 3.10 shows the transverse profiles of time-averaged concentration for the straight plume. The profiles are Gaussian in shape at all points downstream, as expected [Crimaldi et al., 2002, Crimaldi and Koseff, 2006, Rahman and Webster,

2005].

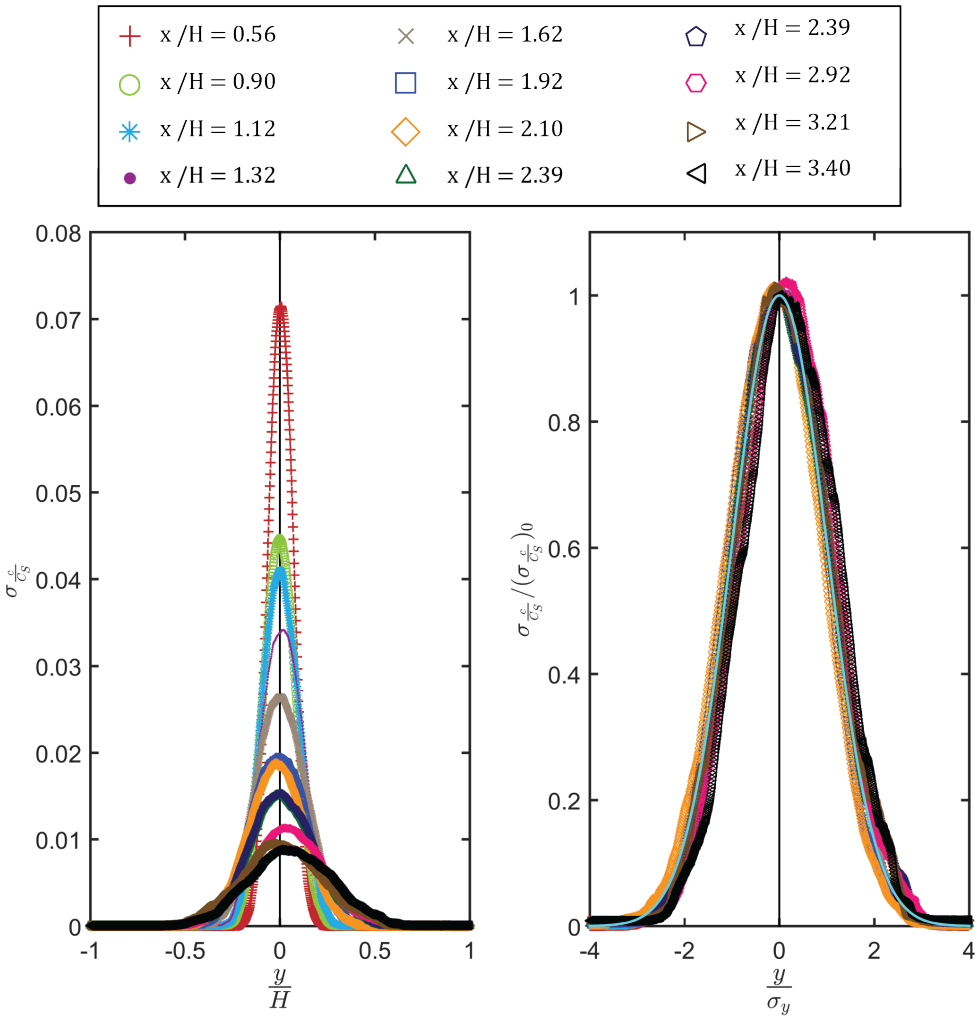

Figure 3.11: Transverse profiles of the standard deviation of the concentration fluctuations for the straight plume. The left panel shows the standard deviation profiles without normalization. The right panel shows the standard deviation profiles normalized by the centerline standard deviation ($\sigma_{\frac{c}{C_S}}/(\sigma_{\frac{c}{C_S}})_0$) versus the transverse coordinate normalized the plume width (σ_y). The cyan line shows a standard Gaussian profile shape.

Figure 3.10 shows the transverse profiles of the standard deviation of the concentration for the straight plume. The profiles match a Gaussian shape well, in agreement

with the smooth bed case in the same flume in Rahman and Webster [2005].

3.5.2 Instantaneous Concentration and Velocity Fields for the Meandering Plume

The instantaneous images of concentration and the instantaneous velocity fields aid substantially in qualitative understanding of the plume behavior. To this end, Figures 3.12 - 3.15 show four distinct flow visualization images for the meandering plume for phase $\phi = 0°$.

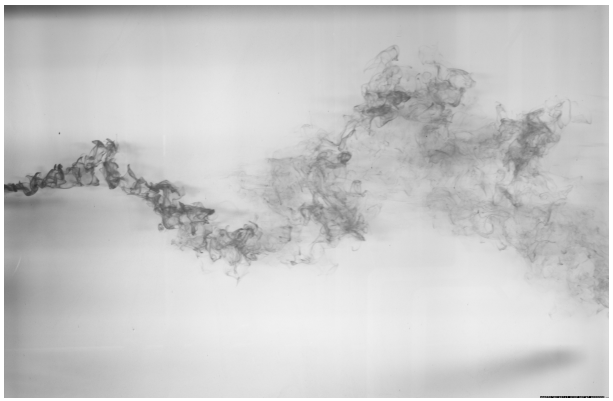

Figure 3.12: First example flow visualization image of the meandering plume for phase $\phi = 0°$.

Figure 3.13: Second example flow visualization image of the meandering plume for phase $\phi = 0°$.

Figure 3.14: Third example flow visualization image of the meandering plume for phase $\phi = 0°$.

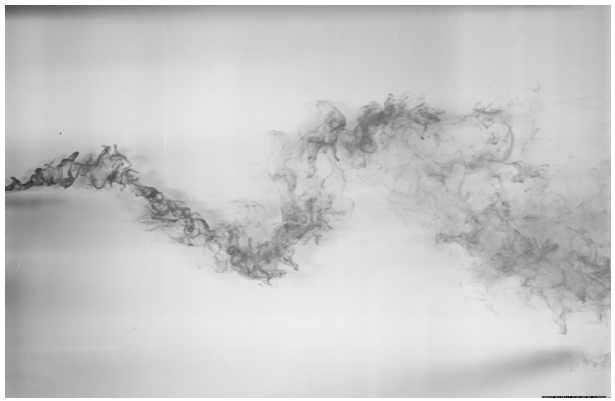

Figure 3.15: Fourth example flow visualization image of the meandering plume for phase $\phi = 0°$.

Figures 3.12 - 3.15 highlight the filamentous nature of the instantaneous concentration in turbulent plumes. One can easily observe the filaments that have been stretched and distorted by turbulent eddies, resulting in the large concentration gradients that make turbulent mixing so effective (see Section 3.3.1). This rapid mixing is observed in the instantaneous images, as the dye is visibly more dilute to the downstream (right) side. Additionally, the large scale meander of the plume centerline is readily visible. Finally, the random nature of the plume is crystallized in the visible differences in tracer distribution between Figures 3.12 - 3.15.

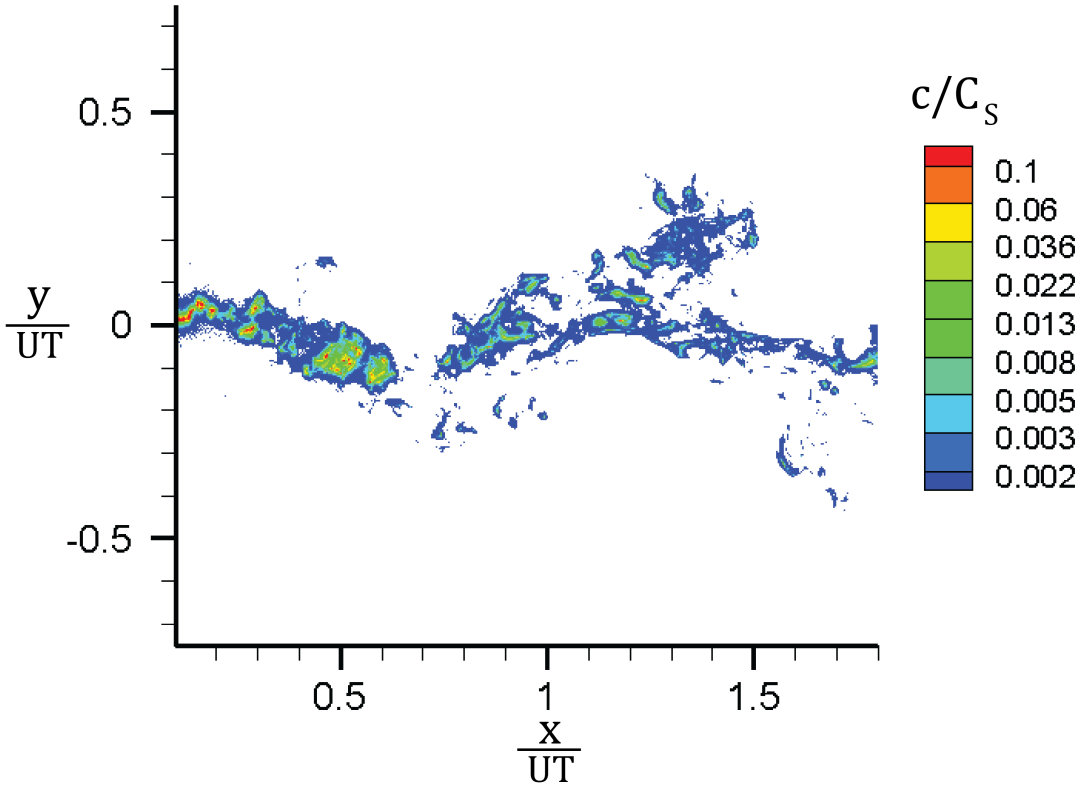

Figure 3.16: An example instantaneous concentration field of the meandering plume for phase $\phi = 0°$. Note the contours are logarithmically spaced.

Figure 3.16 highlights the random nature of the turbulent concentration fluctuations in the plume. The overall serpentine pattern of the plume is obvious in the image, as is the random instantaneous distribution of the dye filaments. For example, in the instantaneous concentration image shown in Figure 3.16 there appears to be near zero dye concentration at $x/UT \approxeq 1$. Yet further downstream at $x/UT \approxeq 1.43$, we observe dye patches exceeding 6% of the source concentration. This despite the fact that (as we will discuss in Section 3.5.3), the phase-averaged concentration declines with distance downstream.

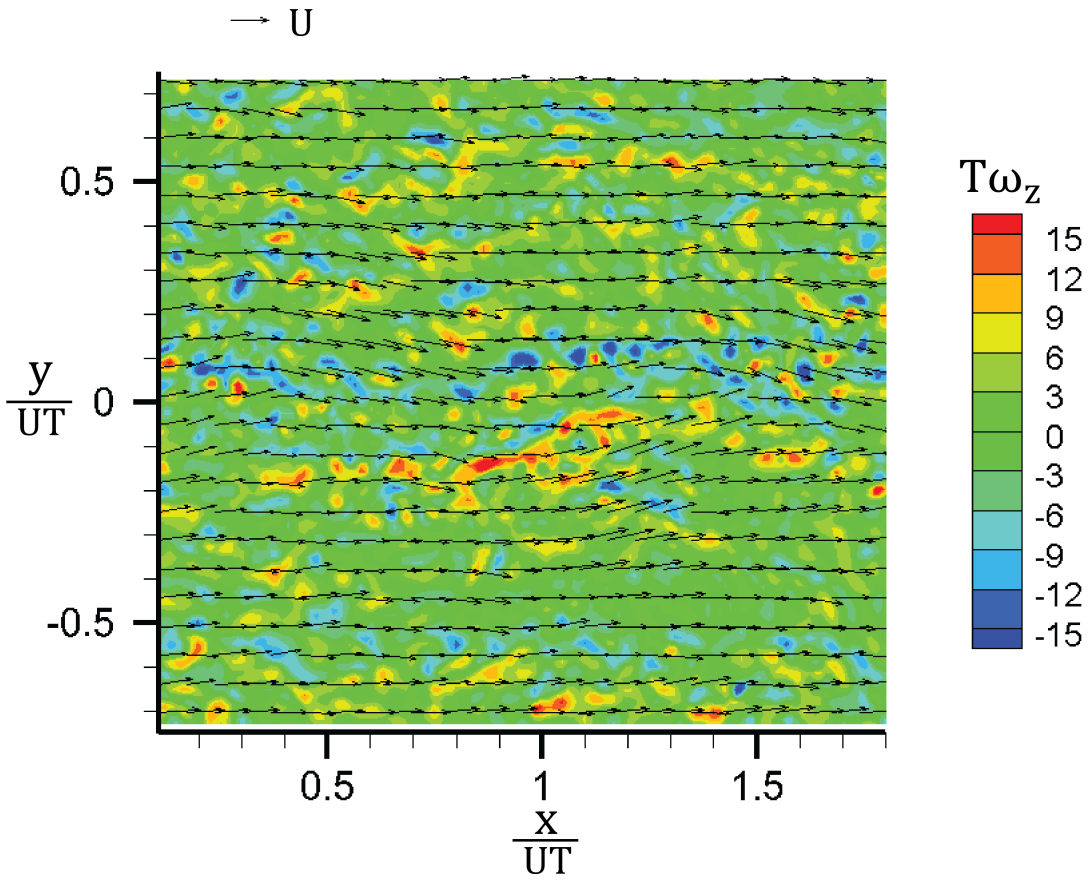

Figure 3.17: Example instantaneous velocity (shown with vectors) and vorticity (shown with color contours) fields for the meandering plume for phase $\phi = 0°$. Only every 5^{th} velocity vector is plotted.

The random nature of the turbulent velocity fluctuations in the meandering plume is illustrated in Figure 3.17. The figure readily reveals the small scale eddies (small patches of large positive and negative ω_z) within the turbulent plume. Also note that the eddies observed in this instantaneous image are not as ordered, nor are they as large, as the plume width-scale alternating sign vortices being shed off the diverting plate, observed phase-averaged flow patterns described in subsequent subsections.

3.5.3 Phase-averaged Concentration for the Meandering Plume

The characteristics of the phase-averaged concentration are critical to plume research, such as the centerline phase-averaged concentration decay and the phase-averaged concentration profiles across the plume. For straight plumes the profiles are simply concentration cross-sections perpendicular to the downstream direction. If the plume meanders however, the orientation of the transverse section is more appropriately perpendicular to the instantaneous centerline, which may be at an angle to the downstream direction as shown in Figure 3.18. As shown in subsequent sections, this transect orientation is aligned perpendicularly to the iso-contours in the phase-averaged concentration field, i.e., a transect along which the greatest turbulent flux would be expected.

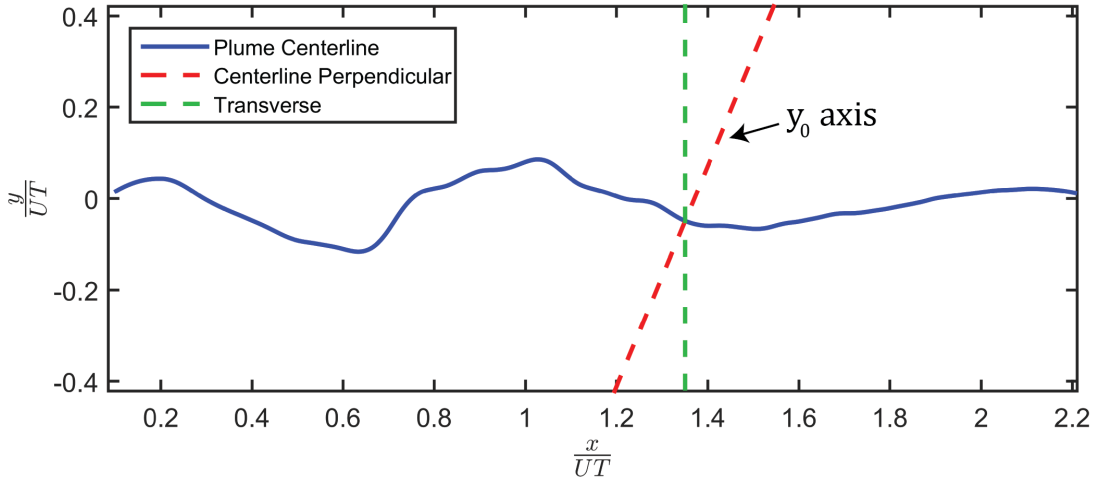

Figure 3.18: Sketch of the plume centerline for the meandering plume for phase $\phi = 0°$, noting a transverse transect and the orientation of a transect that is perpendicular to the local plume centerline.

Therefore, to describe the aforementioned phase-averaged concentration characteristics, defining the centerline is key. The centerline of a plume is typically defined as the location of maximum phase-averaged concentration at each station downstream. The centerline location of the straight plume and all four phases of the meandering plume defined using this criterion are shown in Figure 3.19. Note that the centerline location curves have been smoothed using a smoothing function that employs a local regression with a weighted linear least-squares fit to a 2^{nd} order polynomial (Matlab smooth function with the 'rloess' method).

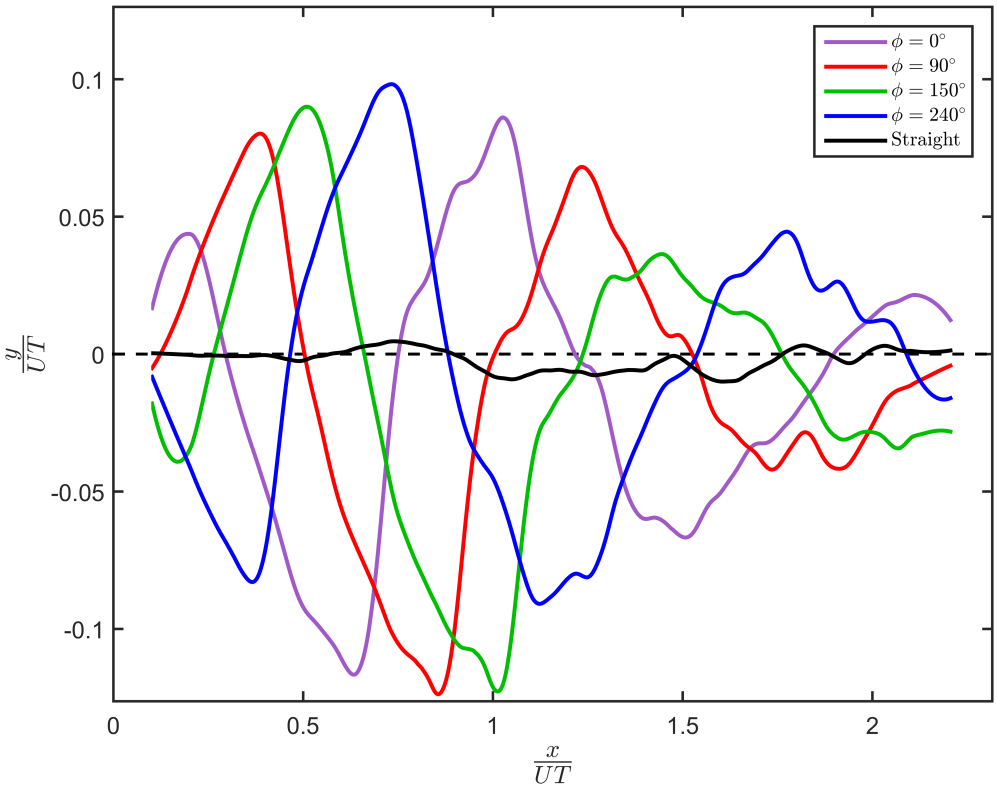

Figure 3.19: Plume centerline location for the meandering plume for phases $\phi = 0°$, $\phi = 90°$, $\phi = 150°$, and $\phi = 240°$ and the straight plume.

Figure 3.19 shows that the amplitude of the centerline meander is initially small at the beginning of the test section, then rapidly increases to a maximum between $\frac{x}{UT} = 0.53$ and $\frac{x}{UT} = 1.5$ downstream of the beginning of the test section. The meander amplitude then slowly decreases with increasing distance downstream. The wavelength of the centerline meander is approximately $\frac{x}{UT} = 0.84$ for the meandering plume for all four phases. Note that the straight plume also exhibits small-scale random meander.

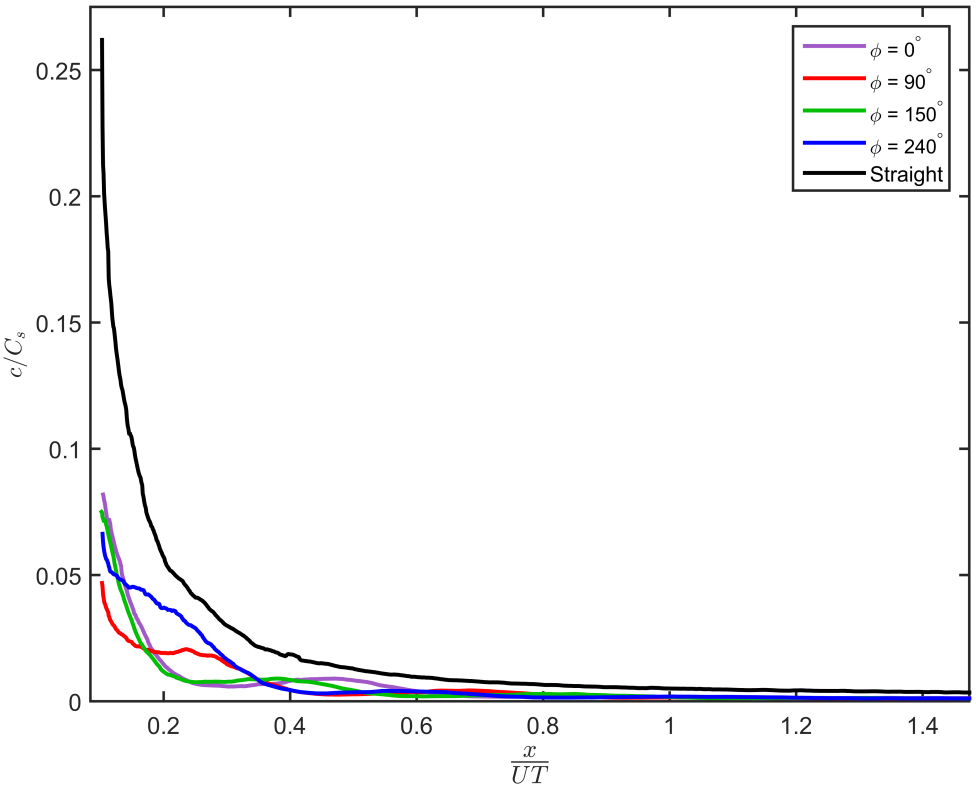

Figure 3.20: Centerline concentration for the $\phi = 0°$, $\phi = 90°$, $\phi = 150°$, $\phi = 240°$, and straight plumes.

Figure 3.20 shows the phase-averaged concentration along the defined centerline. As expected, the concentration is initially high at the beginning of the test section, and rapidly decreases with distance downstream for all plumes. The two features of interest in Figure 3.20 are: (1) the centerline phase-averaged concentration decreases substantially faster for the meandering plumes ($\phi = 0°$, $\phi = 90°$, $\phi = 150°$, $\phi = 240°$) compared to the straight plume and (2) local minimums and maximums of the centerline phase-averaged concentration are observed for each of the four phases of the meandering plume. These local concentration peaks (and valleys) are also observed in the color contour plots of phase averaged concentration (for the meandering plume for phase $\phi = 0°$) in Figure 3.21.

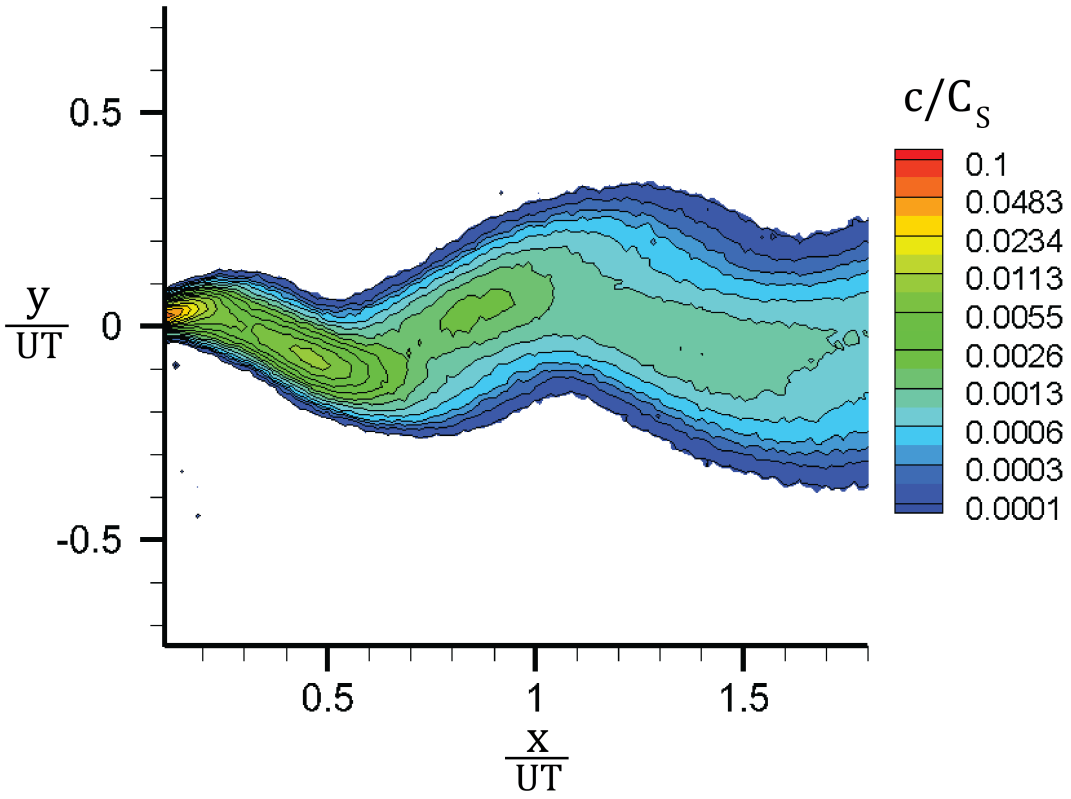

Figure 3.21: Phase-averaged concentration field of the meandering plume for phase $\phi = 0°$. Note that the contours are logarithmically spaced.

The local minimums and maximums of the centerline phase-averaged concentration are the result of the large-scale alternating vortices being periodically shed off the diverting plate; this is discussed in greater detail in Section 3.5.7.1. Consequently, we restrict ourselves to analyzing profiles of phase-averaged concentration at the local maximums.

3.5.3.1 Profiles of Mean Concentration

Profiles of phase-averaged concentration normalized over the source concentration for the meandering plume for phase $\phi = 0°$ are shown in Figure 3.22. The three profiles

are at the x-positions (distance downstream from the beginning of the test section) identified as the aforementioned local peaks in the phase-averaged concentration along the centerline. Note that the x-axis of Figure 3.22 is the distance from the plume centerline along a transect perpendicular to the local plume centerline (y_0).

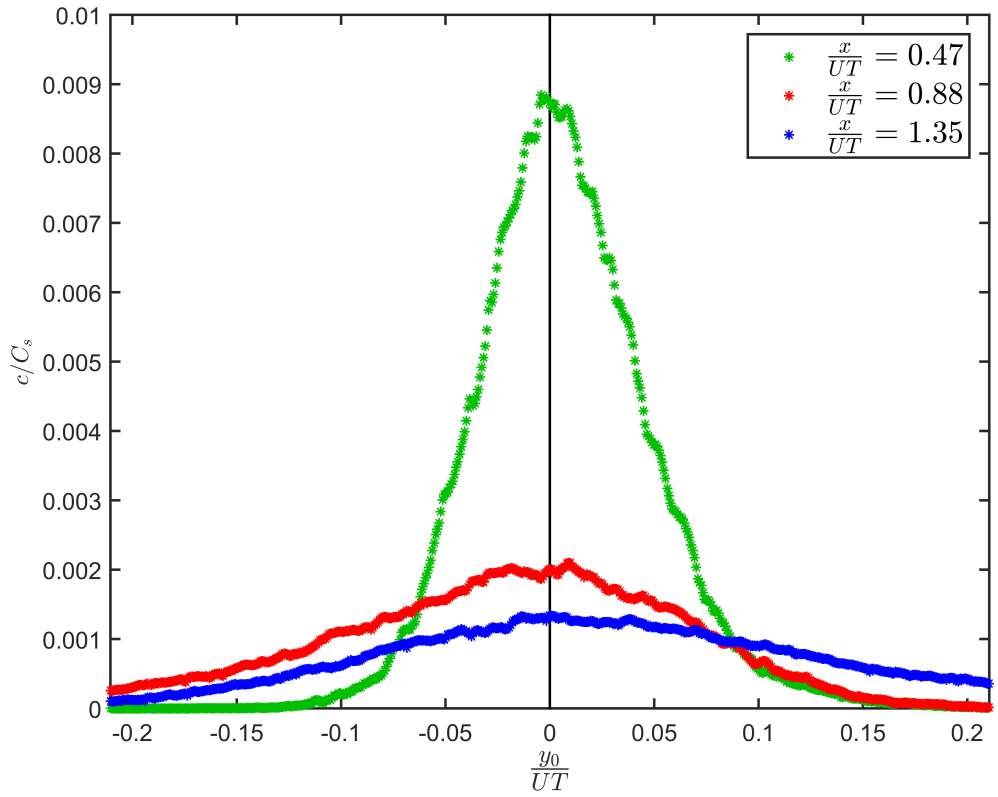

Figure 3.22: Profiles of phase-averaged concentration along transects that are perpendicular to the local plume centerline for the meandering plume for phase $\phi = 0°$.

In contrast to the straight plumes described in Section 3.3.2 and the meandering plume theory of Gifford [1959], Figure 3.22 shows that the phase-averaged concentration profile shapes are not Gaussian. Even at comparably short distances downstream of the release ($\frac{x}{UT} = 0.47$) the profile is noticeably skewed, and the skewness increases with distance downstream. Further, the plume is consistently skewed with the weaker concentration gradient on the concave side of the centerline; this is why the skewness

in the profiles shown in Figure 3.22 appears to switch sides of the plume centerline.

As discussed in Section 3.3.2, concentration profiles are typically normalized by the centerline concentration and the plume width (as measured by the standard deviation of the concentration profile), then compared to each other in an effort to determine whether they are self-similar. The profiles shown in Figure 3.22 are obviously not self-similar if the plume width is estimated using the standard deviation of the entire plume cross-section. However, it is possible to divide the profiles into two parts (one to either side of the plume centerline) and determine the plume width for each part individually. If each side of the plume centerline is normalized by its respective width (with the concentration still normalized by the centerline concentration), the profiles for phases $\phi = 0°$, $\phi = 90°$, $\phi = 150°$, $\phi = 240°$ are self-similar and Gaussian in a piecewise sense, as shown for $\phi = 0°$ in Figure 3.23. Note that the horizontal axis of Figure 3.23 is the distance from the plume centerline along a transect perpendicular to the local plume centerline (y_0).

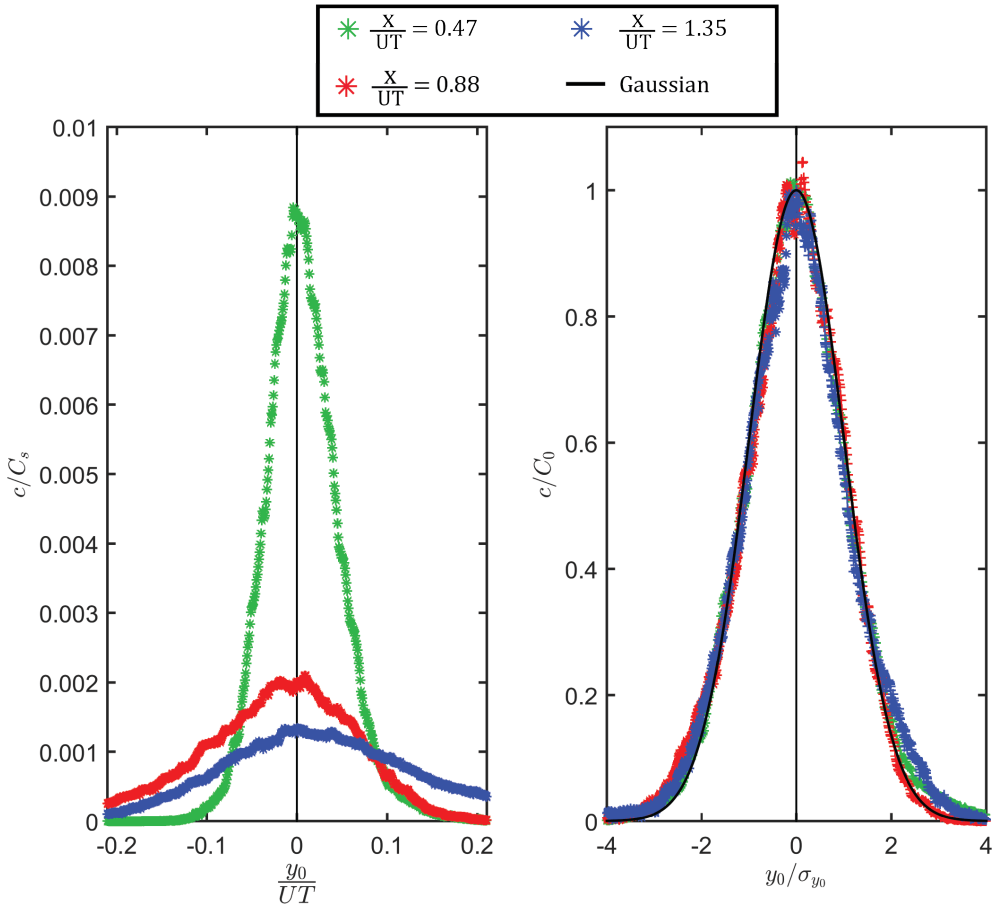

Figure 3.23: Phase-averaged concentration profiles for the meandering plume for phase $\phi = 0°$. The left panel shows the phase-averaged concentration profiles normalized by the source concentration (c/C_s). The right panel shows the phase-averaged concentration profiles normalized by the centerline concentration (c/C_0) versus the transverse coordinate normalized the side-specific plume width ($\sigma_{y_0} = \sigma_L$ if $y_0 < 0$ and $\sigma_{y_0} = \sigma_R$ if $y_0 > 0$).

3.5.3.2 Growth of the Plume Width

Recall that the width of the plume is typically defined in terms of the standard deviation of the concentration profile (i.e. plume width $= 4\sigma$). As we are determining the width of the meandering plumes for each side of the centerline individually, we define the plume width as $2(\sigma_L + \sigma_R)$, where σ_L and σ_R are the standard deviations

of the concentration profile to the left and right of the plume centerline, respectively. To determine the growth of the plume width, it is frequently plotted as a function of distance downstream (x), as shown in Figure 3.24 and on a log-log scale in Figure 3.25. The x-axis is normalized by the water depth and by the free-stream velocity multiplied by the period of the divertng plate motion (UT), and the plume width estimates are normalized by the diameter of the tracer release nozzle (b - the initial plume diameter).

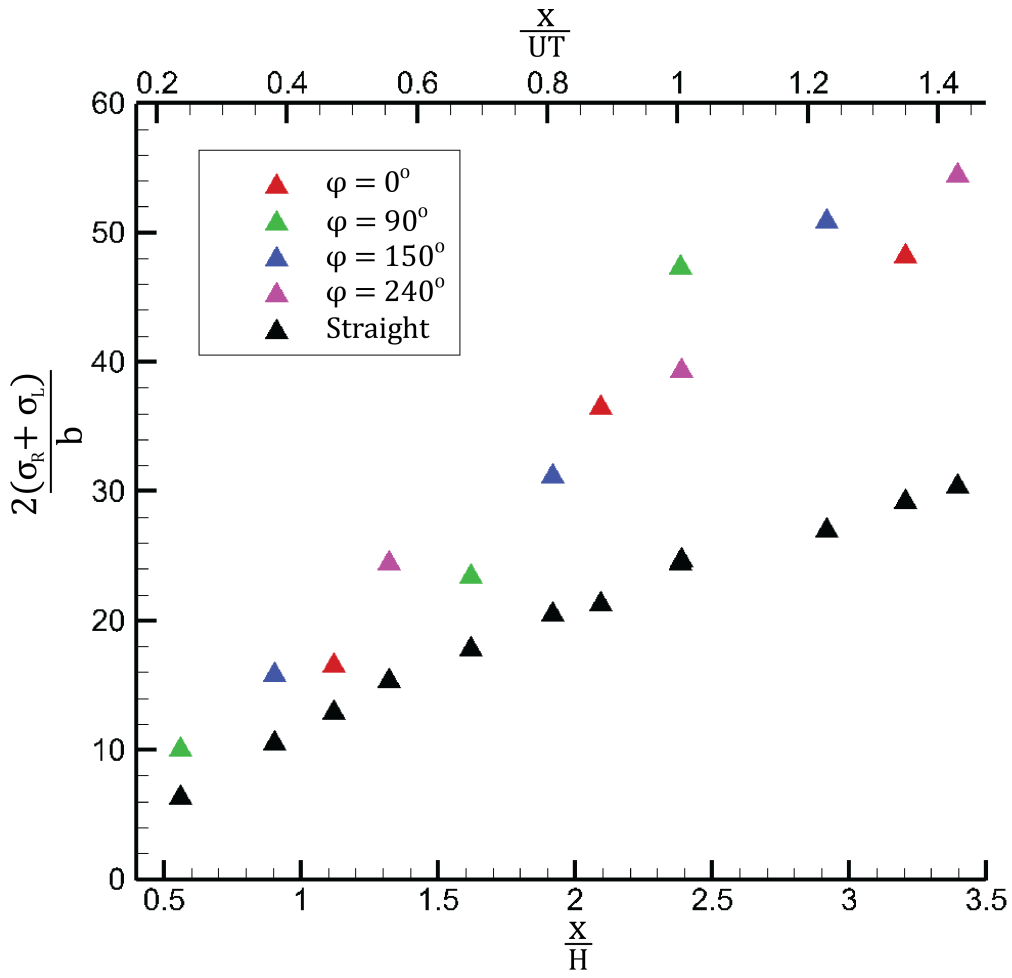

Figure 3.24: The meandering plume width ($2(\sigma_L+\sigma_R)/b$) and straight plume width ($4\sigma/b$) as a function of distance downstream.

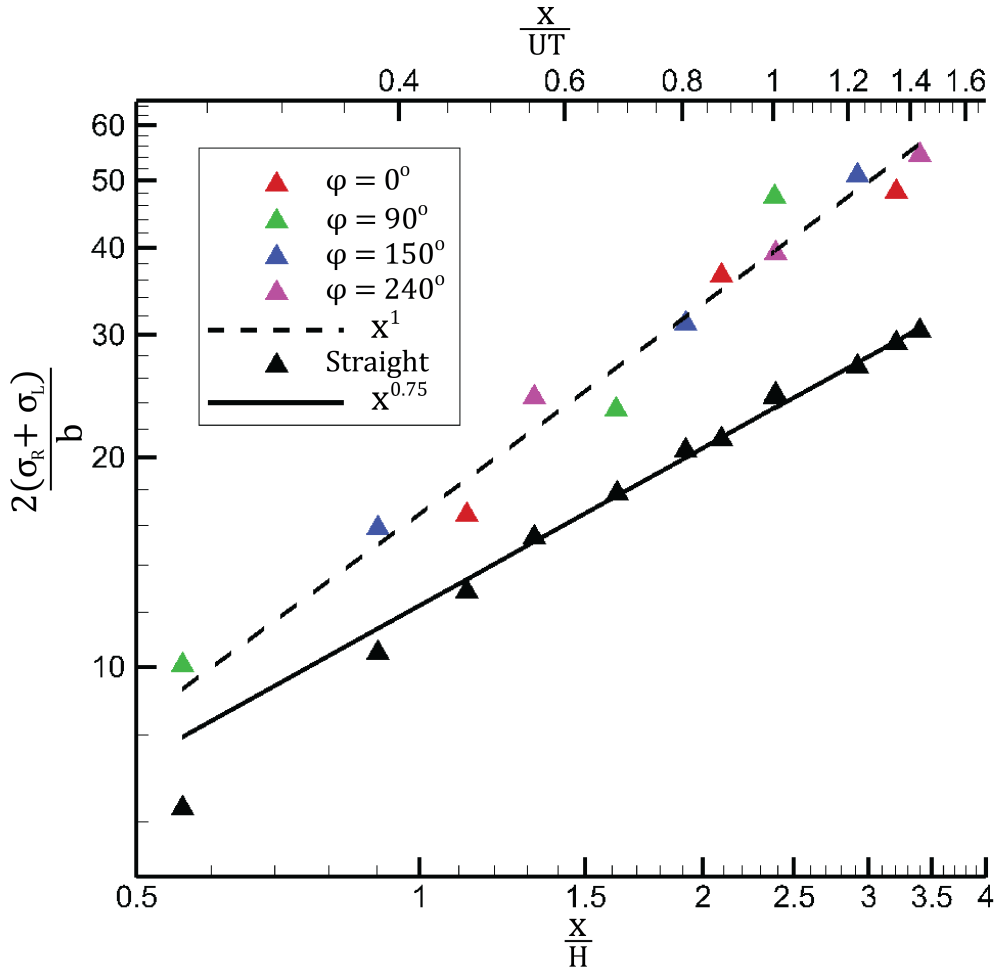

Figure 3.25: The meandering plume width $(2(\sigma_L+\sigma_R)/b)$ and straight plume width $(4\sigma/b$ as a function of distance downstream on log-log axes.

Figures 3.24 and 3.25 show that the meandering plume width increases substantially faster than the straight plume width. As first discussed in Section 3.3.2, the plume width of an unconfined straight plume grows as $x^{1/2}$. The plume width for straight plumes developing in a turbulent boundary layer grows faster, as observed in Figure 3.25. Note that the growth rate we observe in our straight plume control $(x^{0.75})$ is similar to that observed in Rahman and Webster [2005] over the same range of x/H values. However, the plume width for the meandering plume developing in a turbulent boundary layer grows even faster (x^1). This growth rate is consistent across

all four phases of the meandering plume. The combination of increased concentration decay along the plume centerline and increased growth rate of the plume width indicates that the meandering plume dilutes the tracer substantially more rapidly than the straight plume.

3.5.4 Phase-averaged Velocity for the Meandering Plume

The phase-averaged velocity field provides insight into the bulk advection of the dye. Consequently, the phase-averaged velocity vector field from the PIV analysis for the meandering plume for phase $\phi = 0^\circ$ is plotted in Figures 3.26 and 3.27.

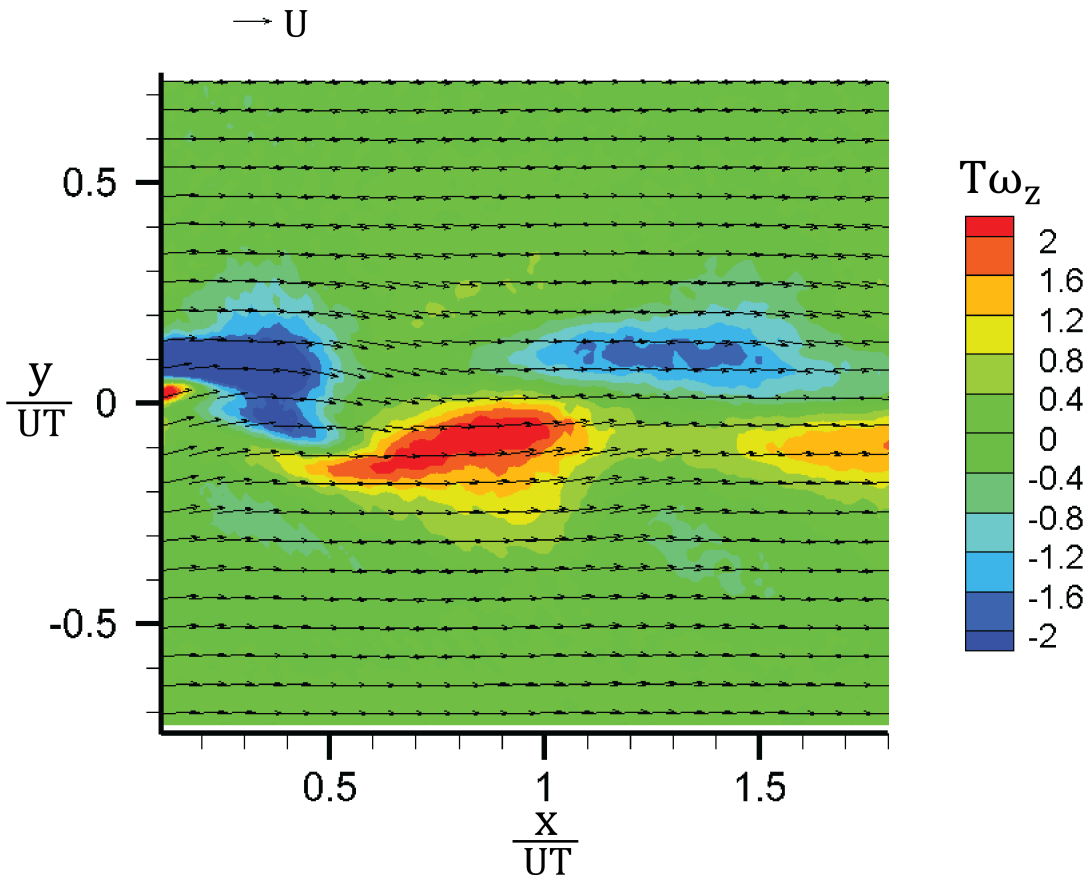

Figure 3.26: Phase-averaged velocity (shown with vectors) and vorticity (shown with color contours) fields for the meandering plume for phase $\phi = 0°$. Every 5^{th} velocity vector is plotted.

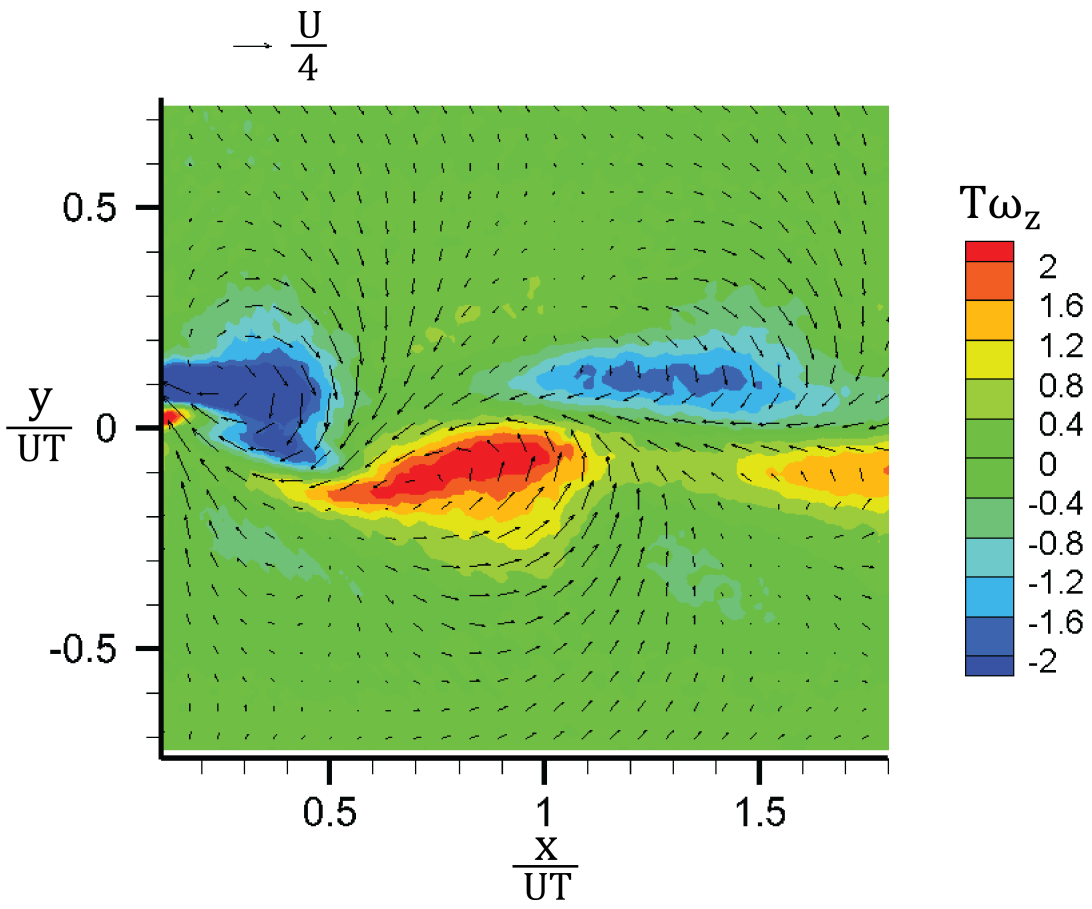

Figure 3.27: Phase-averaged velocity (shown with vectors) and vorticity (shown with color contours) fields for the meandering plume for phase $\phi = 0°$. Vectors shown are of the phase-averaged velocity with the free-stream velocity (U) subtracted. Every 5^{th} velocity vector is plotted.

As expected, Figure 3.26 shows that the velocity is predominantly directed downstream, with the effects of the diverting plate primarily observed in the slight positive and negative y-direction velocities clustered around the plume centerline. The vorticity color contours and the velocity vector field with the free-stream subtracted off in Figure 3.27 are more informative in describing the effects of the diverting plate, as the large-scale alternating sign vortices being shed off the plate are clearly visible in the vector field. Note that the average of the phase-averaged velocity for all four

phases of our meandering plume is 50 mm/s, which agrees well with the uniform velocity upstream of the diverting plate.

To more closely examine the velocity variation, three transects of the phase-averaged x- and y-direction velocities (u and v, respectively) for the meandering plume for phase $\phi = 0°$ are plotted in Figures 3.28 and 3.29, respectively. The transects are at the same downstream positions as the local peaks in concentration defined in Section 3.5.3, but are *not* defined to be perpendicular to the local plume centerline. Rather they describe variation in the y-direction (see Figure 3.18).

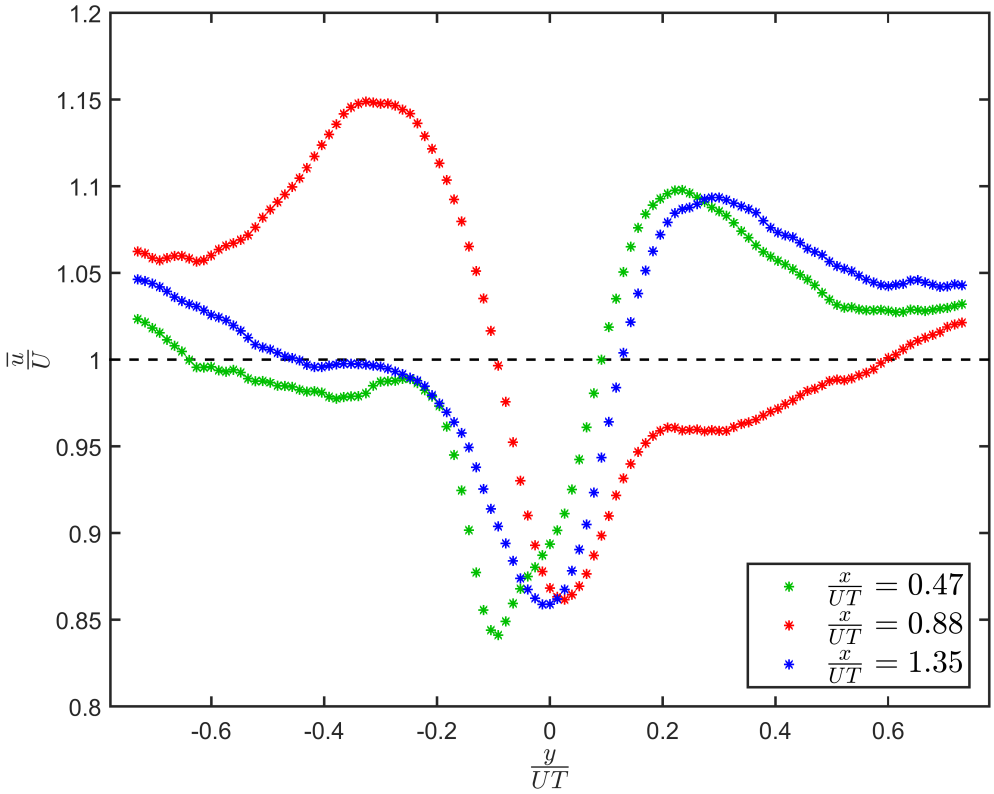

Figure 3.28: Profiles of the phase-averaged x-direction velocity ($\overline{u}$) for the meandering plume for phase $\phi = 0°$. The nominal free-stream velocity is indicated with dashed black line.

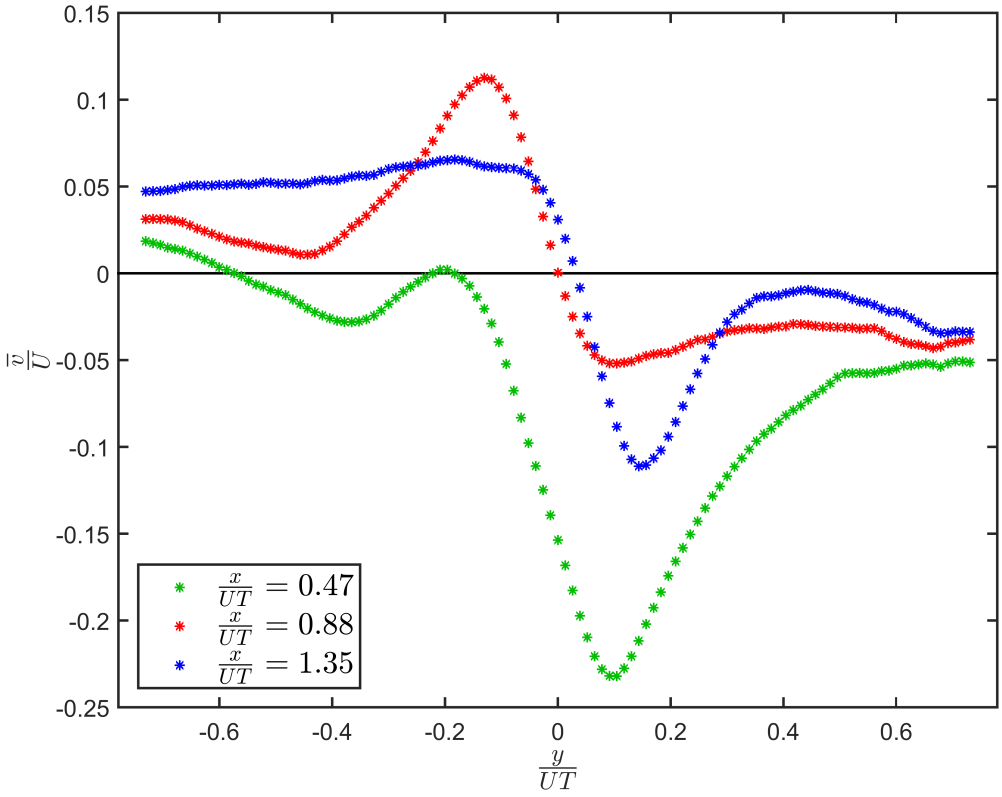

Figure 3.29: Profiles of the phase-averaged y-direction velocity ($\overline{v}$) for the meandering plume for phase $\phi = 0°$.

The downstream (x) direction velocity structure for turbulent wakes is generally characterized by the velocity deficit, the free-stream velocity minus the local velocity at a position in the wake. However, Figure 3.28 indicates that, in the wake of the diverting plate, the local velocity is at times larger and smaller than the free-stream velocity. Also note that based on Figure 3.28 the true free-stream velocity is likely slightly larger than the 50 mm/s discussed in Section 3.4.1, although this could be due to the fact that the test section does not cover the full width of the flume. That the velocity is larger than the free-stream velocity at certain positions within the plume, yet smaller at others, is due to the presence of the large-scale alternating sign vortices being shed off the diverting plate observed in Figure 3.26. This also explains why the

location of the larger-than-free-stream and smaller-than-free-stream velocity regions appears to change sides of the plume centerline, as we switch from a counter-clockwise rotating vortex at $x/UT = 0.47$ to a clockwise rotating vortex at $x/UT = 0.88$, then back to a counter-clockwise rotating vortex at $x/UT = 1.35$. Furthermore, note that (as with a traditional turbulent wake) the maximum deviation from the free-stream velocity decreases with distance downstream. However, this decrease is markedly slower than the decay of the concentration with distance downstream described in Section 3.5.3. This indicates that, as expected, the large-scale alternating sign vortices maintain their strength and coherence comparatively far downstream relative to the dye filaments.

Figure 3.29 shows the y-direction velocity profiles are near zero except for the positive and negative values induced by the alternating sign vortices. As with the x-direction velocity profiles, the maximum deviation from zero y-velocity decreases with distance downstream.

3.5.5 Standard Deviation of the Concentration Fluctuations for the Meandering Plume

As mentioned in Section 3.3.1, the turbulent flux of tracer ($\overline{u_i'c'}$) is critical to the plume evolution. Consequently, it is important to understand the structure of the concentration fluctuations, and their relationship to the velocity fluctuations. To examine the spatial structure of the concentration fluctuations, color contours of the standard deviation of the concentration fluctuations ($\sigma_{\frac{c}{C_s}}$) are plotted in Figure 3.30 for the meandering plume for phase $\phi = 0°$. Profiles of the standard deviation of the concentration fluctuations ($\sigma_{\frac{c}{C_s}}$) are plotted in Figure 3.31 for the meandering plume for phase $\phi = 0°$; the profiles have been smoothed using a moving average smoothing function in Matlab. The three profiles are at the x-positions (distance downstream from the beginning of the test section) identified as the local peaks in the phase-averaged concentration described in Section 3.5.3.1. Note that the horizontal axis of

Figure 3.31 is the distance from the plume centerline along a transect perpendicular to the local plume centerline (y_0).

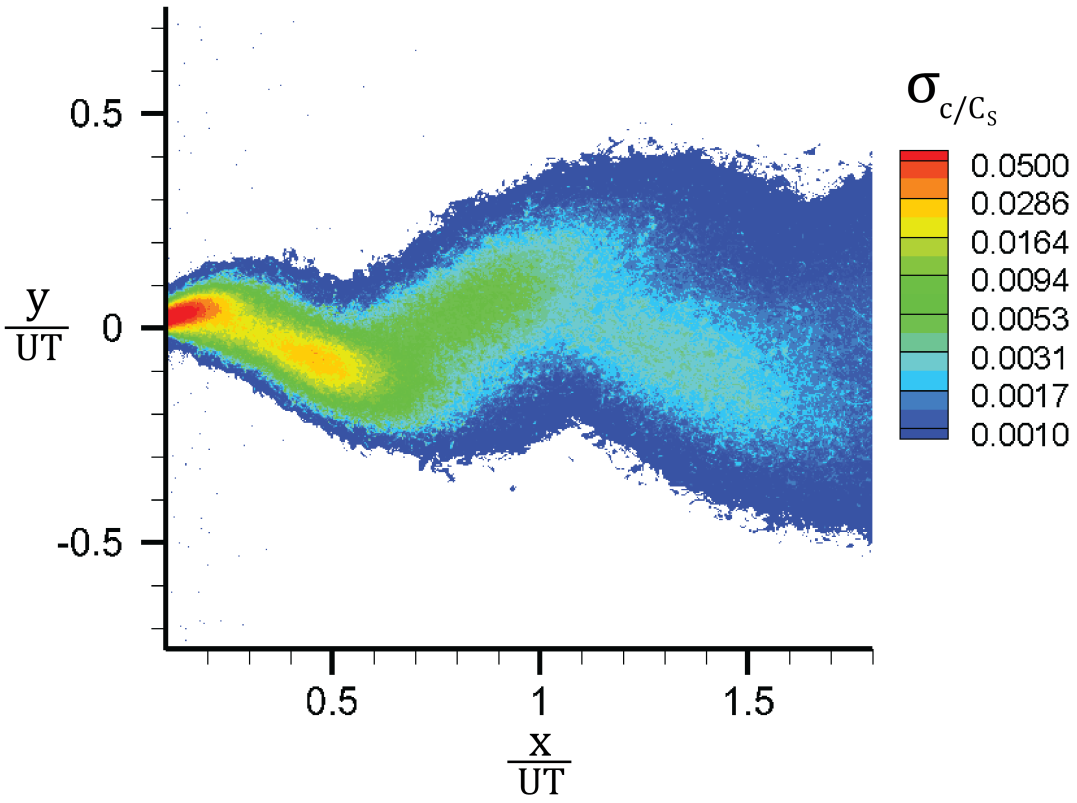

Figure 3.30: Standard deviation of the concentration fluctuations (σ_{c/C_s}) for the meandering plume for phase $\phi = 0°$. Note that the contours are logarithmically spaced.

The spatial distribution of the concentration fluctuations is substantially noisier than that of the phase-averaged concentration (Figure 3.30 compared to Figure 3.21). However, the general structure is qualitatively similar; the intensity of the concentration fluctuations visually appears co-located with high values of the phase-averaged concentration.

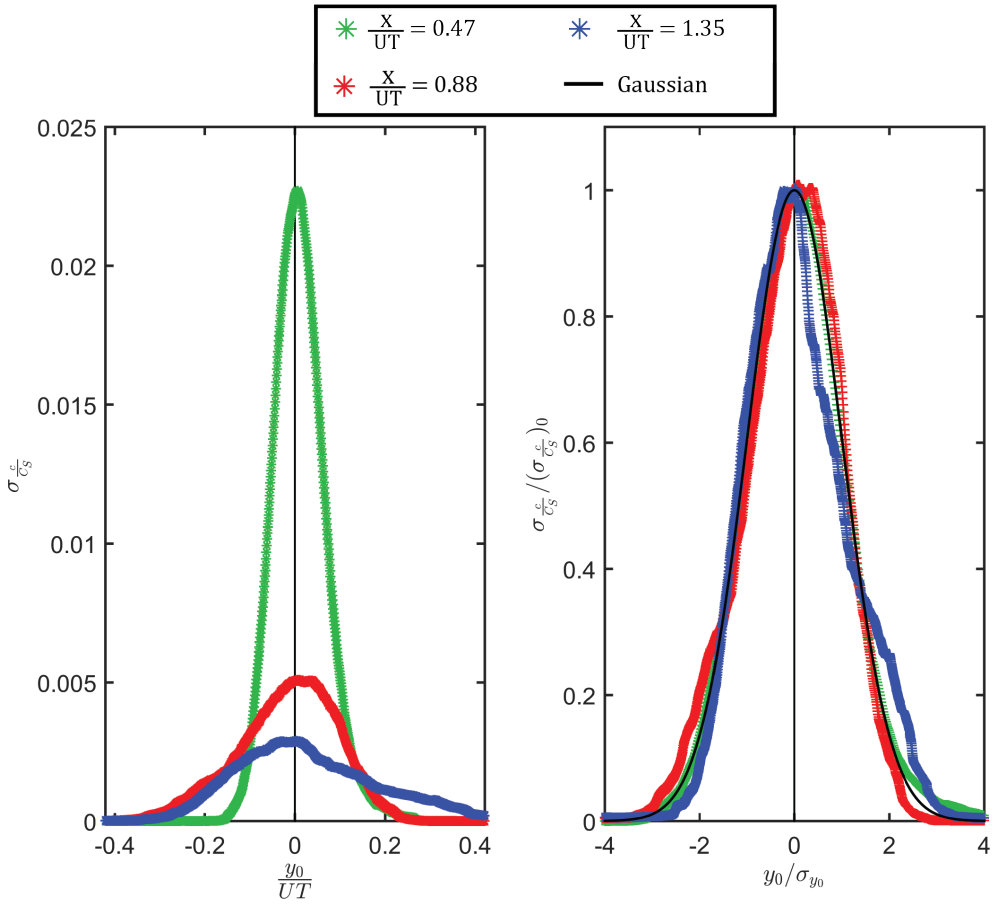

Figure 3.31: Profiles of standard deviation of the concentration fluctuations for the meandering plume for phase $\phi = 0°$. The left panel shows $\sigma_{\frac{c}{C_s}}$. The right panel shows the standard deviation normalized by the centerline value ($\sigma_{\frac{c}{C_S}}/(\sigma_{\frac{c}{C_S}})_0$) versus the transverse coordinate normalized the side-specific plume width ($\sigma_{y_0} = \sigma_L$ if $y_0 < 0$ and $\sigma_{y_0} = \sigma_R$ if $y_0 > 0$).

However, Figure 3.31 highlights a key difference between the standard deviation of the concentration fluctuations and the phase-averaged concentration profiles (Figure 3.23). Unlike the phase-averaged concentration profiles, the concentration standard deviation profiles are not piecewise Gaussian shapes. Note that there is substantial disagreement in the literature regarding the transverse profile shape of the standard deviation of the concentration fluctuations for even straight plumes (e.g., Fackrell

and Robins [1982], Crimaldi et al. [2002], Rahman and Webster [2005], Crimaldi and Koseff [2006]).

3.5.6 Standard Deviation of the Velocity Fluctuations for the Meandering Plume

To examine the spatial structure of the velocity fluctuations, color contours of the standard deviation of the x-velocity (σ_u) and y-velocity (σ_v) are plotted in Figures 3.32 and 3.33, respectively, for the meandering plume for phase $\phi = 0°$. Note that this is the standard deviation computed for all 6706 images in each phase.

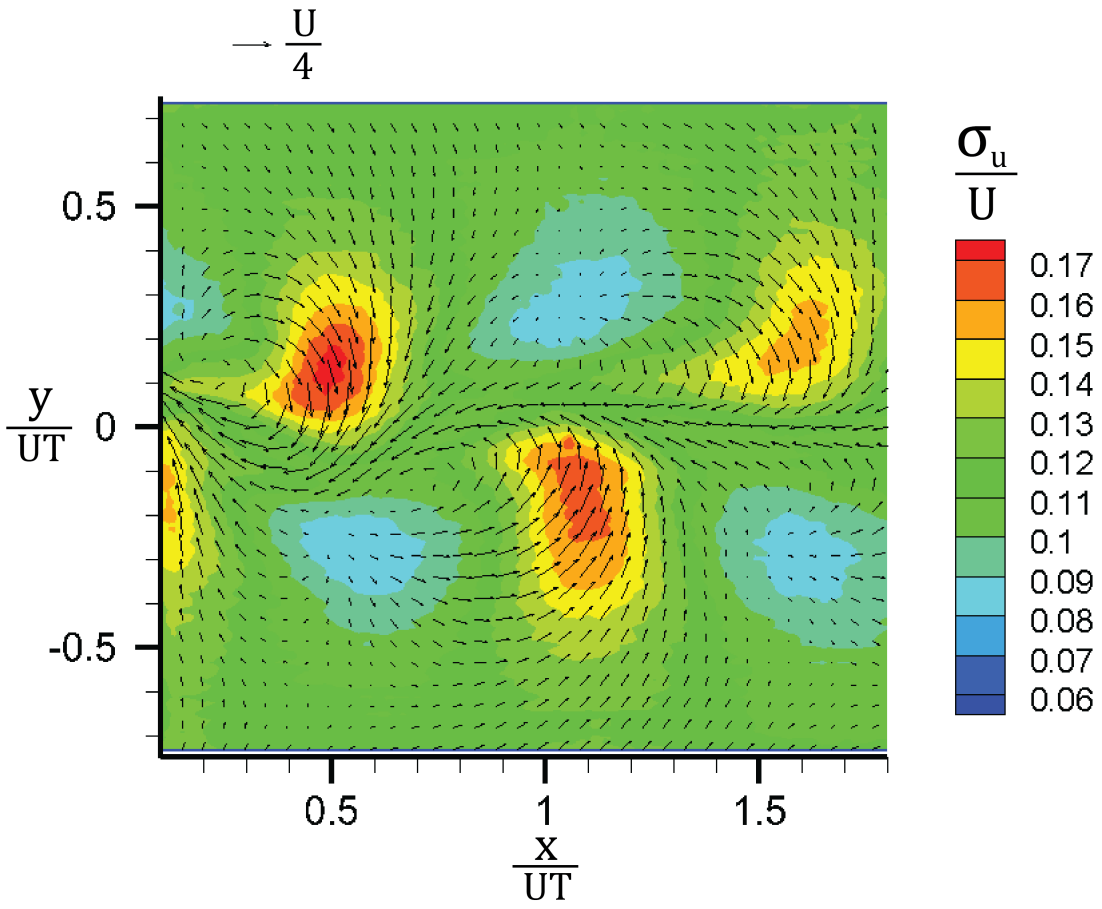

Figure 3.32: Standard deviation of the velocity fluctuations in the x-direction (σ_u/U) for the meandering plume for phase $\phi = 0°$. The vectors indicate the phase-averaged velocity with the free-stream velocity (U) subtracted. Every 4^{th} velocity vector is plotted.

The x-direction velocity fluctuations are strongest on the periphery of the plume structure, effectively located where the free-stream fluid is swept into the plume as shown by the velocity vectors (Figure 3.32). Interestingly, regions of very weak x-direction velocity fluctuations are observed immediately to the opposite side of the plume structure as the regions of strong x-direction velocity fluctuations. The x-direction velocity fluctuations in these regions are weaker than those in the free-stream further away from the plume structure.

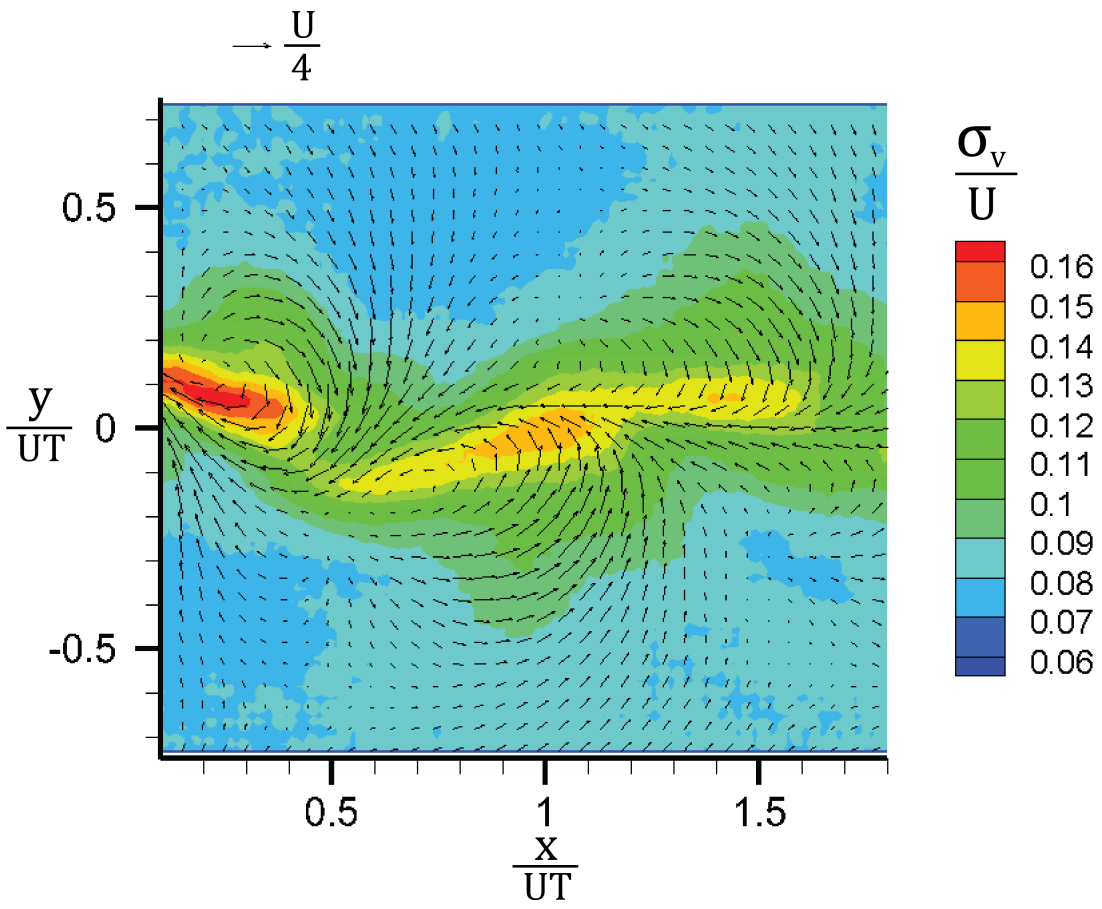

Figure 3.33: Standard deviation of the velocity fluctuations in the y-direction (σ_v/U) for the meandering plume for phase $\phi = 0°$. The vectors indicate the phase-averaged velocity with the free-stream velocity (U) subtracted. Every 4^{th} velocity vector is plotted.

In contrast, the y-direction velocity fluctuations are strongest near the plume centerline (Figure 3.33), although they are also strong in the regions of strongest x-direction velocity fluctuations. Unlike the x-direction velocity fluctuations, the y-direction velocity fluctuations are not markedly weaker than in the free-stream at any position in the vicinity of the plume structure. Similar to the phase-averaged concentration color contour plots (Figure 3.21), we observe local peaks in the y-direction velocity fluctuations on the plume centerline (Figure 3.33).

3.5.7 Effects of the Large-Scale Alternating Vortices on the Meandering Plume

The large-scale alternating vortices being shed off the diverting plate are clearly the defining feature of the flow. Consequently, we want to examine the influence these vortices have on the concentration and velocity fluctuation spatial distributions discussed in Sections 3.5.3 and 3.5.6.

3.5.7.1 Phase-averaged Concentration

Figure 3.34 shows the color levels of the concentration for the meandering plume for phase $\phi = 0°$. The vorticity contours at $T\omega_z = -1.3$ and $T\omega_z = 1.3$ are shown as dashed and solid black lines, respectively, to denote the position of the vortices. It is immediately apparent from Figure 3.34 that the large-scale alternating vortices are responsible for the spatial distribution of phase-averaged concentration and the plume meander. More specifically, the leading edges of the vortices advect the free-stream fluid into the plume and effectively create the meandering pattern.

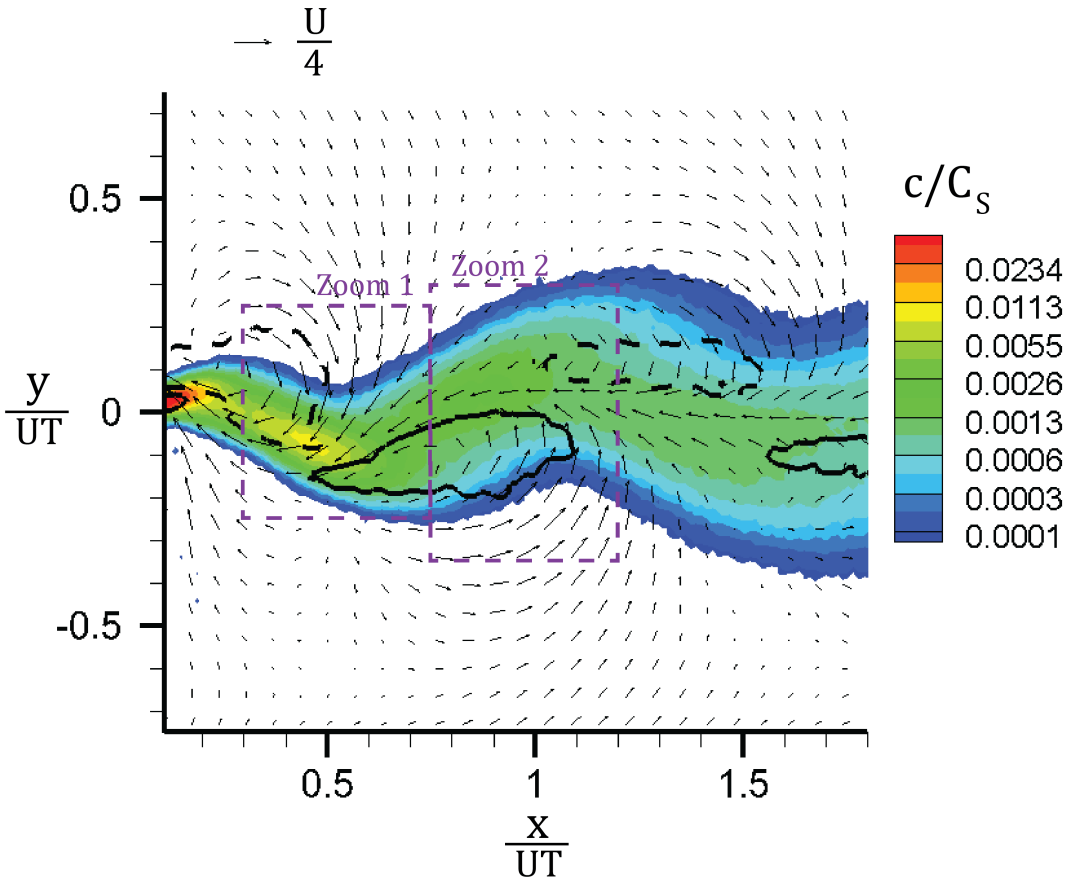

Figure 3.34: Phase-averaged concentration field of the meandering plume for phase $\phi = 0°$. Vorticity contours corresponding to levels $T\omega_z = -1.3$ and $T\omega_z = 1.3$ are shown as dashed and solid black lines, respectively. The vectors indicate the phase-averaged velocity with the free-stream velocity (U) subtracted. Every 5^{th} velocity vector is plotted. The purple boxes define the zoom regions.

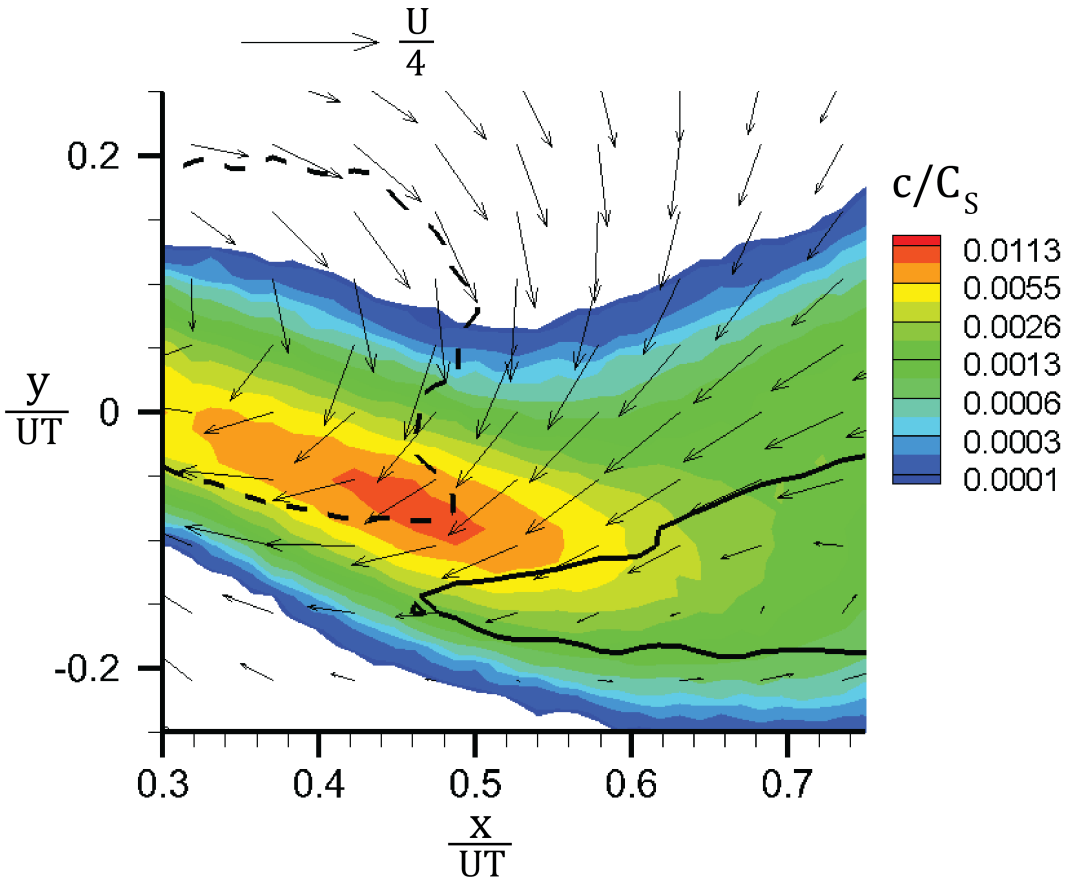

Figure 3.35: Phase-averaged concentration field of the meandering plume for phase $\phi = 0°$ showing the Zoom 1 region defined in Figure 3.34. Vorticity contours corresponding to levels $T\omega_z = -1.3$ and $T\omega_z = 1.3$ are shown as dashed and solid black lines, respectively. The vectors indicate the phase-averaged velocity with the free-stream velocity (U) subtracted. Every 4^{th} velocity vector is plotted.

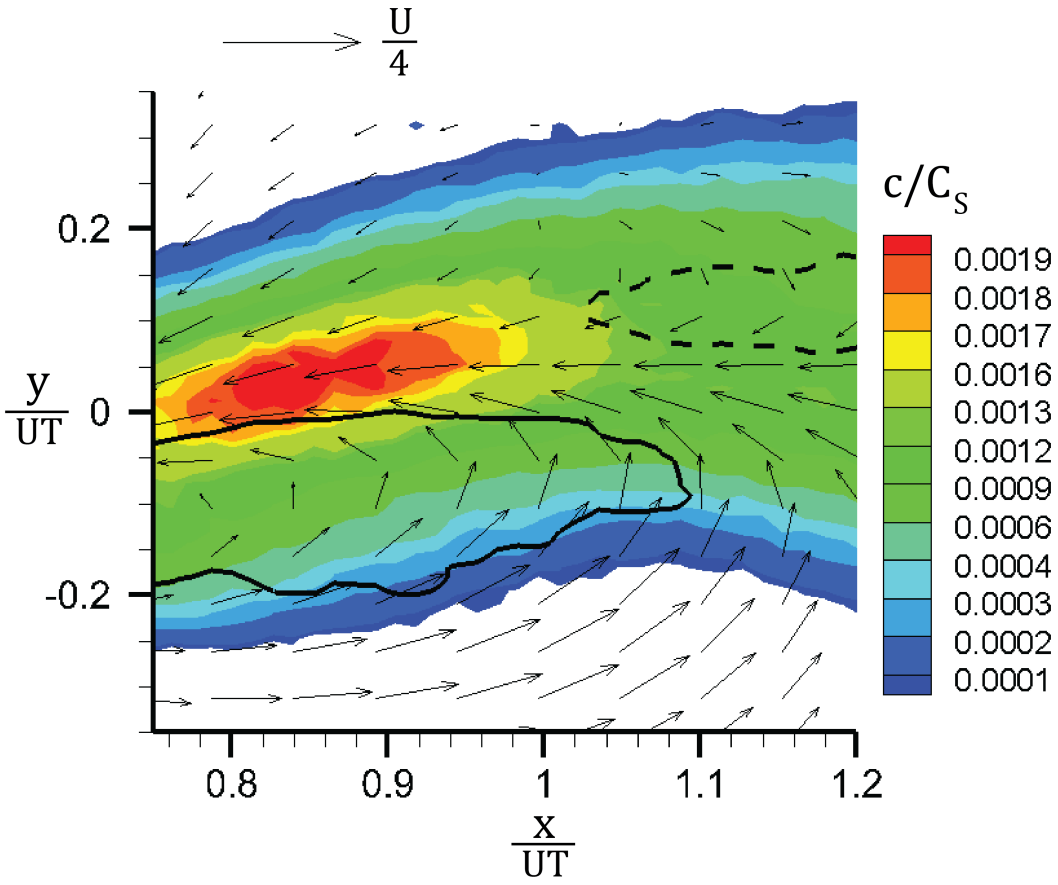

Figure 3.36: Phase-averaged concentration field of the meandering plume for phase $\phi = 0°$ showing the Zoom 2 region defined in Figure 3.34. Vorticity contours corresponding to levels $T\omega_z = -1.3$ and $T\omega_z = 1.3$ are shown as dashed and solid black lines, respectively. The vectors indicate the phase-averaged velocity with the free-stream velocity (U) subtracted. Every 4^{th} velocity vector is plotted.

Taking a closer look at the two sub-windows shown in Figure 3.34 provides insight to the relationship between the vortices and the local concentration peaks. Figures 3.35 and 3.36 show that the fluid being swept in from the free-stream is pinched together and pushed upstream by the combined effects of the two counter rotating vortices. Note that this does not physically correspond to flow reversal, but to a local deceleration of the flow (as the free-stream velocity has been subtracted off in

Figures 3.34, 3.35, and 3.36). This injection of tracer-free fluid contributes to the increased stirring of tracer in the plume, causing the concentration to decrease more quickly with distance downstream than the straight plume (see Figures 3.20, 3.24, and 3.25). However, the local deceleration effectively "piles up" the filaments of tracer that are advecting downstream in the plume. Further evidence of this phenomenon is observed in the plots of the intermittency factor along the plume centerline in Figure 3.37. Note that the intermittency factor is defined as the percentage of time that the concentration at a specific location exceeds a threshold fraction of the source concentration [Chatwin and Sullivan, 1989].

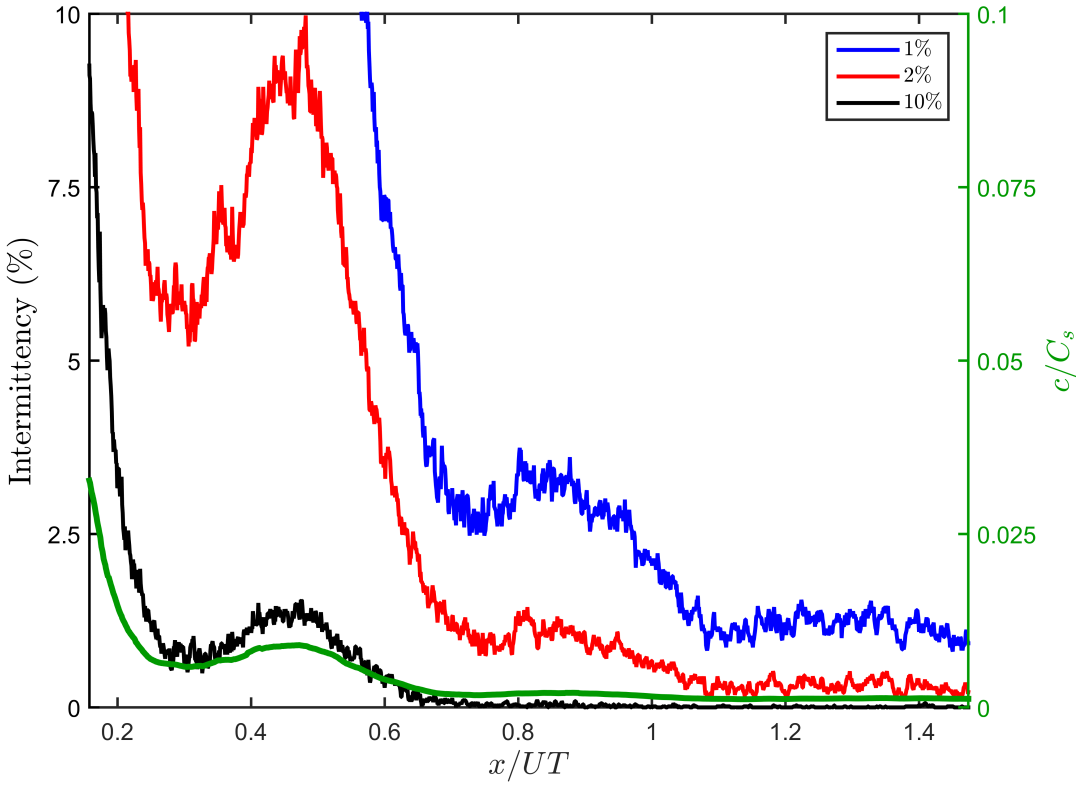

Figure 3.37: Intermittency factor along the plume centerline for three thresholds (1%, 2%, 10%) of the plume source concentration (C_s) for the meandering plume for phase $\phi = 0°$. The phase-averaged concentration along the centerline is shown in green.

We observe a local peak in the intemittency factor co-located with the first peak in the phase-averaged concentration for all of the chosen threshold concentrations (note that the y-axis scale is too small to see the peak in the intermittency factor for a threshold concentration of 1% of the source concentration). Further, we observe local peaks in the intermittency factor at a threshold concentration of 1% and 2% of the source concentration co-located with the second local peak in the phase-averaged concentration (near $x/UT = 0.85$). This indicates that the filaments of high concentration are more likely to be observed between the two vortices because they are "trapped" by the local deceleration in flow. As a result, we observe a local peak in the phase-averaged concentration immediately upstream of where the two counter-rotating vortices meet and the tracer filaments are more likely to congregate. This process is represented pictorially in Figure 3.38.

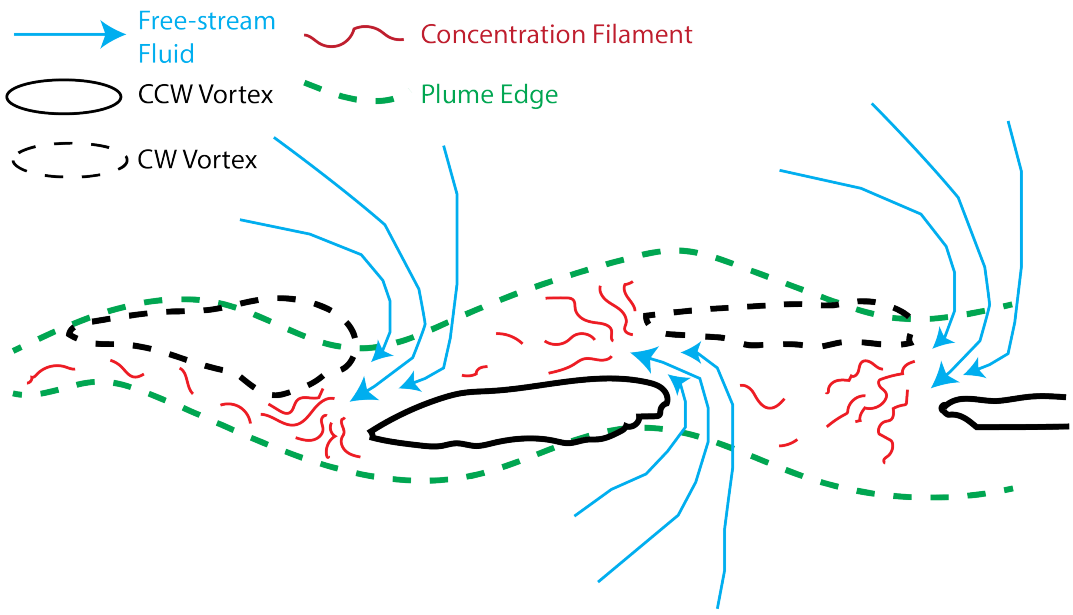

Figure 3.38: Cartoon of the tracer filament transport by the large-scale alternating vortices.

It is important to note that in the wake of a circular cylinder local peaks in

concentration have been observed in the earlier studies of Balu et al. [2001] and von Carmer et al. [2009]. In those two studies the concentration peaks were co-located with the vortex cores, as the concentration filaments were trapped in the vortices being shed off the cylinder. This is a result of the dye being released on the face of the cylinder where the vortices were being shed. The situation here is unique because the plume release is spatially separated from the origin of the vortical structures, thus the tracer filaments are not forcibly congregated by the location of dye injection.

3.5.7.2 Turbulence Statistics

To consider the relationship between the velocity fluctuation spatial distributions and the large-scale alternating vortices, the color levels of the standard deviation of the x-velocity (σ_u) and y-velocity (σ_v) are plotted in Figures 3.39 and 3.40, respectively, for the meandering plume for phase $\phi = 0°$.

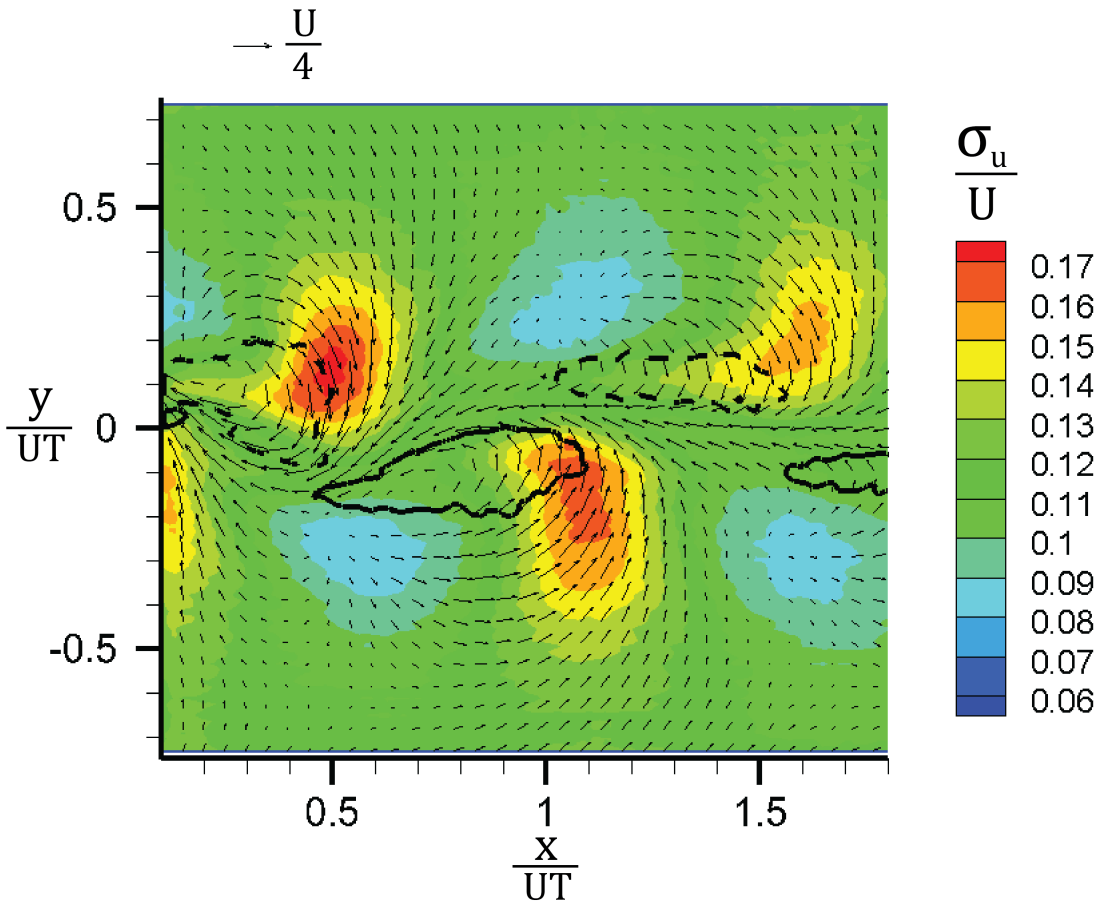

Figure 3.39: Standard deviation of the x-direction velocity (σ_u/U) for the meandering plume for phase $\phi = 0°$. Vorticity contours corresponding to levels $T\omega_z = -1.3$ and $T\omega_z = 1.3$ are shown as dashed and solid black lines, respectively. The vectors indicate the phase-averaged velocity with the free-stream velocity (U) subtracted. Every 4^{th} velocity vector is plotted.

The cause of the observed peaks in the standard deviation of the x-velocity (σ_u/U) is clear from Figure 3.39. Regions of strong fluctuations in the x-velocity correspond to high shear and the corresponding high shear production at the leading edges of the large-scale alternating vortices as they advect downstream, but could also partially represent the effect of minor differences in the location of the large scale alternating sign vortices from the diverting plate in each image. Furthermore, it is perhaps more

obvious that the regions of very weak x-velocity fluctuations, seemingly lower than the x-velocity fluctuations in the free-stream, are the locations in which the phase-averaged velocity is closest to the free-stream velocity. This is evidenced by the very small velocity vector magnitudes in the regions of very weak x-velocity fluctuations. This is also further evidence (along with Figure 3.28) that perhaps the PIV window is not sufficiently wide to observe the true "free-stream" velocity that is entirely unaffected by the plume.

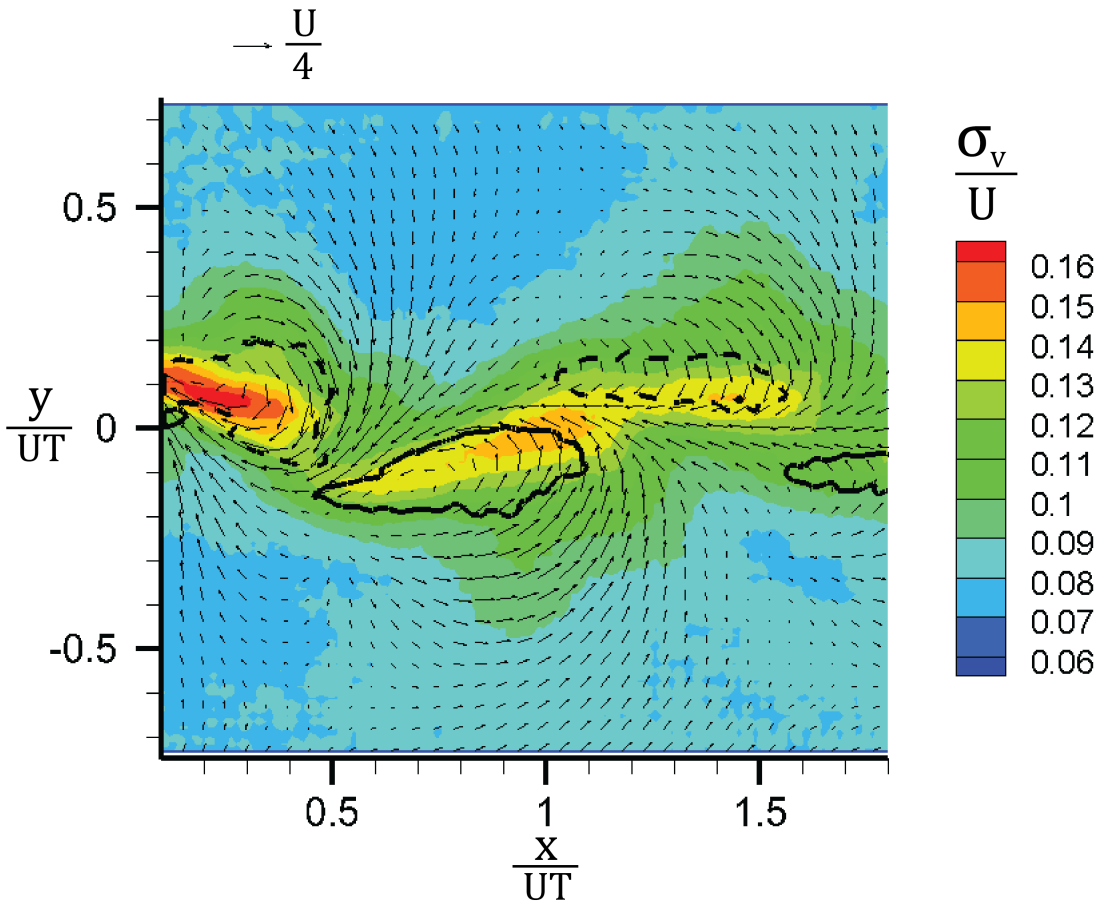

Figure 3.40: Standard deviation of the y-direction velocity (σ_v/U) for the meandering plume for phase $\phi = 0°$. Vorticity contours corresponding to levels $T\omega_z = -1.3$ and $T\omega_z = 1.3$ are shown as dashed and solid black lines, respectively. The vectors indicate the phase-averaged velocity with the free-stream velocity (U) subtracted. Every 4^{th} velocity vector is plotted.

As illustrated in Figure 3.40, the peaks in the standard deviation of the y-velocity (σ_v/U) are co-located with the "plume-side" edge of the large-scale alternating vortices, perhaps more focused towards the leading edge of the vortices, which accounts for the local peaks in the standard deviation of the y-velocity (σ_v/U) observed in Figure 3.33.

Figure 3.41 shows the spatial distribution of TKE ($= \frac{1}{2}\left(\overline{u'u'} + 2\overline{v'v'}\right)/U^2$) for the

meandering plume for phase $\phi = 0°$. At this elevation above the bed in a turbulent boundary layer, we expect $\overline{w'w'}$ to be of similar value to $\overline{v'v'}$ [Pope, 2000], thus $\overline{v'v'}$ is multiplied by two in our estimate of TKE.

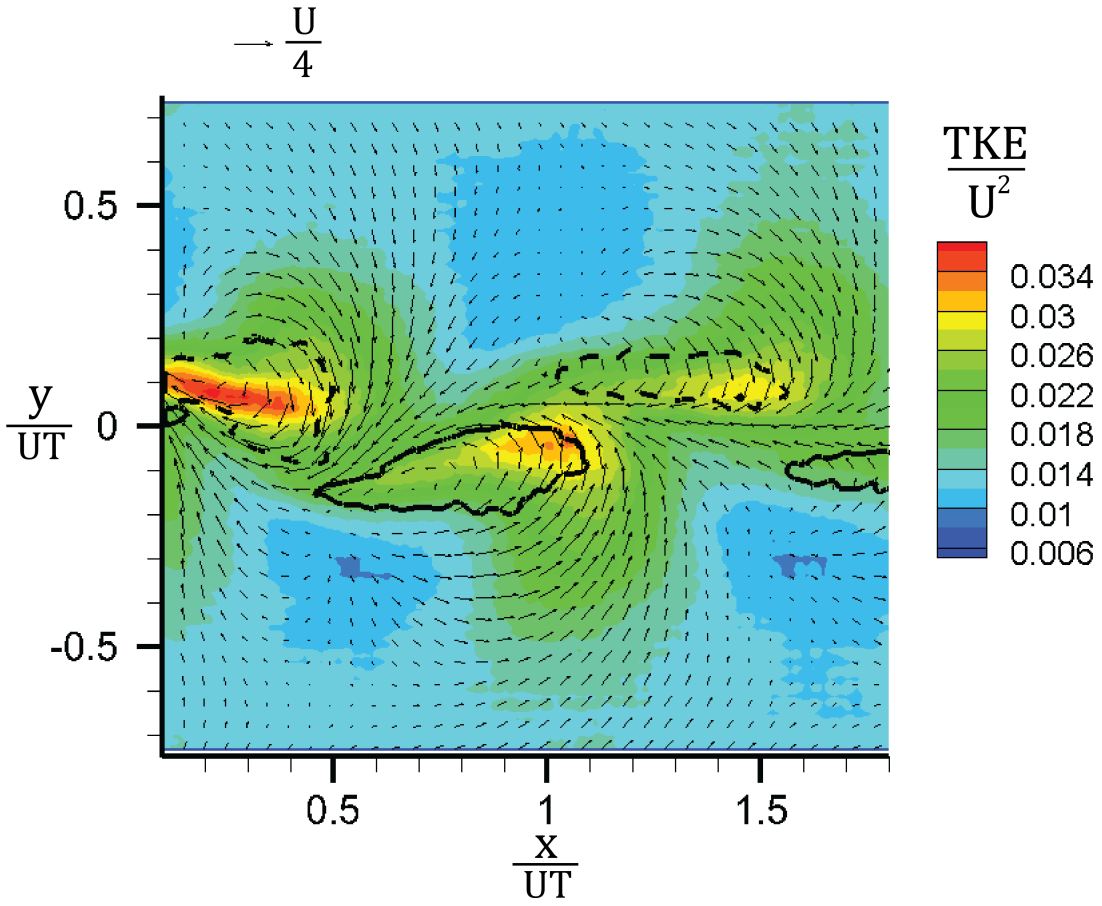

Figure 3.41: Turbulent kinetic energy (TKE/U^2) for the meandering plume for phase $\phi = 0°$. Vorticity contours corresponding to levels $T\omega_z = -1.3$ and $T\omega_z = 1.3$ are shown as dashed and solid black lines, respectively. The vectors indicate the phase-averaged velocity with the free-stream velocity (U) subtracted. Every 4^{th} velocity vector is plotted.

As expected, obvious similarities exist between Figure 3.41 and Figures 3.39 and 3.40. TKE is highest towards the downstream, plume-side edge of the large-scale alternating vortices (as for σ_v/U in Figure 3.40). It is moderately high further away

from the plume, where the free-stream fluid is swept into the plume (as for σ_u/U in Figure 3.39), and also along the plume centerline (as for σ_v in Figure 3.40). The regions of lowest TKE are co-located with the regions of lowest σ_u, where the flow is most like the free-stream flow.

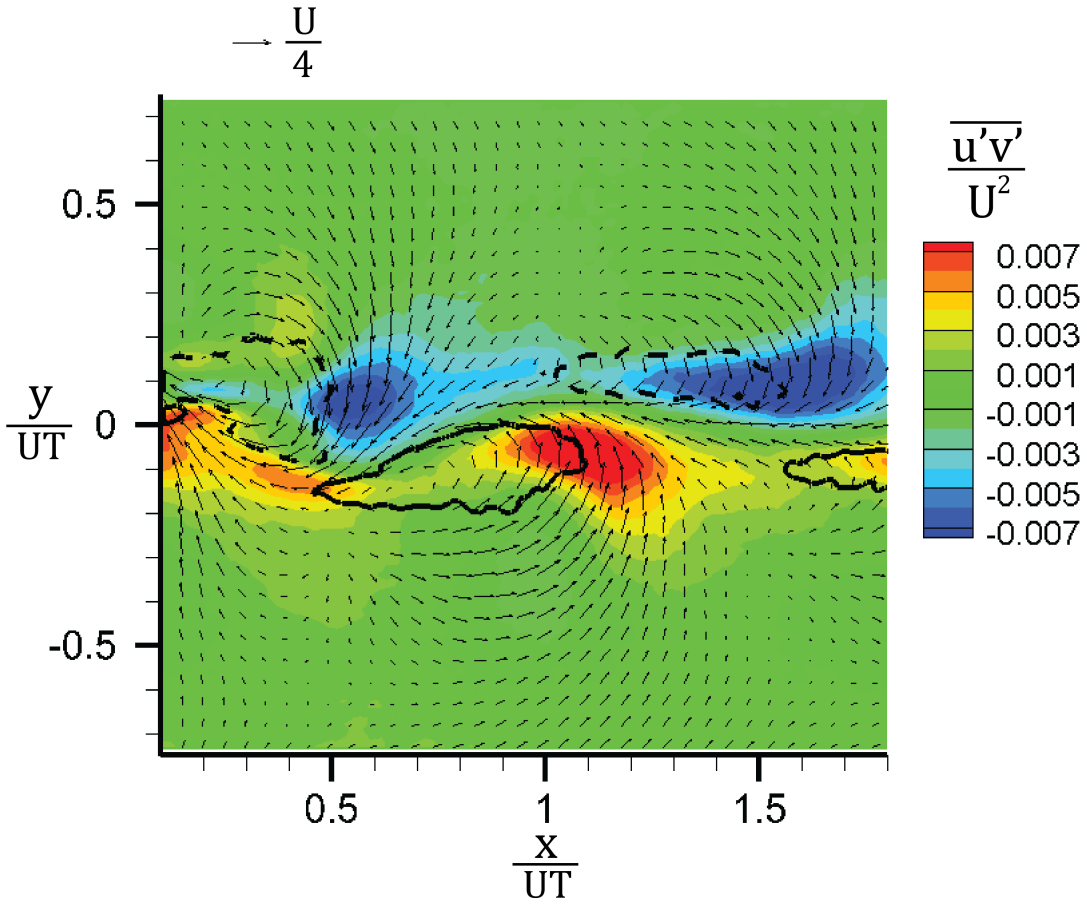

Figure 3.42: Reynolds shear stress ($\overline{u'v'}/U^2$) for the meandering plume for phase $\phi = 0°$. Vorticity contours corresponding to levels $T\omega_z = -1.3$ and $T\omega_z = 1.3$ are shown as dashed and solid black lines, respectively. The vectors indicate the phase-averaged velocity with the free-stream velocity (U) subtracted. Every 4^{th} velocity vector is plotted.

Figure 3.42 shows the spatial distribution of the Reynolds stress ($\overline{u'v'}$) for the meandering plume for phase $\phi = 0°$. Figure 3.42 shows that the regions of highest

Reynolds stress are closely related to the leading edge of the large-scale alternating vortices, immediately downstream of the peaks in TKE. The Reynolds stress is negative in the vicinity of the clockwise-rotating vortices and positive in the vicinity of the counter-clockwise-rotating vortices. Further, the Reynolds stress is near zero on the plume centerline, as well as further away from the plume.

The spatial distributions of TKE and Reynolds stress in Figures 3.41 and 3.42 can be compared to those of other studies of periodic vortices being shed off bluff bodies, such as square [Lyn et al., 1995, Nakagawa et al., 1999, Saha et al., 2000] or circular [Huang et al., 1995, Kim et al., 2006] cylinders. As in our study, the TKE is highest within the cores of the large-scale alternating vortices, and is also high along the hypothetical centerline between the vortices (no plume exists in Lyn et al. [1995], Nakagawa et al. [1999], or Saha et al. [2000], as no tracer was released). Further, the Reynolds stress magnitudes are highest on the leading edge of the large-scale alternating vortices in Lyn et al. [1995], Huang et al. [1995], and Kim et al. [2006] and near zero along the hypothetical centerline between the vortices, similar to the distribution in our study. The only difference of note is that the maximum observed TKE in our study is located towards the downstream edge of the vortices, as opposed to the center as in Lyn et al. [1995]. Similarly, the peaks in the Reynolds stress magnitudes are located slightly further downstream of the vortex cores in our study than in Lyn et al. [1995], Huang et al. [1995], and Kim et al. [2006]. This is likely the result of the shape of the vortices being shed. In Lyn et al. [1995], Huang et al. [1995], Nakagawa et al. [1999], Saha et al. [2000], and Kim et al. [2006] the vortices are circular, whereas our vortices are elliptical with a noticeably greater effect on the velocity field at the downstream edges.

3.5.7.3 Turbulent Flux of Tracer

To consider the relationship between the turbulent flux fields and the large-scale alternating vortices, Figures 3.43 and 3.44 show $\overline{u'c'}$ and $\overline{v'c'}$, respectively, for the meandering plume for phase $\phi = 0°$.

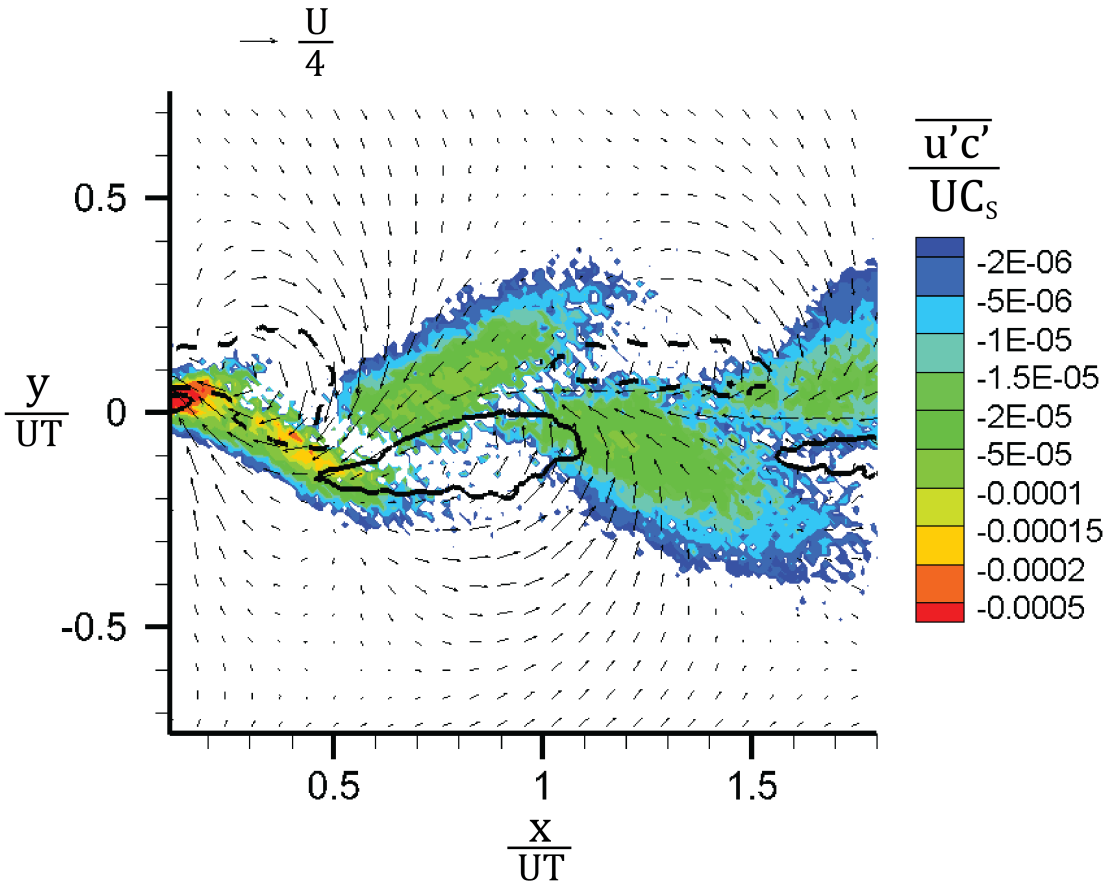

Figure 3.43: Turbulent flux in the x-direction $\left(\frac{\overline{u'c'}}{UC_s}\right)$ for the meandering plume for phase $\phi = 0°$. Vorticity contours corresponding to levels $T\omega_z = -1.3$ and $T\omega_z = 1.3$ are shown as dashed and solid black lines, respectively. The vectors indicate the phase-averaged velocity with the free-stream velocity (U) subtracted. Every 5^{th} velocity vector is plotted.

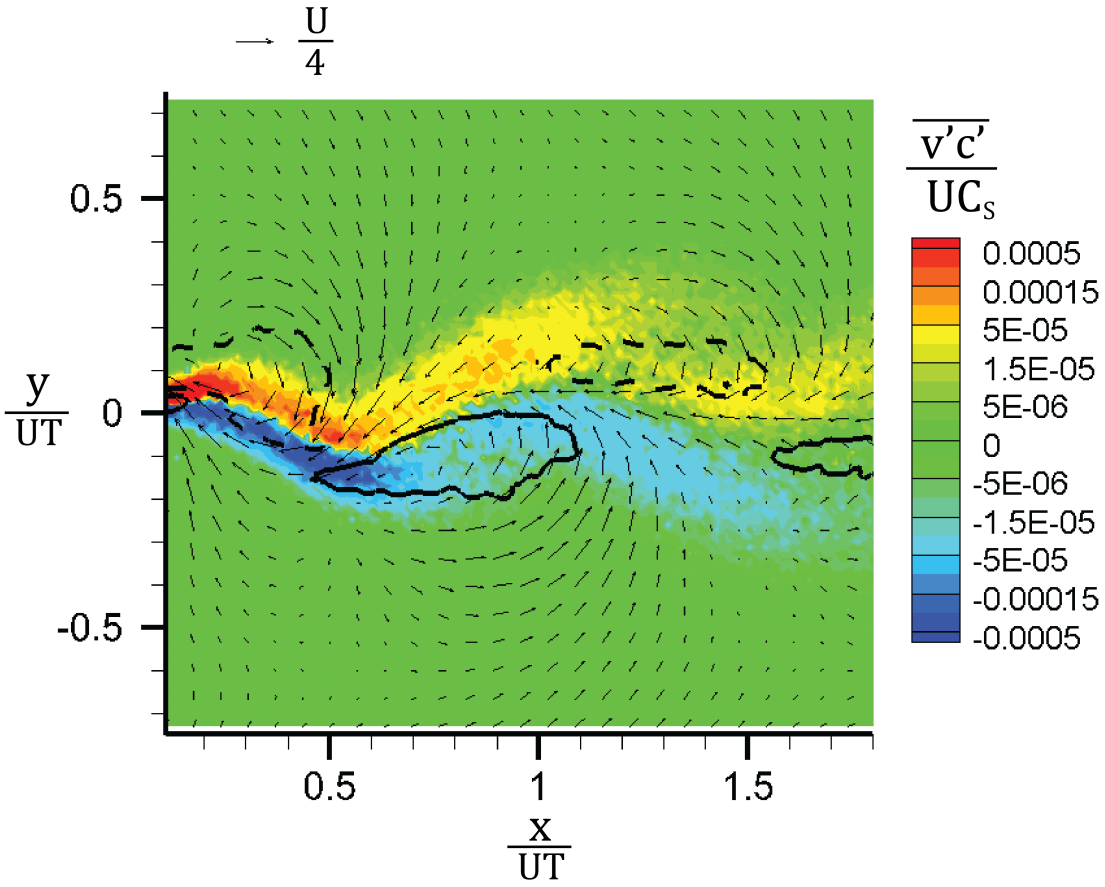

Figure 3.44: Turbulent flux in the y-direction $\left(\frac{\overline{v'c'}}{UC_s}\right)$ for the meandering plume for phase $\phi = 0°$. Vorticity contours corresponding to levels $T\omega_z = -1.3$ and $T\omega_z = 1.3$ are shown as dashed and solid black lines, respectively. The vectors indicate the phase-averaged velocity with the free-stream velocity (U) subtracted. Every 5^{th} velocity vector is plotted.

Figure 3.43 indicates that the largest magnitude of the turbulent flux in the x-direction occurs immediately downstream of the large scale-alternating vortices (similar to the distribution of Reynolds stress observed in Figure 3.42). Furthermore, the turbulent flux in the x-direction decreases in magnitude with distance downstream.

Figure 3.44 indicates that the largest magnitudes of the turbulent flux in the y-direction occurs immediately to either side of the plume centerline. Similar to the

distribution of Reynolds stress observed in Figure 3.42, the turbulent flux in the y-direction changes sign across the plume centerline (albeit with negative turbulent flux in the y-direction at negative values of $\frac{y}{UT}$ and positive turbulent flux in the y-direction at positive values of $\frac{y}{UT}$). As with the turbulent flux in the x-direction, the turbulent flux in the y-direction decreases in magnitude with distance downstream.

3.5.8 Eddy Diffusion Coefficient for the Meandering Plume

Recalling the discussion of turbulent mixing in Section 3.3.1, the turbulent flux term is commonly modeled by assuming that it is equivalent to the concentration gradient multiplied by an eddy-diffusion coefficient, i.e., $\overline{u_i'c'} = -K_{x_i}\frac{\partial c}{\partial x_i}$ (see Equations 3.3, 3.4, and 3.5), analogous to Fickian diffusion. To investigate the possibility of applying this model to our meandering plume, Figure 3.45 shows the $\overline{v'c'}$ field along with the mean concentration contour lines for the meandering plume for phase $\phi = 0°$. Figures 3.46 and 3.47 show the two sub-windows outlined in white in Figure 3.45. Note that $\overline{v'c'}$ is shown rather than $\overline{u'c'}$ because (1) the largest concentration gradients are more closely aligned with the y-axis, and (2) we expect advective transport to dominate the turbulent flux of tracer in the x-direction.

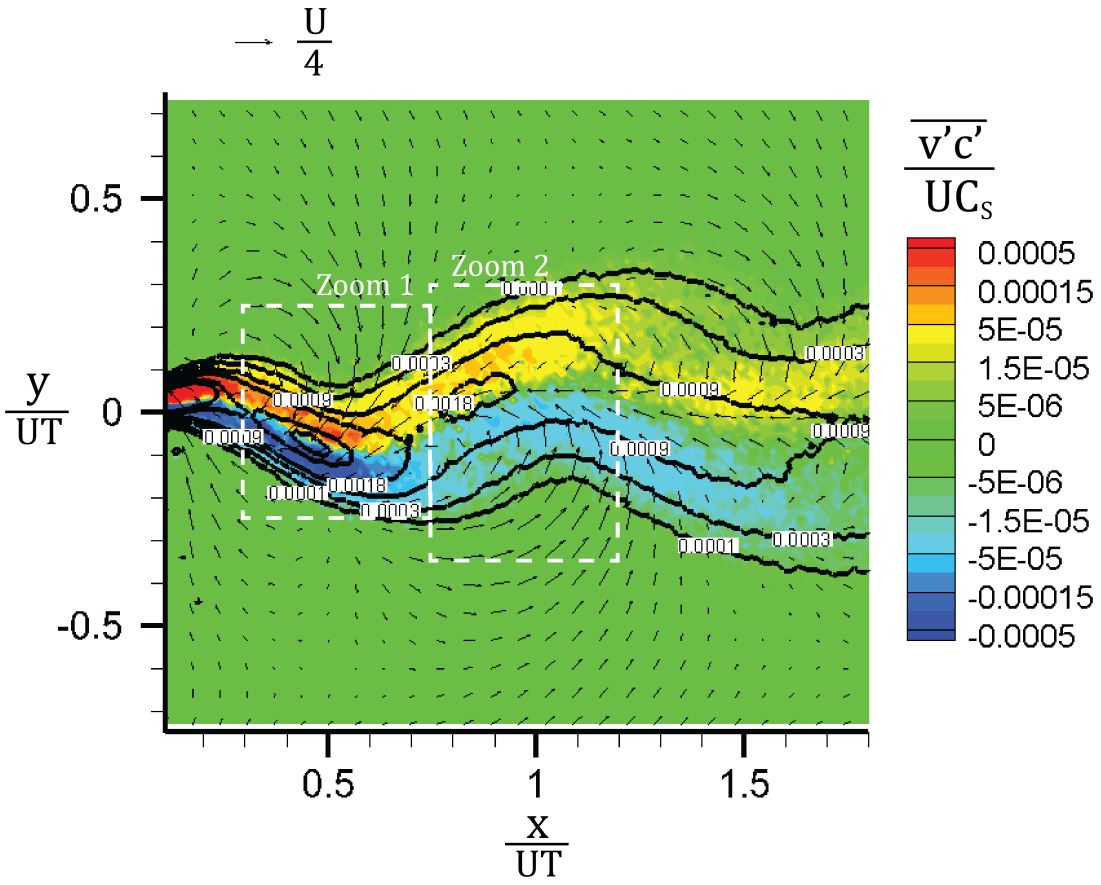

Figure 3.45: Turbulent flux in the y-direction $\left(\frac{\overline{v'c'}}{UC_s}\right)$ for the meandering plume for phase $\phi = 0°$. Concentration contour lines are shown in black (note they are logarithmically spaced). The vectors indicate the phase-averaged velocity with the free-stream velocity (U) subtracted. Every 5^{th} velocity vector is plotted. The white boxes define the zoom regions.

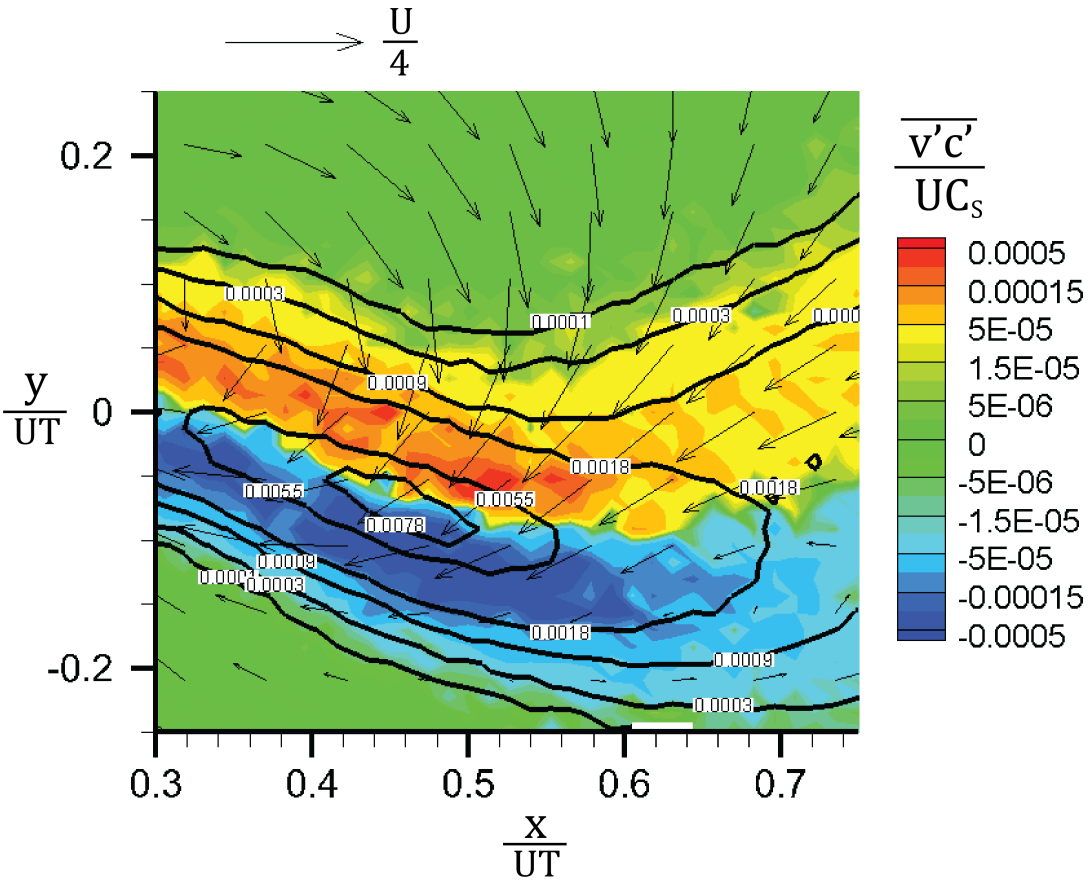

Figure 3.46: Turbulent flux in the y-direction $\left(\frac{\overline{v'c'}}{UC_s}\right)$ for the meandering plume for phase $\phi = 0°$ showing the Zoom 1 region defined in Figure 3.45. Concentration contour lines are shown in black (note they are logarithmically spaced). The vectors indicate the phase-averaged velocity with the free-stream velocity (U) subtracted. Every 4^{th} velocity vector is plotted.

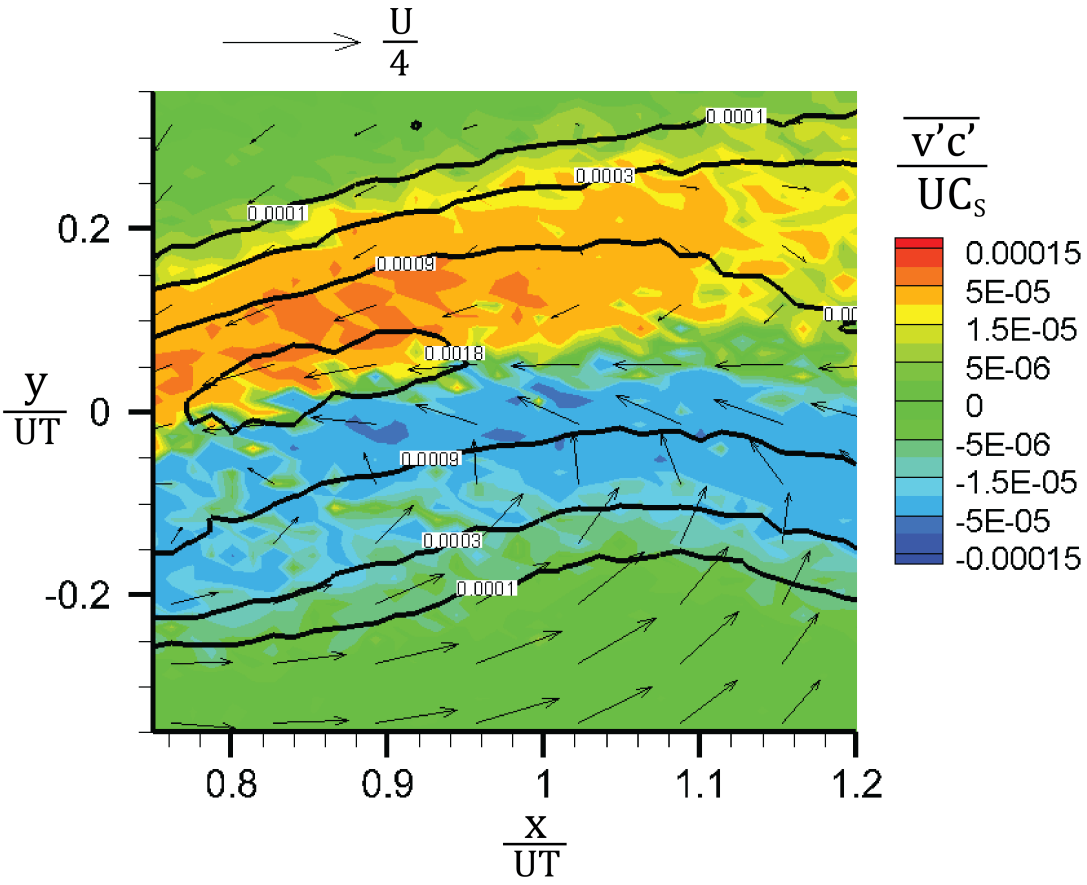

Figure 3.47: Turbulent flux in the y-direction $\left(\frac{\overline{v'c'}}{UC_s}\right)$ for the meandering plume for phase $\phi = 0°$ showing the Zoom 2 region defined in Figure 3.45. Concentration contour lines are shown in black (note they are logarithmically spaced). The vectors indicate the phase-averaged velocity with the free-stream velocity (U) subtracted. Every 4^{th} velocity vector is plotted.

Figures 3.45, 3.46, and 3.47 strongly suggest that the turbulent flux may be modeled as a function of the concentration gradient. Note that $\overline{v'c'}$ is zero on the centerline, which is defined as location of the maximum concentration - where the y-direction concentration gradient is zero. Further, $\overline{v'c'}$ increases rapidly in magnitude away from the centerline (in the vicinity of the maximum y-direction concentration gradient - note the concentration contours are logarithmically spaced) before decreasing

to zero far from the plume centerline, where the concentration (and the y-direction concentration gradient) is zero. Finally, y-direction concentration gradient changes sign across the plume (i.e., the concentration is increasing for $\frac{y}{UT}$ values less than $\frac{y}{UT}$ value of the plume centerline and decreasing for $\frac{y}{UT}$ values greater than $\frac{y}{UT}$ value of the plume centerline), as does the sign of $\overline{v'c'}$.

To confirm the efficacy of the eddy-diffusivity model it is necessary to directly examine the slope of the mean concentration gradient and the turbulent flux. To accomplish this, we extracted mean concentration profiles at 20 downstream positions. As with the concentration profiles in Figures 3.22 and 3.23, the concentration profiles were defined perpendicular to the local plume centerline (see Figure 3.18). The turbulent flux ($\overline{v_0'c'}$) along the concentration profile axis (y_0) was calculated by defining bins along the concentration profile axis and identifying the values of u', v', and c' for each PTV vector in the bin (see Section 3.4.7). Each vector was rotated such that the axes aligned with the local plume centerline axis and the concentration profile axis (y_0), i.e., u_0' and v_0', respectively. $\overline{v_0'c'}$ was calculated at the centroid of each bin along the concentration profile as the time-average of $v_0'c'$ for every PTV vector located in each bin. The slope of the piecewise Gaussian profile fit to the concentration profile (described in Section 3.5.3.1) is used to ensure a smooth and continuous estimate of the mean concentration slope $\left(\frac{\partial C}{\partial y_0}\right)$. An example plot of the turbulent flux along the concentration profile axis as a function of the mean concentration slope is shown in Figure 3.48.

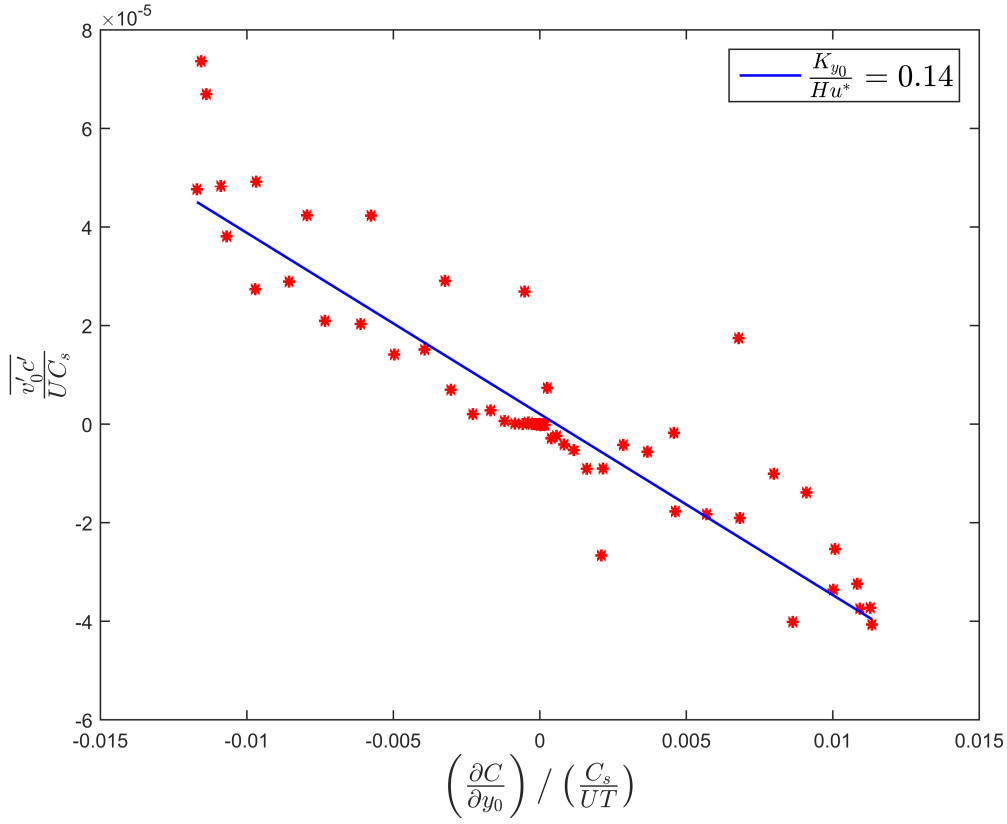

Figure 3.48: Turbulent flux of tracer $\frac{\overline{v_0'c'}}{UC_s}$ in the direction perpendicular to the local plume centerline (i.e., along axis y_0) as a function of the mean concentration gradient $\left[\left(\frac{\partial C}{\partial y_0}\right) / \left(\frac{C_s}{UT}\right)\right]$ in the direction perpendicular to the local plume centerline at $\frac{x}{UT} = 0.95$. The slope of the blue line leads to the estimate of the eddy diffusion coefficient $\left(\frac{K_{y_0}}{Hu^*}\right)$.

Figure 3.48 offers compelling support for a linear relationship between $\overline{v_0'c'}$ and $\left(\frac{\partial C}{\partial y_0}\right)$ along the profile. Despite the substantial scatter $\overline{v_0'c'}$ (as might be expected given the scatter observed in $\overline{u'c'}$ and $\overline{v'c'}$ in Figures 3.43 and 3.44), 82% of the variance in $\overline{v_0'c'}$ is explained by the linear fit. As shown in Figure 3.48, the value of the eddy-diffusion coefficient is calculated as the slope of the best fit line and is reported with the standard non-dimensionalization using the water depth (H) and the shear velocity (u^*).

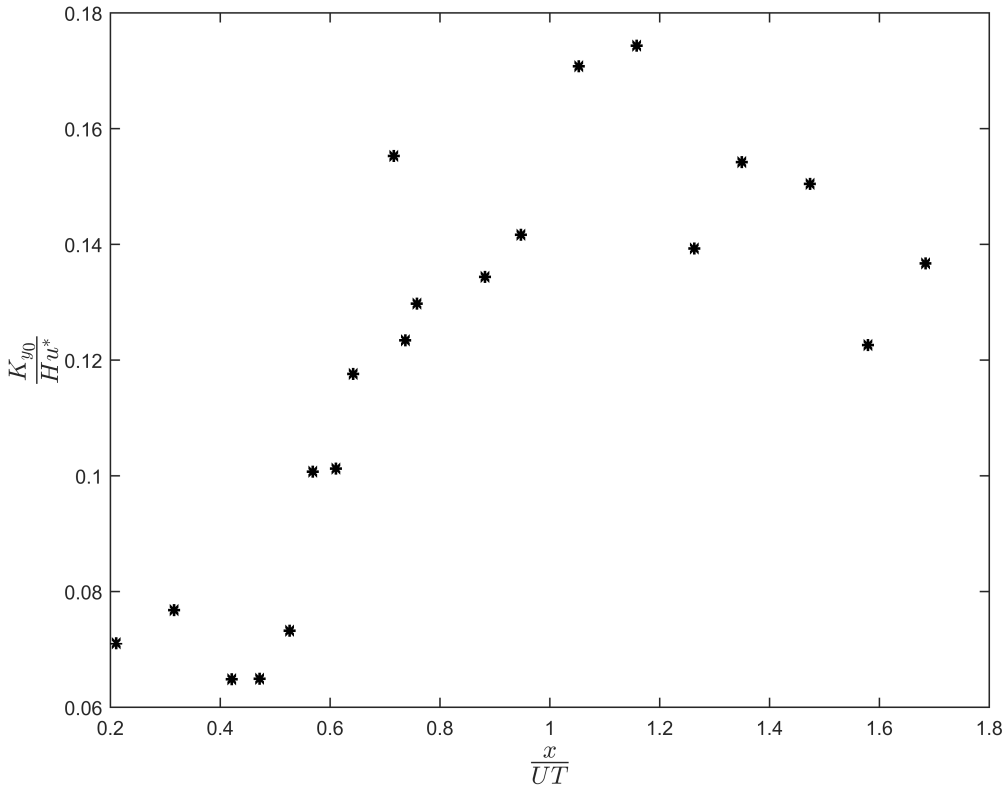

Figure 3.49: Eddy diffusion coefficient $\left(\frac{K_{y_0}}{Hu^*}\right)$ in the direction perpendicular to the local plume centerline (i.e., along axis y_0) as a function of distance downstream $\left(\frac{x}{UT}\right)$.

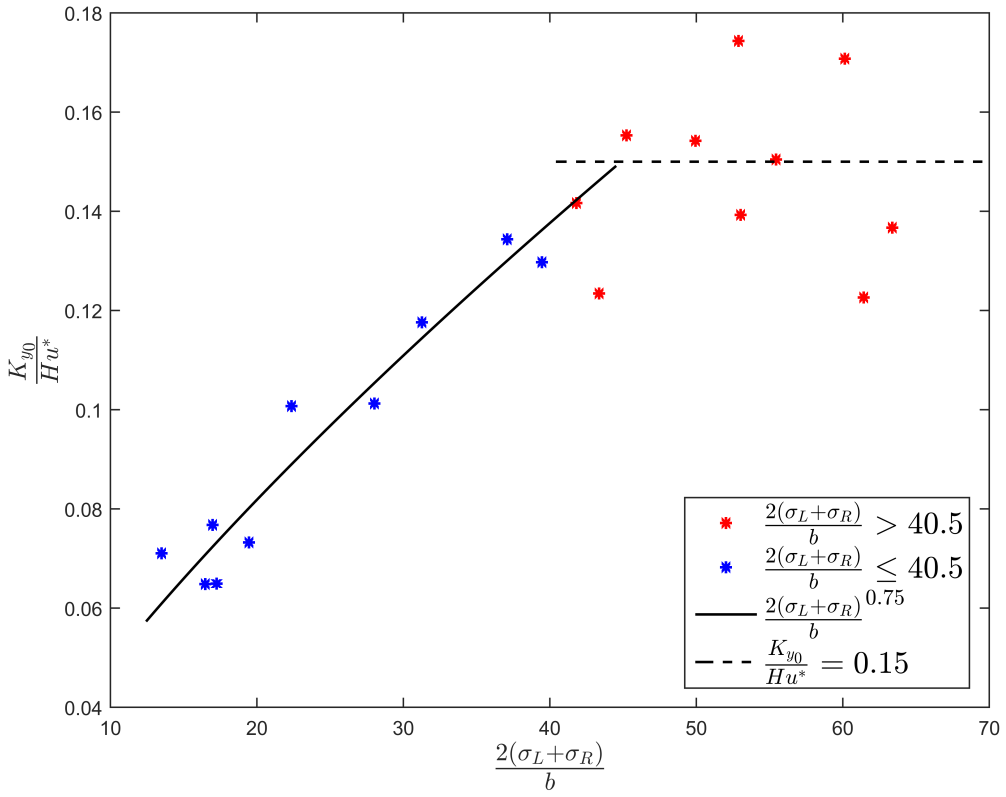

Figure 3.50: Eddy diffusion coefficient $\left(\frac{K_{y0}}{Hu^*}\right)$ in the direction perpendicular to the local plume centerline (i.e., along axis y_0) as a function of the plume width $\left(\frac{2(\sigma_L+\sigma_R)}{b}\right)$.

Figures 3.49 and 3.50, respectively, show that the relationship between the eddy-diffusion coefficient $\left(\frac{K_{y0}}{Hu^*}\right)$ and the distance downstream and the plume width, which is itself a function of distance downstream, as shown in Figures 3.24 and 3.25. The eddy-diffusion coefficient increases with distance downstream until $\frac{x}{UT} \approx 1.0$, at which point it appears to level off or slightly decrease. As observed in Figure 3.50, this region corresponds to a leveling off of $\frac{K_{y0}}{Hu^*}$ as a function of plume width.

The probable cause of the leveling off of the eddy-diffusion coefficient can be traced back to the foundational theory of turbulent mixing discussed in Section 3.3.1. Specifically, only eddies smaller than the scale of the patch of tracer contribute to the turbulent mixing [Roberts and Webster, 2002]. Once the plume/patch of tracer

has reached the size of the largest eddies, we expect the eddy-diffusion coefficient to level off. A general order-of-magnitude estimate of the size of the largest eddies possible in open channel flow is the water depth (H). For our flume $H/b = 48$, (non-dimensionalizing by the initial plume width - the tracer release nozzle diameter $b = 4.2\ mm$). The largest vortices directly observed in our flume are the large-scale alternating vortices induced by the diverting plate. As discussed extensively in Section 3.5.7, these vortices are the dominant feature of our meandering plume.

To investigate this further, we estimated the size of the large-scale alternating vortices as the average of the major and minor axis lengths for all of the large-scale alternating vortices visible in the mean velocity fields for the meandering plume for all four phases. The vortices are defined as corresponding to vorticity levels $T\omega_z = -1.3$ and $T\omega_z = 1.3$, as in Section 3.5.7. Non-dimensionalizing by the initial plume width (the tracer release nozzle diameter $b = 4.2\ mm$), the average size of the large-scale alternating vortices under this criterion is 40.5. Thus, the vortices shed off the diverting plate are of a similar size to the largest turbulent eddies we expect to observe in this flow.

Returning to Figure 3.50, we indeed observe that $\frac{K_{y0}}{Hu^*}$ begins to level off around $\frac{2(\sigma_L+\sigma_R)}{b} = 40.5$ (the red stars in Figure 3.50 correspond to the point in which $\frac{2(\sigma_L+\sigma_R)}{b} > 40.5$).

Using data from numerous sources Fischer et al. [1979] estimated that the transverse eddy-diffusion coefficient in an open channel could be estimated by:

$$K_y \approxeq 0.15Hu^* \tag{3.29}$$

where u^* is the shear velocity. Other studies have reached a similar result with slightly different coefficients (e.g. $k_y \approxeq 0.17Hu^*$ in Webel and Schatzmann [1984]), but in almost all of the cases the transverse eddy diffusion coefficient was bounded by $0.1Hu^* \leq K_y \leq 0.2Hu^*$. In these studies the water depth H is used as an estimate of

the size of the largest eddies, thus the transverse eddy diffusion coefficient levels off at these values once the patch of tracer has exceeded this size. Using the estimate of the shear velocity in our flume from Rahman and Webster [2005] ($u^* = 3.08\ mm/s$ for the smooth bed case) $k_y \cong 0.15Hu^*$ is plotted as a dashed black line in Figure 3.50. This estimate agrees very well with the transverse eddy diffusion coefficients for which the plume width exceeds the size of the largest eddies (which we assume are of comparable size to the vortices shed off the diverting plate).

Lastly, let us consider the growth of the eddy-diffusion coefficient before it reaches the size of the largest eddies. In keeping with the theory that only eddies smaller than the scale of the patch of tracer contribute to the turbulent mixing, it is expected that the eddy-diffusion coefficient scales with the size of the tracer patch (see Section 3.3.1). Richardson [1926] argued based on observation that $K_y \propto L^{\frac{4}{3}}$, where L is the characteristic size of the tracer patch. Many later studies have corroborated this 4/3 dependence [Batchelor, 1952, Brooks, 1960, Foxworthy et al., 1966, Okubo, 1968]. However, in a compilation of many experiments by Okubo [1971] it was found that, although the 4/3-law was obeyed locally within each experiment, when when the data from all experiments were plotted together the eddy-diffusion coefficient scaled as $K_y \propto L^1$. To maintain generality, later studies [Stacey et al., 2000, Fong and Stacey, 2003] have assumed that the eddy-diffusion coefficient can be estimated by:

$$k_y = \alpha L^n \tag{3.30}$$

which allows other values of n to be examined, because, as argued in Stacey et al. [2000], n may vary with distance downstream. To examine the dependence of the eddy-diffusion coefficient on the plume size for our meandering plume, $\frac{K_{y_0}}{Hu^*}$ is plotted as a function of $\frac{2(\sigma_L+\sigma_R)}{b}$ for the data in which $\frac{2(\sigma_L+\sigma_R)}{b} \leq 40.5$ (the largest eddy size) on log-log scale in Figure 3.51. A least-square best-fit to Equation 3.30 is shown as a black line.

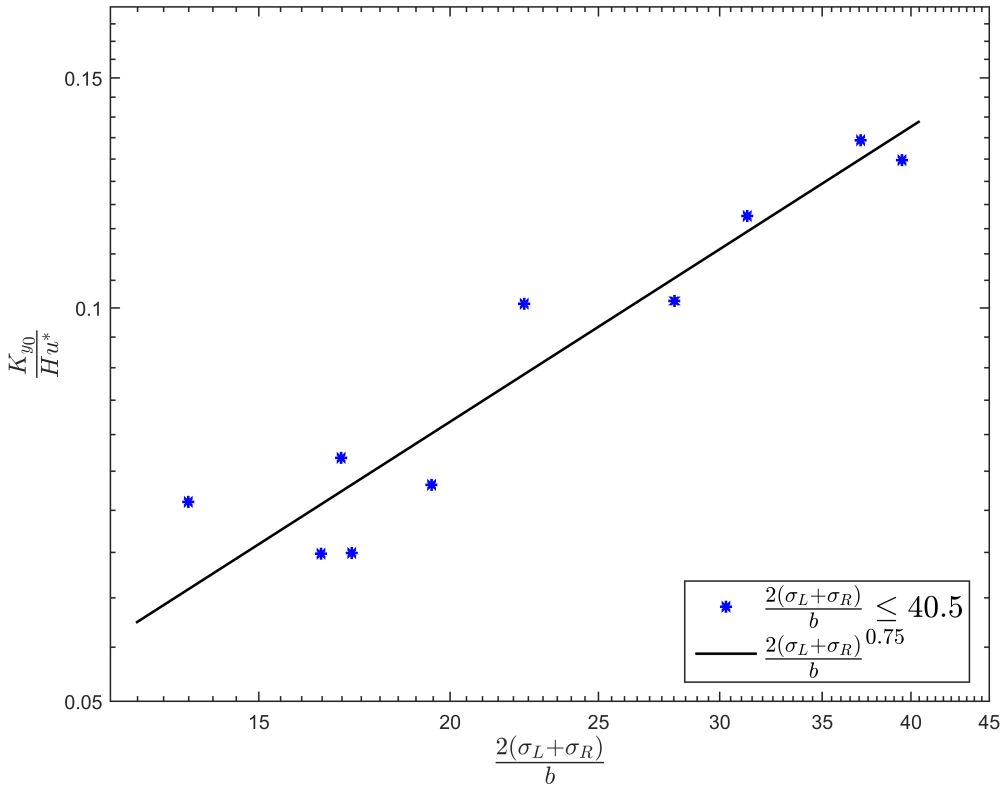

Figure 3.51: Eddy diffusion coefficient $\left(\frac{K_{y_0}}{Hu^*}\right)$ in the direction perpendicular to the local plume centerline (i.e., along axisy_0) as a function of the plume width $\left(\frac{2(\sigma_L+\sigma_R)}{b}\right)$. Only the values for which the plume width is less than the size of the largest vortices.

As the best fit line in Figure 3.51 shows, the eddy-diffusion coefficient for our meandering plume scales with the plume width to the 3/4 $\left(\frac{2(\sigma_L+\sigma_R)}{b}^{3/4}\right)$. This is obviously inconsistent with the Richardson [1926] 4/3-law. One possible cause for this is, as discussed in Okubo [1968] and Liao and Cowen [2010], 4/3-law is predicated on the assumption that the tracer patch exists in the inertial subrange, i.e., $\eta \ll L \ll l$ (where η is the Kolmogorov microscale, L is the characteristic tracer patch size, and l is the integral length scale - see Section 3.3.1). A requirement for the existence of the inertial subrange is that the Reynolds number is extremely high Pope [2000]. Thus one might expect the inertial subrange to be quite obvious in an oceanic turbulent

boundary layer, with higher velocities and much larger length scales. However, it is unlikely that a significant inertial subrange exists in the meandering plume flow. As a result, the eddy-dfiffusion coefficient for our meandering plume flow is a weaker function of the plume width.

3.6 Conclusions

The goal of this study was to examine the mixing of tracer in a meandering plume by phase-locking the plume to separate the fluctuations due to the plume meander from the turbulent velocity and concentration fluctuations. Simultaneous LIF and PIV/PTV experiments were performed on the meandering plume at four phases in the motion of the meander-forcing diverting plate to quantify the concentration and velocity fields; LIF was performed on a straight plume for comparison with the meandering plume structure.

Analysis of the concentration fields allows us to conclude that the phase-averaged concentration profiles for the meandering plume are piecewise Gaussian in shape, however the profiles of the standard deviation of the concentration fluctuations are not (see Section 3.5.3). This contrasts with the concentration structure of straight plumes in this and other studies [Crimaldi et al., 2002, Crimaldi and Koseff, 2006, Rahman and Webster, 2005], in which the mean concentration profiles are Gaussian in a complete (not piecewise) sense, as are the profiles of the standard deviation of the concentration fluctuations. Further, we showed that the plume centerline (maximum) concentration decreases more rapidly with distance downstream for the meandering plume than the straight plume (see Figure 3.20 in Section 3.5.3). The width of the meandering plume also grows more rapidly with distance downstream (x^1) than the width of the straight plume ($x^{0.75}$). Therefore the meandering plume exhibits more rapid dilution of tracer than the straight plume.

Closer examination of the meandering plume velocity (and vorticity) fields highlights the importance of the large-scale alternating vortices shed from the diverting plate. We showed that these structures are the dominant features of the flow and effectively govern the concentration field, the turbulence, and the turbulent flux of tracer in the meandering plume. The large-scale alternating vortices sweep free-stream fluid into the plume, forcing the plume to meander. This forced injection of free-stream fluid contributes to the increased dilution of tracer in the meandering plume compared to the straight plume. The vortices also cause local decelerations in the downstream direction velocity on the plume centerline, which leads to localized "backing-up" of tracer filaments immediately upstream of the point where the two counter-rotating vortices meet. This congregation of tracer filaments leads to local peaks in the phase-averaged concentration along plume centerline.

The large-scale alternating vortices are likewise strongly related to the spatial distributions of TKE and Reynolds stress ($\overline{u'v'}$) in the meandering plume. The largest magnitudes of TKE and $\overline{u'v'}$ appear immediately downstream of the large scale-alternating vortices, effectively co-located with the sweeping of free-stream fluid into the plume (and the correspondingly high shear). These results agree well with other studies examining turbulence due to periodic vortices being shed in the wake of bluff bodies [Huang et al., 1995, Lyn et al., 1995, Nakagawa et al., 1999, Saha et al., 2000, Kim et al., 2006]. The turbulent flux of tracer is also related to the large-scale alternating vortices. The largest magnitude of $\overline{u'c'}$ is located immediately downstream of the large-scale alternating vortices, similar to the distribution of $\overline{u'v'}$. The magnitude of $\overline{v'c'}$ is greatest to either side of the plume centerline and equal to zero on the plume centerline. Local minimum magnitudes in $\overline{v'c'}$ are also observed in the center of the large scale alternating vortices.

Combining our measurements of the mean concentration profiles and turbulent flux terms, we successfully modeled the turbulent flux of tracer in our meandering

plume using the eddy-diffusivity hypothesis (see Section 3.5.8). Unsurprisingly, the size of the plume relative to the largest eddies (which in this case are of similar size to the large-scale alternating vortices induced by the diverting plate) dictates the behavior of the eddy-diffusion coefficient. When the plume width is larger than the size of the largest eddies, the eddy-diffusion coefficient is a constant, given by $K_{y_0} = 0.15Hu^*$ (recall H is the water depth and u^* is the shear velocity). This agrees well with the other studies' estimates of the eddy-diffusion coefficient in open channel flows [Fischer et al., 1979, Webel and Schatzmann, 1984]. When the plume width is smaller than the size of the largest eddies, the eddy-diffusion coefficient scales as the plume width to the 3/4, which is substantially less than the 4/3-law of Richardson [1926]. A key assumption behind the 4/3-law is that the tracer patch size must be in the inertial subrange [Liao and Cowen, 2010], which is not present in our flume (an inertial subrange requires a very high Reynolds number, and a large difference between the largest length scales and the smallest length scales in the flow). Thus, the eddy-diffusion coefficient for our meandering plume flow is a weaker function of the plume width.

These results shed light on the structure of a meandering plume and provide guidance for field studies on larger scale meandering plumes. In particular the finding of a non-symmetric concentration profile is of significance to models of atmospheric meandering plume (in which it is often assumed symmetric). Furthermore, the results are applicable to studies of plumes in the wake of bluff bodies. Finally, this will shed light on the notion of a "flavored eddy" in the wake downstream of biotic structures (e.g. oyster reefs in saltmarshes) in Atema [1996]. We observe local peaks in the concentration structure associated with the presence of the periodic vortices from the diverting plate (as do Balu et al. [2001] and von Carmer et al. [2009]). However, we have no evidence that suggests the instantaneous turbulent vortices are similarly linked to peaks in concentration.

CHAPTER IV

ASSESSMENT OF SINGLE-INSTRUMENT TECHNIQUES FOR REMOVING WAVE BIAS FROM REYNOLDS STRESS ESTIMATES

4.1 Abstract

A new single-instrument method for removing wave bias from Reynolds stress estimates is proposed in the study presented in this chapter. Assuming that the wave motions and the pressure are perfectly coherent, the method uses a linear filter to estimate the wave velocity at the instrument based on the pressure measurement, and then differences the estimated velocity to arrive at an ideally wave-free estimate of the Reynolds stress. This method is compared to two frequency-domain-based single-instrument techniques and a two-instrument method that uses the wave velocity at an adjacent instrument in the linear filter to estimate and remove the wave velocity. No single-instrument technique offers clearly superior performance over the other two in deeper water. The method proposed in this study does offer superior performance over the other single-instrument techniques in shallow water, comparing favorably with the two-instrument method. The advantage of the proposed single-instrument technique is that it limits the financial and logistical issues associated with deploying a second instrument.

4.2 Introduction

High precision estimates of quantities such as the Reynolds stress and Turbulent Kinetic Energy (TKE) are necessary to corroborate hypothesis regarding the hydrodynamics of turbulent boundary layers and wakes [Shaw and Trowbridge, 2001].

They are also critical for to validating current and sediment flux models - which rely heavily on assumptions of the dynamics of boundary layers, in tidally-driven estuary flows [Zheng et al., 2003]. Instruments such as Acoustic Doppler Velocimeters (ADV's) allow for direct point estimates of the Reynolds stresses and TKE. However, as discussed in Shaw and Trowbridge [2001] such measurements are frequently contaminated by energetic surface waves or internal waves, which may contain several orders of magnitude more energy than the turbulent velocity fluctuations in the coastal ocean environment [Grant et al., 1984, Grant and Madsen, 1986, Huntley and Hazen, 1988, Trowbridge, 1998, Shaw and Trowbridge, 2001, Kirincich and Rosman, 2011]. Of special concern is the potential for misalignment of the instrument coordinate axis with the true coordinate axis, which causes significant wave bias terms to influence Reynolds stress estimates [Trowbridge, 1998].

Several techniques have been proposed to alleviate the wave contamination. Among the most accepted are the family of two-instrument techniques following the velocity differencing methodology of Trowbridge [1998]. In brief, Trowbridge [1998] proposes subtracting the velocity at a nearby instrument (instrument 2) from the velocity at the instrument of interest (instrument 1), reasoning that the wave velocities at the two instruments are equal and thus will cancel upon differencing. Shaw and Trowbridge [2001] extended this work by proposing a linear filtering scheme to alter one of the two velocity components in the covariance to correct for variations in the velocity between the two nearby instruments. The linear filter is intended to predict the wave velocity at the instrument 1 given the velocity at the instrument 2 and then the predicted velocity is subtracted from the instrument 1 velocity. Feddersen and Williams [2007] apply the linear filter to both velocity components in the covariance, and present a technique for assessing the effectiveness of each method in removing the wave bias (the Ogive curve test). While these two-instrument techniques have proven effective in the offshore [Shaw and Trowbridge, 2001] and nearshore [Feddersen and

Williams, 2007] regions, it is desirable from a financial and logistical standpoint to make use of a single-instrument technique. Single-instrument techniques have been proposed that rely on frequency domain analysis to separate the wave signal from the turbulence [Bricker and Monismith, 2007, Wilson et al., 2013], but suffer in effectiveness if the wave motions occupy the same frequency range as the turbulent fluctuations contributing to the Reynolds stress [Trowbridge, 1998]. Unfortunately, this is a common occurrence in the field.

The aforementioned wave bias removal techniques are generally tested for fairly energetic surface wave conditions, e.g., surface wave rms velocity of $0.12\,m/s$ in Shaw and Trowbridge (2001) and significant wave height $H_s = 1\,m$ in Feddersen and Williams (2007). While these waves are easily large enough to overwhelm the true Reynolds stress terms, the waves need not be so large to result in significant errors. For synthetic test data, a two degree instrument coordinate axis tilt and the presence of a wave field with significant wave height $H_s = 6\,cm$ can result in a $1\,cm^2s^{-2}$ error in the estimated $\overline{u'w'}$ Reynolds stress if unaccounted for (assuming the waves are propagating in the x-direction). Given that observed Reynolds stresses near the bed in coastal and estuarine environments are typically on the order of $1.0 - 2.0\,cm^2s^{-2}$ [Shaw and Trowbridge, 2001, Bricker and Monismith, 2007, Feddersen and Williams, 2007, Wilson et al., 2013], this represents a significant error. In sheltered estuarine channels the significant wave height may be on the order of centimeters, but must nonetheless be accounted for. The resulting signal of the waves may be difficult to detect and remove.

This study proposes a single-instrument technique that makes use of the linear filtration scheme of Shaw and Trowbridge [2001] and Feddersen and Williams [2007]. However, rather than using the velocity at an adjacent instrument to predict the wave velocity at the instrument of interest, the pressure signal at the same instrument is used, under the assumption that it is coherent with the wave velocity. The proposed

technique removes the issue of separating the wave and turbulence components in the frequency domain that is typical of single-instrument approaches . The performance of the proposed method is compared to two existing frequency-based single-instrument techniques [Bricker and Monismith, 2007, Wilson et al., 2013], as well as the Feddersen and Williams [2007] two-instrument extraction technique for a series of synthetic data sets, seventeen deployments at four sites in comparatively shallow estuarine channels near Wassaw Sound in Savannah, Georgia, and two days of continuous monitoring at a single site in the deeper water of Monterey Bay, California.

4.3 Background

In the event that waves, current, and turbulence are all present in a flow, the instantaneous horizontal velocity (u) can be decomposed as:

$$u = \bar{u} + \tilde{u} + u' \tag{4.1}$$

where $\bar{u}$, $\tilde{u}$, and u' are the mean, wave, and turbulent velocity components, respectively. As in Feddersen and Williams [2007] it is assumed that the flow is statistically stationary over the sampling period, and that the wave and turbulent velocity fluctuations are uncorrelated (e.g. $\overline{\tilde{u}u'} = 0$).

In a simple exercise, Shaw and Trowbridge [2001] and Feddersen and Williams [2007] showed that in the event of sensor rotation by angle θ, the horizontal and vertical velocities with the mean removed (U and W) are estimated at the sensor (to first order in θ) by $U = \tilde{u} + u' + \theta\,(\tilde{w} + w')$ and $W = \tilde{w} + w' + \theta\,(\tilde{u} + u')$, respectively. Further, straightforward evaluation of the covariance of these terms (e.g. $\overline{UW}$) results in wave bias terms $\overline{\tilde{u}\tilde{w}}$, $\overline{\theta\tilde{u}^2}$, and $\overline{\theta\tilde{w}^2}$ that become larger than the desired Reynolds stress ($\overline{u'w'}$) with increasing θ [Feddersen and Williams, 2007]. Since it is effectively impossible to deploy instruments in the field such that θ is zero, Reynolds stress measurements are always contaminated by the presence of waves. A variety of

techniques have been proposed to reduce the wave bias terms. This study presents a new single-instrument method and compares it to two existing single-instrument techniques [Bricker and Monismith, 2007, Wilson et al., 2013] as well as the most recent of the two-instrument velocity differencing methods, Feddersen and Williams [2007].

4.3.1 Feddersen and Williams (2007) Two-Instrument Method

The Feddersen and Williams [2007] wave bias removal method (FW07) is an extension of the earlier Shaw and Trowbridge [2001] method. The basic principle is to place an additional instrument (instrument 2) adjacent to the instrument at the location of interest (instrument 1), then use the linear filtration method of Shaw and Trowbridge [2001] to predict the wave velocity at instrument 1 from instrument 2. This predicted velocity is then subtracted from the velocity at instrument 1 to reduce the effects of wave bias. The separation distance is chosen such that it is larger than the "correlation scale" of the turbulence, yet much smaller than the wavelength of the contaminating waves (assumed to be equal to the correlation scale of the waves - Shaw and Trowbridge [2001]). In Shaw and Trowbridge [2001], Feddersen and Williams [2007], and the Monterey Bay field data in this study the sensors are separated vertically. In contrast, in the Wassaw Sound field data in this study and Trowbridge and Elgar [2001] (employing the earlier Trowbridge [1998] wave bias removal method), the sensors are separated horizontally. Note the Shaw and Trowbridge [2001] linear filtration scheme is not limited to vertically separated sensors [Shaw and Trowbridge, 2001].

If the wave motions between instruments 1 and 2 are perfectly coherent, the estimated x-direction wave velocity at instrument 1 ($\hat{U_1}$) is assumed to be related to the de-meaned x-direction velocity at instrument 2 (U_2) by the following expression [Feddersen and Williams, 2007]:

$$\hat{U}_1(t) = \int_{-\frac{T}{2}}^{\frac{T}{2}} h(t-\tau) U_2(t) d\tau \tag{4.2}$$

where $h(t)$ are the estimated filter weights describing the relationship between the wave velocities between the two sensors and T is the convolution time of the filter (assumed to be equal to the peak wave period). As discussed in Shaw and Trowbridge [2001], this estimate of the wave velocity ($\hat{U}_1$) will contain a turbulence component, but it will not affect the final solution if, as assumed, the turbulence at instruments 1 and 2 are spatially incoherent.

The vector of filter weights ($\mathbf{h}$) is given as the least squares solution of a transversal filter model [Haykin, 1996, Shaw and Trowbridge, 2001]:

$$\mathbf{h} = \left(\mathbf{A}^\top \mathbf{A}\right)^{-1} \mathbf{A}^\top \mathbf{U}_1 \tag{4.3}$$

where $\mathbf{U}_1$ is a vector of demeaned x-direction velocity at instrument 1 and $\mathbf{A}$ is an $M \times 3N$ matrix of all three components of the velocity at instrument 2. M is the total number of data points in the sampling period and N is the number of data points in the convolution time (T) to the nearest odd number. The m^{th} row of matrix $\mathbf{A}$ is:

$$\begin{aligned}
&\left[U_2\left(m - \frac{N-1}{2}\right), ..., U_2\left(m\right), ..., U_2\left(m + \frac{N-1}{2}\right),\right. \\
&V_2\left(m - \frac{N-1}{2}\right), ..., V_2\left(m\right), ..., V_2\left(m + \frac{N-1}{2}\right), \\
&\left.W_2\left(m - \frac{N-1}{2}\right), ..., W_2\left(m\right), ..., W_2\left(m + \frac{N-1}{2}\right)\right]
\end{aligned} \tag{4.4}$$

where $U_2(m)$, $V_2(m)$, and $W_2(m)$ are the components of de-meaned velocity vector $\mathbf{U}_2$ at data point m. The estimate of the x-direction wave velocity at instrument 1 ($\hat{\mathbf{U}}_1$) is then found by convoluting matrix $\mathbf{A}$ with the vector of filter weights ($\mathbf{h}$):

$$\hat{\mathbf{U}}_1 = \mathbf{A}\mathbf{h} \tag{4.5}$$

The x-direction wave velocity estimated from the linear filter is subtracted from the actual velocity at instrument 1 to yield a differenced velocity that is ideally wave free (i.e., $\Delta\hat{U}_1 = U_1 - \hat{U}_1$). In the Shaw and Trowbridge [2001] method, one of the velocity terms in the covariance is replaced with the differenced velocity to estimate the Reynolds stress at instrument 1 (e.g. $\overline{u_1'w_1'} \approx \overline{\Delta\hat{U}_1 W_1}$, where W_1 is the z-direction wave velocity at instrument 1). Note that Shaw and Trowbridge [2001] recommend differencing the horizontal velocity as opposed to the z-direction velocity (i.e., $\Delta\hat{W}_1$), but both formulations are presented. FW07 involves repeating the velocity differencing procedure (i.e., Equations 4.2 - 4.5) for the second component, and using both differenced velocity terms in the covariance to estimate the Reynolds stress (e.g., $\overline{u_1'w_1'} \approx \overline{\Delta\hat{U}_1\Delta\hat{W}_1}$).

4.3.2 Young and Webster Single-Instrument Method

The steps in the Young and Webster wave bias removal method (YW) are similar to FW07. The key difference is that pressure signal at the same instrument is used to estimate the wave velocity at the instrument of interest, rather than the velocity at an adjacent instrument (thus subscripts denoting the instrument are dropped). We note here that the velocity and pressure sensor are physically offset for many instruments, but that we expect this offset to be much smaller than the wavelength of the waves (and much smaller than the physical seperation between the two instruments in the two-instrument methods). The assumption is that the wave motions and the pressure signal are perfectly coherent at the instrument, thus the estimated x-direction wave velocity ($\hat{U}$) is related to the de-meaned pressure signal ($\hat{P}$, where $\hat{P} = P - \overline{P}$) by:

$$\hat{U}(t) = \int_{-\frac{T}{2}}^{\frac{T}{2}} h(t-\tau)\hat{P}(t)d\tau \tag{4.6}$$

As before, $h(t)$ are the estimated filter weights and T is the convolution time of the filter. The vector of filter weights ($\mathbf{h}$) are likewise given by $\mathbf{h} = \left(\mathbf{A}^\top\mathbf{A}\right)^{-1}\mathbf{A}^\top\mathbf{U}$,

where $\mathbf{A}$ is an $M \times N$ matrix containing de-meaned pressure data ($\hat{P}$). M and N are the total number of data points and the number of filter weights, respectively. Therefore, the m^{th} row of matrix $\mathbf{A}$ is:

$$\left[\hat{P}\left(m - \frac{N-1}{2}\right), ..., \hat{P}\left(m\right), ..., \hat{P}\left(m + \frac{N-1}{2}\right)\right] \tag{4.7}$$

The estimate of x-direction wave velocity ($\hat{\mathbf{U}}$) is again found by convoluting matrix $\mathbf{A}$ with the vector of filter weights ($\mathbf{h}$), i.e., $\hat{\mathbf{U}} = \mathbf{Ah}$. The estimate is subtracted from the actual velocity at the instrument to yield a differenced velocity ($\Delta\hat{U} = U - \hat{U}$) that is ideally wave free. As in FW07, these steps are repeated for the second velocity component in the covariance and both differenced velocities are used to estimate the Reynolds stress (e.g., $\overline{u'w'} \approx \overline{\Delta\hat{U}\Delta\hat{W}}$).

4.3.3 Bricker and Monismith (2007) Single-Instrument Method

The Bricker and Monismith [2007] wave bias removal method (BM07) is a single-instrument frequency-based technique. The goal is to identify a localized spike in the power spectral density function (PSD) of the de-meaned velocity signal (S_{UU}), which is presumably due to the contaminating waves. The wave component of the PSD ($S_{\tilde{u}\tilde{u}}$) is isolated and used to calculate the wave contribution to the covariance (e.g. $\overline{\tilde{u}\tilde{w}}$). This is subtracted from the total covariance ($\overline{UW}$) to yield the Reynolds stress ($\overline{u'w'}$).

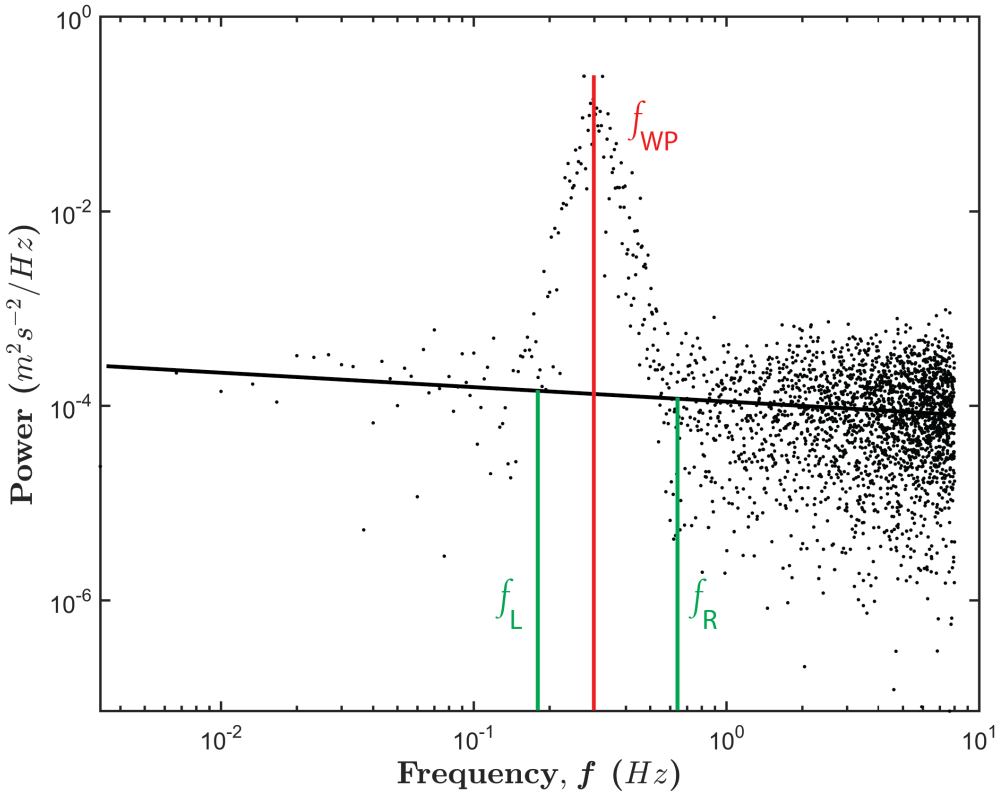

Figure 4.1: PSD of the de-meaned x-direction velocity (S_{UU}) for a synthetic dataset. The black dots are the PSD and the black line is a best fit to the PSD outside the wave peak. The peak frequency within the wave peak f_{WP} is shown and labeled in red. The left f_L and right f_R frequency bounds of the wave peak are shown and labeled in green.

An outline of the BM07 steps for computing $\overline{u'w'}$ proceeds as follows. As shown in Figure 4.1, the PSD of the de-meaned x-direction velocity (S_{UU}) is examined with the intent of identifying the range of frequencies contaminated by wave energy. The frequency of the wave peak f_{WP} is the frequency above $0.1\,Hz$ with the largest value of the PSD. This frequency is straightforward to identify for both field and synthetic datasets so long as the waves are sufficiently large. The same cannot be said for the left (f_L) and right (f_R) frequency bounds of the wave peak, which are dataset specific

[Bricker and Monismith, 2007, Wilson et al., 2013]. For the data presented in this study and in Wilson et al. [2013] the left frequency bound (f_L) of the wave peak was specified as 70% of the peak frequency (f_{WP}) and the right frequency bound (f_R) as $f_{WP} + 0.5\,Hz$. A straight line is fit to the data points outside the wave peak range via a least-squares regression. All points at lower frequencies than f_L are included in the fit, and half that number of points at higher frequencies than f_R are included. This is an attempt to avoid aliasing the wave energy to higher frequencies, which may occur if the waves advect higher frequency turbulent eddies past the sensor [Lumley and Terray, 1983, Gross et al., 1994, Bricker and Monismith, 2007].

The wave contribution to the PSD is assumed to be all of the energy, in the identified wave peak range, between the best fit line and the PSD. All the energy below the best fit line (as well as all the energy outside the identified wave peak range) is assumed to be due to the turbulence. Thus, the PSD of the x-direction wave velocity ($S_{\tilde{u}\tilde{u}}$) is equal to the PSD of the de-meaned velocity signal (S_{UU}), in the frequency domain bounded by f_L and f_R, minus the linear fit in the same frequency domain. $S_{\tilde{u}\tilde{u}}$ is used to compute the magnitude of the wave velocity fluctuations ($|\tilde{u}_j|$) at discrete frequencies f_j by the following expression [Bricker and Monismith, 2007]:

$$S_{\tilde{u}\tilde{u}}(f_j) = \frac{1}{df}|\tilde{u_j}|^2 \tag{4.8}$$

Note that the index j only refers to the frequencies in the range between f_L and f_R, as opposed to the entire spectrum. The phase of $|\tilde{u}_j|$ is assumed equal to that of the de-meaned x-direction velocity (U) and is obtained by computing the discrete Fourier transform of the de-meaned x-direction velocity (U_j). The phase of U_j ($\angle U_j$) is given by $\angle U_j = arctan\left[\frac{Im(U_j)}{Re(U_j)}\right]$, where $Im(U_j)$ and $Re(U_j)$ are the imaginary and real components of U_j, respectively.

This process is repeated for the second component in the covariance (e.g., W, the de-meaned z-direction velocity) such that the wave component of the covariance ($\overline{\tilde{u}\tilde{w}}$)

can be directly estimated from the following expression:

$$\overline{\tilde{u}\tilde{w}} = \sum_j |\tilde{u}_j||\tilde{w}_j| cos\left(\angle W_j - \angle U_j\right) \tag{4.9}$$

where j remains the indices of the discrete frequencies between f_L and f_R. The Reynolds stress ($\overline{u'w'}$) is then recovered by subtracting the wave component of the covariance ($\overline{\tilde{u}\tilde{w}}$) from the covariance of the de-meaned velocities ($\overline{UW}$), e.g., $\overline{u'w'} = \overline{UW} - \overline{\tilde{u}\tilde{w}}$, under the assumption that the wave and turbulent velocity fluctuations are uncorrelated.

4.3.4 Wilson et al. (2013) Single-Instrument Method

The Wilson et al. [2013] wave bias removal method (WWW13) is a frequency-based technique that uses the coherence between the pressure and the velocity signals to identify and remove the contribution wave contribution to the covariance. The assumption is that the coherence between the pressure and the velocity is entirely due to the wave influence, and the PSDs of the de-meaned velocities are adjusted accordingly. The Reynold stress is computed from the modified PSD in the same manner as the wave contribution to the de-meaned velocity covariance is reconstructed in BM07.

For example, to obtain $\overline{u'w'}$, the coherence function, $\gamma^2(f_j)$, for the de-meaned x-direction velocity (U) and the de-meaned pressure (P) is given at discrete frequency f_j as:

$$\gamma^2(f_j) = \frac{S_{UP}(f_j)S^*_{UP}(f_j)}{S_{UU}(f_j)S_{PP}(f_j)} \tag{4.10}$$

where S_{UP} is the cross spectral density (CSD) of U and P, S^*_{UP} is the complex conjugate of S_{UP}, and S_{UU} and S_{PP} are the PSDs of U and P, respectively. It is important to note that in WWW13, the index j refers to all frequencies in the spectra (unlike BM07, in which it was restricted to the frequencies in the identified

wave peak). If the coherence between the pressure and the velocity is entirely due to the waves, then the PSD of the x-direction turbulent velocity fluctuations, $S_{u'u'}$, can be estimated by:

$$S_{u'u'}(f_j) = \left[1 - \gamma^2(f_j)\right] S_{UU}(f_j) \tag{4.11}$$

The magnitude of the turbulent velocity fluctuations ($|u'_j|$) at f_j are determined by $S_{u'u'}(f_j) = \frac{1}{df}|u'_j|^2$. As in BM07, the phase is assumed to be equal to the phase of the de-meaned x-direction velocity (U) . The phase is likewise given by $\angle U_j = arctan\left[\frac{Im(U_j)}{Re(U_j)}\right]$, where U_j is the discrete Fourier transform of U, and $Im(U_j)$ and $Re(U_j)$ are the imaginary and real components of U_j, respectively. These steps are repeated for the vertical velocity (W) and the Reynolds stress ($\overline{u'w'}$) is directly estimated by $\overline{u'w'} = \sum_j |u'_j||w'_j| cos\left(\angle W_j - \angle U_j\right)$.

4.3.5 The Feddersen and Williams (2007) Ogive Curve Test

The accuracy of the estimates of Reynolds stresses for field datasets are not directly verifiable. However, the estimates can be accepted or rejected based on the characteristics of the Reynolds stress Ogive curves. The Ogive curve of $\overline{u'w'}$ ($Og_{\overline{u'w'}}$) is the moniker given to the non-dimensional integrated co-spectra of $\overline{u'w'}$, which is computed from the following expression [Feddersen and Williams, 2007]:

$$Og_{\overline{u'w'}}(f) = \frac{\int Co_{\overline{u'w'}}(\hat{f})d\hat{f}}{\overline{u'w'}} \tag{4.12}$$

where f is frequency and $Co_{\overline{u'w'}}$ is the cospectrum of $\overline{u'w'}$. The Ogive curve of $\overline{v'w'}$ ($Og_{\overline{v'w'}}$) is formulated in a similar fashion. Therefore, the Ogive curves are plots of the cumulative energy at all frequencies less than or equal to f, normalized by the total energy. The Ogive curves are plotted as a function of non-dimensional wavenumber $\left(\frac{2\pi f z}{V}\right)$, where V is the steady free stream velocity in the turbulent boundary layer. The free stream velocity is not steady in turbulent boundary layers

contaminated by waves (due to the orbital wave motions), thus Shaw and Trowbridge [2001] and Feddersen and Williams [2007] replace the free stream velocity with the mean alongshore current ($\overline{u}$) in the non-dimensional wavenumber $\left(\frac{2\pi fz}{\overline{u}}\right)$. Kaimal et al. [1972] and later Soulsby [1977] found that eddies with non-dimensional wavenumber in the range $10^{-1} < \left(\frac{2\pi fz}{V}\right) < 10^{1}$ contributed most of the energy to the Reynolds stress. Thus, this is the range of focus in the Feddersen and Williams [2007] Ogive curve test.

For synthetic data, the Ogive curves of the Reynolds stress estimates from the four methods can be directly compared to the true Ogive curve. For field data, Feddersen and Williams [2007] recommend qualitatively comparing the estimated Ogive curves to Ogive curves from atmospheric turbulent boundary layer measurements in Kaimal et al. [1972]. The curves cannot be quantitatively compared to the Kaimal et al. [1972] curves due to the inexactness of replacing the (ideal and unphysical) steady free stream velocity (V) with the mean alongshore current ($\overline{u}$) in the formulation of the non-dimensional wavenumber. Therefore, Feddersen and Williams [2007] propose explicitly rejecting Reynolds stress estimates if the Ogive curve ever falls outside the range of $-0.5 < Og < 1.6$ on the non-dimensional wavenumber interval $10^{-1} < \left(\frac{2\pi fz}{\overline{u}}\right) < 10^{1}$ (i.e., the non-dimensional frequency range that forms the bulk of the contribution to the Reynolds stresses), although the cutoff is selected based on admittedly heuristic analysis.

4.4 Methods

As described in Section 4.3.5, one of the challenges in assessing the effectiveness of wave bias removal techniques is the inability to compare the estimated Reynolds stress against the ground truth for a field dataset. Studies that suggest new methods compare the results from the presented method against the results from previous methods [Shaw and Trowbridge, 2001, Feddersen and Williams, 2007, Bricker and

Monismith, 2007, Wilson et al., 2013]. The Feddersen and Williams [2007] Ogive curve test is a major step forward in this regard, but does not directly assess the accuracy of the Reynolds stress estimate. Therefore, we perform the four wave bias removal techniques described in Section 2 on a series of synthetic data, as well as a series of field data collected in Wassaw Sound near Savannah, GA and in Monterey Bay, CA. The synthetic data allows direct assessment of the accuracy of the Reynolds stress estimates from the four wave bias removal techniques. It also allows comparisons of the estimated Ogive curves under idealized conditions, before comparing the techniques for field data.

4.4.1 Synthetic Signal Generation

The synthetic data are intended to represent hypothetical data as similar to our Wassaw Sound field data as possible. Thus, the current, wind, wave, and turbulence characteristics are estimated from the Wassaw Sound datasets. The water depth was $3\,m$, corresponding to the maximum tidal range during spring tide in the vicinity of Wassaw Sound [Gross and Werner, 1997]. The instrument measurement volume was $10\,cm$ above the bed as in the Wassaw Sound field measurements. The two instruments (for FW07) were separated in the x-direction (the mean current direction) by $1\,m$, mirroring the field data collection. Seventy (70) individual bursts were specified for each of four wave angles relative to the current (x) direction (10°, 33°, 56° and 80°). The range of mean currents in the synthetic bursts spanned $-1.5 \times U_{max}$ to $1.5 \times U_{max}$, where $U_{max} = 20\,\frac{cm}{s}$, similar to the maximum current observed in the Wassaw Sound field data. This value of U_{max} was also similar to that observed in Seim et al. [2002] and Feddersen and Williams [2007]. The sign convention for the current was such that waves propagate with positive mean current and against negative mean current.

The hypothetical Reynolds stress tensor was specified for the scenario of maximum

observed current, $U_{max} = 20\,\frac{cm}{s}$, and scaled up or down linearly based on the ratio of the mean current selected for the individual burst (U) to U_{max}. The value of $\overline{u'w'}$ in the hypothetical Reynolds stress tensor was equal to the value observed in the Wilson et al. [2013] dataset at U_{max} (similar values of $\overline{u'w'}$ were observed in Feddersen and Williams [2007]. The sign of $\overline{u'w'}$ was specified to be opposite the sign of the mean velocity for the burst. The value of $\overline{v'w'}$ was assumed to be half of $\overline{u'w'}$ (because $\overline{v'w'}$ was not reported in Wilson et al. [2013]), which is similar to the ratios of $\overline{v'w'}$ to $\overline{u'w'}$ observed in Feddersen and Williams [2007]. The value of $\overline{u'v'}$ was assumed to be equal to zero as in an idealized flat plate turbulent boundary layer [Pope, 2000].

The diagonals of the hypothetical Reynolds stress tensor were specified from the TKE observed in the Wilson et al. [2013] dataset at $U_{max} = 20\,\frac{cm}{s}$. The individual components were set equal to a fraction of $\overline{u'^2}$ based on the plots of normalized Reynolds stress components as a function of boundary layer thickness (δ) in Pope [2000]. The plot was generated based on DNS results in Spalart [1988] and the relative height within the boundary layer was assumed to be $\frac{z}{\delta} = 0.25$. The TKE was set equal to a function of $\overline{u'^2}$ with the other two components ($\overline{v'^2}$ and $\overline{w'^2}$) subbed in as functions of $\overline{u'^2}$. The resulting expression was solved for $\overline{u'^2}$, then $\overline{v'^2}$ and $\overline{w'^2}$ were determined by their respective fractions of $\overline{u'^2}$.

The specified Reynolds stress tensor for mean current velocity $U = U_{max}$ was therefore:

$$Re = \begin{bmatrix} 10 & 0 & -2 \\ 0 & 6.4 & 1 \\ -2 & 1 & 3.4 \end{bmatrix} \times 10^{-4}\, m^2 s^{-2} \tag{4.13}$$

The turbulence component was generated in Matlab (Mathworks, Natick, Massachusetts, USA) using a multivariate normal random number generator (mvnrnd), with zero mean and covariance matrix equal to the scaled Reynolds stress tensor.

The wave component was generated based on a modified TMA spectrum outlined in Young [1999]. The TMA spectrum was proposed in Bouws et al. [1985, 1987] as a shallow water ocean wave spectrum and the naming convention is the first letter of the three datasets used for field verification (Texel, MARSEN, ARSLOE). The TMA spectrum was modified by Young and Verhagen [1996] to describe fetch limited shallow water waves, analogous to those found in more sheltered estuarine channels. The spectral density (S) of the modified TMA spectrum is given by [Morang et al., 2002]:

$$S(f) = \frac{\alpha g^2 \Phi}{(2\pi)^4 f^5} exp\left[-\frac{5}{4}\left(\frac{f}{f_p}\right)^{-4}\right] \gamma^{exp\left[-\frac{\left(\frac{f}{f_p}-1\right)^2}{2\sigma^2}\right]} \tag{4.14}$$

where g is the acceleration due to gravity and f is frequency. f_p is the frequency of the spectral peak and is computed from $f_p = 3.5\left[\frac{g^2 F}{U_{10}^3}\right]^{-0.33}$, where F is the fetch length and U_{10} is the wind speed $10\,m$ above the sea surface. F is assumed to be $1000\,m$ (the approximate channel width in the vicinity of two of our four Wassaw Sound deployment sites) and U_{10} is assumed to be $4\,\frac{m}{s}$, corresponding to the peak sustained wind speed at the Skidaway Institute of Oceanography (Skidaway Island, Savannah, GA) weather station during the June 20^{th} 2010 deployments. The coefficients α, Φ and γ are determined from the following expressions [Kitaigordskii et al., 1975, Young and Verhagen, 1996]:

$$\alpha = 0.0091\kappa^{0.24} \tag{4.15}$$

$$\Phi \approx \begin{cases} \frac{1}{2}\omega^{*2} & \text{for } \omega^* \leq 1 \\ 1 - \frac{1}{2}\left(2-\omega^*\right)^2 & \text{for } \omega^* > 1 \end{cases} \tag{4.16}$$

$$\gamma = -5.8 log_{10}\left(D\right) + 1.1 \qquad \text{for } 0.05 \leq D < 1 \tag{4.17}$$

where κ is the non-dimensionalized peak wavenumber given by $\kappa = \frac{U_{10}^2 k_p}{g}$, k_p is the wavenumber at peak frequency f_p (determined from linear dispersion), ω^* is the non-dimensionalized angular frequency given by $\omega^* = \omega\sqrt{\frac{d}{g}}$ (ω is the angular frequency corresponding to f), and D is the non-dimensionalized water depth given by $D = \frac{gd}{U_{10}^2}$. The parameter σ equals 0.12 as suggested by Young and Verhagen [1996]. In the event that the waves are propagating against the current, each frequency in the spectrum is checked to determine if the waves at that frequency are able to propagate against the current. If not, the energy at that frequency is set to zero. Each frequency component is randomly assigned a phase, and the wave velocities are reconstructed given the wave angle and the amplitudes from the wave spectra using linear thoery and making no assumptions about the regimes of the waves. The wavenumbers for each frequency computed from linear waves dispersion including current effects.

Instrument noise is added as an additional component to the synthetic velocity signal using a normal random number generator in Matlab (normrnd). The expected uncertainty in the velocity components and the pressure for the Nortek Vector ADVs used in this study is 0.5% of the maximum observed value in the burst. To generate the noise signal, this value is assumed to be equal to twice the standard deviation used in the normal random number generator (the mean is zero). The mean current, wave, turbulence, and noise signals are added together to generate the synthetic time record. As with the Wassaw Sound field data, the synthetic bursts are five minutes of data at $16\,Hz$, corresponding to 4800 data points. The resulting three-dimensional velocities are rotated 2° about the x and y axes to simulate tilt between the true coordinate axis and the instrument coordinate axis (which introduces wave bias in $\overline{VW}$ and $\overline{UW}$, respectively). An example of a synthetic burst is shown in Figure 4.2. Note that the wave characteristics (e.g. $H_s = 11.6\,cm$ and $T_m = 3.0\,sec$) are comparable to those of the largest waves we observe in the Wassaw Sound dataset.

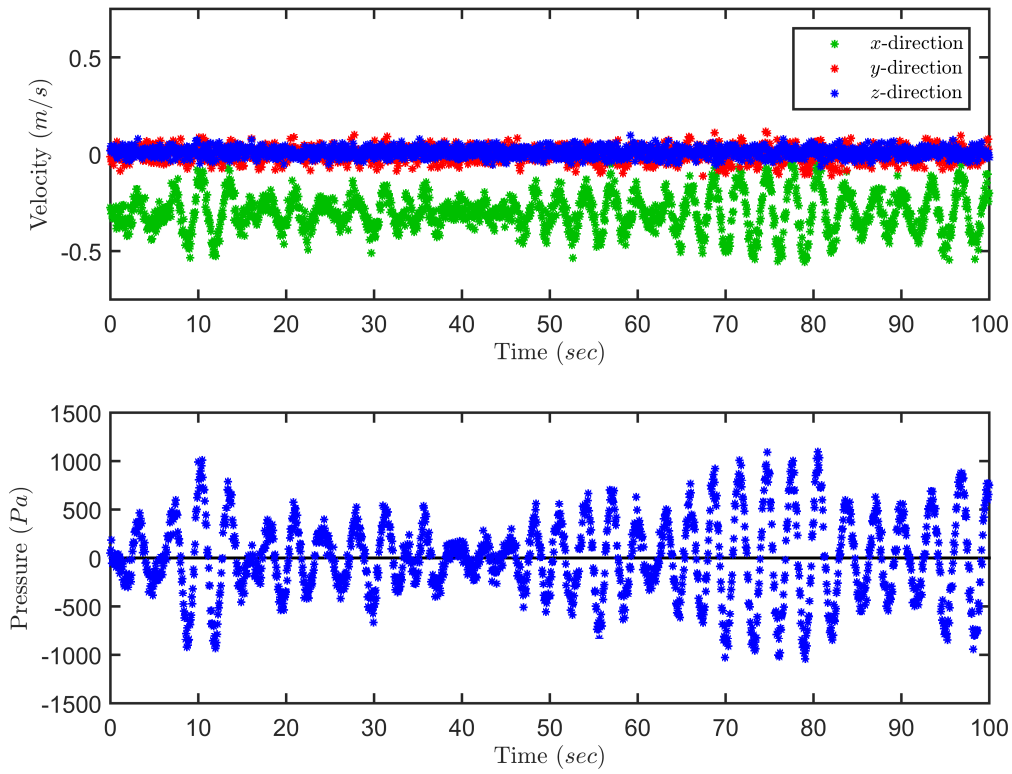

Figure 4.2: Plot of the three velocity components and the de-meaned pressure for the first 100 seconds of a synthetic burst. The current velocity is $-30\,\frac{cm}{s}$, the wave angle is 10° relative to the current (x) direction, the significant wave height $H_s = 11.6\,cm$, the mean wave period $T_m = 3.0\,sec$, $\sigma_u = 8.9\,\frac{cm}{s}$, $\sigma_v = 3.4\,\frac{cm}{s}$, and $\sigma_w = 2.3\,\frac{cm}{s}$.

4.4.2 Wassaw Sound Data Collection and Filtering

The Wassaw Sound data are a subset of the field data presented in Wilson et al. [2013]. Two Acoustic Doppler Velocimeters (ADV's, Nortek Vector - Nortek AS, Rud, Norway) spaced apart in the alongshore (initial x-axis) direction were placed at four different sites in the vicinity of Wassaw Sound (Savannah, GA, USA) during June 2010 - August 2010, for a total of seventeen datasets (see Table 4.1). One of the sites is a narrow sheltered estuarine channel (Skidaway Narrows) exposed to a very small fetch (the channel width is approximately $165\,m$). Two more of the sites

are to either side of the Wilmington river (Priests Landing and Across from Priests Landing) and are exposed to a larger fetch than Skidaway Narrows (the channel width is approximately $1000\,m$), but substantially smaller than that expected of coastal or ocean waves. The last site (Dead Man's Hammock) is exposed to the full fetch of Wassaw Sound (approximately $4000\,m$). The instruments were placed during low tide, thus the water depths encompassed in the data range from the minimum instrument submersion depth ($\sim 30\,cm$) to the maximum inundation during spring tide ($\sim 3\,m$). The flow measurements were made $10\,cm$ above the bed. The locations of the four instrument deployment sites (Priests Landing -PL, Across from Priests Landing - APL, Dead Man's Hammock - DMH, and Skidaway Narrows SN) are shown in Figure 4.3. Data were collected during spring and mean tide at all four deployment locations, and during neap tide at the APL and PL sites.

Figure 4.3: Map (courtesy of Google Maps) of the four instrument deployment sites (shown as red and black squares): Across from Priests Landing (APL), Priests Landing (PL), Dead Man's Hammock (DMH), and Skidaway Narrows (SN). A map of the southeastern United States marking the location of Wassaw Sound is shown in the bottom left of the figure (courtesy of Google Earth).

Table 4.1: Description of the Wassaw Sound data, including the location, the total number of bursts remaining after pre-filtering, the largest significant wave height (H_s) observed in the dataset, and the mean wave period (T_m) of the burst with the largest significant wave height. Data name convention is the abbreviated instrument deployment location, the abbreviated tidal type, and the launch date in parenthesis.

Data Name	**Location**	**# Bursts post Pre-Filt.**	**Peak** H_s (cm)	T_m (sec)
APL M (07/26/2010)	Across from Priests Landing	149	4.9	3.1
APL NP (08/17/2010)	Across from Priests Landing	145	6.3	3.6
APL SP (07/17/2010)	Across from Priests Landing	138	7.0	3.9
DMH M (06/18/2010)	Dead Man's Hammock	104	11.4	3.5
DMH SP (08/09/2010)	Dead Man's Hammock	144	17.6	3.8
PL M (06/18/2010)	Priests Landing	141	4.1	3.8
PL M (06/20/2010)	Priests Landing	127	4.1	3.7
PL M (06/22/2010)	Priests Landing	113	3.7	3.0
PL M (07/21/2010)	Priests Landing	457	12.9	3.0
PL NP (07/29/2010)	Priests Landing	150	7.3	3.5
PL SP (06/11/2010)	Priests Landing	146	6.5	4.1

Continued on next page

Table 4.1 – continued from previous page				
Data Name	**Location**	**# Bursts post Pre-Filt.**	**Peak** H_s (cm)	T_m (sec)
PL SP (06/13/2010)	Priests Landing	144	7.5	4.0
PL SP (06/15/2010)	Priests Landing	120	2.7	3.6
PL SP (07/14/2010)	Priests Landing	136	5.9	4.1
PL SP (07/16/2010)	Priests Landing	138	5.9	4.1
SN M (07/20/2010)	Skidaway Narrows	142	1.7	3.5
SN SP (07/14/2010)	Skidaway Narrows	126	1.4	4.1

The ADV's measured the three velocity vector components, pressure, beam correlation coefficients, and other parameters at $16\,Hz$. Data were collected in 15 minute intervals, 5 minutes of continuous sampling followed by 10 minutes of non-sampling. The ADV data was pre-filtered prior to the application of the wave bias removal techniques. Following the recommendation of Chanson et al. [2008], bursts for which the average correlation coefficient of the three beams was less than 70% were discarded, as well as any bursts for which the average correlation coefficient was less than 70% for 500 consecutive samples. The bursts discarded due to these restrictions typically coincided with probe exposure during low tide. The data in the remaining bursts were filtered using the phase filtering method of Goring and Nikora [2002]. This method identifies and removes erroneous spikes in the data due to aliasing of the Doppler signal. Prior to spike detection, the horizontal velocities are rotated to maximize the mean x-direction velocity. The spikes are then identified as points that exceed the universal threshold. The identified spikes are removed and replaced by a synthetic

data point generated from a third order polynomial fit to the 24 surrounding data points (12 to each side). The horizontal velocities are again rotated to maximize the mean x-direction velocity once the spikes have been identified and removed.

4.4.3 Monterey Bay Data Collection and Filtering

While the Wassaw Sound data provides an excellent test of the four methods in shallow estuarine conditions, we also desired to compare the methods in deeper waters with larger waves, like those in Monterey Bay, CA. The Monterey Bay field data were graciously provided to us by Brock Woodson from his collaboration with Stephen Monismith. More specific details on the Monterey Bay field data collection can be found in the resulting paper, Walter et al. [2014]. The authors placed a tripod just off the coast of Hopkins Marine Station (HMS - Stanford University) in the southern tip of Monterey Bay, CA (MB). The mean water depth at the site was approximately $15\,m$. The precise tripod location is shown in Figure 4.4. Affixed to the tripod were six Nortek ADV's located 0.3, 1, 2, 4, 6, and $8\,m$ above the bed. The ADV's were offset from the tower $1\,m$ with horizontal arms. Each ADV was deployed and synchronized with a fast-response thermistor (Precision Measurement Engineering, Inc. model FP07) and a ceramic plate conductivity sensor. The ADV's and the temperature and conductivity sensors sampled continuously at $64\,Hz$ for thirty days. The ADV's measured the three velocity vector components, pressure, beam correlation coefficients, as well as other parameters, and the temperature and conductivity probes allow for concurrent estimates of the water density at the instrument. Only two days of data from the instruments located at 1 and $2\,m$ above the bed are considered in this study (see Table 4.2).

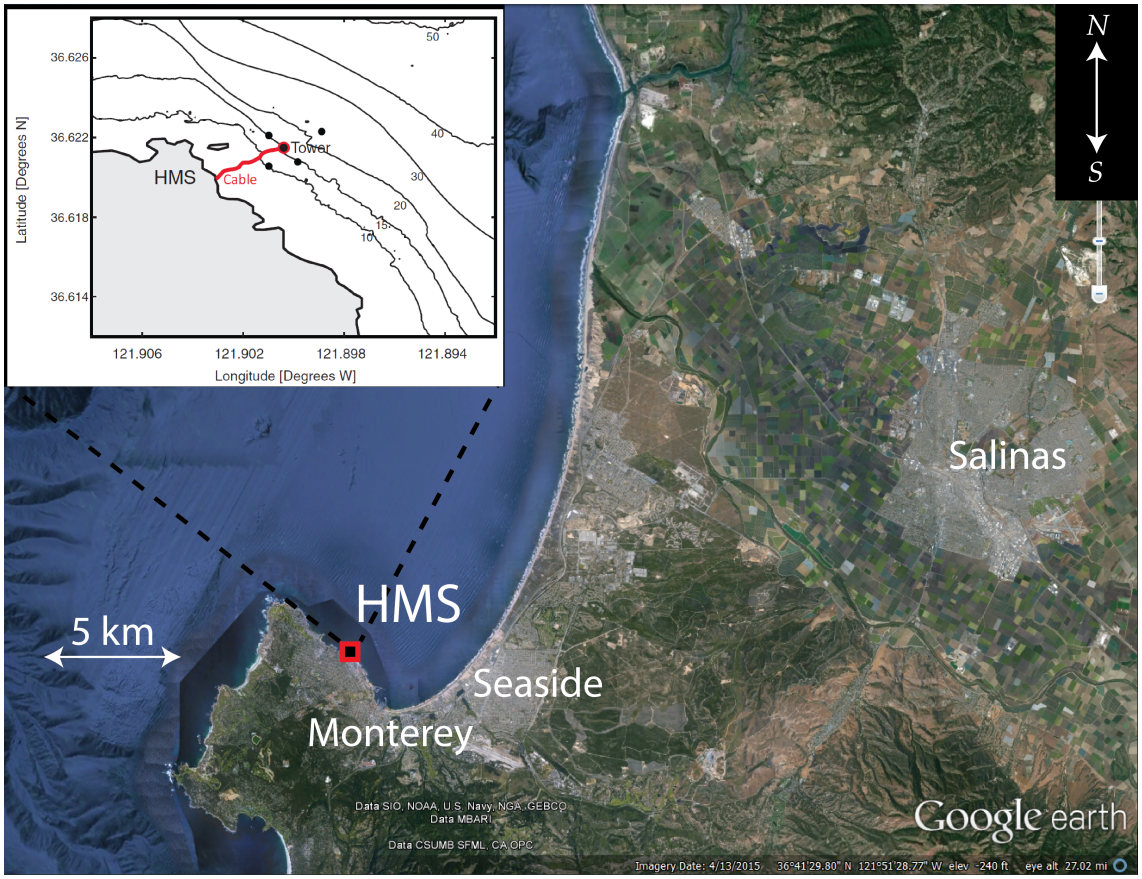

Figure 4.4: Map (courtesy of Google Earth) of Monterey Bay and Hopkins Marine Station (HMS). The inset Figure in the upper left hand corner is the location of the tripod relative to HMS. Image partially reproduced from Walter et al. [2014].

Table 4.2: Description of the Monterey Bay data, including the location, the total number of bursts remaining after pre-filtering, the largest significant wave height (H_s) observed in the dataset, and the mean wave period (T_m) of the burst with the largest significant wave height. Data name convention is the abbreviated instrument deployment location and the date of data collection in parenthesis.

Data Name	**Location**	**# Bursts post Pre-Filt.**	**Peak** H_s (cm)	T_m (sec)
MB (04/22/2013)	Monterey Bay	188	35.3	7.2
MB (05/04/2013)	Monterey Bay	203	22.6	7.3

The continuous datasets were divided into five-minute bursts ($19,200$ data points) to better compare the results to those from the Wassaw Sound data. As with the Wassaw Sound data, ADV data were pre-filtered by removing bursts for which the average correlation coefficient of the three beams was less than 70% and bursts for which the average correlation coefficient was less than 70% for 2000 consecutive samples. The data in the remaining bursts were also filtered using the phase filtering method of Goring and Nikora [2002].

4.5 Results and Discussion

4.5.1 Synthetic Data

The purpose of the synthetic data is to allow each of the estimated Reynolds stresses ($\overline{u'w'}$ and $\overline{v'w'}$) and the TKE for the four methods discussed to be directly compared to the "correct" values, rather than to each other. Furthermore, the Ogive curves of $\overline{u'w'}$ and $\overline{v'w'}$ can be directly compared to the "true" Ogive curves for the given dataset. The implication is that any of the methods that struggle under the pristine synthetic data conditions are likely to experience similar or greater issues for

the field data.

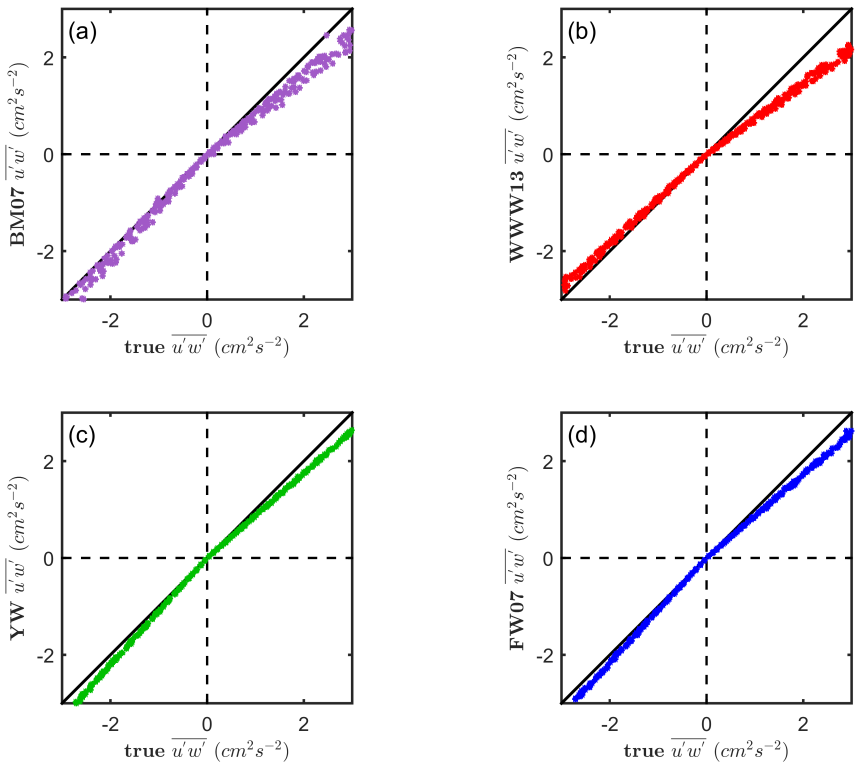

Figure 4.5: Comparison of $\overline{u'w'}$ values for the four wave bias removal techniques vs. the true values for the synthetic bursts, (a) BM07, (b) WWW13, (c) YW, and (d) FW07. As a reference, the line indicates a perfect match.

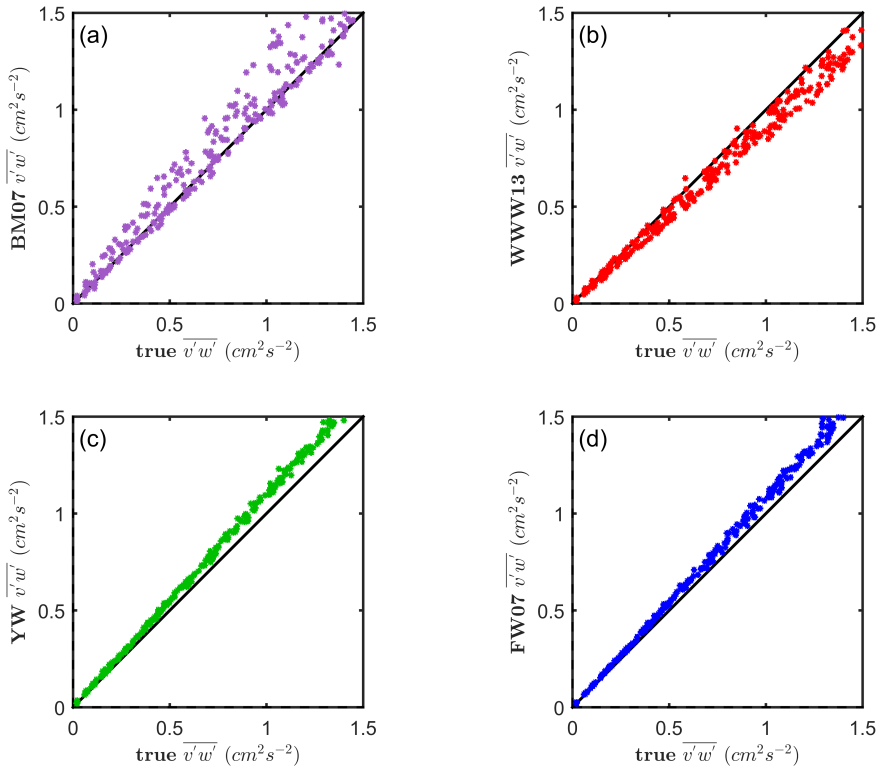

Figure 4.6: Comparison of $\overline{v'w'}$ values for the four wave bias removal techniques vs. the true values for the synthetic bursts, (a) BM07, (b) WWW13, (c) YW, and (d) FW07. As a reference, the line indicates a perfect match.

As shown in Figure 4.5, BM07 significantly under-predicts $\overline{u'w'}$ when the waves oppose the current direction (negative $\overline{u}$ and thus positive $\overline{u'w'}$), and slightly over-predicts $\overline{u'w'}$ when the waves and the current are in the same direction (positive $\overline{u}$ and thus negative $\overline{u'w'}$). This is quantified by the slopes of the best fit lines (0.813 for positive $\overline{u'w'}$ and 1.066 for negative $\overline{u'w'}$) in Table 4.3. The estimates are also substantially more scattered than those of the other three methods, as shown by the standard error of the linear fits (Table 4.3), which are nearly an order of magnitude larger than the standard error of the YW and FW07 estimates. WWW13 under-predicts the true $\overline{u'w'}$ for both cases, significantly for waves opposing the current

(slope of 0.728), and slightly for waves with the current (0.921). The estimates display less scatter than BM07 (Table 4.3), yet still more than YW or FW07. YW and FW07 are virtually indistinguishable. Both methods under-predict $\overline{u'w'}$ for waves opposing the current (slope of 0.875 and 0.861 for YW and FW07, respectively), although to a lesser extent than BM07, and to a substantially lesser extent than WWW13. The two methods both over-predict $\overline{u'w'}$ for waves with the current to a slightly greater extent than BM07 (1.102 and 1.081 for YW and FW07, respectively), but display substantially less scatter than either BM07 or WWW13 (Table 4.3).

Figure 4.5 reveals that $\overline{v'w'}$ is consistently over-predicted for BM07, YW, and FW07 (slopes of 1.064, 1.096, and 1.079, respectively). Of the three, BM07 over-predicts to a lesser extent but with substantially more scatter (Table 4.3). WWW13 consistently under-predicts $\overline{v'w'}$ (slope of 0.915), and the scatter of the estimates is greater than YW or the FW07, yet less than BM07 (Table 4.3).

Table 4.3: Comparison of the four wave bias removal techniques for the synthetic data. The first two rows are the number of bursts which failed the Feddersen and Williams [2007] Ogive curve test for $\overline{u'w'}$ and $\overline{v'w'}$, respectively. The next two rows are the mean squared error of the $\overline{u'w'}$ and $\overline{v'w'}$ Ogive curves to the "true" Ogive curves, averaged over all bursts which passed the Feddersen and Williams [2007] Ogive curve test. The last three rows indicate the slopes of the best fit lines (forced through the origin) to plots of the "true" $\overline{u'w'}$, $\overline{v'w'}$, and TKE on the x-axis and the wave bias method estimate on the y-axis. The standard error of the linear fits appears in parenthesis below the slope.

Parameter	**BM07**	**WWW13**	**YW**	**FW07**
Number of Bursts Failed $Og_{\overline{u'w'}}$ Test	6	0	0	0
Continued on next page				

Table 4.3 – continued from previous page				
Parameter	**BM07**	**WWW13**	**YW**	**FW07**
Number of Bursts Failed $Og_{\overline{v'w'}}$ Test	4	0	0	0
MSE $Og_{\overline{u'w'}}$	3.33×10^{-2}	2.10×10^{-3}	1.60×10^{-4}	0.67×10^{-4}
MSE $Og_{\overline{v'w'}}$	7.52×10^{-2}	2.20×10^{-3}	2.93×10^{-4}	1.40×10^{-4}
Slope of $+\overline{u'w'}$ best fit line (standard error)	0.813 (4.9×10^{-3})	0.728 (2.8×10^{-3})	0.875 (0.8×10^{-3})	0.861 (0.9×10^{-3})
Slope of $-\overline{u'w'}$ best fit line (standard error)	1.066 (5.2×10^{-3})	0.921 (2.3×10^{-3})	1.102 (0.9×10^{-3})	1.081 (1.0×10^{-3})
Slope of $\overline{v'w'}$ best fit line (standard error)	1.064 (6.4×10^{-3})	0.915 (2.7×10^{-3})	1.096 (0.9×10^{-3})	1.079 (1.0×10^{-3})
Slope of TKE best fit line (standard error)	0.986 (1.7×10^{-3})	0.877 (0.9×10^{-3})	1.007 (0.6×10^{-3})	1.026 (0.4×10^{-3})

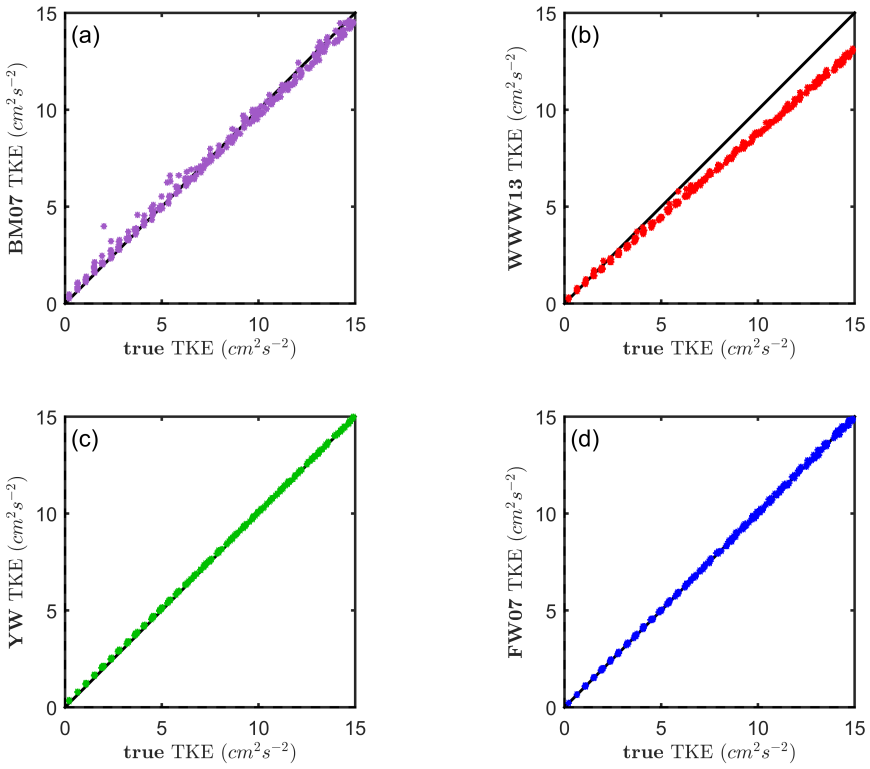

Figure 4.7: Comparison of TKE values for the four wave bias removal techniques vs. the true values for the synthetic bursts. (a) BM07, (b) WWW13, (c) YW, and (d) FW07. As a reference, the line indicates a perfect match.

As shown in Figure 4.7, YW and FW07 show excellent agreement with the true value of the TKE (slopes of 1.007 and 1.026, respectively). BM07 slightly under-predicts the TKE (slope of 0.986). However, the BM07 estimates again display substantial scatter, whereas the YW and FW07 estimates are far less variable (Table 4.3). WWW13 consistently under-predicts the TKE (slope of 0.877), yet does so with less scatter than BM07 (Table 4.3).

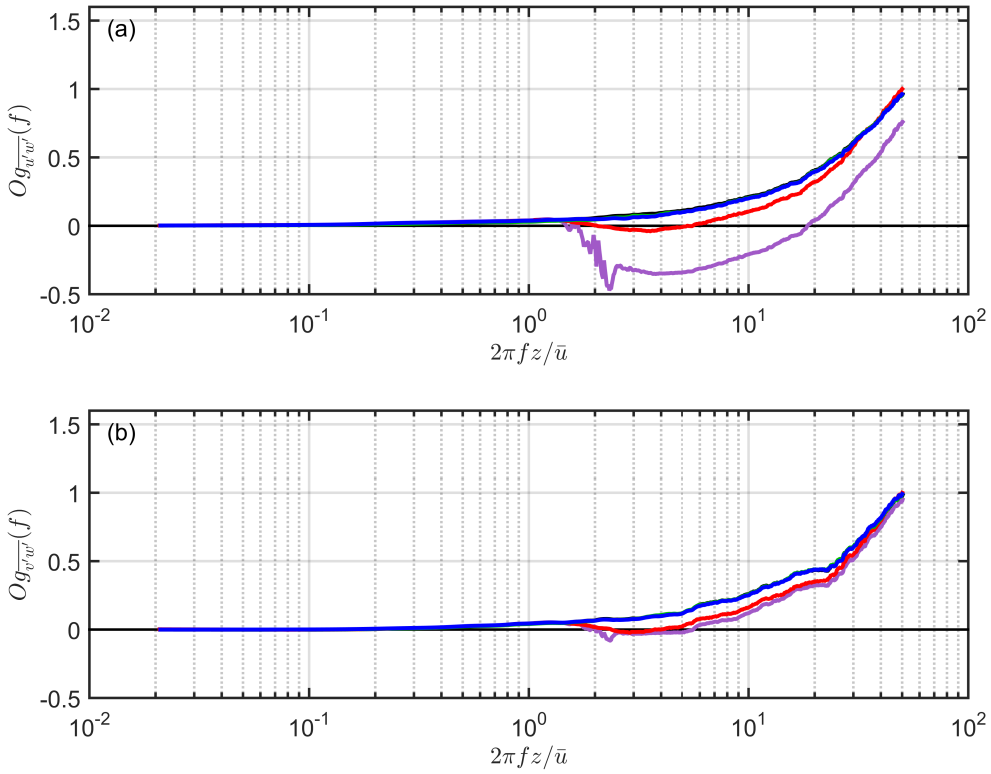

Figure 4.8: Ogive curves of (a) $\overline{u'w'}$ and (b) $\overline{v'w'}$ for a synthetic burst. The current velocity is $-10\,\frac{cm}{s}$, the wave angle is 10° relative to the current (x) direction, the significant wave height $H_s = 11.6\,cm$, the mean wave period $T_m = 3.0\,sec$, $\sigma_u = 9.2\,\frac{cm}{s}$, $\sigma_v = 2.4\,\frac{cm}{s}$, $\sigma_w = 1.4\,\frac{cm}{s}$, and the "true" $\overline{u'w'}$ and $\overline{v'w'}$ Reynolds stresses are $1.0\,cm^2s^{-2}$ and $0.5\,cm^2s^{-2}$, respectively. Four methods are shown: BM07 (purple), WWW13 (red), YW (green), and FW07 (blue). The "true" Ogive curve and the YW Ogive curve are obscured by near-perfect overlap with the FW07 Ogive curve

The Ogive curves for $\overline{u'w'}$ and $\overline{v'w'}$ for the four wave bias removal methods are compared against the true Ogive curve in Figure 4.8. YW and FW07 show near-perfect agreement with the "true" Ogive curves for the synthetic dataset (note that the curves are obscured by overlap). This is corroborated by Table 4.3, as the mean squared errors of the YW and FW07 Ogive curves are an order of magnitude smaller

than the MSE for the WWW13 Ogive curves, and two orders of magnitude smaller than the MSE for the BM07 Ogive curves. The WWW13 Ogive curves show some slight deviation from the true curves (Figure 4.8). The curves begin to slightly underestimate the true Ogive curves shortly after reaching the frequencies contaminated by the waves, and slowly approach the true Ogive curves for higher frequencies. This is quantified by the mean squared error of the WWW13 Ogive curves (Table 4.3). The BM07 method Ogive curves are the farthest from the true Ogive curves by a substantial margin. The BM07 $Og_{\overline{v'w'}}$ curve shown in Figure 4.8 follows the same behavior as the WWW13 curve, albeit slightly underestimating the true $Og_{\overline{v'w'}}$ to a greater extent than WWW13. However, BM07 is clearly not able to identify and remove the wave contribution in the x-direction (i.e., the primary wave propagation direction for this burst), as the BM07 $\overline{u'w'}$ Ogive curve in Figure 4.8 (a) exhibits drastic deviation from the other three methods and the true Ogive curve. The mean squared errors of the BM07 estimates (which passed the Feddersen and Williams [2007] Ogive curve test) are two orders of magnitude higher than the YW and FW07 estimates (Table 4.3.

The results from the synthetic data analysis are not surprising given the way each method attempts to separate the wave and the turbulence component of the velocity signal. BM07 seems to come closer to estimating the true $\overline{u'w'}$, $\overline{v'w'}$, and TKE than WWW13, more or less in line with the YW and FW07 estimates, but displays the most scatter of the four methods. This reflects the inexactness of identifying the bounds of the wave peak (an issue compounded in analysis of field data), as well as the fairly drastic alterations of the frequency characteristics of the velocity signals (i.e., identifying the PSD above the linear fit in the wave peak as the complete and self-contained wave PSD). This is revealed in the Ogive curves in Figure 4.8, as well as the mean squared error of the $\overline{u'w'}$ and $\overline{v'w'}$ Ogive curve fits in Table 4.3, in which BM07 was the clear outlier of the four methods. Despite the idealized nature of the

synthetic data, the BM07 Ogive curve for the burst in Figure 4.8 comes very close to being rejected under the Feddersen and Williams [2007] Ogive curve test criterion. In fact, BM07 yielded the only synthetic data Ogive curves that failed the Feddersen and Williams [2007] Ogive curve test (see Table 4.3). WWW13 alters the frequency characteristics of the signal less drastically than BM07 (i.e., scaling down the PSDs at each frequency based on the coherence, rather than entirely removing an isolated portion of the PSDs), thus the WWW13 Ogive curves come closer to the true curves. That said, WWW13 appears to constantly identify a portion of the turbulence energy as being due to wave influence, thus it consistently underestimates the true values of $\overline{u'w'}$, $\overline{v'w'}$, and TKE. YW and FW07 perform the best for the synthetic bursts, coming the closest to the true $\overline{u'w'}$, $\overline{v'w'}$, and TKE values with the least amount of scatter. Further, YW and FW07 do not directly alter the frequency characteristics of the velocity signal, thus, the YW and FW07 Ogive curves are nearly identical to the true curves (at least for the synthetic bursts).

4.5.2 Wassaw Sound Field Data

As discussed in Section 4.3.5, the accuracy of the Reynolds stresses and TKE estimates for the four methods are not directly verifiable. To circumvent this, the estimates can be accepted or rejected based on the characteristics of the Reynolds stress Ogive curves [Feddersen and Williams, 2007] as described in Section 4.3.5. Figure 4.9 shows plots of the Ogive curves for the four methods for a PL SP (07/14/2010) burst.

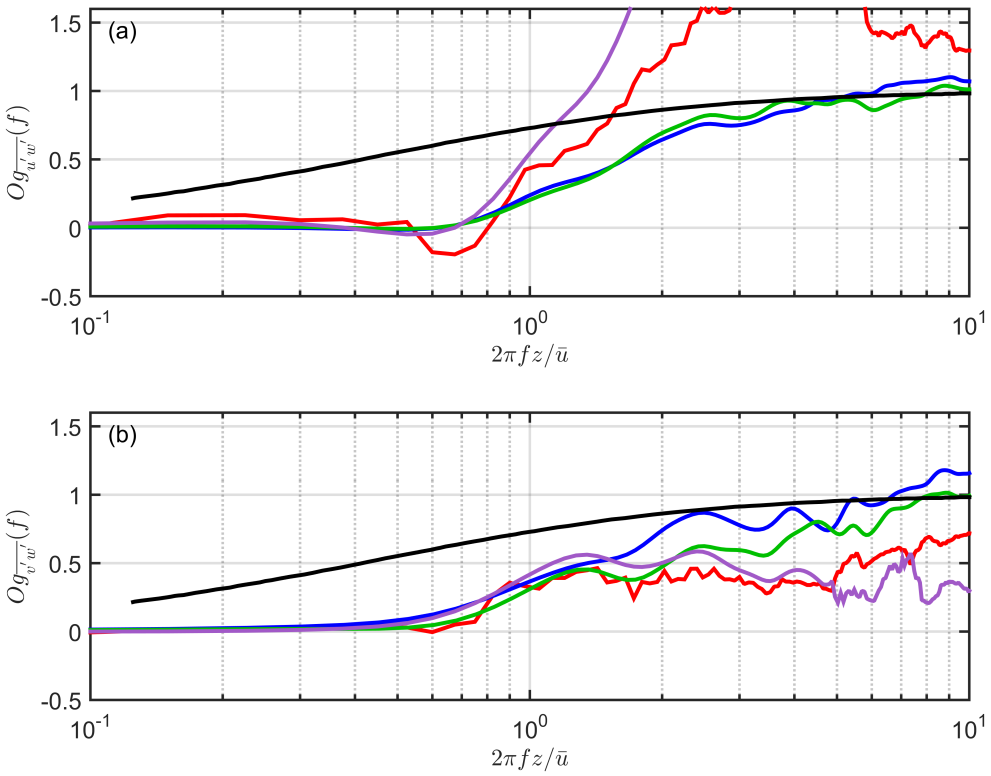

Figure 4.9: Ogive curves for (a) $\overline{u'w'}$ and (b) $\overline{v'w'}$ for a PL SP (07/14/2010) burst. The Kaimal et al. [1972] curve is shown in black and four methods are shown: BM07 (purple), WWW13 (red), YW (green), and FW07 (blue). For this burst, the mean velocity $\overline{u} = 2.8\ \frac{cm}{s}$, the significant wave height $H_s = 1.5\,cm$, the mean wave period $T_m = 0.75\,sec$, $\sigma_u = 0.9\ \frac{cm}{s}$, $\sigma_v = 1.2\ \frac{cm}{s}$, and $\sigma_w = 0.4\ \frac{cm}{s}$.

Under the Feddersen and Williams [2007] Ogive curve criterion (rejecting Reynolds stress estimates if the Ogive curve ever falls outside the range of $-0.5 < Og < 1.6$ in the non-dimensional wavenumber interval $10^{-1} < \frac{2\pi fz}{\overline{u}} < 10^{1}$), the WWW13 and BM07 $\overline{u'w'}$ estimates would be rejected for this burst, as the Ogive curves exceed 1.6. The $\overline{v'w'}$ estimates would not be rejected, although they do not match the Kaimal et al. [1972] curve as well as the YW and FW07 estimates. Table 4.4 shows the percent of all bursts that passed the $\overline{u'w'}$ and $\overline{v'w'}$ Ogive curve tests. For both the

$\overline{u'w'}$ and $\overline{v'w'}$ Ogive curve tests, FW07 passes the most bursts, followed in order by YW, WWW13, and BM07. The difference between the best-performing (FW07) and worst-performing (BM07) methods amounts to 3% of the total number of bursts (approximately 80 bursts).

Table 4.4: Comparison of the four wave bias removal techniques for the Wassaw Sound field data. The first two rows are the percent of all bursts that passed the $\overline{u'w'}$ and $\overline{v'w'}$ Ogive curve tests, respectively. The last three rows indicate the mean of the slopes of the best fit lines (forced through the origin) to plots of the FW07 estimated value on the x-axis and the selected single-instrument method value on the y-axis for $\overline{u'w'}$, $\overline{v'w'}$, and TKE for each burst. The mean of the standard errors of the linear fits appears in parenthesis below the slopes.

Parameter	**BM07**	**WWW13**	**YW**	**FW07**
Percent Passed $Og_{\overline{u'w'}}$ Test (%)	86.8	87.5	88.6	89.9
Percent Passed $Og_{\overline{v'w'}}$ Test (%)	66.1	68.2	68.4	69.3
Slope of $\overline{u'w'}$ best fit line (standard error)	0.824 (7.7×10^{-3})	0.863 (5.5×10^{-3})	1.026 (5.7×10^{-3})	N/A
Slope of $\overline{v'w'}$ best fit line (standard error)	0.876 (22.8×10^{-3})	0.842 (14.6×10^{-3})	0.976 (17.1×10^{-3})	N/A
Slope of TKE best fit line (standard error)	0.848 (6.1×10^{-3})	0.902 (2.8×10^{-3})	1.041 (2.5×10^{-3})	N/A

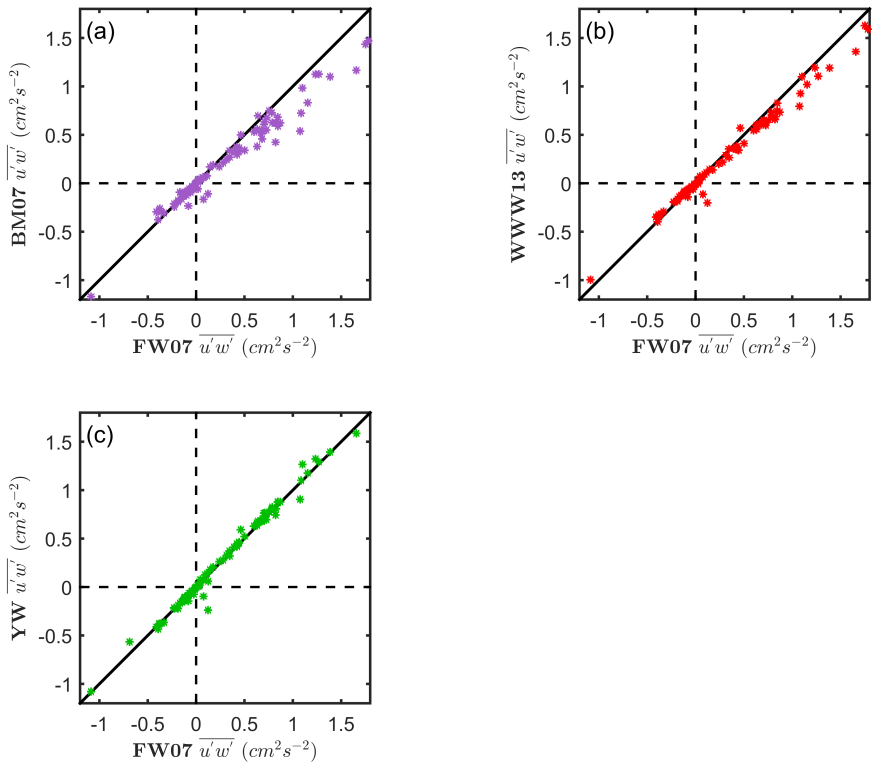

Figure 4.10: Comparison of $\overline{u'w'}$ values for the single-instrument techniques vs. FW07 for all bursts in which both methods passed the $\overline{u'w'}$ Ogive curve test for the PL SP (06/15/2010) dataset. (a) BM07, (b) WWW13 , and (c) YW. As a reference, the black line indicates a perfect match.

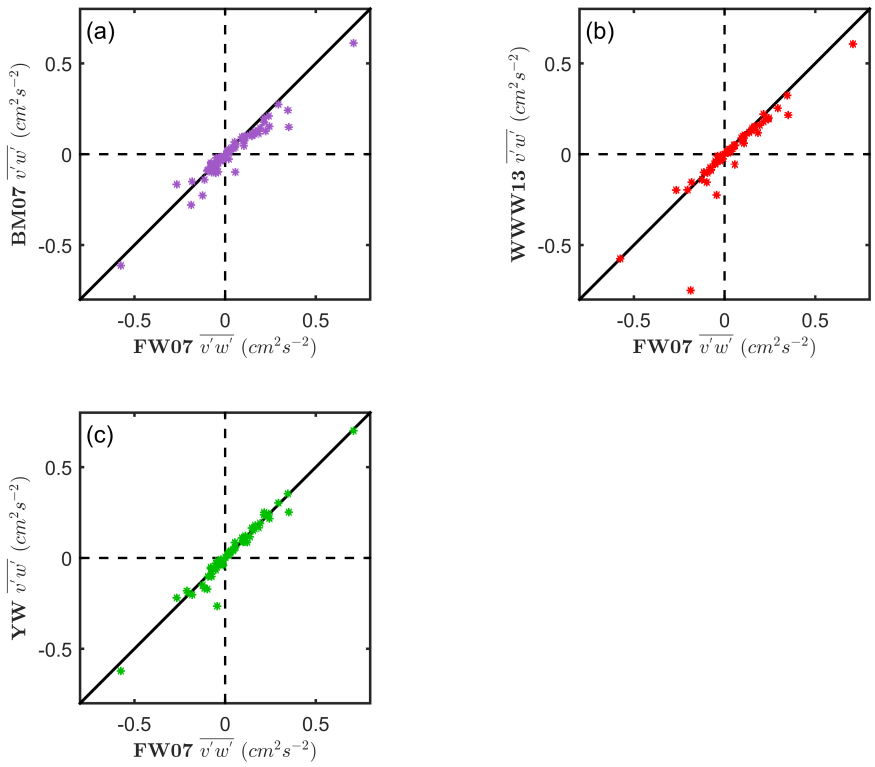

Figure 4.11: Comparison of $\overline{v'w'}$ values for the single-instrument techniques vs. FW07 for all bursts in which both methods passed the $\overline{v'w'}$ Ogive curve test for the PL SP (06/15/2010) dataset. (a) BM07, (b) WWW13 , and (c) YW. As a reference, the black line indicates a perfect match.

As discussed in Section 4.5.1, FW07 and YW performed the best of the four methods at estimating $\overline{u'w'}$, $\overline{v'w'}$, and TKE for the synthetic data. Thus, the established FW07 is chosen as the benchmark method in inter-method comparisons for the field data. Note that FW07 compares favorably with the Shaw and Trowbridge [2001] two-instrument method [Feddersen and Williams, 2007].

Figures 4.10 and 4.11 show the inter-method comparisons for the $\overline{u'w'}$ and $\overline{v'w'}$ estimates, respectively, for the PL SP (06/15/2010) bursts. BM07 predicts noticeably lower $\overline{u'w'}$ and $\overline{v'w'}$ values than FW07, with substantial scatter observed in both plots,

most visibly in the $\overline{u'w'}$ estimates. The WWW13 method predicts somewhat lower $\overline{u'w'}$ and slightly lower $\overline{v'w'}$ values than FW07, and appears to have less scatter than the BM07 estimates. The YW to FW07 comparisons nearly exactly match the 45° line for both $\overline{u'w'}$ and $\overline{v'w'}$, although some scatter is observed in both plots.

Conclusions drawn from the dataset shown in Figures 4.10 and 4.11 extend to all the data, as shown in Table 4.4. Of the three single-instrument methods, the YW $\overline{u'w'}$ and $\overline{v'w'}$ estimates come closer to replicating the estimates of FW07 (mean slopes of 1.026 and 0.976 for $\overline{u'w'}$ and $\overline{v'w'}$, respectively). The WWW13 estimates are next closest for $\overline{u'w'}$ and the BM07 estimates next closest for $\overline{v'w'}$, although the gap between these two methods is substantially smaller than the gap between them and the YW estimates (for both $\overline{u'w'}$ and $\overline{v'w'}$). Of the three single-instrument methods, WWW13 displays the least scatter between the best-fit line and the data for the $\overline{u'w'}$ and $\overline{v'w'}$ estimate comparisons, followed by YW, then BM07, as indicated by the standard errors of the best fit line (Table 4.4). The standard error is chosen in lieu of the mean squared error (as in Table 4.3) because no "true" estimate of $\overline{u'w'}$ and $\overline{v'w'}$ exist for the field data. The standard error therefore indicates how well one can predict the results of the FW07 method from the single-instrument method if the appropriate scaling factor is known (i.e,, the mean slope of the best fit line).

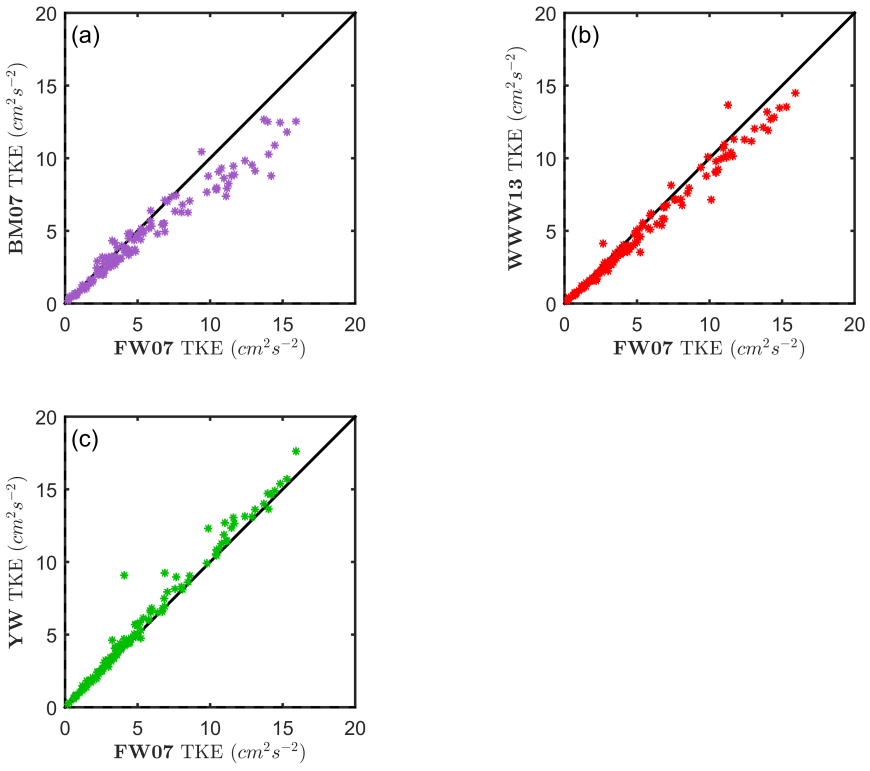

Figure 4.12: Comparison TKE values for the single-instrument techniques vs. FW07 for all bursts in which both methods passed the $\overline{u'w'}$ Ogive curve test for the APL SP (07/17/2010) dataset. (a) BM07, (b) WWW13, and (c) YW. As a reference, the black line indicates a perfect match.

Similar behavior is observed in the inter-method comparisons of the TKE estimates for the APL SP (07/17/2010) bursts shown in Figure 4.12. As with the BM07 $\overline{u'w'}$ and $\overline{v'w'}$ estimates, the BM07 TKE estimates are noticeably lower than the FW07 estimates. Likewise, the WWW13 TKE values are lower than the FW07 estimates, although to a lesser extent than the BM07 estimates. The YW TKE estimates again most closely align with FW07. These conclusions from Figure 4.12 are readily extended to the rest of the data, as shown in Table 4.4. The mean slope of the best-fit line between the YW and FW07 TKE estimates is 1.041, with a decline to

the WWW13 comparison (mean slope of 0.902) and another to the BM07 comparison (mean slope of 0.848). The mean standard error of the YW best fit lines is the least, followed by WWW13, and BM07 (Table 4.4).

In summary, YW best matches the Wassaw Sound field data results of FW07 of the three single-instrument wave bias removal techniques. The YW estimates of $\overline{u'w'}$, $\overline{v'w'}$, and TKE all compare quite favorably with those from FW07. Interestingly, the WWW13 estimates of $\overline{u'w'}$ and TKE are closer to the FW07 estimates than BM07, in contrast to the synthetic data results, which suggested that the BM07 estimates better matched the FW07 (and "true") estimates, albeit with more scatter. This could be a consequence of the difficulty identifying the wave peak in the BM07 method for the comparatively small waves in the Wassaw Sound field data, versus the relative ease of identification for the synthetic datasets. For such small waves it is possible that the peak in the PSD does not correspond to the wave contamination, thus BM07 removes energy that should properly be identified as turbulence induced. As with the synthetic bursts, WWW13 yields lower estimates of $\overline{u'w'}$, $\overline{v'w'}$, and TKE than FW07, consistently identifying a portion of the turbulence energy as wave energy. Of the three single-instrument wave bias removal techniques the YW method passes the most Ogive curve tests for both $\overline{u'w'}$ and $\overline{v'w'}$ (FW07 passes the most overall). That said, the difference between the best and worst performing methods (FW07 and BM07) is fairly slight, indicating that the large differences observed in the synthetic data Ogive curves for the BM07 estimate (and smaller differences for WWW13) did not manifest en masse as failed Ogive curve tests for the Wassaw Sound field data.

4.5.3 Monterey Bay Field Data

Table 4.5 shows the percent of all bursts that passed the $\overline{u'w'}$ and $\overline{v'w'}$ Ogive curve tests for the Monterey Bay data. For the $\overline{u'w'}$ Ogive curve tests, YW passes the most bursts, followed by FW07, BM07, and WWW13. For the $\overline{v'w'}$ Ogive curve

tests, YW passes the most bursts, followed by BM07, FW07, and WWW13. Despite the larger waves in Monterey Bay, the difference between the best-performing (YW) and worst-performing (WWW13) methods remains small, again roughly 3% of the total number of bursts for the $\overline{u'w'}$ estimates.

Table 4.5: Comparison of the four wave bias removal techniques for the Monterey Bay field data. The first two rows are the percent of all bursts that passed the $\overline{u'w'}$ and $\overline{v'w'}$ Ogive curve tests, respectively. The last three rows indicate the mean of the slopes of the best fit lines (forced through the origin) to plots of the FW07 estimated value on the x-axis and the selected single-instrument method value on the y-axis for $\overline{u'w'}$, $\overline{v'w'}$, TKE and for each burst. The mean of the standard errors of the linear fits appears in parenthesis below the slopes.

Parameter	**BM07**	**WWW13**	**YW**	**FW07**
Percent Passed $Og_{\overline{u'w'}}$ Test (%)	87.4	86.4	89.1	88.4
Percent Passed $Og_{\overline{v'w'}}$ Test (%)	95.7	95.0	96.3	95.1
Slope of $\overline{u'w'}$ best fit line (standard error)	1.032 (23.6×10^{-3})	0.872 (15.2×10^{-3})	0.977 (13.8×10^{-3})	N/A
Slope of $\overline{v'w'}$ best fit line (standard error)	1.347 (37.1×10^{-3})	1.114 (24.3×10^{-3})	1.152 (21.9×10^{-3})	N/A
Slope of TKE best fit line (standard error)	1.055 (7.4×10^{-3})	0.995 (5.9×10^{-3})	1.157 (6.9×10^{-3})	N/A

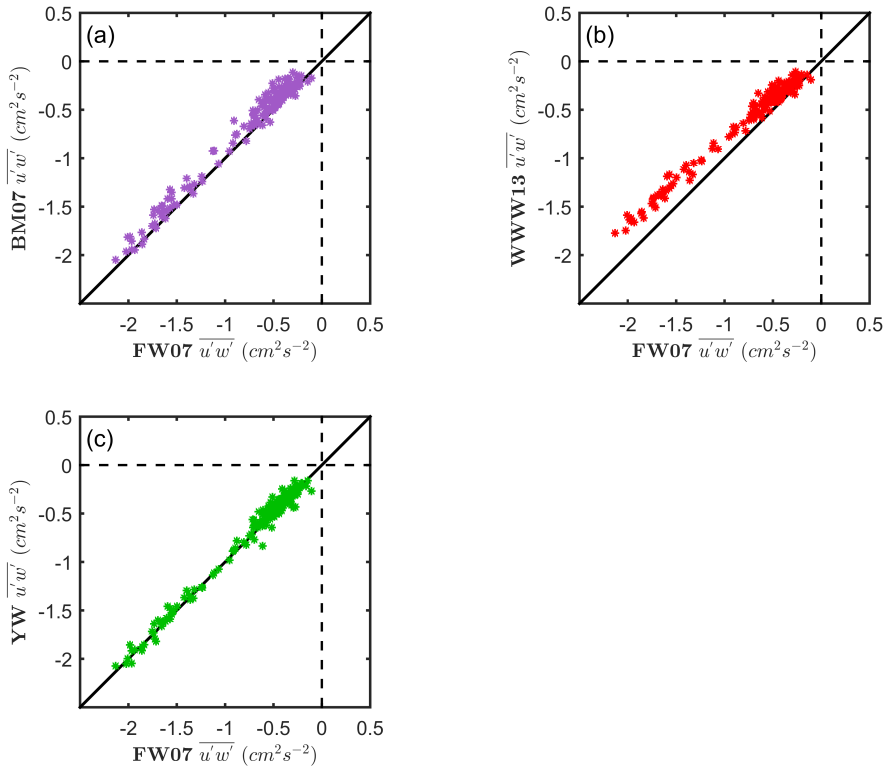

Figure 4.13: Comparison of $\overline{u'w'}$ values for the single-instrument technique vs. FW07 for all bursts in which both methods passed the $\overline{u'w'}$ Ogive curve test for the MB (04/22/2013) dataset. (a) BM07, (b) WWW13, and (c) YW. As a reference, the black line indicates a perfect match.

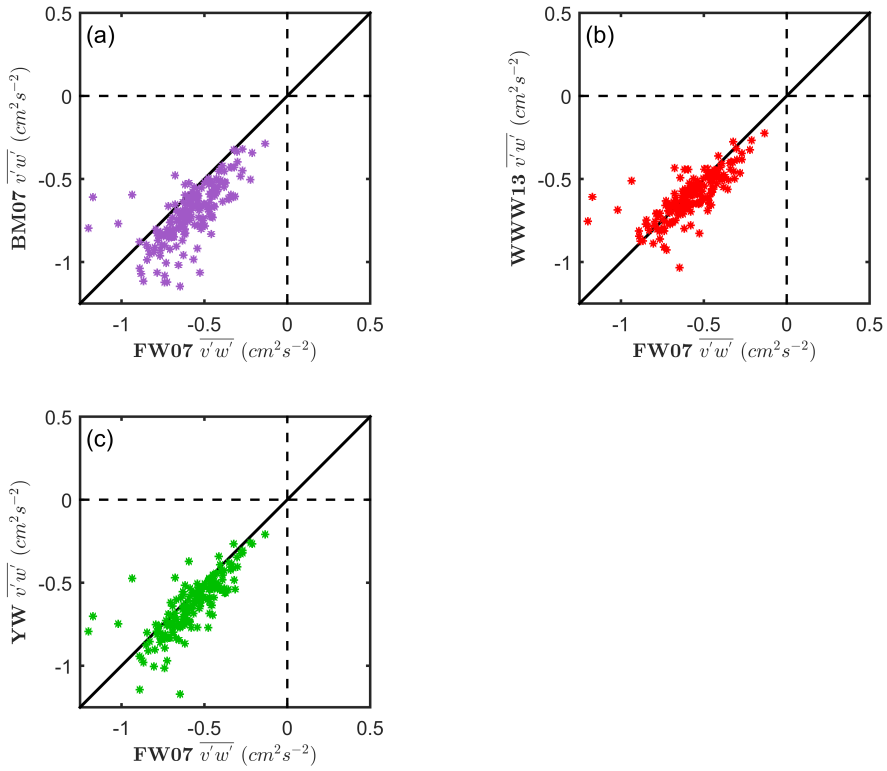

Figure 4.14: Comparison of $\overline{v'w'}$ values for the single-instrument technique vs. FW07 for all bursts in which both methods passed the $\overline{v'w'}$ Ogive curve test for the MB (04/22/2013) dataset. (a) BM07, (b) WWW13, and (c) YW. As a reference, the black line indicates a perfect match.

As with the Wassaw Sound data in Section 4.5.2, the FW07 is chosen as the benchmark method in inter-method comparisons for the field data. Figures 4.13 and 4.14 show the inter-method comparisons of the $\overline{u'w'}$ and $\overline{v'w'}$ estimates, respectively, for the MB (04/22/2013) bursts. BM07 predicts smaller $\overline{u'w'}$ and larger $\overline{v'w'}$ than FW07 for the MB (04/22/2013) bursts, with substantial scatter observed in both plots, most noticeably in the $\overline{v'w'}$ estimates. WWW13 predicts noticeably smaller $\overline{u'w'}$ values but similar $\overline{v'w'}$ values to FW07 and appears to have less scatter than the BM07 estimates. YW predicts nearly identical $\overline{u'w'}$ as FW07, yet over-predicts $\overline{v'w'}$

relative to FW07, with scatter similar to the WWW13 comparison.

The majority of the conclusions drawn from Figures 4.13 and 4.14 can be extended to the full dataset, with the notable exception of the BM07 estimates (Table 4.5). The mean slope of the BM07 $\overline{u'w'}$ best fit lines is 1.032, seemingly comparable to the mean slope of the YW $\overline{u'w'}$ best fit lines (0.977). This is due to wildly different slopes of the BM07 $\overline{u'w'}$ best fit lines for the two days of Monterey Bay data. The slope of the BM07 $\overline{u'w'}$ best fit line for MB (04/22/2013) is 0.923, whereas for the MB (05/04/2013) it is 1.140, which averages to a mean slope near 1. The other slope estimates are more consistent across the two days. Of the three single-instrument methods, the YW $\overline{u'w'}$ estimates come closer to replicating the estimates of FW07 (mean slope of 0.977). This is followed by the BM07 estimates, although the mean slope of 1.032 is not representative as just discussed. WWW13 $\overline{u'w'}$ estimates are the furthest away from the FW07 estimates (mean slope of 0.872). Interestingly, WWW13 yields $\overline{v'w'}$ estimates closest to FW07 (mean slope 1.114), followed by YW (1.152) and BM07 (1.347). Of the three single-instrument methods, YW displays the least scatter between the best-fit line and the data for the $\overline{u'w'}$ and $\overline{v'w'}$ comparisons, followed by WWW13, then BM07 (Table 4.5). Note that the standard error difference between YW and WWW13 is fairly small, whereas the scatter in the BM07 estimates is noticeably larger.

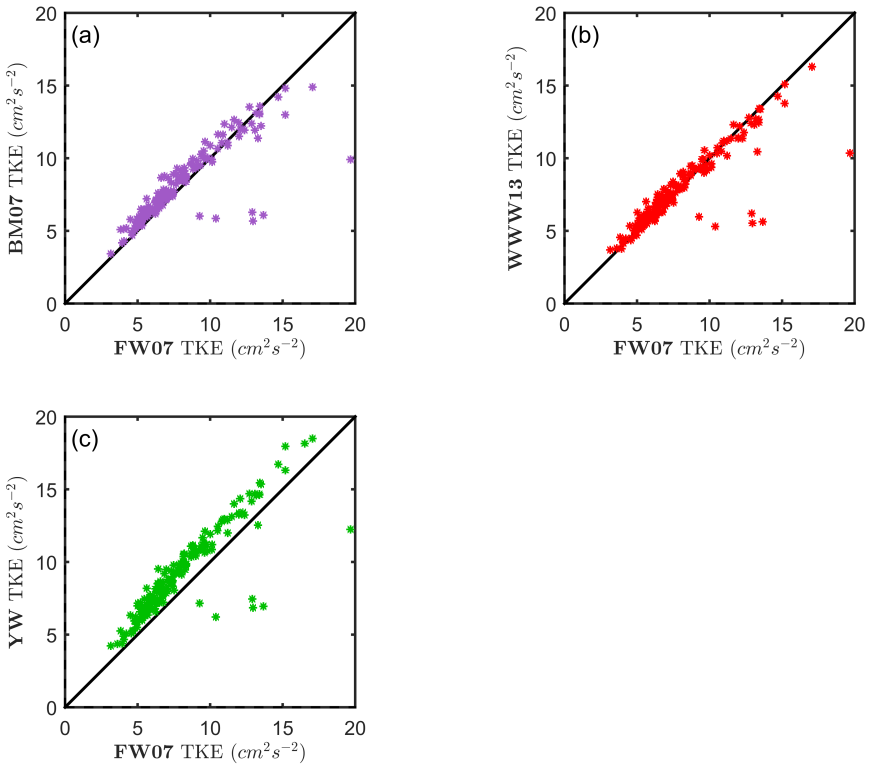

Figure 4.15: Comparison of TKE values for the single-instrument techniques vs. FW07 for all bursts in which both methods passed the $\overline{u'w'}$ Ogive curve test for the MB (04/22/2013) dataset. (a) BM07, (b) WWW13, and (c) YW. As a reference, the black line indicates a perfect match.

The inter-method comparisons of the TKE estimates for the MB (04/22/2013) bursts are shown in Figure 4.15. The WWW13 TKE estimates are the closest to the FW07 estimates (mean slope of 0.995), followed by the BM07 estimates (1.055) and the YW estimates (1.157). The scatter in the best fit lines is similar for the three methods (Table 4.5).

In summary, for the Monterey Bay dataset, YW passes the most Ogive curve tests of the four methods presented, including the FW07 method. YW also comes the closest to matching the FW07 $\overline{u'w'}$ estimates, yet matches the FW07 $\overline{v'w'}$ estimates

less well than WWW13 and matches the FW07 TKE estimates less well than either WWW13 or BM07. As with the Wassaw Sound field data, the difference in the percentage of bursts that passed the Ogive curve tests between the four methods is fairly slight. Overall, the frequency-based single-instrument techniques (BM07 and WWW13) are more successful for the Monterey Bay data relative to the Wassaw Sound data. This is likely due to the deeper water depth in Monterey Bay effectively filtering out the signal from small waves and higher frequency waves from the signal near the bed. Consider, using linear dispersion, the kh value for the longest period waves observed in the Wassaw Sound dataset is $kh = 0.63$, whereas the kh value for the longest period waves observed in the Monterey Bay dataset is $kh = 1.34$. Both datasets are in the transitional range between shallow water and deep water waves, but the waves in Monterey Bay are closer to the deep water regime. The shallow water depths of Wassaw Sound allow high frequency waves to contaminate the velocity signal near the bed, and combined with the smaller wave heights this makes the wave-induced peaks in the PSD hard to identify (for BM07). Further, smaller waves over a wider range of frequencies means a lesser portion of the coherence between the pressure and the velocity at each frequency is due to wave influence (relative to turbulence), thus WWW13 consistently removes energy that is due to turbulence. When the waves are larger and the signal is concentrated in a narrower frequency band (due to the depth effects filtering out the signal of higher frequency waves) the wave-induced peak in the PSD is much clearer and the coherence between the pressure and the velocity is overwhelmingly due to wave influence, mitigating these effects.

4.6 Conclusions

The goal of this study was to propose a new single-instrument technique to remove wave bias from estimates of the Reynolds stress and TKE. The method presented

in this study makes use of the Shaw and Trowbridge [2001] adaptive filtering scheme to predict the wave velocity at the instrument from the pressure at the instrument (as opposed to the velocity at an adjacent instrument as in the Shaw and Trowbridge [2001] and FW07 methods). The velocity differencing procedure of Trowbridge [1998] is then employed to estimate the Reynolds stresses and TKE. The new method was compared to two frequency based single-instrument wave bias removal techniques (BM07 and WWW13), as well as the two-instrument FW07.

Of the three single-instrument methods, the method proposed in this study (YW) performs the best for the synthetic data and the shallow estuarine channel data in Wassaw Sound. Along with FW07, it comes the closest to predicting the "true" $\overline{u'w'}$, $\overline{v'w'}$, and TKE for the synthetic datasets with minimal scatter relative to the frequency-based single-instrument techniques. Additionally the YW (and FW07) Ogive curves for the synthetic bursts were indistinguishable from the "true" Ogive curves for both $\overline{u'w'}$ and $\overline{v'w'}$, whereas the BM07 and WWW13 methods both displayed deviations from the "true" Ogive curves. In the case of BM07, these deviations were quite large. For the Wassaw Sound data, the difference in the percent of bursts passing the Feddersen and Williams [2007] Ogive curve tests for YW and FW07 is slight (FW07 passes 1.3% and 0.9% more bursts for $\overline{u'w'}$ and $\overline{v'w'}$, respectively), and the YW estimates of $\overline{u'w'}$, $\overline{v'w'}$, and TKE agree very well with those of FW07 (linear fit slopes of 1.026, 0.976, and 1.041, respectively). For the Wassaw Sound data, the BM07 and WWW13 methods do not compare as favorably to FW07 due to the limitations in frequency-based delineation of the wave and turbulence components that become significant for shallow water signals contaminated by waves.

In the deeper water of Monterey Bay no individual single-instrument method offers clearly superior performance to the others. The percent of bursts passing the Feddersen and Williams [2007] Ogive curve tests is highest for YW, and YW best matches the FW07 $\overline{u'w'}$ estimates. However, for $\overline{v'w'}$ and TKE it is surpassed by one

or both of the frequency-based single-instrument techniques. The deep water acts as a natural low-pass filter for the wave signal, as only larger, lower frequency waves can be detected near the bed. This alleviates the issues plaguing the frequency-based single-instrument techniques in shallow water.

Therefore, the wave bias removal method proposed in this study (YW) offers wave bias removal capability most comparable to FW07 in shallow water. In deeper water the three single-instrument techniques are more or less equivalently comparable to FW07. The caveat of these comparisons, of course, is that the accuracy of the FW07 method is not fully defined despite its wide-scale acceptance. Our hope is that this will prove beneficial to future studies with a limited number of instruments, particularly in shallower estuarine channels in which the wave influence may be more difficult to identify and remove.

CHAPTER V

CONCLUSIONS AND CONCLUDING REMARKS

5.1 Conclusions

5.1.1 Conclusions of the Surface Tidal Flow Chapter

In Chapter 2 of this study, we examined the flow in an estuarine saltmarsh, specifically the flow on the high marsh through the dense marsh vegetation, the presence of differential water levels between the marsh and the adjacent estuary channel, and the effect of the resulting pressure gradient on marsh flow. We observed large differences in the water surface elevation between the main channel and the saltmarsh, and the correspondingly large pressure gradients substantially affected the flow at all of our flow measurement instruments. At one instrument the flow was entirely governed by the pressure gradient, and we were able to model the flow using the Darcy-Weisbach/Lindner's Equation model. Our hope is that this model may prove superior to the current numerical modeling techniques used to estimate the drag coefficient in the marsh.

5.1.2 Conclusions of the Meandering Plume Chapter

In Chapter 3 of this study, we examined the mixing of tracer in a meandering plume by phase-locking the plume to separate the fluctuations due to the plume meander from the turbulent velocity and concentration fluctuations. We conducted simultaneous LIF and PIV/PTV experiments on the meandering plume at four phases in the motion of the meander-forcing diverting plate to quantify the concentration and velocity fields. Our results show that the phase-averaged concentration profiles for the meandering plume match a piecewise Gaussian shape, but the profiles of the standard deviation of the concentration fluctuations are not. The phase-averaged

centerline concentration for the meandering plume decreased more quickly with distance downstream than the centerline mean concentration for the straight plume. Further, the plume width of the meandering plume grew more quickly with distance downstream than the straight plume width. This indicates more rapid dilution in the meandering plume than the straight plume. Furthermore, we showed the importance of the vortices shed from the diverting plate, which led to local peaks in the concentration as well as governed the distribution of the turbulence statistics and the turbulent flux. Finally, we were able to model the turbulent flux using the eddy-diffusivity hypothesis.

5.1.3 Conclusions of the Wave Bias Removal Chapter

In Chapter 4 of this study, we proposed a new single-instrument technique to remove wave bias from estimates of the Reynolds stress and TKE in wavy environments. The technique uses the pressure measurement at the instrument to estimate the wave velocity at the instrument. The estimated wave velocity is subtracted from the velocity measured at the instrument to remove the wave effects. We compared this method to two frequency-based single-instrument techniques, as well as a benchmark two-instrument technique. Our results show that our single-instrument technique is superior to the two frequency-based single instruments in shallow water, and the three single-instrument techniques are effectively equivalent in deeper water.

5.2 Unique Contributions

The unique contributions of this work include the following:

- Measured the water surface elevation within the saltmarsh using pressure transducers combined with GPS survey measurements with sufficient accuracy to quantify the pressure gradient over small spatial scales ($< 100\ m$).
- Corroborated the observation of large estuary channel-to-saltmarsh pressure

gradients in the modeling study of Bruder et al. [2014].

- As a result, we were able to quantitatively relate the pressure gradient to the flow through the marsh vegetation using the Darcy-Weisbach/Lindner's model, overcoming a long-standing barrier in directly relating flow-through-saltmarsh-vegetation studies to flow-through-vegetation studies and quantitative relationships developed in flumes.

- The Darcy-Weisbach/Lindner's model may prove superior to current techniques for parameterizing the drag in the marsh.

- Analyzed simultaneous LIF and PIV/PTV on a phase-locked meandering plume, which allowed us to separate the fluctuations due to the plume meander from the turbulent velocity and concentration fluctuations.

- Our PTV velocity analysis combined with the LIF concentration fields allowed us to directly estimate the turbulent flux of tracer in the plume.

- Consequently, we were able to directly examine the fundamental theory behind the use of the eddy-diffusion coefficient for modeling turbulent flux, rather than relying on a best fit of the mean concentration profiles to analytical solutions for a given functional form of the eddy-diffusion coefficient.

- Proposed a new single-instrument method for removing wave bias from Reynolds stress estimates based upon the linear filtration scheme of Shaw and Trowbridge [2001], as opposed to a frequency-based technique.

- Compared three single-instrument methods (and a benchmark two-instrument method) using the Feddersen and Williams [2007] Ogive curve test (among others) for both shallow estuarine and deeper coastal waves.

5.3 Limitations and Challenges

5.3.1 Limitations and Challenges of the Surface Tidal Flow Chapter

Our work in the saltmarsh presented several unique challenges, many of which contribute to the limitations of the study. Perhaps the chief limitation of the Chapter 2 portion of the study is the limited number of instruments deployed. Our choice to deploy all our instruments along a single transect perpendicular to the main channel (Little Ogeechee River) meant that we were only able to quantify the pressure gradient in the along-transect direction. This noticeably impacted our ability to draw conclusions from the ADV at station C, as we were unable to calculate the pressure gradient along the natural depression (the depression was more or less perpendicular to our transect). Also due to the limited number of instruments, we are also unable to determine how the estuary channel-to-saltmarsh pressure gradient at different locations in the marsh.

Additionally, although we were able to determine the pressure gradient across spatial distances on the order of 100 m, we likely did not achieve sufficient accuracy to calculate the pressure gradient over distances of ≈ 10 m. Consequently, although we were able to capture the larger scale flow exchange between the large estuarine channel (Little Ogeechee River) and the saltmarsh, we were not able to do the same between the saltmarsh and the smaller tidal creek (station B). Our choice of instrument placement is partially responsible for this, but it is also due to the smaller spatial distances over which this exchange occurs.

Furthermore, whereas our measured pressure gradient is effectively averaged between stations F and D (i.e., over a distance of ≈ 100 m), our vegetation parameters used in the model are taken from a 1 $m \times 1$ m stand of grass near the ADV at station E. The vegetation varies substantially between the two stations, so it is entirely possible that a single stand of grass is not representative of the conditions that the flow experiences. This limitation also contributes to the difficulty modelers experience

when attempting to describe the estuarine and, in particular, the marsh flow, specifically the inability to accurately account for the vegetation variation in the saltmarsh without exhaustive field measurements.

I would be remiss if I did not briefly discuss the unique challenges that working in an estuarine saltmarsh presents. While the key limitation of the study is the limited number of instruments, we would not have been able to deploy any additional instruments on a single day, nor survey all of them during a single low-tide, given the number of researchers present during the experiment (3). The saltmarsh is fully inundated during high tide. Thus, we only have access to our instruments during low tide, more specifically, when the creek at station B is dry enough to walk across (i.e., when the bottom is visible). This effectively gives researchers a three-hour window in which to deploy, check, and survey the instruments. The total station vertical elevation measurements were not sufficiently accurate to measure the pressure gradient, and the GPS vertical elevation estimates require at least two hours of continuous data collection. This does not leave much time allotted for traversing the marsh to reach a large number of far-flung instruments. Additionally, it is unsafe for a researcher to be by him/herself when traversing the marsh. In many areas the marsh mud is extremely soft, thus wrong steps can cause an individual to be buried in the mud to sufficient extent that they are not able to extricate themselves without aid. This is also why it is unsafe to cross the creek at station B if the bottom is not visible. The necessity of employing the "buddy"-system, coupled with the limited time in which to work, make it effectively impossible to deploy additional instruments along (for example) a nearby transect, without at least one additional researcher present. Note that our instruments did not appreciably settle over the course of this deployment, so we may be able to survey the instruments every other day.

Lastly, it should be noted that this experiment was performed in November 2014, after an attempt in August 2014 was aborted. The August attempt was aborted

because two of the three researchers on the project suffered heat exhaustion on the first day while scouting the instrument deployment sites, carrying no equipment save water and a camera. One researcher, in particular, likely came very close to needing medical attention for heat stroke. Walking even a short distance across the marsh is a strenuous activity under ideal conditions, carrying no equipment. The extreme heat and humidity at the experiment site (Savannah, GA), effectively make it difficult to conduct this experiment during the summer months. Consequently, although we do not expect significant seasonal variation, it would be difficult to confirm this.

5.3.2 Limitations and Challenges of the Meandering Plume Chapter

Perhaps the most critical limitation of this chapter (that will not be remedied from the future work discussed in Section 5.4.2) is that simultaneous PIV and LIF data do not exist for the straight plume presented in this study. We were able to show that the plume meander leads to more rapid dilution of tracer with distance downstream compared to the straight plume, because the increased growth of the plume width for the meandering plume combined with the more rapid centerline concentration decrease for the meandering plume indicates more rapid dilution. However, as we are not able to quantify the turbulent flux terms for the straight plume (due to the lack of velocity measurements), we cannot directly compare the magnitudes of the turbulent flux or the estimated eddy-diffusion coefficients for the meandering plume to the benchmark straight plume case. Consequently, we are unable to conclusively explain *why* the plume meander leads to more rapid dilution of tracer with distance downstream.

The biggest challenge that I faced through this chapter was the difficulty in finding enough hard drive space, and space on the server, to be able to manage and process all of the data. As might be expected, 6706 high-resolution LIF images for four phases of the meandering plume, as well as an additional 6706 LIF images for the

straight plume, results in a substantial amount of data (approximately 4 TB in total). The PIV images and analysis for the four meandering plume phases is another 4 TB of data (when you delete the intermediate image-processing images), and the PTV analysis for each phase amounts to 3 TB for each phase. That amount of data takes a long time to process (and even to move).

5.3.3 Limitations and Challenges of the Wave Bias Removal Chapter

The critical limitation of Chapter 4, as with all wave bias removal studies, is the inability to know the true Reynolds stress and TKE for field data. To circumvent this, many studies [Shaw and Trowbridge, 2001, Bricker and Monismith, 2007, Feddersen and Williams, 2007, Wilson et al., 2013] rely on a comparison of their newly proposed method with a commonly accepted one, e.g., Trowbridge [1998] or Shaw and Trowbridge [2001], depending on the date of the study in question. Additionally, as done in this study, one can also generate a synthetic signal to test the different methods. This has the obvious advantage of benchmarking the various methods against the "correct" estimations of the turbulence parameters, but necessarily represents a test under idealized conditions. The Feddersen and Williams [2007] Ogive curve test is a step forward in this regard, as it allows the Ogive curves of the Reynolds stress estimates for the various methods to be compared with the results of Kaimal et al. [1972]. However, the acceptance or rejection of the results of the Ogive curve test is still based on qualitatively determined cutoffs. Consequently, we simply do not have the means to be certain whether any wave bias removal method produces the true values of the Reynolds stress or TKE in the field.

5.4 Future Directions

5.4.1 Future Directions of the Surface Tidal Flow Chapter

The future direction for the portion of the study addressed in Chapter 2, the tidally-driven flow through the saltmarsh requires some additional background to

explain. In Chapter 1, it was stated that many researchers have linked ebb-dominant tidal asymmetry in large estuarine channels to the presence of extensive vegetated saltmarshes adjacent to the channel [Boone and Byrne, 1981, Speer and Aubrey, 1985, Dronkers, 1986, Friedrichs and Aubrey, 1988, Parker, 1991, Blanton et al., 2002, Zheng et al., 2003, Bruder et al., 2014]. However, the precise physical mechanism by which the vegetated saltmashes could cause ebb-dominance remains elusive.

Based upon model results in Bruder et al. [2014], Brittany Bruder and Kevin Haas have hypothesized an additional link in the physical forcing that drives ebb dominance in areas with extensive tidal storage, such as vegetated saltmarshes (pers. comm.). They hypothesized that the large difference in water surface elevation between the saltmarsh and the estuary channel coincides with a large difference in the water surface elevation between the estuary channel and the ocean during ebb tide (which does not occur during flood tide). Consequently, the flux in ebb tide is larger than the flux during flood tide.

In Chapter 2 of this study, we have demonstrated the existence of large estuary channel-to-saltmarsh pressure gradients at the Rose Dhu experiment site. We have also confirmed that this governs the flow in the marsh and between the marsh and the nearby estuary channel (Little Ogeechee River), including a rapid draining of the saltmarsh into the estuary channel during ebb-tide. However, due to the aforementioned equipment and personnel limitations of our experiment, we were not able to simultaneously quantify all the physical mechanisms necessary to fully validate this hypothesis. To do so, we would require simultaneous measurements of the water surface elevation at the mouth of the estuary (to quantify the estuary channel-to-ocean pressure gradient) in addition to the repetition of the water surface elevation measurements described in this study. It would also require simultaneous measurements of the volume flux in the nearby Little Ogeechee River (likely through boat-mounted ADCP measurements), which are necessary to verify that the channel experiences

ebb-dominance, and that the timing of peak ebb is linked to the draining of the marsh. Linking the flux in the estuary channel to the draining of the saltmarsh requires repeating the velocity measurement in the saltmarsh near the main channel bank.

5.4.2 Future Directions of the Meandering Plume Chapter

The results presented in Chapter 3 were primarily restricted to the meandering plume for phase $\phi = 0°$. This is partially done to keep the number of figures in this chapter manageable, but is also because the analysis of the turbulent flux (and thus estimates of eddy-diffusivity) are only complete for the meandering plume for phase $\phi = 0°$. This is a direct consequence of the aforementioned limitations and challenges of this chapter discussed in Section 5.3.2 (it takes a full week of constant server processing to go from raw LIF and PIV/PTV images to field plots of $\overline{v'c'}$ and $\overline{u'c'}$ for each phase). Consequently, our next task is to analyze the turbulent flux results for the other three meandering plume phases. The field plots of $\overline{v'c'}$ and $\overline{u'c'}$ for the other three phases are unlikely to meaningfully different from those presented in Figures 3.43 and 3.44 for the $\phi = 0°$ phase. However, additional the results from the other three phases will provide additional data to be shown in Figures 3.48, 3.50, and 3.51. This will allow us to firm up the conclusions of Section 3.5.8 as we move to put this chapter in journal article form.

In the more distant future, we would like to repeat the straight plume experiment while collecting simultaneous LIF and PIV/PTV data (rather than solely LIF data). This will allows us to directly compare the turbulent flux between the meandering and straight plumes and explain the cause of the increased dilution for the meandering plume (see Section 5.3.2 for more thorough discussion).

5.4.3 Future Directions of the Wave Bias Removal Chapter

The future direction for the portion of the study presented in Chapter 4 is to examine the effect of horizontally versus vertically separated instruments for the two-sensor technique in this study (the Feddersen and Williams [2007] wave bias removal technique). As briefly mentioned in Section 4.3.1, the two instruments are horizontally spaced for the Wassaw Sound dataset and vertically spaced for the Monterey Bay dataset. Directly comparing the two instrument configurations for an identical dataset would allow us to determine if certain situations exist (e.g. measurements with horizontally separated sensors in the tidal range, where it is effectively impossible to vertically separate the sensors) in which the two-instrument technique is hampered by the inability to place the sensors in an optimal configuration. This would allows us to directly compare the two-instrument techniques efficacy in the sub-optimal and optimal configurations to the single-instrument technique proposed in this study, which we are currently unable to account for.

Linear wave theory suggests that, for "shallow water" progressive waves, the dominant velocity component (i.e., the horizontal velocity component, u) is depth invariant [Dean and Dalrymple, 1991]. This is the theoretical argument for the use of vertically separated sensors in the Shaw and Trowbridge [2001] and Feddersen and Williams [2007] wave extraction techniques, i.e., the horizontal wave velocity is equal at both sensors. Both Shaw and Trowbridge [2001] and Feddersen and Williams [2007] vertically separate their sensors accordingly. Attempting to use the Shaw and Trowbridge [2001] family of wave extraction techniques on two horizontally-separated sensors introduces a small but persistent phase shift in the horizontal and vertical velocity, which must be corrected for (as Shaw and Trowbridge [2001] attempt to do with the linear filtration technique discussed in Section 4.3.1).

That said, valid reasons remain for horizontally separating sensors, particularly in the context of very near bed measurements, i.e., in the bottom boundary layer.

Classic linear wave theory assumes irrotational, inviscid flow, thus the first-order-linear-wave solution for progressive waves does not meet the no-slip condition at the bed. In real flows, the assumption of depth uniform horizontal velocity may be valid for the vast majority of the water column. But, very near the bed the magnitude of the horizontal wave velocity will necessarily be a function of depth. Additionally, in the first-order-shallow-water-progressive-wave solution, the vertical wave velocity magnitude is strongly a function of depth - this effect is a persistent inaccuracy in the Trowbridge [1998] wave extraction method (a precursor to the Shaw and Trowbridge [2001] method) with vertically-separated sensors near the bed. Furthermore, the most robust of the three wave extraction methods discussed in Shaw and Trowbridge [2001] (i.e., the Trowbridge [1998] method) results in estimates of Reynolds stress that are an average of the Reynolds stress between the two sensors. This is a critical conceptual issue with this approach, because the Reynolds stress in a turbulent boundary layer is a function of height above the bed [Tennekes and Lumley, 1972].

As a result of these factors, when attempting to extract wave energy from very near bed estimates of Reynolds stress, it may be more advantageous to simply live with the phase shift, and horizontally space the two sensors at the same height above the bed, such that the velocity measurements are equally modulated by depth, and the Reynolds stress is averaged at two positions with the same height above the bed. It is worth noting that the Trowbridge [1998] wave extraction method has been successfully applied with horizontally-separated ADV's in Trowbridge and Elgar [2001] to diagnose alongshore momentum and turbulence dynamics near Duck, North Carolina (USA).

References

J. R. L. Allen. A continuity-based sedimentological model for temperate-zone tidal salt marshes. *Journal of the Geophysical Society*, 151:41–49, 1994.

J. R. L. Allen. Morphodynamics of holocene salt marshes: A review sketch from the Atlantic and Southern North Sea coasts of Europe. *Quaternary Science Reviews*, 19:1155–1231, 2000.

D. M. Alongi and A. I. Robertson. Factors regulating benthic food chains in tropical river deltas and adjacent shelf areas. *Geo-Marine Letters*, 15:145–152, 1995.

D. Anfossi, D. Oettl, G. Degrazia, and A. Goulart. An analysis of sonic anemometer observations in low wind speed conditions. *Boundary-Layer Meteorology*, 114:179–203, 2005.

C. Arcoumanis, J. J. McGuirk, and J. M. L. M. Palma. On the use of fluorescent dyes for concentration measurements in water flows. *Experiments in Fluids*, 10:177–180, 1990.

P. S. Arya. *Air pollution meteorology and dispersion*. Oxford University Press, Oxford, UK, 1999.

J. Atema. Eddy chemotaxis and odor landscapes: exploration of nature with animal sensors. *Biological Bulletin*, 191:129–138, 1996.

J. Aucan and P. V. Ridd. Tidal asymmetry in creeks surrounded by saltflats and mangroves with small swamp slopes. *Wetlands Ecology and Management*, 8:223–231, 2000.

L. Augustin, J. Irish, and P. Lynett. Laboratory and numerical studies of wave damping by emergent and near-emergent wetland vegetation. *Coastal Engineering*, 56:332–340, 2009.

C. J. Baker. The laminar horseshoe vortex. *Journal of Fluid Mechanics*, 95:347–367, 1979.

C. J. Baker. The turbulent horseshoe vortex. *Journal of Wind Engineering and Industrial Aerodynamics*, 6:9–23, 1980.

C. J. Baker. The position of points of maximum and minimum shear stress upstream of cylinders mounted normal to flat plates. *Journal of Wind Engineering and Industrial Aerodynamics*, 18:263–274, 1985.

C. J. Baker. The oscillation of horseshoe vortex systems. *Journal of Fluids Engineering*, 113:489–495, 1991.

F. Ballio, C. Bettoni, and S. Franzetti. A survey of time-averaged characteristics of laminar and turbulent horseshoe vortices. *Journal of Fluids Engineering*, 120: 233–242, 1998.

M. Balu, R. Balachandar, and H. Wood. Concentration estimation in two-dimensional bluff body wakes using image processing and neural networks. *Journal of Flow Visualization and Image Processing*, 8:121–139, 2001.

B. M. Bara, D. J. Wilson, and B. W. Zelt. Concentration fluctuation profiles from a water channel simulation of a ground level release. *Atmospheric Environment*, 26: 1053–1062, 1992.

P. J. Barry. Stochastic properties of atmospheric diffusivity. Technical report, National Research Council of Canada, 1977.

G. K. Batchelor. Diffusion in a field of homogeneous turbulence. II. The relative motion of particles. *Proceedings of the Cambridge Philisophical Society*, 48:345–362, 1952.

G. K. Batchelor. Computation of the energy spectrum in homogeneous two-dimensional turbulence. *Physics of Fluids Supplimentary Material*, II:233–239, 1969.

T. P. Bayliss-Smith, R. Healey, R. Lailey, T. Spencer, and D. R. Stoddart. Tidal flows in salt marsh creeks. *Estuarine and Coastal Marine Science*, 9:235–255, 1979.

J. O. Blanton, G. Lin, and S. A. Elston. Tidal current asymmetry in shallow estuaries and tidal creeks. *Continental Shelf Research*, 22:1731–1743, 2002.

J. C. Bo, D. L. Hui, and L. D. Fang. Study of concentration fields in turbulent wake regions. *Journal of Hydraulic Research*, 41:311–318, 2003.

S. Bomminayuni, B. Bruder, T. Stoesser, and K. Haas. Assessment of hydrokinetic energy near Rose Dhu Island, Georgia. *Journal of Renewable and Sustainable Energy*, 4:063107, 2012.

J. D. Boone and R. J. Byrne. On basin hypsometry and the morphodynamic response of coastal inlet systems. *Marine Geology*, 40:27–48, 1981.

E. Bouws, H. Günther, W. Rosenthal, and C. L. Vincent. Similarity of the wind wave spectrum in finite depth water, 1. spectral form. *Journal of Geophysical Research*, 90:975–986, 1985.

E. Bouws, H. Günther, W. Rosenthal, and C. L. Vincent. Similarity of the wind wave spectrum in finite depth water, 2. statistical relationships between shape and growth stage parameters. *Deutsche Hydrographische Zeitschrift*, 40:1–24, 1987.

J. D. Bricker and S. G. Monismith. Spectral wave-turbulence decomposition. *Journal of Atmospheric and Oceanic Technology*, 24:1479–1487, 2007.

N. H. Brooks. Diffusion of sewage effluent in an ocean current. In *Proceedings of the First International Conference on Waste Disposal in the Marine Environment*, Berkely, CA, 1960.

B. Bruder, S. Bomminayuni, T. Stoesser, and K. Haas. Modeling tidal distortion in the Ogeechee Estuary. *Ocean Modelling*, 82:60–69, 2014.

H. Chanson, M. Trevethan, and S. Aoki. Acoustic Doppler velocimetry (ADV) in small estuary: Field experience and signal post-processing. *Flow Measurement and Instrumentation*, 19:307–313, 2008.

P. C. Chatwin and P. J. Sullivan. The intermittency factor of scalars in turbulence. *Physics of Fluids A - Fluid Dynamics*, 1:761–763, 1989.

N. Cheng and H. T. Nguyen. Hydraulic radius for evaluating resistance induced by simulated emergent vegetation in open channel flows. *Journal of Hydraulic Engineering*, 137:995–1004, 2011.

A. Cramp, M. Coulson, A. James, and J. Berry. A note on the observed and predicted flow patterns around islands - Flat holm, the Bristol channel. *International Journal of Remote Sensing*, 12:1111–1118, 1991.

J. P. Crimaldi and J. R. Koseff. High-resolution measurements of the spatial and temporal structure of a turbulent plume. *Experiments in Fluids*, 31:90–102, 2001.

J. P. Crimaldi and J. R. Koseff. Structure of turbulent plumes from a momentumless source in a smooth bed. *Environmental Fluid Mechanics*, 6:573–592, 2006.

J. P. Crimaldi, M. B. Wiley, and J. R. Koseff. The relationship between mean and instantaneous structure in turbulent passive scalar plumes. *Journal of Turbulence*, 3:1–24, 2002.

N. Dankers, M. Binsbergen, K. Zegers, R. Laane, and M. R. van der Loeff. Transportation of water, particulate and dissolved organic and inorganic matter between a salt marsh and the Ems-Dollard Estuary, The Netherlands. *Estuarine Coastal and Shelf Science*, 19:143–165, 1984.

B. Dargahi. The turbulent flow field around a circular cylinder. *Experiments in Fluids*, 8:1–12, 1989.

B. Dargahi. Controlling mechanism of local scour. *ASCE Journal of Hydraulic Engineering*, 116:1197–1214, 1990.

R. G. D. Davidson-Arnott, D. van Proosdij, J. Ollerhead, and L. Schostak. Hydrodynamics and sedimentation in salt marshes: Examples from a macrotidal marsh, Bay of Fundy. *Geomorphology*, 48:209–231, 2002.

R. G. Dean and R. A. Dalrymple. *Water Wave Mechanics for Engineers and Scientists*. World Scientific Publishing, Hackensack, NJ, 1991.

T. P. DeFelice, D. J. Meyer, G. Xian, J. Christopherson, and R. Cahalan. Landsat-7 reveals more than just surface features in remote areas of the globe. *Bulletin of the American Meteorology Society*, 81:1047–1049, 2000.

G. A. Degrazia, O. L. L. Moraes, and J. Goedart. Estimation of lagrangian paramaters from a diffusion experiment. *Nuovo Cimento*, 14C:615–621, 1991.

B. Dickman. *Chemical and hydromechanical cue structure in the context of turbulent odor plume tracking*. PhD thesis, Georgia Institute of Technology, Atlanta, GA, 2008.

J. Dronkers. Tidal asymmetry and estaurine morphology. *Netherlands Journal of Sea Research*, 20:117–131, 1986.

W. C. Eiser and B. Kjerfve. Marsh topography and hypsometric characteristics of a South Carolina salt marsh. *Estuarine Coastal and Shelf Science*, 23:595–605, 1986.

M. El Hassan, J. Bourgeois, and R. Martinuzzi. Boundary layer effect on the vortex shedding of wall-mounted rectangular cylinder. *Experiments in Fluids*, 56:33, 2015.

D. Etling. On plume meandering under stable stratification. *Atmospheric Environment*, 24:1979–1985, 1990.

J. E. Fackrell and A. G. Robins. Concentration fluctuations and fluxes in plumes from point sources in a turbulent boundary layer. *Journal of Fluid Mechanics*, 117: 1–26, 1982.

F. Feddersen and A. J. Williams. Direct estimation of the Reynolds stress vertical structure in the nearshore. *Journal of Atmospheric and Oceanic Technology*, 24: 102–116, 2007.

M. C. Ferner and M. J. Weissburg. Slow-moving predatory gastropods track prey odors in fast and turbulent flow. *Journal of Experimental Biology*, 208:809–819, 2005.

E. Ferrero, L. Mortarini, S. Alessandrini, and C. Lacagnina. Application of a bivariate gamma distribution for a chemically reacting plume in the atmosphere. *Boundary-Layer Meteorology*, 147:123–137, 2013.

H. B. Fischer, E. J. List, R. C. Y. Koh, J. Imberger, and N. H. Brooks. *Mixing in Inland and Coastal Waters*. Academic Press, New York, 1979.

J. Fleming, R. L. Simpson, and W. J. Devenport. An experimental study of a turbulent wing-body junction and wake flow. Technical Report VPI&SU Report VPI-AOE-179, Virginia Polytechnic Institute and State University, Blacksburg, VA, 1991.

J. Fleming, R. L. Simpson, and W. J. Devenport. An experimental study of a turbulent wing-body junction flow. *Experiments in Fluids*, 14:366–378, 1993.

Fluid Dynamics and Flow Control Research Laboratory - Chulalongkorn University. Smoke-wire image of a horseshoe vortex around a rectangular block. http://fmeabj.lecturer.eng.chula.ac.th/FMRL/public_html/Flow%20Visualization/Flow%20Images/Horseshoe%20Vortex/FMRL%20Horseshoe%20Vortex%20Frame.htm. [Online; accessed 13-January-2016].

D. A. Fong and M. T. Stacey. Horizontal dispersion of a near-bed coastal plume. *Journal of Fluid Mechanics*, 489:239–267, 2003.

J. E. Foxworthy, R. B. Tibby, and G. M. Barsom. Dispersion of a surface waste field in the sea. *Journal of the Water Pollution Control Federation*, 38:1170–1193, 1966.

P. Franzese. Lagrangian stochastic modeling of a fluctuating plume in the convective boundary layer. *Atmospheric Environment*, 37:1691–1701, 2003.

P. Franzese and M. Cassiani. A statistical theory of turbulent relative dispersion. *Journal of Fluid Mechanics*, 571:391–417, 2007.

J. R. French and D. R. Stoddart. Hydrodynamics of salt marsh creek systems: Implications for marsh morphological development and material exchange. *Earth Surface Processes and Landforms*, 17:235–252, 1992.

F. N. Frenkiel. Turbulent diffusion: mean concentration distribution in a floe field of homogeneous turbulence. *Advances in applied mechanics*, 3:61–107, 1953.

C. T. Friedrichs and D. G. Aubrey. Non-linear tidal distortion in shallow well-mixed estuaries: A synthesis. *Estuarine, Coastal and Shelf Science*, 27:521–545, 1988.

H. Fu and D. Rockwell. Shallow flow past a cylinder: control of the near wake. *Journal of Fluid Mechanics*, 539:1–24, 2005a.

H. Fu and D. Rockwell. Shallow flow past a cylinder: transition phenomena at low reynolds number. *Journal of Fluid Mechanics*, 540:75–97, 2005b.

R. M. Gailis, A. Hill, E. Yee, and T. Hilderman. Extension of a fluctuating plume model of tracer dispersion to a sheared boundary layer and to a large array of obstacles. *Boundary-Layer Meteorology*, 122:577–607, 2007.

M. C. Gambi, A. R. M. Nowell, and P. A. Jumars. Flume observations on flow dynamics in *Zostera marina* (eelgrass) beds. *Earth Surface Processes and Landforms*, 17:235–252, 1992.

L. R. Gardner. A modeling study of the dynamics of pore water seepage from intertidal marsh sediments. *Estuarine Coastal and Shelf Science*, 62:691–698, 2005.

L. R. Gardner, H. W. Reeves, and P. M. Thibodeau. Groundwater dynamics along forest-marsh transects in a southeastern salt marsh, USA: Description, interpretation and challenges for numerical modeling. *Wetlands Ecology and Management*, 10:145–159, 2002.

K. B. Gedan, M. L. Kirwan, E. Wolanski, E. Barbier, and B. R. Silliman. The present and future of role of coastal wetlands in protecting shorelines: answering recent challenges to the paradigm. *Climatic Change*, 106:7–29, 2011.

F. Gifford, Jr. Statistical properties of a fluctuating plume dispersion model. *Advances in Geophysics*, 6:117–136, 1959.

F. Gifford, Jr. Horizontal diffusion in the atmosphere: a Lagrangian-dynamical theory. *Atmospheric Environment*, 16:505–512, 1982.

D. G. Goring and V. I. Nikora. Despiking acoustic Doppler velocimeter data. *Journal of Hydraulic Engineering*, 128:117–126, 2002.

W. D. Grant and O. S. Madsen. The continental shelf-bottom boundary layer. *Annual Review of Fluid Mechanics*, 18:265–305, 1986.

W. D. Grant, A .J. Williams, and S. M. Glenn. Bottom stress estimates and their prediction on the Northern California continental shelf during CODE-1. The importance of wave-current interaction. *Journal of Physical Oceanography*, 14:506–527, 1984.

T. F. Gross and F. E. Werner. Finite element model of wassaw sound with synthetic marsh flooding boundary conditions. In M. L. Spaulding and A. F. Blumberg, editors, *Estuarine and Coastal Modeling*. ASCE, Reston, VA, 1997.

T. F. Gross, A. J. Williams, and E. A. Terray. Bottom boundary layer spectral dissipation estimates in the presence of wave motions. *Continental Shelf Reserach*, 14:1239–1256, 1994.

S. R. Hanna. Lateral turbulence intensity and plume meandering during stable conditions. *Journal of Applied Meteorology*, 22:1424–1430, 1983.

S. R. Hanna. Concentration fluctuations in a smoke plume. *Atmospheric Environment*, 18:1091–1106, 1984a.

S. R. Hanna. The exponential probability density function and concentration fluctuations in smoke plumes. *Boundary-Layer Meteorology*, 29:361–375, 1984b.

S. R. Hanna. Spectra of concentration fluctuations: the two time scales of a meandering plume. *Atmospheric Environment*, 20:1131–1137, 1986.

S. R. Hanna and E. M. Insley. Time series analysis of of concentration and wind fluctuations. *Boundary-Layer Meteorology*, 47:131–147, 1989.

S. Haykin. *Adaptive Filter Theory (3rd Ed.)*. Prentice Hall, Upper Saddle River, New Jersey, 1996.

J. Hazelden and L. A. Boorman. The role of soil and vegetation processes in the control of organic and mineral fluxes in some western European salt marshes. *Journal of Coastal Research*, 15:15–31, 1999.

R. G. Healey, K. Pye, D. R. Stoddart, and T. P. Bayliss-Smith. Velocity variations in salt marsh creeks, Norfolk, England. *Estuarine Coastal and Shelf Science*, 13: 535–545, 1981.

E. M. Horstman, C. M. Dohmen-Janssen, and S. J. M. H. Hulscher. Flow routing in mangrove forests: A field study in Trang province, Thailand. *Continental Shelf Research*, 71:52–67, 2013.

B. L. Howes and D. D. Goehringer. Porewater drainage and dissolved organic carbon and nutrient losses through the intertidal creekbanks of a New England salt marsh. *Marine Ecology Progress Series*, 114:289–301, 1994.

H. Huang, C. Chen, J. O. Blanton, and F. A. Andrade. A numerical study of tidal asymmetry in Okatee Creek, South Carolina. *Estuarine Coastal and Shelf Science*, 78:190–202, 2008.

Z. Huang, J. G. Kawall, J. F. Keffer, and J. A. Ferré. On the entrainment process in plane turbulent wakes. *Physics of Fluids*, 7:1130, 1995.

J. C. Hunt, C. J. Abell, J. A. Peterka, and H. Woo. Kinematical studies of the flows around free and surface-mounted obstacles: Applying topology to flow visualization. *Journal of Fluid Mechanics*, 86:179–200, 1978.

D. A. Huntley and D. G. Hazen. Seabed stresses in combined wave and steady flow conditions on the Nova Scotia continental shelf: Field measurements and predictions. *Journal of Physical Oceanography*, 18:347–362, 1988.

R. G. Ingram and V. H. Chu. Flow around islands in Rupert Bay: An investigation of the bottom friction effect. *Journal of Geophysical Research*, 92:14521–14533, 1987.

R. S. Jadhav and S. G. Buchberger. Effect of vegetation on flow through free water surface wetlands. *Ecological Engineering*, 4:481–496, 1995.

J. Järvelä. Flow resistance of flexible and stiff vegetation: A flume study with natural plants. *Journal of Hydrology*, 269:44–54, 2002.

J. Järvelä. Determination of flow resistance caused by non-submerged woody vegetation. *International Journal of River Basin Management*, 2:61–70, 2004.

C. D. Jones. On the structure of instantaneous plumes in the atmosphere. *Journal of Hazardous Materials*, 7:87–112, 1983.

R. Kadlec. Overland flow in wetlands: Vegetation resistance. *Journal of Hydraulic Engineering - ASCE*, 116:691–707, 1990.

J. C. Kaimal and J. J. Finnigan. *Atmospheric Boundary Layer Flows: Their Structure and Measurement*. Oxford University Press, New York, 1994.

J .C. Kaimal, J. C. Wyngaard, Y. Izumi, and O. R. Coté. Spectral charercteristics of surface layer turbulence. *Quarterly Journal of the Royal Meteorological Society*, 98:563–589, 1972.

U. K. Kaul, D. Kwak, and G. Wagner. A computational study of saddle point separation and horseshoe vortex system. In *AIAA 23rd Aerospace Sciences Meeting*, Reno, NV, 1985. AIAA-85-0182.

M. J. Khan, A. Ahmend, and J. R. Trosper. Dynamics of the juncture vortex. *AIAA Journal*, 33:1273–1278, 1995.

S. A. Kim, D. A. Walker, and R. L. Simpson. Observation and measurements of flow structures in the stagnation region of a wing-body junction. Technical Report VPI&SU Report VPI-E-91-20, Virginia Polytechnic Institute and State University, Blacksburg, VA, 1991.

W. Kim, J. Y. Yoo, and J. Sung. Dynamics of vortex lock-on in a perturbed cylinder wake. *Physics of Fluids*, 18:074103, 2006.

A. R. Kirincich and J. H. Rosman. A comparison of methods for estimating reynolds stress from adcp measurements in wavy environments. *Journal of Atmospheric and Oceanic Technology*, 28:1539–1553, 2011.

G. Kirkil and G. Constantinescu. A numerical study of the laminar necklace vortex system and ite effect on the wake for a circular cylinder. *Physics of Fluids*, 24: 073602, 2012.

S. A. Kitaigordskii, V. P. Krasitskii, and M. M. Zaslavskii. On phillips theory of equilibrium range in the spectra of wind-generated gravity waves. *Journal of Physical Oceanography*, 5:410–420, 1975.

B. Kjerfve, L. B. Miranda, and E. Wolanski. Modelling water circulation in an estuary and intertidal salt marsh system. *Netherlands Journal of Sea Research*, 28:141–147, 1991.

D. L. Koch and A. J. C. Ladd. Moderate reynolds number flows through periodic and random arrays of aligned cylinders. *Journal of Fluid Mechanics*, 349:31–66, 1997.

A. N. Kolmogorov. Dissipation of energy a locally isotropic turbulence. *Doklady Akademii Nauk SSSR*, 32:16–18, 1941.

P.K. Kundu and I.M. Cohen. *Fluid Mechanics*. Elsevier Academic Press, 2004.

J. K. Lee, L. C. Roig, H. L. Jenter, and H. M. Visser. Drag coefficients for modeling flow through emergent vegetation in the Florida Everglades. *Ecological Engineering*, 22:237–248, 2004.

J. T. Lee and G. L. Stone. The use of eulerian initial conditions in a Lagrangian model of turbulence diffusion. In *Sixth Symposium on Turbulence and Diffusion*, Boston, MA, 1983.

L. A. Leonard and M. E. Luther. Flow hydrodynamics in tidal marsh canopies. *Limnology and Oceanography*, 40:1474–1484, 1995.

L. B. Leopold, J. N. Collins, and L. M. Collins. Hydrology of some tidal channels in estuarine marshland near San Francisco. *Catena*, 20:469–493, 1993.

Q. Liao and E. A. Cowen. Relative dispersion of a scalar plume in a turbulent boundary layer. *Journal of Fluid Mechanics*, 661:412–445, 2010.

K. Lindner. *The Flow Resistance of Cultivated Plants*. PhD thesis, Leichtweiss Institute of Hydraulic Engineering, Technical University of Braunschweig, Germany, 1992.

R. J. Lowe, J. R. Koseff, and S. G. Monismith. Oscillatory flow through submerged canopies: 1. Velocity structure. *Journal of Geophysical Research*, 110:C10016, 2005.

A. K. Luhar, M. F. Hibbard, and M. S. Borgas. A skewed meandering plume model for concentration statistics in the convective boundary layer. *Atmospheric Environment*, 34:3599–3616, 2000.

J. L. Lumley and E. A. Terray. Kinematics of turbulence convected by a random wave field. *Journal of Physical Oceanography*, 13:2000–2007, 1983.

S. C. Luo, X. H. Tong, and B. C. Khoo. Transition phenomena in the wake of a square cylinder. *Journal of Fluids and Structures*, 23(2):227–248, 2007.

D. A. Lyn, S. Einav, W. Rodi, and J. H. Park. A laser-Doppler velocimetry study of the ensemble-averaged characteristics of the turbulent near wake of a square cylinder. *Journal of Fluid Mechanics*, 304:285–319, 1995.

H. G. Maas, A. Grün, and D. Papantoniou. Particle tracking in three dimensional turbulent flows - part 1: Photogrammetric determination of particle coordinates. *Experiments in Fluids*, 15:133–146, 1993.

N. Malik, T. Dracos, and D. Papantoniou. Particle tracking in three dimensional turbulent flows - part 2: Particle tracking. *Experiments in Fluids*, 15:279–294, 1993.

K. H. Mann and J. R. N. Lazier. *Dynamics of marine ecosystems: Biological-physical interactions in the ocean*. Blackwell Science, Malden, MA, 2006.

M. Marro, C. Nironi, P. Salizzoni, and L. Soulhac. Dispersion of a passive scalar fluctuating plume in a turbulent boundary layer. Part II: Analytical modelling. *Boundary-Layer Meteorology*, 156:447–469, 2015.

R. H. Maryon. Determining crosswing variance for low frequency wind meander. *Atmospheric Environment*, 32:115–121, 1998.

S. Mathieson, A. Cattrijsse, M. J. Costa, P. Drake, M. Elliott, J. Gardner, and J. Marchand. Fish assemblages of European tidal marshes: a functional guilds-based comparison. *Marine Ecology Progress Series*, 204:225–242, 2000.

Y. Mazda, D. Kobashi, and S. Okada. Tidal-scale hydrodynamics within mangrove swamps. *Wetlands Ecology and Management*, 13:647–655, 2005.

Y. Mazda, E. Wolanski, and P. V. Ridd. *The role of physical processes in mangrove environments: Manual for the preservation and utilization of mangrove ecosystems.* Terrapub, Tokyo, 2007.

B. W. Melville. Pier and abutment scour: integrated approach. *ASCE Journal of Hydraulic Engineering*, 123:125–136, 1997.

L. F. Moody. Friction factors for pipe flow. *Transactions of the ASME*, 66:671–684, 1944.

P. A. Moore and J. L. Grills. Chemical orientation to food by the crayfish *Orconectes rusticus*: influence of hydrodynamics. *Animal Behavior*, 58:953–963, 1999.

A. Morang, Z. Demirbilek, D. B. King, D. L. Ward, and J. A. Melby. *Coastal Engineering Manual.* U. S. Army Corps of Engineers, Washington, D.C., 2002. Engineer Manual 1110-2-1100.

L. Mortarini, P. Franzese, and E. Ferrero. A fluctuating plume model for concentration fluctuations in a plant canopy. *Atmospheric Environment*, 43:921–927, 2009.

R. J. Murgatroyd. Estimations from geostrophic trajectories of horizontal diffusivity in the mid-latitude troposphere and lower stratosphere. *Quarterly Journal of the Royal Meteorological Society*, 95:40–61, 1969.

J. Murlis. The structure of odor plumes. In T. L. Payne, M. C. Birch, and C. E. J. Kennedy, editors, *Mechanisms in insect olfaction.* Clarendon Press, Oxford, UK, 1986.

J. Murlis and C. D. Jones. Fine-scale structure of odor plumes in relation to insect orientation to distant pheromone and other attractant sources. *Physiological Entomology*, 6:71–86, 1981.

A. Murota, T. Fukuhara, and M. Sato. Turbulence structure in vegetated open channel flows. *Journal of Hydroscience and Hydraulic Engineering*, 2:47–61, 1984.

K. R. Mylne. Concentration fluctuation measurements in a plume dispersing in a stable surface layer. *Boundary-Layer Meteorology*, 60:15–48, 1992.

K. R. Mylne. The vertical profile of concentration fluctuations in near-surface plumes. *Boundary-Layer Meteorology*, 65:111–136, 1993.

S. Nakagawa, K. Nitta, and M. Senda. An experimental study on unsteady turbulent near wake of a rectangular cylinder in channel flow. *Experiments in Fluids*, 27: 284–294, 1999.

H. M. Nepf. Drag, turbulence, and diffusion in flow through emergent vegetation. *Water Reseources Research*, 35:479–489, 1999.

C. Nironi, P. Salizzoni, M. Marro, P. Mejean, N. Grosjean, and L. Soulhac. Dispersion of a passive scalar fluctuating plume in a turbulent boundary layer. Part I: Velocity and concentration measurements. *Boundary-Layer Meteorology*, 156:415–446, 2015.

D. Oettl, R. A. Almbauer, and P. J. Sturm. A new method to estimate diffusion in stable, low wind conditions. *Journal of Applied Meteorology*, 40:259–268, 2001.

D. Oettl, A. Goulart, G. Degrazia, and D. Anfossi. A new hypothesis on meandering atmospheric flows in low wind speed conditions. *Atmospheric Environment*, 39: 1739–1748, 2005.

A. Okubo. Some remarks on the importance of the "shear effect" on horizontal diffusion. *Journal of the Oceanographic Society of Japan*, 24:60–69, 1968.

A. Okubo. Oceanic diffusion diagrams. *Deep-Sea Research*, 18:789–802, 1971.

N. A. Ozturk, A. Akcayoglu, and B. Sahin. Downstream particle image velocimetry measurements of a circular cylinder-plate junction. *Proceedings of the Institution of Mechanical Engineers Part C - Journal of Mechanical Engineering Science*, 223: 1837–1849, 2009.

B. B. Parker. The relative importance of the various nonlinear mechanisms in a wide range of tidal interactions (review). In B. B. Parker, editor, *Tidal Hydrodynamics*. Wiley, New York, 1991.

J. S. Pethick. Velocity surges and asymmetry in tidal channels. *Estuarine and Coastal Marine Science*, 11:331–345, 1980.

F. J. Pierce and J. Shin. The development of a turbulent vortex system. *Journal of Fluids Engineering*, 114:559–565, 1992.

S. B. Pope. *Turbulent Flows*. Cambridge University Press, Cambridge, 2000.

A. W. Pringle. Erosion of a cyclic saltmarsh in Morecambe Bay, North-West England. *Earth Surface Processes and Landforms*, 20:387–405, 1995.

M. Raffel, C. Willert, S. Wereley, and J. Kompenhans. *Particle Image Velocimetry: A Practical Guide*. Springer-Verlag, 2007.

S. Rahman and D. R. Webster. The effect of bed roughness on scalar fluctuations in turbulent boundary layers. *Experiments in Fluids*, 38:372–384, 2005.

M. R. Raupach, R. A. Antonia, and S. Rajagopalan. Rough-wall turbulent boundary layers. *Applied Mechanics Reviews*, 44:1–25, 1991.

A. M. Reynolds. Representation of internal plume structure in Gifford's meandering plume model. *Atmospheric Environment*, 34:2539–2545, 2000.

W. C. Reynolds and A. K. M. F. Hussain. The mechanics of an organized wave in turbulent shear flow. Part 3. Theoretical models and comparisons with experiments. *Journal of Fluid Mechanics*, 54:263–288, 1972.

L. F. Richardson. Atmospheric diffusion shown on a distance-neighbor graph. *Proceedings of the Royal Society of London*, A110:709–739, 1926.

D. J. Ride. A model for the observed intermittency of a meandering plume. *Journal of Hazardous Materials*, 19:131–137, 1988.

K. C. Riffe, S. M. Henderson, and J. C. Mullarney. Wave dissipation by flexible vegetation. *Geophysical Research Letters*, 38:L18607, 2011.

A. Rinaldo, S. Fagherazzi, S. Lanzoni, M. Marani, and W. E. Dietrich. Tidal networks 2. watershed delineation and comparative network morphology. *Water Resources Research*, 35:3905–3917, 1999a.

A. Rinaldo, S. Fagherazzi, S. Lanzoni, M. Marani, and W. E. Dietrich. Tidal networks 3. landscape-forming discharges and studies in empirical geomorphic relationships. *Water Resources Research*, 35:3919–3929, 1999b.

P. J. Roberts and D. R. Webster. Turbulent diffusion. In H. H. Shen, A. H. D. Cheng, K. Wang, M. H. Teng, and C. C. K. Liu, editors, *Environmental Fluid Mechanics: Theories and Applications*. American Society of Civil Engineers, Reston, VA, 2002.

E. P. Rood. *Experimental investigation of the turbulent large scale temporal flow in the wing-body junction*. PhD thesis, The Catholic University of America, Washington, DC, 1984a.

E. P. Rood. The seperate spatial extents of the trailing horseshoe root vortex legs from a wing and plate junction. In *AIAA 17th Fluid Dynamics, Plasma Dynamics, and Lasers Conference*, Snowmass, CO, 1984b. AIAA-84-1526.

E. P. Rood and J. E. Keller. Evidence of large scale time dependent flow in the wing-wall interaction wake. In D. C. Wiggert, editor, *Unsteady Turbulent Boundary Layers and Friction*. The American Society of Mechanical Engineers: Fluids Engineering Division, New York, 1984.

A. K. Saha, K. Muralidhar, and G. Biswas. Vortex structures and kinetic energy budget in two-dimensional flow past a square cylinder. *Computers and Fluids*, 29: 669–694, 2000.

B. Sahin and N. A. Ozturk. Behavior of flow at the junction of cylinder and base plate in deep water. *Measurement*, 42:225–240, 2009.

B. Sahin, N. A. Ozturk, and H. Akilli. Horseshoe vortex system in the vicinity of the vertical cylinder mounted on a flat plate. *Flow Measurement and Instrumentation*, 18:57–68, 2007.

C. V. Seal, C. R. Smith, O. Akin, and D. Rockwell. Quantitative characteristics of laminar, unsteady necklace vortex system at a rectangular block-flat plate juncture. *Journal of Fluid Mechanics*, 286:117–135, 1995.

H. E. Seim, J. O. Blanton, and T. Gross. Direct stress measurements in a shallow, sinuous estuary. *Continental Shelf Research*, 22:1565–1578, 2002.

J. M. Seitzman and R. K. Hanson. Planar fluorescence imaging in gases. In A.M.K.P. Taylor, editor, *Instrumentation for Flows with Combustion*. Academic Press, Cambridge, Massachusetts, 1993.

W. J. Shaw and J. H. Trowbridge. The direct estimation of near-bottom turbulent fluxes in the presence of energetic wave motions. *Journal of Atmospheric and Oceanic Technology*, 18:1540–1557, 2001.

R. L. Simpson. Junction flows. *Annual Review of Fluid Mechanics*, 33:415–443, 2001.

D. L. Smee and M. J. Weissburg. Clamming up: Environmental forces diminish the perceptive ability of bivalve prey. *Ecology*, 87:1587–1598, 2006.

R. L. Soulsby. Similarity scaling of turbulence spectra in marine and atmospheric boundary layers. *Journal of Physical Oceanography*, 7:934–937, 1977.

P. R. Spalart. Direct simulation of a turbulent boundary layer up to $re_\theta = 1410$. *Journal of Fluid Mechanics*, 187:61–98, 1988.

M. Spalding, A. McIvor, M. Beck, I. Möller, D. Reed, P. Rubinoff, T. Spencer, T. Tolhurst, T. Wamsley, B. van Wesenbeeck, E. Wolanski, and C. Woodroffe. Coastal ecosystems: a critical element of risk reduction. *Conservation Letters*, 11:1–9, 2013.

P. E. Speer and D. G. Aubrey. A study of non-linear tidal propagation in shallow inlet/estuarine systems part 2: Theory. *Estuarine, Coastal and Shelf Science*, 21: 207–224, 1985.

M. T. Stacey, E. A. Cowen, T. M. Powell, E. Dobbins, S. G. Monismith, and J. R. Koseff. Plume dispersion in a stratified, near-coastal flow: measurements and modeling. *Continental Shelf Research*, 20:637–663, 2000.

T. Stoesser, C. A. M. E. Wilson, P. D. Bates, and A. Dittrich. Application of a 3d numerical model to a river with vegetated floodplains. *Journal of Hydroinformatics*, 5:99–112, 2003.

B. M. Stone and H. T. Shen. Hydraulic resistance of flow in channels with cylindrical roughness. *Journal of Hydraulic Engineering*, 128:500–506, 2002.

R. I. Sykes. The variance in time-averaged samples from an intermittent plume. *Atmospheric Environment*, 18:121–123, 1984.

Y. Tanino and H. M. Nepf. Laboratory investigation of mean drag in a random array of rigid, emergent cylinders. *Journal of Hydraulic Engineering*, 134:34–41, 2008.

G. I. Taylor. Diffusion by continuous movements. *Proceedings of the London Mathematical Society*, 2:196, 1921.

S. Temmerman, T. J. Bouma, G. Govers, and Z. B. D. Lauwaet. Flow paths of water and sediment in a tidal marsh: Relations with marsh developmental stage and tidal inundation height. *Estuaries*, 28:338–352, 2005a.

S. Temmerman, T. J. Bouma, G. Govers, Z. B. Wang, M. B. De Vries, and P. M. J. Herman. Impact of vegetation on flow routing and sedimentation patterns: Three-dimensional modeling for a tidal marsh. *Journal of Geophysical Research Earth Surface*, 110:F04019, 2005b.

S. Temmerman, P. Moonen, J. Schoelynck, G. Govers, and T. J. Bouma. Impact of vegetation die-off on spatial flow patterns over a tidal marsh. *Geophysical Research Letters*, 39:L03406, 2012.

H. Tennekes. Similarity relations, scaling laws and spectral dynamics. In F. Niewstadt and H. Van Dop, editors, *Atmospheric turbulence and air pollution modelling*. D. Reidel Publishing Company, Dordrecht, 1982.

H. Tennekes and J.L. Lumley. *A first course in turbulence*. MIT Press, Cambridge, MA, 1972.

A. S. W. Thomas. The unsteady characteristics of laminar junction flow. *Physics of Fluids*, 30:283–285, 1987.

R. E. Thompson and J. F. R. Gower. Vortex streets in the wake of the Aleutian Islands. *Monthly Weather Review*, 105:873–884, 1977.

R. Torres and R. Styles. Effects of topographic structure on salt marsh currents. *Journal of Geophysical Research - Earth Surface*, 112:F02023, 2007.

H. J. Tracy and C. M. Lester. Resistance coefficients and velocity distribution smooth rectangular channel. Technical Report 1592-A, United States Geological Survey, 1961.

J. H. Trowbridge. On a technique for measurement of turbulent shear stress in the presence of surface waves. *Journal of Atmospheric and Oceanic Technology*, 15: 290–298, 1998.

J. H. Trowbridge and S. Elgar. Turbulence measurements in the surf zone. *Journal of Physical Oceanography*, 31:2403–2417, 2001.

V. A. Tsihrintzis. Variation of roughness coefficients for unsubmerged and submerged vegetation discussion. *Journal of Hydraulic Engineering*, 127:241–244, 2001.

C. F. v. Carmer and G. H. Jirka. On turbulence and transport in shallow wake flows. *Environmental Hydraulics and Eco-Hydraulics*, Theme B, Proceedings:80–86, 2001.

M. Van Dyke. *An Album of Fluid Motion*. The Parabolic Press, Stanford, 1982.

M. Van Dyke. *An Album of Fluid Motion*. The Parabolic Press, Stanford, 2002.

W. Vandenbruwaene, C. Schwarz, T. J. Bouma, P. Meire, and S. Temmerman. Landscape-scale flow patterns over a vegetated tidal marsh and unvegetated tidal flat: Implications for the landform properties of the intertidal floodplain. *Geomorphology*, 231:40–52, 2015.

M. R. Visbal. Structure of laminar junction flows. *AIAA Journal*, 29:1273–1282, 1991.

C. F. von Carmer, A. C. Rummel, and G. H. Jirka. Mass transport in shallow turbulent wake flow by planar concentration analysis technique. *Journal of Hydraulic Engineering*, 135:257–270, 2009.

T. von Karman. Über laminare und turbulente Reibyng. *Zeitschrift für Angewandte Mathematik und Mechanik*, 1:233–252, 1921.

R. K. Walter, M. E. Squibb, C. B. Woodson, J. R. Koseff, and S. G. Monismith. Stratified turbulence in the nearshore coastal ocean: Dynamics and evolution in the presence of internal bores. *Journal of Geophysical Research: Oceans*, 119:8709–8730, 2014.

F. C. Wang, T. S. Lu, and W. B. Sikora. Intertidal marsh suspended sediment transport processes. Terrebonne Bay, Louisiana, USA. *Journal of Coastal Research*, 9:209–220, 1993.

G. Webel and M. Schatzmann. Transverse mixing in open channel flow. *Journal of Hydraulic Engineering*, 110:423–435, 1984.

D. R. Webster. Structure of turbulent chemical plumes. In R. L. Woodfin, editor, *Trace chemical sensing of explosives*. John Wiley and Sons, Hoboken, NJ, 2007.

D. R. Webster, S. Rahman, and L. P. Dosi. Laser-induced fluorescence measurements of a turbulent plume. *Journal of Engineering Mechanics*, 129:1130–1137, 2003.

M. J. Weissburg and R. K. Zimmer-Faust. Life and death in a moving fluid: hydrodynamic effects on chemosensory-mediated predation. *Ecology*, 74:1428–1443, 1993.

M. J. Weissburg and R. K. Zimmer-Faust. Odor plumes and how blue crabs use them in finding prey. *Journal of Experimental Biology*, 197:349–375, 1994.

A. M. Wilson and L. R. Gardner. Tidally driven groundwater flow and solute exchange in a marsh: Numerical simulations. *Water Resources Research*, 42:W01405, 2006.

D. J. Wilson, A. G. Robins, and J. E. Fackrell. Intermittency and conditionally-averaged concentration fluctuation statistics in plumes. *Atmospheric Environment*, 19:1053–1064, 1985.

M. L. Wilson and M. J. Weissburg. Biotic structure indirectly affects associated prey in a predator-specific manner via changes in the sensory environment. *Oecologia*, 171:427–438, 2013.

M. L. Wilson, D. R. Webster, and M. J. Weissburg. Spatial and temporal variation in the hydrodynamic landscape in intertidal salt marsh systems. *Limnology and Oceanography: Fluids and Environments*, 3:156–172, 2013.

E. Wolanski and M. Elliott. *Estuarine Ecohydrology (2nd Ed.)*. Elsevier, Amsterdam, 2015.

E. Wolanski, J. Imberger, and M. L. Heron. Island wakes in shallow coastal waters. *Journal of Geophysical Research*, 89:10553–10569, 1984.

F. C. Wu, H. W. Shen, and Y. J. Chou. Variation of roughness coefficients for unsubmerged and submerged vegetation. *Journal of Hydraulic Engineering*, 125: 934–942, 1999.

W. Wu. A 3-D phase-averaged model for shallow-water flow with waves in vegetated water. *Ocean Dynamics*, 64:1061–1071, 2014.

E. Yee and D. J. Wilson. A comparison of the detailed structure in dispersing tracer plumes measured in grid-generated turbulence with a meandering plume model incorporating internal fluctuations. *Boundary-Layer Meteorology*, 94:253–296, 2000.

E. Yee, D. J. Wilson, and B. W. Zelt. Probability distributions of concentration fluctuations of a weakly diffusive passive plume in a turbulent boundary layer. *Boundary-Layer Meteorology*, 64:321–354, 1993.

E. Yee, R. Chan, P. R. Kosteniuk, G. M. Chandler, C. A. Biltoft, and J. F. Bowers. Experimental measurements of concentration fluctuations and scales in a dispersing plume in the atmospheric surface layer obtaining using a very fast response concentration detector. *Journal of Applied Meteorology*, 33:996–1016, 1994.

E. Yee, R. Chan, P. R. Kosteniuk, G. M. Chandler, C. A. Biltoft, and J. F. Bowers. The vertical structure of concentration fluctuation statistics in plumes dispersion in the atmospheric surface layer. *Boundary-Layer Meteorology*, 76:41–67, 1995.

I. R. Young. *Wind-generated ocean waves*. Elsevier, Amsterdam, 1999.

I. R. Young and L. A. Verhagen. The growth of fetch limited waves in water of finite depth. part 2. spectral wave evolution. *Coastal Engineering*, 29:79–99, 1996.

L. Zheng, C. Chen, and H. Liu. A modeling study of the Satilla River Estuary, Georgia. 1: Flooding-drying process and water exchange over the salt marsh-estuary-shelf complex. *Estuaries*, 26:651–669, 2003.